Plasmon-mediated energy transfer and super-resolution imaging in the near field of nanostructured materials

Dorian Bouchet

THÈSE DE DOCTORAT

de l'Université de recherche Paris Sciences et Lettres
PSL Research University

Préparée à l'ESPCI Paris

Plasmon-mediated energy transfer and super-resolution imaging in the near field of nanostructured materials

École doctorale n°564
PHYSIQUE EN ÎLE-DE-FRANCE

Spécialité PHYSIQUE

Soutenue par **Dorian BOUCHET**
le 27 novembre 2017

Dirigée par **Valentina KRACHMALNICOFF**
et par **Yannick DE WILDE**

COMPOSITION DU JURY :

Jean-Jacques GREFFET
Président

Pascale SENELLART
Rapporteur

Fabrice VALLÉE
Rapporteur

Sophie BRASSELET
Examinateur

Yannick DE WILDE
Directeur de thèse

Valentina KRACHMALNICOFF
Encadrante

Rémi CARMINATI
Invité

Thèse de doctorat de l'Université de recherche
Paris Sciences et Lettres

Présentée par

Dorian Bouchet

à l'Institut Langevin – Ondes et Images

Plasmon-mediated energy transfer and super-resolution imaging in the near field of nanostructured materials

---

Soutenue le 27 novembre 2017
devant le jury composé de :

Jean-Jacques Greffet	Président
Pascale Senellart	Rapporteur
Fabrice Vallée	Rapporteur
Sophie Brasselet	Examinateur
Yannick De Wilde	Directeur de thèse
Valentina Krachmalnicoff	Encadrante
Rémi Carminati	Invité

Remerciements

Pour commencer ce mémoire de thèse, je tiens à remercier les personnes que j'ai côtoyées quotidiennement à l'Institut Langevin et qui, de par leur enthousiasme et leur simplicité, font de la recherche une passion.

Je pense tout d'abord à Valentina Krachmalnicoff, qui a encadré mes travaux de thèse. Merci pour la confiance que tu m'as accordé pendant ces années ; grâce à ton soutien scientifique et humain, j'ai pu découvrir un domaine qui était nouveau pour moi, avec le privilège de pouvoir aborder une certaine variété de sujets. Merci pour tout Valentina, ce fut une vraie chance d'avoir pu effectuer ma thèse avec toi.

Je pense aussi à mon directeur de thèse Yannick de Wilde. Merci pour ta disponibilité ainsi que pour ton enthousiasme, qui est toujours largement supérieur à une manip qui ne fonctionne pas. Je pense également à Rémi Carminati, qui m'a aussi suivi pendant ces trois années de thèse. Merci d'avoir rendu accessible des idées parfois complexes, nos discussions ont été pour moi une forte source de motivation. Et je pense bien sûr à Ignacio Izeddin, à Sébastien Bidault et à Romain Pierrat, qui m'ont régulièrement éclairé au cours de ma thèse. Merci aussi à Samuel Grésillon, à Arthur Goetschy, à Pierre Millien, à Florian Bigourdan ; merci à vous tous d'avoir toujours donné votre temps sans compter.

Pendant quelques mois, j'ai pu travailler en binôme avec Mathieu Mivelle puis avec Jules Scholler. Mathieu a récemment obtenu un poste au CNRS et Jules commence une thèse à l'Institut Langevin. Je vous souhaite le meilleur pour vos projets respectifs ! Je souhaite également bonne chance à Guillaume Blanquer et à Vivien Loo pour la suite de leurs travaux au sein de l'équipe.

Les travaux effectués lors de ma thèse ont impliqué de nombreuses personnes à qui je souhaite exprimer ma gratitude. Je remercie Da Cao, Alexandre Cazé et Etienne Castanié pour le travail qu'ils ont effectué avant ma thèse et que j'ai largement utilisé ; Emmanuel Lhuillier pour la qualité des boîtes quantiques qu'il a synthétisé ; Sandrine Ithurria, Thomas Pons et Nicolas Lequeux pour leurs conseils concernant la préparation d'échantillons ; Abdel Souilah pour la conception de pièces mécaniques ; Ivan Rech et Angelo Gulinatti pour les détecteurs de photons qu'ils ont conçus ; Julien Proust, Bruno Gallas, Igor Ozerov et Nicolas Bonod pour les antennes diélectriques qu'ils ont développées et fabriquées.

J'adresse mes sincères remerciements à Pascale Senellart et Fabrice Vallée, qui ont été les rapporteurs de cette thèse, ainsi qu'à Sophie Brasselet et à Jean-Jacques Greffet d'avoir participé à mon jury de thèse. Je remercie également Arnaud Tourin, pour sa disponibilité en tant que directeur de laboratoire ainsi que pour son rôle lors de l'attribution du financement de ma thèse. J'aimerais aussi remercier Rodolphe Vaillon, Laurent Lebrun et Denise Blanc, qui ont été mes professeurs à l'INSA de Lyon. Merci à vous pour vos excellents cours ainsi que pour vos conseils lors de mon choix de thèse.

Je pense aussi aux copains de l'INSA et à ceux de Sophie Barat, merci pour ces années avec vous. Merci à ma famille, en particulier à ma grand-mère Nanou et à mes parents, pour votre patience et pour tout ce que vous nous avez offert. Merci à Élodie pour son aide en maths pendant ma thèse (tu as gardé un niveau correct en proba) et à Célia pour nous rappeler que les sciences humaines sont aussi des sciences (même si c'est dur à croire).

Enfin, je remercie Céline, notamment pour avoir corrigé de nombreuses fautes d'anglais dans ma thèse ainsi que pour ses mots de soutien signés Richard Feynman. Merci de partager ces moments avec moi.

Résumé

Dans cette thèse, nous associons mesures expérimentales et modélisation des données pour étudier l'émission spontanée d'émetteurs fluorescents en environnement nano-structuré. Le mémoire est organisé en deux parties.

Dans la première partie, nous étudions le transfert d'énergie entre émetteurs fluorescents en environnement plasmonique et sur des distances micrométriques. Pour commencer, nous caractérisons le transfert d'énergie entre deux ensembles d'émetteurs situés en champ proche d'une surface d'argent. Nous déterminons ainsi la dépendance en distance du taux de transfert d'énergie sur des distances micrométriques. Nous couplons ensuite une boite quantique et une bille fluorescente à un nano-fil d'argent et nous étudions le transfert d'énergie entre ces deux émetteurs, distants de plusieurs micromètres. Nous démontrons notamment le clignotement corrélé de ces deux émetteurs grâce à l'étude de la fonction de corrélation de leur intensité de fluorescence.

Dans la seconde partie, nous sondons les variations spatiales de densité locale d'états électromagnétiques induites par des environnements nano-structurés grâce à différentes techniques de microscopie à super-résolution. A l'aide d'un microscope à balayage, nous réalisons tout d'abord une étude en trois dimensions de l'interaction de champ proche entre une bille fluorescente et différentes antennes en silicium. Nous introduisons ensuite une technique stochastique permettant de déterminer expérimentalement la position et le taux d'amortissement de molécules uniques photo-activées, avec une précision de localisation de l'ordre de 10 nm. Enfin, nous utilisons l'information de Fisher afin d'estimer les bornes inférieures de l'erreur type des estimations de positions et de taux d'amortissement réalisées dans le cadre de mesures sur molécules uniques.

Mots-clés

Durée de vie de fluorescence, Champ proche, Emission spontanée, Densité d'états électromagnétiques, Plasmon de surface, antenne diélectrique, Imagerie de super-résolution, Molécule unique, Borne de Cramér-Rao

Summary

In this thesis, we perform experimental measurements and data modelling to investigate spontaneous emission of fluorescent emitters in nanostructured environments. The manuscript is organised into two main parts.

In the first part, we study micrometre-range energy transfer between fluorescent emitters in plasmonic environments. First of all, we characterise plasmon-mediated energy transfer between ensembles of fluorescent emitters located in the near field of a silver film. We thus determine the distance dependence of the energy transfer rate over micrometre distances. We then couple a single quantum dot and a fluorescent nanobead to a silver nanowire and we study evidences of the energy transfer between the two emitters, separated by several micrometres. We notably demonstrate a correlated blinking of the two emitters through the study of the correlation function of their fluorescence intensity.

In the second part, we probe sub-wavelength spatial variations of the local density of electromagnetic states induced by nanostructured environments by means of different super-resolution microscopy techniques. To start with, we perform a three-dimensional study of the near-field interaction between a fluorescent nanobead and different silicon nanoantennas using a scanning-probe microscope. We then introduce a stochastic technique to experimentally determine the position and the fluorescence decay rate of single photo-activated molecules, with a localisation precision of the order of 10 nm. Finally, we use the Fisher information to estimate lower bounds on the standard errors on position and decay rate estimates performed in the context of single-molecule microscopy.

Keywords

Fluorescence lifetime, Near field, Spontaneous emission, Electromagnetic density of states, Surface plasmon, Dielectric antenna, Super-resolution imaging, Single molecule, Cramér-Rao bound

Contents

General introduction

Nature provides us with a complexity which is a fantastic playground for scientists. Physics aims at modelling this complexity, and experiments are performed in order to confirm or infirm that nature does operate in the way predicted by theories. From this point of view, the study of the interaction between light and matter is an important field of fundamental research, with several potential applications. Indeed, light-matter interaction is responsible of most of our perception of the world. A better understanding of this interaction is thus likely to provide us with new observation tools to study living organisms for instance. Furthermore, it will perhaps allow us to collect more efficiently the energy radiated by the sun, which is an important source of renewable energy on earth.

In this thesis, we study specific aspects of light-matter interaction on the nanometre scale and at visible frequencies. The wavelength of light is then comparable to the distances in-between the objects, resulting in a specific interaction between them referred to as *near-field* interaction. This interaction can be characterised by measuring the properties of nanometre-scale fluorescent sources in different types of nanostructured environments. We are specifically interested in the fluorescence decay rate noted Γ which is the average number of emitted photons per unit time. The decay rate is not an intrinsic emission property but it can be either enhanced or reduced, depending on the local environment of the emitter. For instance, optical antennas can be designed to enhance the rate of spontaneous emission, in order to obtain bright nanosources emitting photons at a high rate. In biology, several applications including sensing and imaging techniques are based on the determination of decay rate variations induced by the environment.

In the following paragraphs, we will present several experiments extracted from the literature in order to introduce different concepts exploited in this thesis. The first experiment shows the influence of a silver mirror upon the decay rate of fluorescent emitters. The second experiment details a technique used to precisely determine the position of fluorescent emitters, well below the diffraction limit. For the sake of curiosity, we will also present acoustic analogues of these experiments, illustrating that electromagnetic waves and acoustic waves can be described by using a similar formalism.

Drexhage's experiment Drexhage's experiment is a milestone in the field of nanophotonics. In 1970, he demonstrated that the excited-state lifetime of a fluorescent emitter

depends on its local environment [1]. To do so, he studied the spontaneous emission of a thin layer of europium ions (Eu^{3+}) located above a silver mirror, as represented in Fig. 1 (inset). Using several layers of fatty acids as a spacer, he was able to precisely control the distance d between the ions and the mirror. Thus, he could measure the distance dependence of the lifetime enhancement due to the silver mirror, as shown in Fig. 1. The observed oscillations are explained by the interferences between the field reflected by the mirror and the non-reflected part, using an orientational average for the dipole moment of the ions. At this time, the dissipation of energy within the materials was neglected, explaining the disagreement between the theory and the experiment at small distance from the mirror. However, this experiment remains the first experimental evidence of the influence of the environment on spontaneous emission.

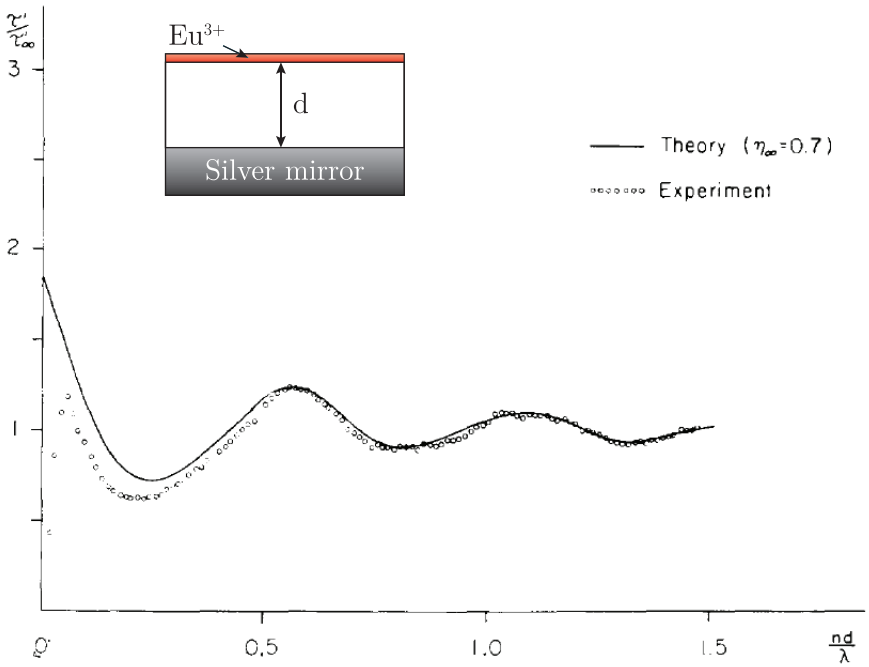

Figure 1 – *Excited-state lifetime enhancement versus distance to the silver mirror. Image reproduced from Ref. [1]. Inset: Sketch of the experiment.*

Recently, an analogue of this experiment using sound waves was carried out by Langguth *et al.* [2]. For this purpose, the authors used a Chinese gong located in front of a concrete wall acting as a reflector, as represented in Fig. 2 (left). The gong was excited using a wooden sphere rolling down a rail, and the response of the gong was measured using a small magnet glued on the backside of the gong. By inducing a current in a pickup coil, the vibrations of the gong could be monitored in the time domain. Then, the authors identified the different vibration modes of the gong by performing a Fourier transform on the signal. For the two lowest modes, they fitted Lorentzian functions to the observed peaks and they recovered the resonance frequency f and the damping rate γ. By performing this experiment for several distance d between the gong and the wall, they could study the distance dependence of both the resonance frequency and the damping rate for the two vibration modes, as shown in Fig. 2 (right). For both modes, the damping rate γ shows several oscillations that are the direct analogue of the oscillations of the fluorescence decay rate observed by Drexhage. As in the original experiment, these oscillations are explained by the interferences between the field reflected by the mirror and the non-reflected part.

In addition, the shift of the resonance frequency due to the presence of the reflector can also be observed, as opposed to experiments in optics for which the expected frequency shifts are extremely small as compared to the linewidth of the fluorescent emitters.

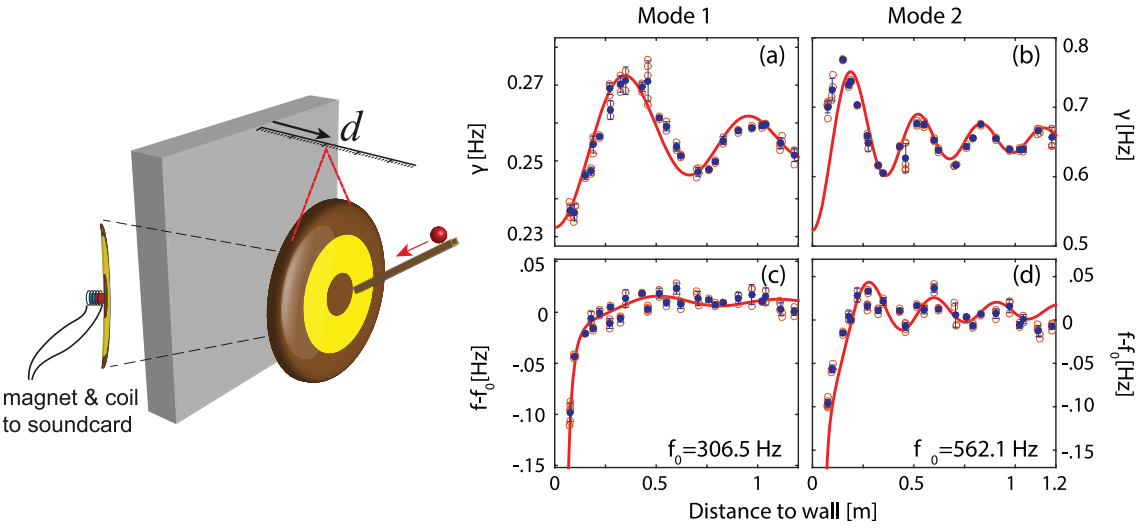

Figure 2 – *Left: Sketch of the time-domain version of Drexhage's experiment for an acoustic source. Right: Damping rate and frequency shift versus distance to the wall for the two lowest frequency modes. Images reproduced from Ref. [2].*

From these two experiments, we can see that the spontaneous emission rate of fluorescent emitters – and equivalently the linewidth of vibration modes of a Chinese gong – can be tuned using a simple reflector. These effects can be described in terms of spatial variations in the local density of states (LDOS) caused by the reflector. The influence of the density of electromagnetic states upon spontaneous emission is a central theme in this thesis, since we will primarily study spontaneous emission of fluorescent emitters in various environments.

Photo-activated localisation microscopy Classically, the resolution of optical microscopy is assumed to be limited to approximately 300 nm due to the diffraction limit. However, the resolution can be greatly improved if only one pointlike object emits in a diffraction-limited region at a single time. One major step towards the achievement of high resolution imaging at optical frequencies was achieved in 2006 by Betzig *et al.* with the development of photo-activated localisation microscopy (PALM) [3]. The authors developed a method to isolate single molecules at high density based on the serial photo-activation and photobleaching of fluorescent molecules. To do so, photo-activatable fluorescent proteins must be tagged on different cells of interest. A brief laser pulse randomly activates a few molecules, and a continuous laser is then used to excite them until photobleaching. During this time, an electron-multiplying charge-coupled device (EM-CCD) camera records wide-field images of the sample forming an image stack from which more than 10^5 molecules can usually be localised, as shown in Fig. 3 (left). A few diffraction limited spots can indeed be identified on many frames (frames A to D). However, the individual emitters can be localised with a much higher precision (frames A' to D') by fitting the expected PSF to each of these individual distributions. By repeating this procedure many times, it is possible to reconstruct an image with a resolution down to 10 nm (frames E' and F'). In comparison to the diffraction limited images (frames E and F), the achieved

enhancement of the resolution is remarkable. Using this technique, the authors imaged intra-cellular structures inside a COS-7 cell derived from an African green monkey kidney tissue. Figure 3 (right) shows the reconstructed image. The achieved resolution allowed the authors to discern the distribution of specific target proteins (CD63 antigens) inside a lysosome – a specialised subunit within the cell acting as a waste disposal system. This work contributed to the attribution of the Nobel Prize in Chemistry 2014 to Eric Betzig, Stefan Hell and William Moerner for the development of super-resolved fluorescence microscopy.

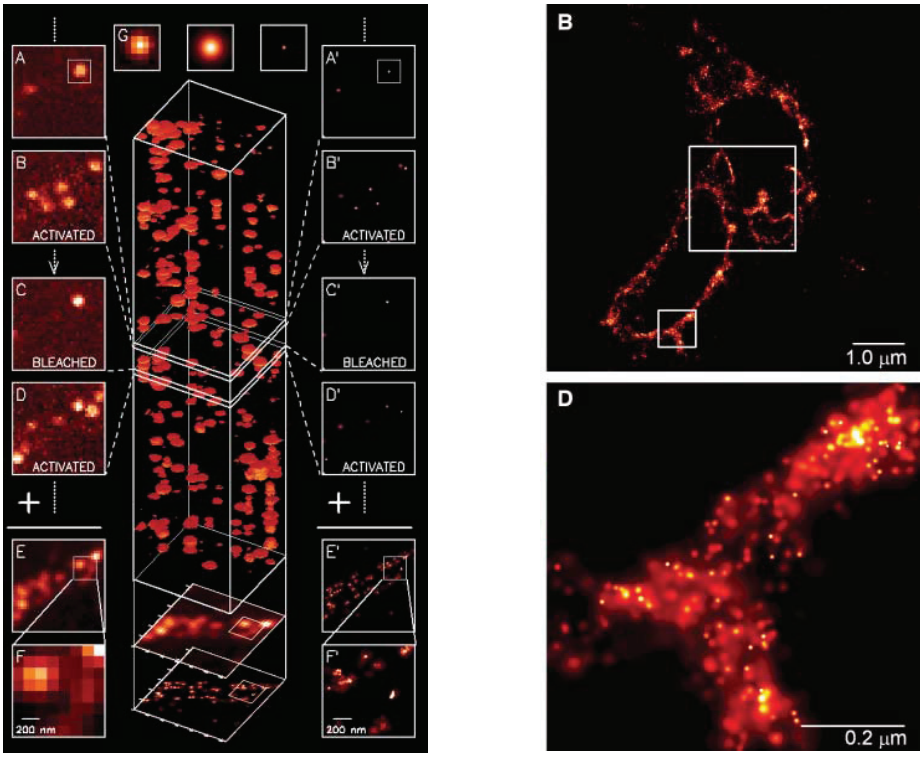

Figure 3 – *Left: Scheme of principle of a PALM experiment. The vertical parallelepiped represents the acquisition over time of a large number of frames. Right: Reconstructed images of intra-cellular structures. The image on the top is the reconstructed wide-field image. The image on the bottom is a magnified view extracted from the smaller box. Images reproduced from Ref. [3].*

Errico *et al.* recently proposed an adaptation of this method for the imaging of blood flow using ultrasound frequencies [4]. Instead of using fluorescent molecules, the authors used the scattering properties of 3-µm-diameter microbubbles at ultrasound frequencies. These inert contrast agents were injected in a rat vein and were observed using an ultrafast ultrasound scanner. Then, the signal scattered by each microbubble was analysed in order to retrieve the position of the bubble during its travel in the brain vessels. By finding the centroid of the signal measured from each bubble, the authors achieved a resolution of the order of 10 µm, well below the diffraction limit for ultrasound waves which is around 1 mm. Moreover, the velocity of each microbubble was evaluated by tracking the position of each bubble in time, as illustrated in Fig. 4 (left). Hence, the authors retrieved the in-plane velocity of the blood flow with a large dynamic range (from 1 mm/s to 14 mm/s). Figure 4 (right) shows a complete functional map of the cerebrovascular system in a living

rat, obtained using this technique. On this map, we can clearly identify different vessels with opposite blood flow directions and different velocities, depending on their diameter. This technique is an interesting tool to investigate the various diseases that modify the microvascular blood flow – such as arteriosclerosis – since the approach allows a precise determination of both the position and the velocity of contrast agents in blood.

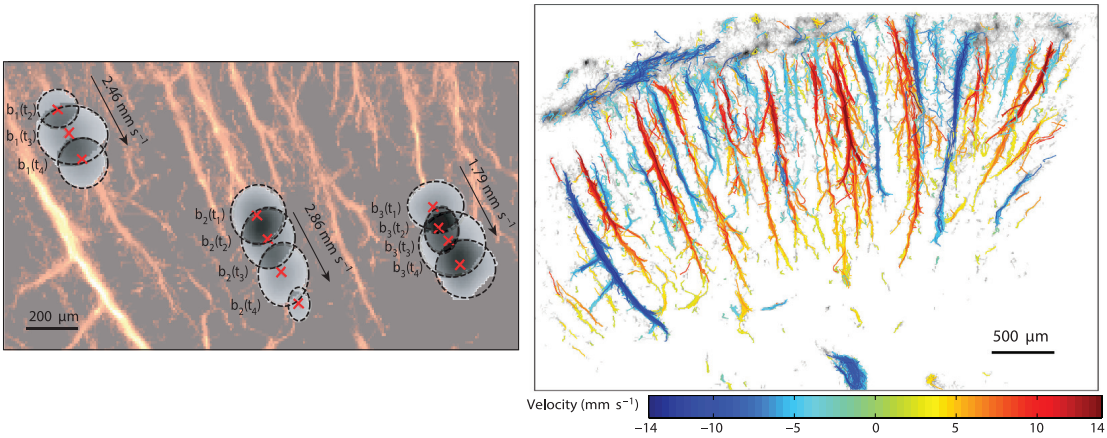

Figure 4 – *Left: Sketch of the localisation and the tracking of single microbubbles. Right: Reconstructed image of the blood flow velocity in the rat brain. Images reproduced from Ref. [4].*

From these two experiments, we can see that it is possible to retrieve the position of a single emitter – either a fluorescent molecule or a microbubble – with a very high precision. Then, successive measurements on different emitters can be used to reconstruct a super-resolved image. The resolution is then determined by the precision of position estimations for the individual emitters. This technique will specifically be used in Chapter 5 to study the LDOS variations induced by a silver nanowire.

Presentation of the manuscript In this thesis, we start by investigating the modification of the energy transfer rate between fluorescent emitters induced by plasmonic environments. Then, we take advantage of super-resolution techniques in order to probe sub-wavelength spatial variations of the LDOS induced by dielectric and plasmonic environments. The manuscript is organised in an introductory chapter and two main parts, that we now briefly describe.

- Chapter 1 is an introductory chapter in which we describe light-matter interaction using a classical approach. We focus on the modification of the emission rate of a fluorescent emitter due to its environment. This effect is usually referred to as the *Purcell effect*, from the work of Purcell in 1946 [5]. As an introduction to Part I, we calculate the rate of energy transfer between two fluorescent emitters in the general case of an inhomogeneous environment. We also introduce Part II by presenting near-field and far-field approaches to super-resolution imaging.

In the first part of this thesis, we characterise the occurrence of micrometre-range energy transfer between fluorescent emitters in plasmonic environments. We study the occurrence of energy transfer in two configurations, by using either a silver film or a silver nanowire.

- In Chapter 2, we characterise plasmon-mediated energy transfer between fluorescent

emitters located on the top of a thin silver film. We specifically study the occurrence of energy transfer in both the nanometre-range and micrometre-range regimes. In the latter case, we show that the distance dependence of the energy transfer rate is determined by the surface-plasmon propagation length at the transition energy of the emitters. We also calculate an approximate value of the efficiency of the energy transfer process using the Green formalism.

- In Chapter 3, we present the results of an experiment showing two independent evidences of micrometre-range energy transfer mediated by single plasmons. The energy transfer occurs between a single quantum dot and a fluorescent nanobead located in the near field of a silver nanowire. The first evidence of the energy transfer is based on the measurement of the decay histograms of the two emitters, and the second evidence is the demonstration of their correlated blinking. We also discuss the experimental conditions required to demonstrate the occurrence of energy transfer between two single emitters on the base of the measurement of the second-order correlation function.

In the second part of this thesis, we introduce a scanning-probe technique and a stochastic technique to probe the sub-wavelength spatial variations of the LDOS induced by nanostructured environments. We also discuss the precision of such measurements.

- In Chapter 4, we present a three-dimensional study of the near-field interaction between a fluorescent nanobead and silicon nanoantennas using a scanning-probe technique with a fluorescent near-field probe. We notably characterise the spatial variations of the LDOS due to the Mie resonances of the silicon antennas. We also highlight the strong directionality of the emission as well as the enhancement of the excitation intensity due to the antennas. These results are supported by finite-difference time-domain (FDTD) simulations.

- In Chapter 5, we introduce an experimental technique inspired by photo-activated localisation microscopy for the simultaneous determination of the fluorescence decay rate of single molecules and their respective positions with a localisation precision of the order of 10 nm. We detail the technique used for the measurements, which requires a 50:50 beamsplitter to split the fluorescence intensity towards an EM-CCD camera and a single photon avalanche diode (SPAD). Since no more than one molecule is typically active at a single time on the area conjugated to the SPAD, we show that the position of the molecules can be associated with their decay rate. As a result, we present a super-resolved decay rate map reconstructed from more than 3,000 single molecules. We finally characterise the spatial variations of the LDOS induced by the presence of a silver nanowire on the sample, in good agreement with FDTD simulations.

- In Chapter 6, we evaluate lower bounds on the standard errors on the position and decay rate estimates in the context of the experiment performed in Chapter 5. To this end, we calculate the information matrices associated with EM-CCD and SPAD measurements. We then calculate the corresponding Cramér-Rao lower bounds and discuss the precision and accuracy of actual estimations using a numerical approach. Finally, we introduce some guidelines to design an experimental setup dedicated to single-molecule localisation and time-resolved single-photon detection.

CHAPTER 1

An introduction to fluorescence

In this first chapter, we present a description of the interaction between a quantum emitter and the electromagnetic field in the weak-coupling regime. First of all, we develop an expression of the decay rate of the emitter as well as the rate of energy transfer between two emitters. These expressions will notably be used in Chapters 2 and 3 to describe plasmon-mediated energy transfer between fluorescent emitters. Then, we investigate near-field and far-field approaches to fluorescence microscopy. On the one hand, we introduce the near-field approach that will be used in Chapter 4 to map the density of states around silicon nanoantennas. On the other hand, we present the far-field approach that will be used in Chapter 5 to localise single fluorescent molecules in the vicinity of silver nanowires.

1.1 Spontaneous emission in the dipole approximation

In this section, we present a model to describe the electromagnetic interaction between a quantum emitter and its environment, in the electric dipole approximation and in the weak-coupling regime.

1.1.1 Probability distribution of the excited-state lifetime

Let us conceptually isolate a system of interest from the surrounding environment. Spontaneous emission is one of the possible interaction processes between this system and its environment: from an excited state, the system can emit a quantum of energy ΔE in the form of a photon and decay to a lower energy state. Quantum mechanics associate an angular frequency ω to such transitions so that $\Delta E = \hbar\omega$ where $\hbar$ is the reduced Planck constant.

This thesis primarily focuses on the emission rate noted Γ and defined as the average number of emitted photons per unit time. It is straightforwardly related to the average excited-state lifetime $\tau = 1/\Gamma$. In general, a probability density function (PDF) can be

estimated by repeating many times the same measurement on the same system. Based on this principle, time-correlated single-photon counting (TCSPC) can be used to estimate the PDF of the excited-state lifetime of an emitter. Figure 1.1a illustrates the principle of the measurement: a pulsed laser excites the emitter at a high repetition rate and a single-photon avalanche diode (SPAD) detects photons coming from the emitter. For each detection event, an electronic board determines the time delay Δt between the excitation pulse and the emission of a photon. These delays are then histogrammed and used to estimate the decay rate of the emitter.

As an illustration, we perform a measurement on a semiconductor quantum dot (QD) placed on a glass substrate. Its emission is characterised by an wavelength in free space λ_0 of the order of 600 nm, which corresponds to an angular frequency ω of approximately 3×10^{15} rad/s. The resulting decay histogram (Fig. 1.1b, light red curve) follows an exponential distribution that is a characteristic of photon emission by a two-level system in the *weak-coupling regime*. In this regime, a photon emitted in the electromagnetic field has a low probability of being absorbed back by the emitter. In contrast, in the *strong-coupling regime*, the emitter strongly interacts with one mode of the electromagnetic field, resulting in mode splitting and leading to the apparition of the so-called *Rabi oscillations*. Such effects are outside the scope of this thesis, which specifically focuses on photon emission in the weak-coupling regime.

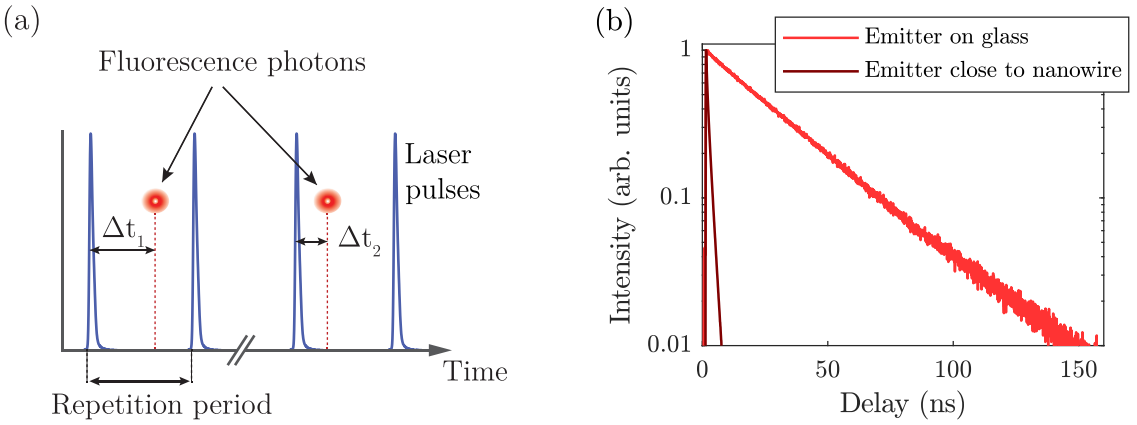

Figure 1.1 – *(a) Principle of time-correlated single-photon counting. (b) Normalised decay histogram measured on a QD on a glass substrate (red curve) and in the near field of a silver nanowire (dark red curve).*

For comparison purposes, we also measure the decay histogram of a second QD located a few nanometres away from a silver nanowire (Fig. 1.1b, dark red curve). This measurement clearly demonstrates that the fluorescence decay rate of an emitter strongly depends on its environment, since the decay rate of the second QD is much larger than the decay rate of the first one. In order to give a quantitative description of this effect, and more generally of the influence of the environment on the decay rate of an emitter in the weak-coupling regime, we can assume the emitted radiation to be monochromatic. Note that, in practice, the linewidth associated with a given transition is broadened by several effects. Indeed, any emitter is subject to lifetime broadening since frequency and time are Fourier transform duals. Furthermore, in solids at room temperature, broadening occurs due to the interaction between the emitter and its environment through various dissipation processes, such as phonon emission – the emission of a quantum of vibrational motion. As

a first approximation, we can consider that the emitter radiates at a single frequency if it does not interact with a strongly dispersive environment. In addition, we assume that the emission frequency does not depend on the environment. In general, the energy levels can be modified under external influence, such as a strong electric field (Stark effect) or magnetic field (Zeeman effect). However, frequency shifts due to the emitter's own field are extremely small in optics. Thus, in the weak-coupling regime and in the absence of strong external fields, the emission frequency can be considered as an intrinsic property of the emitter. Finally, we assume that the electromagnetic field generated by the emitter is weak, so that the response of the environment is linear.

1.1.2 The dipole approximation

The most complete description of spontaneous emission, and more generally of light-matter interaction, is provided by the theory of quantum electrodynamics (QED), in which both radiation and matter are quantised. In contrast, in the classical theory, light is described as a wave and matter is treated with an effective theory. In most experiments, a classical formalism can predict light-matter interaction with a good accuracy using Maxwell's equations, that are the same in both the classical and the quantum pictures.

In both the classical and the quantum pictures, light-matter interaction is usually described by decomposing the electric scalar potential and the magnetic vector potential into a Taylor series with origin at the centre of the charge distribution [6]. Let us consider the first terms involved in this expansion, called the *multipolar expansion*:

- The electric monopole interaction term describes the motion of a charged system submitted to an electric field. For such systems, a common approach is to find the equilibrium position and then to solve the problem for higher-order interaction terms. There is no magnetic monopole interaction term in the multipolar expansion.
- The electric and magnetic dipole interaction terms depend on the fields at the centre of the charge distribution. These terms also depend on the intrinsic properties of the emitting system. At optical frequencies, emitters preferentially interact with the electric field because of selection rules that constrain the possible transitions of the system. For this reason, the magnetic dipole interaction term is often not considered in optics.
- The electric and magnetic quadrupole interaction terms depend on the gradient of the fields at the centre of the distribution. We consider that the fields are sufficiently homogeneous over the dimensions of the emitting system so that these terms do not contribute. This argument also holds for higher order interaction terms.

Hence, the electric dipole interaction usually prevails for small emitters at optical frequencies. This does not hold for a few specific emitters such as lanthanide ions that have a forbidden transition under the electric dipole approximation. In such cases, electric and magnetic dipole interaction terms have the same order of magnitude, and it is possible to detect the interaction between these emitters and the magnetic field [7–9]. However, the electric dipole approximation is generally sufficient to characterise light-matter interaction at optical frequencies. Then, the intrinsic properties of an emitter can be described by its dipole moment noted $\boldsymbol{\mu}$.

1.2 Emission rate of an electric dipole

We now calculate the average value of the power dissipated in the electromagnetic field by a classical oscillator and relate it to the decay rate of a two-level quantum system.

1.2.1 Power emitted by an oscillating dipole

For a classical oscillator in the linear regime, we can describe the emitting system by a current density noted $\mathbf{j}(\mathbf{r},\omega)$ and the environment by a relative permittivity noted $\epsilon(\mathbf{r},\omega)$. This situation is represented in Fig. 1.2. Using this model, we can study light-matter interaction between an emitter and an arbitrary environment by solving Maxwell's equations for the electric field $\mathbf{E}(\mathbf{r},\omega)$. This amounts to solve the Helmholtz equation in the frequency domain expressed by

$$\boldsymbol{\nabla}\times\boldsymbol{\nabla}\times\mathbf{E}(\mathbf{r},\omega)-\frac{\omega^2}{c^2}\epsilon(\mathbf{r},\omega)\,\mathbf{E}(\mathbf{r},\omega)=i\omega\mu_0\,\mathbf{j}(\mathbf{r},\omega)\;. \tag{1.1}$$

Importantly, the relative permittivity $\epsilon(\mathbf{r},\omega)$ is a complex number, whose real part is related to the energy scattered by the medium and whose imaginary part is related to the energy gain or loss within the medium.

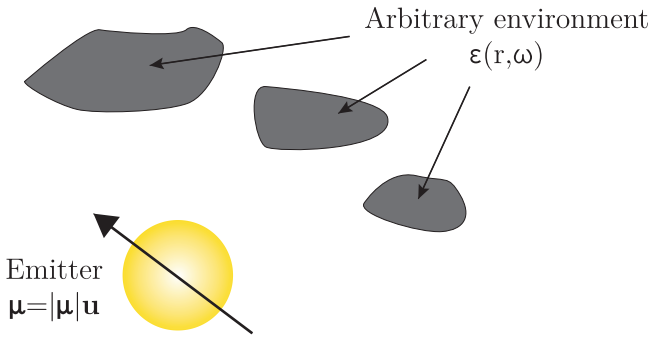

Figure 1.2 – *Representation of an electric dipole in an arbitrary environment.*

Assuming that the emitter can be modelled by a pointlike electric dipole, the associated current density is expressed in terms of its dipole moment $\boldsymbol{\mu}$ and the Dirac delta function δ as follows:

$$\mathbf{j}(\mathbf{r},\omega)=-i\omega\boldsymbol{\mu}\,\delta(\mathbf{r}-\mathbf{r}_0)\;. \tag{1.2}$$

By definition, the electric dyadic Green function $\mathbf{G}(\mathbf{r},\mathbf{r}_0,\omega)$ is the impulse response of Eq. (1.1) that verifies the outgoing-wave boundary condition as well as the interface conditions for the electric field. The dyadic Green function is therefore related to the electric field radiated by the dipole through

$$\mathbf{E}(\mathbf{r},\omega)=\mu_0\omega^2\mathbf{G}(\mathbf{r},\mathbf{r}_0,\omega)\boldsymbol{\mu}\;. \tag{1.3}$$

The power transferred from the dipole to the field can directly be found by considering the Lorentz force acting on charges due to the electric field. The average value of the power transferred from the dipole to the electromagnetic field at the frequency ω is then

$$P(\omega)=\frac{\omega}{2}\,\mathrm{Im}\left\{\boldsymbol{\mu}^*\cdot\mathbf{E}(\mathbf{r}_0,\omega)\right\}\;. \tag{1.4}$$

In the weak-coupling regime, and assuming that the field generated by the dipole does not modify the dipole moment $\boldsymbol{\mu}$, it follows that the power transferred from the dipole to the field is related to the imaginary part of the electric dyadic Green function through the relation

$$P(\omega) = \frac{\mu_0 \omega^3}{2} |\boldsymbol{\mu}|^2 \operatorname{Im} \{\mathbf{u} \cdot \mathbf{G}(\mathbf{r}_0, \mathbf{r}_0, \omega)\, \mathbf{u}\} \ , \tag{1.5}$$

where $\mathbf{u}$ is the unit vector in the direction of the dipole moment. This expression shows that the power transferred from the dipole to the field at a given frequency depends on both the intrinsic properties of the emitter and its environment. While the dipole moment $\boldsymbol{\mu}$ describes the intrinsic properties of the emitter, the influence of the environment is accounted for using the electric dyadic Green function $\mathbf{G}(\mathbf{r}_0, \mathbf{r}_0, \omega)$. The dependence of dipole emission upon the environment can be interpreted as follows: the electric field radiated by the dipole can polarise the surrounding medium, that in turn radiates and creates a field that can interfere with the original field. Due to this effect, the electric field at the dipole position can be either enhanced or reduced, thus modifying the power transferred from the dipole to the field. If the dipole is embedded in a homogeneous medium of refractive index $n = \sqrt{\epsilon}$, the power transferred from the dipole to the field simplifies to

$$P_0(\omega) = \frac{n \mu_0 \omega^4 |\boldsymbol{\mu}|^2}{12 \pi c} \ . \tag{1.6}$$

1.2.2 Decay rate of a two-level system

While the oscillating dipole is the representation of an emitter in the classical picture, the derivation of the lifetime PDF requires a QED treatment. Indeed, energy states are not included in the classical picture. In the quantum picture, we may represent the emitter by a two-level system. Let us study the overall system defined by the two-level system and the electromagnetic field. In the weak-coupling regime, this system can be described by an excited state $|i\rangle$ of energy E_i as well as a set of final states $|f\rangle$ of identical energy E_f. Assuming that the transition probability from $|i\rangle$ to $|f\rangle$ is low, the lifetime PDF is a decreasing exponential function and Fermi's Golden rule can be used to calculate the decay rate Γ. The decay rate reads in this limit [10]

$$\Gamma(\omega) = \frac{2 \mu_0 \omega^2}{\hbar} |\boldsymbol{\mu}|^2 \operatorname{Im} \{\mathbf{u} \cdot \mathbf{G}(\mathbf{r}_0, \mathbf{r}_0, \omega)\, \mathbf{u}\} \ . \tag{1.7}$$

This important formula shows that a specific environment can either enhance or reduce the decay rate of a quantum emitter. In a homogeneous medium of refractive index n, it simplifies to

$$\Gamma_0(\omega) = \frac{n \mu_0 \omega^3 |\boldsymbol{\mu}|^2}{3 \pi \hbar c} \ . \tag{1.8}$$

We can establish a correspondence between the power $P(\omega)$ emitted by the classical oscillator and the decay rate $\Gamma(\omega)$ of the two-level system. Indeed, the power emitted by the oscillator at the frequency ω corresponds to the product of the decay rate of the two-level system times the quantum of energy $\hbar\omega$. To make the correspondence, the classical dipole moment must also be replaced by twice the quantum dipole moment. This factor of two can be taken as a correspondence rule for the classical calculation to give the same result as the quantum one.

As a consequence, the enhancement of the decay rate of the quantum emitter due to its environment is exactly the same as the enhancement of the power dissipated by a classical oscillator. In many cases, the reference situation is a homogeneous medium, and the modification of the decay rate due to the environment is given by

$$\frac{\Gamma(\omega)}{\Gamma_0(\omega)} = \frac{P(\omega)}{P_0(\omega)} = \frac{6\pi c}{n\omega} \operatorname{Im}\left\{\mathbf{u} \cdot \mathbf{G}(\mathbf{r}_0, \mathbf{r}_0, \omega)\, \mathbf{u}\right\} \ . \tag{1.9}$$

We can go one step further and express the influence of the environment on the emission process in terms of the local density of states (LDOS). The LDOS is defined as the density of electromagnetic modes at the frequency ω and at the position $\mathbf{r}_0$. Because the physical meaning of the LDOS is ambiguous for an open absorbing medium, we follow the work of Carminati *et al.* [11] and use the subsequent expression as a definition of the LDOS:

$$\rho_{\mathbf{u}}(\mathbf{r}_0, \omega) = \frac{2\omega}{\pi c^2} \operatorname{Im}\left\{\mathbf{u} \cdot \mathbf{G}(\mathbf{r}_0, \mathbf{r}_0, \omega)\, \mathbf{u}\right\} \ . \tag{1.10}$$

This definition coincides with the usual definition of the LDOS if a discrete set of eigenmodes can be defined. As we can see from Eqs. (1.9) and (1.10), the modification of the decay rate of a quantum emitter due to its environment is proportional to the modification of the LDOS at the position of the emitter.

1.2.3 Intrinsic quantum yield

In general, the electromagnetic interaction is not the only possible decay process for an emitter. As an example, we already pointed out that an emitter can decay from an excited state to a lower energy state due to vibrational transitions by emitting a phonon. Such processes increase the decay rate of the emitter without increasing the number of emitted photons. Hence we consider these processes as losses and we characterise them by a decay rate Γ_{losses} that can depend on the environment, through the temperature of the surrounding medium for instance. However, it is generally assumed that the environment has a weaker influence on the decay rate Γ_{losses} than on the electromagnetic decay rate Γ given by Eq. (1.7). As a first approximation, it is usually considered that Γ_{losses} is an intrinsic property of the emitter that can be experimentally determined using measurements performed in a homogeneous, non-absorbing reference environment. For this reason, the intrinsic losses are commonly characterised by the *intrinsic quantum yield* of the emitter defined by

$$\eta_i = \frac{\Gamma_0}{\Gamma_0 + \Gamma_{losses}} \ , \tag{1.11}$$

where Γ_0 is the decay rate of the emitter due to spontaneous emission in the homogeneous environment of reference. Note that Γ_0 can be calculated by using Eq. (1.8).

We now consider that this emitter is located in a non-homogeneous, dispersive environment. The total decay rate Γ^{tot} of the emitter is then given by $\Gamma^{tot} = \Gamma + \Gamma_{losses}$ where Γ is the decay rate due to the electromagnetic interaction and Γ_{losses} is the decay rate due to other interaction processes[1]. This can equivalently be expressed in terms of the intrinsic quantum yield, which reads

$$\Gamma^{tot} = \Gamma + \frac{1 - \eta_i}{\eta_i}\, \Gamma_0 \ . \tag{1.12}$$

[1] The radiative and non-radiative part of the electromagnetic decay rate Γ are often distinguished [12,13]. This reads $\Gamma = \Gamma_R + \Gamma_{NR}$, where Γ_R and Γ_{NR} are respectively the radiative and non-radiative decay rates. Using these notations, the total decay rate reads $\Gamma^{tot} = \Gamma_R + \Gamma_{NR} + \Gamma_{losses}$.

As a consequence of lossy transitions, the influence of the environment on the decay rate of an emitter is more difficult to observe if the emitter has a low intrinsic quantum yield. Indeed, the modification of the total decay rate due to a given environment is

$$\frac{\Gamma^{tot}}{\Gamma_0^{tot}} = 1 + \eta_i \left(\frac{\Gamma}{\Gamma_0} - 1 \right) , \tag{1.13}$$

where $\Gamma_0^{tot} = \Gamma_0 + \Gamma_{losses}$. If the intrinsic quantum yield is of unity, the modification of the total decay rate due to the environment is directly given by Eq. (1.9). In contrast, the modification of the total decay rate is less pronounced if the quantum yield is low because the total transition rate is also driven by the competing decay processes.

1.3 Energy transfer between two emitters

We previously studied the spontaneous emission of an emitter in an arbitrary environment. Now, we consider the specific situation in which a second emitter is likely to be excited by the first emitter. We refer to the first emitter as the *donor* and to the second emitter as the *acceptor*.

1.3.1 Energy transfer rate

In order to calculate the rate of energy transfer from a donor to an acceptor, we describe both emitters by their dipole moments noted $\boldsymbol{\mu}_D$ for the donor and $\boldsymbol{\mu}_A$ for the acceptor, as represented in Fig. 1.3. Assuming that the acceptor dipole moment $\boldsymbol{\mu}_A$ is entirely induced by the donor field, it can be expressed by

$$\boldsymbol{\mu}_A = \boldsymbol{\alpha}_A \, \mathbf{E}_D(\mathbf{r}_A, \omega) , \tag{1.14}$$

where $\boldsymbol{\alpha}_A = \alpha_A \, \mathbf{u}_A \otimes \mathbf{u}_A$ is the polarisability tensor of the acceptor and $\mathbf{u}_A$ is the unit vector defining the orientation of the acceptor dipole moment. In the linear regime, the polarisability of the acceptor α_A does not depend on the excitation field. Note that this does not hold in the saturation regime: for high excitation fields, the rate of absorption by a two-level system is indeed limited by the rate of spontaneous emission.

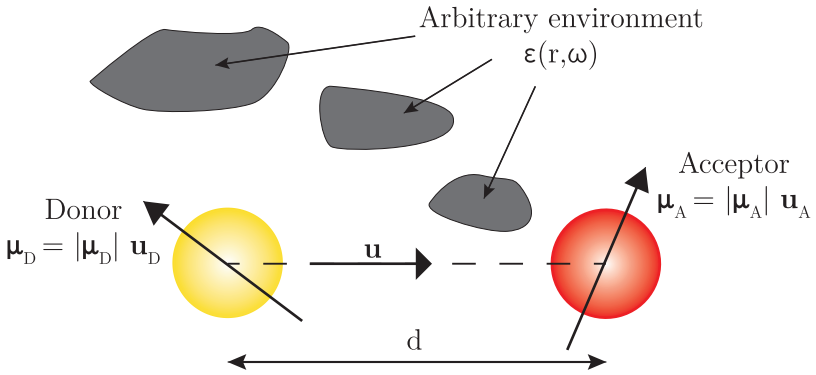

Figure 1.3 – *Representation of a donor and an acceptor in an arbitrary environment.*

The average value of the power transferred from the acceptor to the electromagnetic field at the frequency ω is expressed by

$$P_A(\omega) = \frac{\omega}{2} \operatorname{Im} \left\{ \boldsymbol{\mu}_A^* \cdot \mathbf{E}(\mathbf{r}_A, \omega) \right\} . \tag{1.15}$$

In this formula, the electric field evaluated at the position $\mathbf{r}_A$ can be written as the sum of the field $\mathbf{E}_D(\mathbf{r}_A, \omega)$ generated by the donor and the field $\mathbf{E}_A(\mathbf{r}_A, \omega)$ generated by the acceptor. At room temperature, these two fields can be considered as incoherent if the field generated by the acceptor is due to absorption-emission processes. Indeed, the pure dephasing rate due to the interaction between each emitter and phonons is usually much faster than both the decay rate and the transfer rate. In contrast, the field generated by the acceptor due to elastic scattering is coherent with the donor's field. For this reason, we consider that scattering by the acceptor is negligible or that it is separately accounted for in the model. In addition, we assume that the Stokes shift due to the vibrational dissipation in the acceptor is small, so that we can use the same frequency ω to describe both the donor and the acceptor emission. Under these assumptions, it is possible to separately calculate the power $P_{D\to A}(\omega)$ emitted by the donor and absorbed by the acceptor and the self-induced power $P_{A\to A}(\omega)$. From Eqs. (1.14) and (1.15), it follows that the power transferred from the donor to the acceptor is

$$P_{D\to A}(\omega) = \frac{\omega}{2} \operatorname{Im}\{\alpha_A\} |\mathbf{u}_A \cdot \mathbf{E}_D(\mathbf{r}_A, \omega)|^2 \,. \tag{1.16}$$

This can be rewritten by using the dyadic Green function to express the donor field. We obtain

$$P_{D\to A}(\omega) = \frac{\mu_0^2 \omega^5}{2} \operatorname{Im}\{\alpha_A\} |\boldsymbol{\mu}_D|^2 |\mathbf{u}_A \cdot \mathbf{G}(\mathbf{r}_A, \mathbf{r}_D, \omega)\, \mathbf{u}_D|^2 \,. \tag{1.17}$$

Thus, the power transferred from the donor to the acceptor can be calculated from the dyadic Green function by using a classical formalism. From perturbation theory applied to two quantum emitters, Dung, Knöll and Welsch showed that a similar expression can be derived for the rate of energy transfer between two quantum emitters [14]. Once again, a correspondence can be established between the classical and the quantum pictures. More precisely, the energy transfer rate between two quantum emitters is related to the power transferred between two classical oscillators by the following expression:

$$\frac{\Gamma_{D\to A}(\omega)}{\Gamma_0(\omega)} = \frac{P_{D\to A}(\omega)}{P_0(\omega)} = \frac{6\pi c \omega \mu_0}{n} \operatorname{Im}\{\alpha_A\} |\mathbf{u}_A \cdot \mathbf{G}(\mathbf{r}_A, \mathbf{r}_D, \omega)\, \mathbf{u}_D|^2 \,, \tag{1.18}$$

where $\Gamma_0(\omega)$ and $P_0(\omega)$ are the decay rate and the power dissipated by the donor in a reference homogeneous medium. As we can see from this formula, the energy transfer rate depends on the absolute square of the dyadic Green function.

The occurrence of energy transfer between a donor and an acceptor is commonly characterised by the *energy transfer efficiency* noted η_{et}. It is defined as the ratio of the energy transfer rate $\Gamma_{D\to A}$ to the total decay rate of the donor Γ_D^{tot}. Thus, it characterises the probability for the donor of exciting the acceptor among all the possible decay processes. Note that the total decay rate of the donor is given by $\Gamma_D^{tot} = \Gamma_D + \Gamma_{D\to A} + \Gamma_{losses}$ where Γ_D is the decay rate of the donor without the acceptor and Γ_{losses} is the decay rate due to intrinsic losses. Thus, the energy transfer efficiency depends on the intrinsic quantum yield of the donor while the energy transfer rate does not depend on the intrinsic quantum yields of the emitters.

1.3.2 Expression of the polarisability

We previously introduced the polarisability to describe the dynamical response of the acceptor to the electric field. Most of the time, this quantity is expressed in terms of

scattering and absorption cross-sections. These quantities are defined so that the total radiant fluxes scattered and absorbed by the system are given by the product between the respective cross-sections and the irradiance of a plane wave incident on the system. Thus, the scattering and absorption cross-sections both have the dimension of an area. We can write the polarisability in terms of the absorption cross-section only as we do not consider the scattering of the donor field by the acceptor.

To relate polarisability and absorption cross-section, we can at first calculate the intensity $I_0(\omega)$ of a plane wave from the flux of the Poynting vector. We obtain

$$I_0(\omega) = \frac{1}{2}\sqrt{\frac{\epsilon_0}{\mu_0}} n |\mathbf{E}_{exc}(\mathbf{r}_0, \omega)|^2 \,, \tag{1.19}$$

where $\mathbf{E}_{exc}(\mathbf{r}_0, \omega)$ is the value of the field at the position $\mathbf{r}_0$ and n is the refractive index of the medium. Then, we calculate the power absorbed by the acceptor and average it over the three orthogonal orientations of the dipole moment. We obtain

$$P_{abs} = \frac{\omega}{2} \operatorname{Im}\{\alpha\} \left\langle |\mathbf{u} \cdot \mathbf{E}_{exc}(\mathbf{r}_A, \omega)|^2 \right\rangle \,. \tag{1.20}$$

This expression can be simplified by integrating the unit vector $\mathbf{u}$ over the solid angle defining the three-dimensional space, leading to

$$P_{abs} = \frac{\omega}{6} \operatorname{Im}\{\alpha\} |\mathbf{E}_{exc}(\mathbf{r}_A, \omega)|^2 \,. \tag{1.21}$$

The absorption cross-section σ is defined so that $\sigma I_0(\omega)$ equals the average power absorbed by the emitter. Using this definition, the absorption cross-section of the acceptor σ_A reads

$$\sigma_A = \frac{\omega}{3n}\sqrt{\frac{\mu_0}{\epsilon_0}} \operatorname{Im}\{\alpha_A\} \,. \tag{1.22}$$

This formula relates the polarisability of the acceptor to its absorption cross-section. It can be used to calculate the energy transfer rate given by Eq. (1.18). We finally obtain

$$\frac{\Gamma_{D\to A}(\omega)}{\Gamma_0(\omega)} = \frac{P_{D\to A}(\omega)}{P_0(\omega)} = 18\pi\sigma_A \, |\mathbf{u}_A \cdot \mathbf{G}(\mathbf{r}_A, \mathbf{r}_D, \omega)\, \mathbf{u}_D|^2 \,. \tag{1.23}$$

1.3.3 Förster resonance energy transfer

From Eq. (1.23), we can derive a simple expression for the energy transfer rate in homogeneous medium of refractive index n and in the limit of small distance d between donor and acceptor. In this limit, energy transfer occurs through dipole-dipole interaction and is referred to as *Förster resonance energy transfer* (FRET). The absolute square of the homogeneous Green function is then given by [15]

$$|\mathbf{u}_A \cdot \mathbf{G}(\mathbf{r_A}, \mathbf{r}_D, \omega)\mathbf{u}_D|^2 \approx \frac{c^4}{16\pi^2 n^4 \omega^4 d^6} \left[\mathbf{u}_A \cdot \mathbf{u}_D - 3(\mathbf{u} \cdot \mathbf{u}_D)(\mathbf{u} \cdot \mathbf{u}_A)\right]^2 \,, \tag{1.24}$$

where $\mathbf{u}$ is the unit vector pointing from the donor to the acceptor. In the literature, the factor in square brackets is noted κ and is used to characterise the dependence of the energy transfer on the orientation of the two dipole moments. More precisely, κ^2 takes values between 0 and 4 and the orientational average $\langle\kappa^2\rangle = 2/3$ is used for ensemble measurements.

The energy transfer rate calculated under Förster's approximation is usually normalised by the decay rate of the emitter in the same medium of refractive index n. From Eqs. (1.23) and (1.24), it follows that

$$\frac{\Gamma_{D\to A}(\omega)}{\Gamma_0(\omega)} = \frac{9c^4\kappa^2\sigma_A}{8\pi n^4\omega^4 d^6} \,. \tag{1.25}$$

In general, the donor is characterised by a broadband emission spectrum. Hence it can be useful to express the energy transfer rate averaged over the donor emission spectrum. Since n and σ_A both depend on the emission frequency, the averaged energy transfer rate is expressed by

$$\int_0^\infty \frac{\Gamma_{D\to A}(\omega)}{\Gamma_0(\omega)} f_D(\omega)\,\mathrm{d}\,\omega = \frac{9c^4\kappa^2}{8\pi d^6}\int_0^\infty \frac{f_D(\omega)\sigma_A(\omega)}{n^4(\omega)\omega^4}\,\mathrm{d}\,\omega \,, \tag{1.26}$$

where $f_D(\omega)$ is the normalised emission spectrum of the donor. Equation (1.26) is the common expression of the FRET rate. The transfer rate is inversely proportional to the sixth power of the distance d between the donor and the acceptor, that makes the process very sensitive to small changes in this distance. The energy transfer rate typically becomes negligible when d exceeds 10 nm. In Chapters 2 and 3, we will show that shaping the environment allows the observation of energy transfer between fluorescent emitters on distances that are much larger than what would be allowed by dipole-dipole interaction.

1.4 Fluorescence microscopy

We previously studied the time dependence of the excited state and we showed that the decay rate of an emitter depends on its environment. In this section, we investigate the precision with which an emitter can be localised in space with a far-field microscope, and we introduce a near-field microscope that can be use to achieve a deterministic control over the position of a fluorescent emitter.

1.4.1 Angular spectrum representation of electromagnetic waves

In order to determine the position of an emitter with respect to its environment, one can excite the emitter and collect the emitted photons using an optical microscope. The position of the emitter is then estimated from this knowledge, and the standard deviation of the distribution followed by the position estimate characterises the precision of the localisation procedure. To determine the achievable localisation precision, we must study the spatial dependence of the electric field generated by the emitter. In general, the electric field can be expressed using a spatial Fourier transform along one or several coordinates, a method referred to as the *angular spectrum representation*. Performing a Fourier transformation on the variable $\mathbf{R} = (x, y)$, the electric field in the frequency domain is expressed by

$$\mathbf{E}(\mathbf{r}) = \iint_{-\infty}^{+\infty} \tilde{\mathbf{E}}(\mathbf{K}, z)\exp\left(i\mathbf{K}\cdot\mathbf{R}\right)\frac{\mathrm{d}^2\,\mathbf{K}}{4\pi^2} \,, \tag{1.27}$$

where $\mathbf{r} = (x, y, z)$ is the point of observation, $\mathbf{K} = (k_x, k_y)$ is the transverse component of the wavevector and $\tilde{\mathbf{E}}(\mathbf{K}, z)$ is the conjugate of the electric field in Fourier space. The angular spectrum representation is particularly useful to model propagation of the electric

field in homogeneous media. It can also be used to calculate the dyadic Green function in some specific geometries such as an interface between two semi-infinite media, as shown in Appendix A. Moreover, this representation reveals the spatial frequencies associated with the electric field in a given plane, which strongly influence the localisation precision.

In general, the electric field in the sample plane ($z = 0$) can be generated by several emitters in the presence of an arbitrary environment. If we consider that the electric field is known for $z = 0$, we can calculate it after propagation in a homogeneous medium by using the angular spectrum representation. The Fourier coefficients noted $\tilde{\mathbf{E}}(\mathbf{K}, z)$ in Eq. (1.27) can be determined by solving the free-space Helmholtz equation. Assuming that the direction of propagation is in the upper half space ($z > 0$), this leads to

$$\tilde{\mathbf{E}}(\mathbf{K}, z) = \tilde{\mathbf{E}}(\mathbf{K}, z = 0) \exp(ik_z z) \,, \tag{1.28}$$

where k_z is the component of the wavevector in the z-direction. It follows that the electric field at the observation point is

$$\mathbf{E}(\mathbf{r}) = \iint_{-\infty}^{+\infty} \tilde{\mathbf{E}}(\mathbf{K}, z = 0) \exp\left(i[\mathbf{K} \cdot \mathbf{R} + k_z z]\right) \frac{\mathrm{d}^2 \mathbf{K}}{4\pi^2} \,. \tag{1.29}$$

The field propagator is given by $\exp(ik_z z)$ in this expression, which clearly highlights the conditions required for field propagation. If $k_x^2 + k_y^2 < k^2$ then k_z is a real number and the field can propagate along the z-direction. In contrast, if $k_x^2 + k_y^2 > k^2$ then k_z is an imaginary number and the field exponentially decays along the z-direction.

The field in the sample plane is generally a sum of propagative and evanescent contributions. The highest frequency components are due to the presence of inhomogeneities in the sample plane, reducing the length scales the electromagnetic field varies on. However, if the intensity is measured far from this plane, the highest spatial frequency components are filtered by the propagation process and the localisation precision depends on the wavelength of the photons in free space[2]. The region in space where the contribution of the evanescent part of the electric field is negligible is called the *far field*. In contrast, the *near field* is the region that is sufficiently close to the system of interest so that the contribution of the evanescent part of the electric field remains appreciable.

1.4.2 Far-field microscopy

We can now consider how one localises a pointlike emitter from the far field using an optical microscope. In the simplified scheme represented in Fig. 1.4, a microscope is described by an objective and a tube lens. The emitter is located in the focal plane of the objective and the image is formed in the focal plane of the tube lens. The PDF that describes the intensity distribution generated by the dipole in the image plane is called the *point spread function* (PSF), and the variance of the PSF strongly influences the achievable localisation precision. As a matter of simplicity, we consider that the emitter is embedded in a homogeneous medium of refractive index n and that the image plane is in a medium of refractive index n'.

[2]In practice, the collection process by the microscope objective acts as an additional low-pass filter reducing even more the spectrum of spatial frequencies.

The exact calculation of the electric field generated in the image plane by a dipole was performed by Sheppard and Wilson for microscopes of large numerical aperture [16]. First of all, the electric field before the first interface – labelled (a) in Fig. 1.4 – can be calculated using the homogeneous Green function in the far-field approximation. Then, the field after the first lens (b) is derived by using Fresnel coefficients at the interface. The field propagates as a plane wave in between the lens – from (b) to (c) – and the field after the second lens (d) is found again using Fresnel coefficients. Finally the angular spectrum representation of a focused beam can be used to find the field in the image plane.

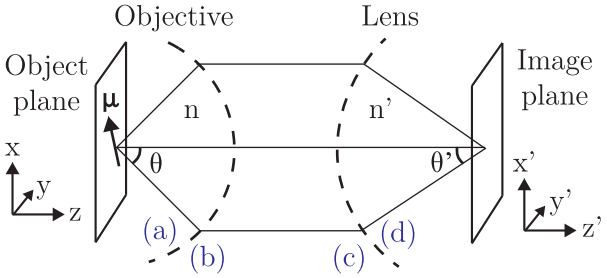

Figure 1.4 – *Simplified representation of a far-field microscope. The black lines representing light rays are shown for illustration purposes, as they are only an approximate representation of the calculations performed in Ref. [16].*

A simpler expression of the electric field in the focal plane can be obtained using the paraxial approximation. This approximation is justified on the image side as the numerical aperture of the tube lens is low. Furthermore, it turns out that the paraxial approximation can also be used on the object side. Indeed, the difference between the exact calculation and the paraxial approximate is small even for objectives with a high numerical aperture [17]. In order to express the electric field using the paraxial approximation, we introduce the magnification of the optical system M and the numerical aperture of the objective NA. We also define $r' = \sqrt{x'^2 + y'^2}$ and we express the PSF in polar coordinates due to the rotational symmetry of the problem. The intensity distribution in the image plane generated by a dipole oriented along the object plane ($\boldsymbol{\mu} = \mu_x \mathbf{u}_x$) is then

$$|\mathbf{E}_x(r')|^2 = \frac{\pi^3 \mu_x^2 \mathrm{NA}^4}{\epsilon_0^2 n n' \lambda_0^6 M^2} \left\{ \frac{1}{\pi r'^2} \, J_1^2 \left(\frac{2\pi \mathrm{NA} r'}{M \lambda_0} \right) \right\} , \tag{1.30}$$

where J_1 is the first-order Bessel functions of the first kind. Similarly, the intensity distribution in the image plane due to a dipole oriented along the normal to the object plane ($\boldsymbol{\mu} = \mu_z \mathbf{u}_z$) is

$$|\mathbf{E}_z(r')|^2 = \frac{\pi^3 \mu_z^2 \mathrm{NA}^6}{2\epsilon_0^2 n^3 n' \lambda_0^6 M^2} \left\{ \frac{2}{\pi r'^2} \, J_2^2 \left(\frac{2\pi \mathrm{NA} r'}{M \lambda_0} \right) \right\} , \tag{1.31}$$

where J_2 is the second-order Bessel functions of the first kind. Equations (1.30) and (1.31) can both be found in Ref. [17]. For each expression, the term in curly brackets is the 2-dimensional PDF that describes the intensity distribution in the image plane. Since this term is normalised so that the area under the density function equals unity, the prefactor of each expression gives the power emitted towards the image plane. The term in curly brackets in Eq. (1.30) can be identified with the diffraction pattern resulting from the illumination of a circular aperture by a plane wave, referred to as the *Airy pattern*.

As an illustration, we consider a dipole characterised by a free-space emission wavelength of 670 nm and we assume collection to be performed by an oil objective characterised by

a ×100 magnification and a 1.4 numerical aperture, as in typical single-molecule experiments. Figure 1.5a shows the intensity in the image plane obtained for a dipole moment oriented along the x-axis. For comparison purposes, the intensity obtained for a dipole moment of same amplitude but oriented along the z-axis is shown in Fig. 1.5b.

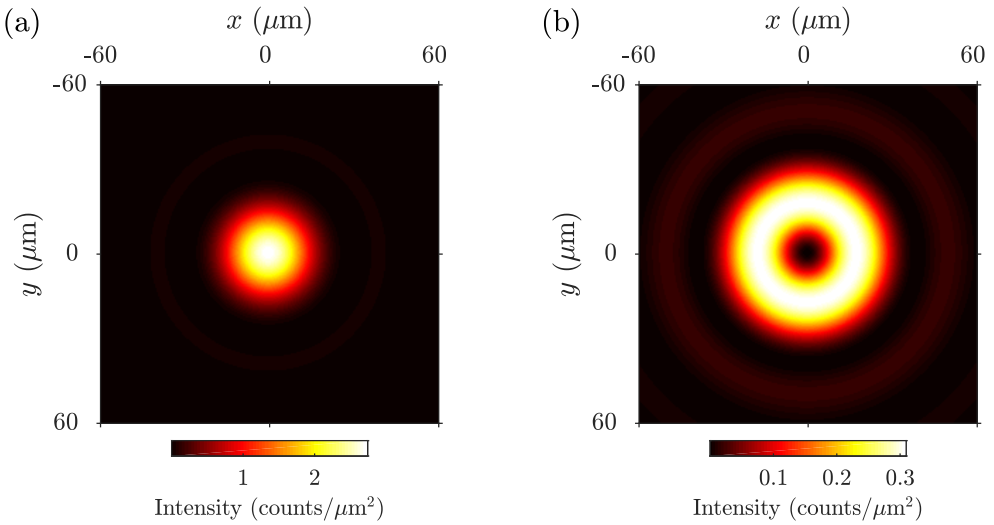

Figure 1.5 – *Intensity distributions in the image plane respectively generated by (a) a dipole oriented in the object plane and (b) a dipole oriented along the normal to the object plane. Each dipole is embedded in a homogeneous medium of index n=1.5.*

The total power detected in the image plane is lower when the dipole is oriented along the z-axis. More precisely, the ratio of the number of photons detected in the two different cases can be calculated from the prefactors of Eqs. (1.30) and (1.31) which gives $\mathrm{NA}^2/2n^2 \approx 0.44$. It means that a lower fraction of the total emission is collected by the objective if the dipole moment is oriented along the z-axis. Furthermore, the variance of the associated PSF is larger than the variance of the Airy function. It is thus much harder to detect an emitter with a dipole moment oriented along the z-axis, as a consequence of both the lower fraction of collected photons and the larger variance of the PSF.

In many experiments, it makes sense to consider the intensity distribution averaged over the different orientations of the dipole moment. For instance, this can be used for the study of several emitters with similar properties and located at the same place, or to analyse the fluorescence of single emitters that exhibit fast wobbling behaviour around a fixed position. From Eqs. (1.30) and (1.31), we can calculate the average of the intensity distribution over the three orthogonal orientations of the dipole moment, which reads

$$|\mathbf{E}_{avg}(r')|^2 = \frac{\pi^3 |\boldsymbol{\mu}|^2 \mathrm{NA}^4}{\epsilon_0^2 n n' \lambda_0^6 M^2} \left\{ \frac{2}{3\pi r'^2} \left[J_1^2\left(\frac{2\pi \mathrm{NA} r'}{M\lambda_0}\right) + \frac{\mathrm{NA}^2}{2n^2} J_2^2\left(\frac{2\pi \mathrm{NA} r'}{M\lambda_0}\right) \right] \right\} . \tag{1.32}$$

In this expression, the term in curly brackets is the PDF that describes the intensity distribution in the image plane. As before, the prefactor gives the power emitted towards the image plane. As shown in Fig. 1.6, the intensity profile averaged over the three orientations of the dipole moment is very similar to the Airy function, although with a slightly larger spread. This is a consequence of the lower number of photons collected by the objective from dipoles oriented along the z-direction.

These results have important consequences for the localisation of a single emitter. If only

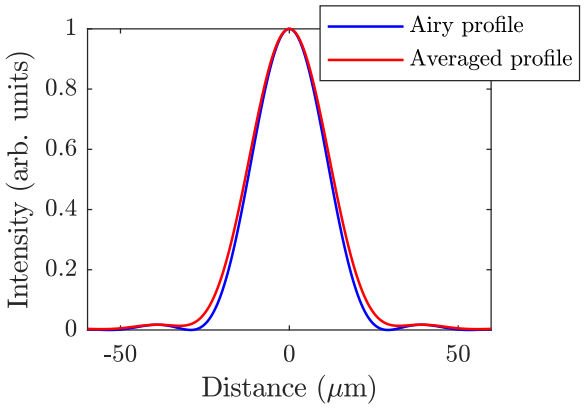

Figure 1.6 – *Comparison between the intensity profile calculated for a dipole moment oriented in the object plane (blue curve) and the intensity profile averaged over the three orientations of the dipole moment (red curve).*

one emitter is located in the object plane, its position can be determined by estimating the centroid of the measured PSF. The localisation is usually performed by fitting a two-dimensional Gaussian function or an Airy function to the measured PSF. While a Gaussian function is often a good approximate, the Airy function is the true PSF for an emitter with a dipole moment oriented in the object plane. The typical localisation precision for single molecules using far-field detection is usually characterised using the standard deviation of the PDF followed by the position estimates. A lower bound for the localisation precision can be calculated using the Fisher information, as introduced in the context of single-molecule microscopy by Ober, Ram and Ward [18]. It is of the order of 10 nm for typical acquisition conditions, as we will see in Chapter 6.

If several emitters are located in the object plane, the minimal distance in-between two specific emitters required to resolve them is the so-called *resolution limit*. By extension, the resolution of an image refers to the highest spatial frequencies characterising the image. The resolution limit of a far-field microscope is classically defined by the distance between the principal maximum and the first zero of the Airy function; this is referred to as the *Rayleigh criterion*. From Eq. (1.30), it follows that this distance noted r_{res} is expressed by

$$r_{res} \approx 1.22 \frac{\lambda_0}{2\mathrm{NA}} \,. \tag{1.33}$$

In the context of single-molecule microscopy, the Rayleigh criterion cannot be used to define the resolution of an image since position estimates follow a Gaussian distribution. In this case, the resolution can be defined by the full width at half maximum (FWHM) of the distribution, which is approximately equal to 2.4 times the standard deviation of the Gaussian function.

1.4.3 Near-field microscopy

We previously assumed that the highest spatial frequencies of the electric field were lost due to the propagation process. However, sub-wavelength inhomogeneities in the environment can transfer some near-field information to the far field. This information can notably be useful to estimate the position of a given emitter. To do so, the inhomogeneities must scatter – or at least interact with – the electric field generated by one or several emitters.

By collecting the scattered light, it is possible to retrieve a near-field information. This idea was proposed by Synge [19] and has led to the development of various types of scanning optical near-field microscopes (SNOMs).

In many SNOMs, the tip of an atomic force microscope (AFM) is mechanically coupled to a small tuning fork, forming a oscillating system. Its oscillation frequency changes due to tip-sample interaction when the apex of the tip is close to a surface, typically for tip-sample distances of the order of 20 nm. By measuring this frequency shift, it is possible to implement a feedback loop to keep a constant distance between the apex of the tip and the sample. In the presence of an electric field, the tip can be polarised and act as an induced dipole whose emission directly depends on the local field. In particular, the number of photons scattered by the tip depends on this field. Using a piezoelectric positioning system, it is possible to scan the tip over the sample with a resolution down to 1 nm. Consequently, SNOMs can be used to locally probe the electric field and resolve its high spatial frequency components.

A slightly different approach has been developed during the last few years at Institut Langevin [20, 21]. As represented in Fig. 1.7, a fluorescent emitter is grafted at the apex of an AFM tip, so that the position of the emitter can be controlled with a nanometre precision by using the piezoelectric positioning system of the AFM. Using this setup, Krachmalnicoff *et al.* notably presented a simultaneous characterisation of the topography of a plasmonic antenna along with the intensity and the decay rate of a fluorescent bead in the near field of this antenna [22].

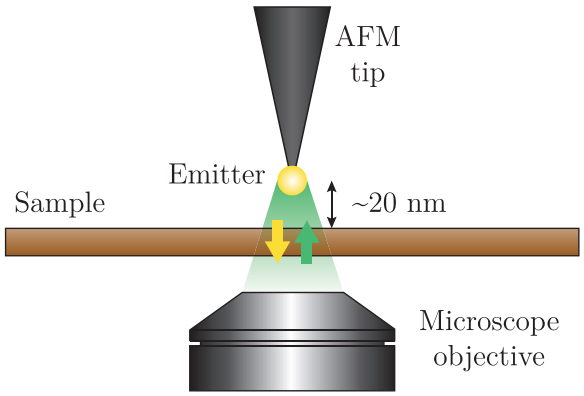

Figure 1.7 – *SNOM with an active probe. A pulsed laser excites the emitter and fluorescence photons are measured using a TCSPC system. The sample is moved along the three dimensions to perform the acquisition of topography, intensity and decay rate maps.*

This SNOM is a useful tool to characterise the interaction between an emitter and its environment with a very good resolution – the resolution is mainly limited by the size of the emitter and by the distance in-between the emitter and the surface of the sample. Currently, the resolution of this SNOM is typically of the order of 50 nm due to experimental constraints. In Chapter 4, we will detail the working principle of this microscope and we will present a characterisation of the interaction between a fluorescent bead and silicon antennas performed using this SNOM.

1.5 Conclusion

In this chapter, we introduced a few concepts that will be useful for the understanding of this thesis. More precisely, we described fluorescent emission and detailed the electric dipole approximation, which is generally justified for small emitters at optical frequencies. Under this approximation, we calculated the power dissipated by a classical oscillator and showed that it can be related to the decay rate of a quantum emitter. We also defined the LDOS to quantify the effect of the environment on the emission rate, and we introduced the intrinsic quantum yield to account for non-radiative transitions.

We used a similar formalism to calculate the rate of incoherent energy transfer between two emitters, from a donor to an acceptor. We established a correspondence between the power transferred between two oscillators and the energy transfer rate between two quantum emitters. Then, we introduced the absorption cross-section to describe the response of the acceptor to an electric field and we calculated the energy transfer rate in a homogeneous medium and in the dipole-dipole approximation. This sets the basis for the study of micrometre-range plasmon-mediated energy transfer, presented in Chapters 2 and 3.

We also discussed near-field and far-field approaches to fluorescence microscopy. A precise control of the position of the emitter can be achieved by grafting the emitter on an AFM tip, even though it remains a technical challenge. From the far field, the position of a given emitter can be estimated from the measured PSF with a good precision, assuming that only one pointlike object emits in a diffraction-limited region. Both approaches can be used to map LDOS variations induced by nanostructures, as we will see in Chapters 4 and 5.

Throughout the following chapters, we will study spontaneous emission of fluorescent emitters in various environments. We will take advantage of nanostructures that are resonant with the electromagnetic field to modify the emission properties – and specifically the emission rate – of fluorescent emitters. This work fits into the field of nanophotonics, which ultimately aims to control the electromagnetic field on the nanometre scale.

Part I

Micrometre-range plasmon-mediated energy transfer

CHAPTER 2

Plasmon-mediated energy transfer above a silver film

In this chapter, we present a characterisation of plasmon-mediated energy transfer in the micrometre-range regime. First of all, we introduce the principle of the experiment and the context of this work. Then, we present the properties of surface plasmons, which are used to propagate energy from a donor to an acceptor. After the description of the experimental setup, we present experimental evidences of the occurrence of energy transfer, both in the nanometre-range (called *short-range*) and in the micrometre-range (called *long-range*) regimes. In the latter case, we specifically demonstrate that the distance dependence of the energy transfer rate is determined by the surface-plasmon propagation length at the transition energy of the emitters. Finally, we estimate an effective distance between the emitters and the silver mirror and we calculate an approximate value of the efficiency of the energy transfer process by using the Green formalism.

2.1 Introduction

One of the first observations of fluorescence energy transfer was reported in 1923 [23]. In this pioneering experiment, Cario and Frank studied a mixture of mercury and thallium vapour. By exciting the mixture at a frequency corresponding to a transition energy of the mercury atom, they observed the emission spectra of both atoms and were able to conclude that thallium was indirectly excited via mercury atoms. This effect was likely to be due to a non-radiative transfer of energy from the excited mercury atoms to the thallium atoms, which can be excited at the mercury emission frequency. However, this effect was not clearly identified at this time.

Thirty years later, Förster derived an analytical expression for the energy transfer rate due to dipole-dipole interaction. In 1959, he notably gave a comprehensive review of his work in the Faraday Discussions that were then dedicated to energy transfer [24]. Since then, the name *Förster resonance energy transfer* (FRET) is used to describe this phenomenon. In the expression developed by Förster, the rate of energy transfer is inversely proportional to

the sixth power of the distance d between donor and acceptor, as expressed by Eq. (1.26). This applies to energy transfer in homogeneous medium and in the short-range limit.

FRET is now widely employed as a nanoscopic rule. Indeed, since the rate of the process scales as d^{-6}, it is significant over a very short range of distances, of the order of 10 nm for typical fluorescent emitters. Thus, by attaching FRET probes to specific sites in molecules, one can obtain useful information on scales that are unreachable with conventional optics. As an example, Suzuki *et al.* used FRET probes to study the molecular mechanism of muscle contraction [25]. More precisely, they monitored the change of conformation of a motor protein called myosin using a FRET pair, allowing them to determine the working stroke of the protein.

In the recent years, several studies were dedicated to the control of FRET by nanostructures. In 2000, Andrew and Barnes studied the occurrence of FRET in an optical microcavity constituted by two silver mirrors [26]. In this work, they experimentally demonstrated that the energy transfer rate is influenced by the local density of states (LDOS). Since then, different configurations were tested in order to modify the features of the energy transfer. Among them, Reil *et al.* tuned the resonance of a close-by metallic nanoparticle across the transition energy of the molecules to enhance the energy transfer rate [27]. Blum *et al.* studied the influence of the LDOS on a FRET pair by controlling the distance between the FRET pair and a silver mirror [28]. Recently, Ghenuche *et al.* obtained a 5-fold enhancement of the energy transfer rate by using a resonant aluminium nanogap antenna providing a strong field confinement [29]. On the theoretical side, Wubs and Vos highlighted that the position-dependent FRET rate and the LDOS at the donor transition frequency are completely uncorrelated for any nondispersive medium [30], providing some insight in the debate about nanophotonic control of the energy transfer via the LDOS.

In general, FRET remains an inefficient process for donor-to-acceptor distances larger than 10 nm due to the short range of dipole-dipole interaction. Increasing the efficiency of the energy transfer process in the micrometer range is a current experimental challenge in nanophotonics, as it would allow a great control over the interaction between the two emitter through their respective environments. It could also lead to the development of interesting applications, such as a more efficient harvesting of solar energy. Indeed, it is possible to increase the effective absorption cross-section of acceptor molecules by associating them with a cluster of donor molecules that absorb light and efficiently transfer the excitation energy to the acceptor molecules [31, 32].

Towards the achievement of efficient long-range energy transfer, Andrew and Barnes suggested an original approach for the control of energy transfer by plasmonic structures [33]. In 2004, they experimentally demonstrated a 120-nm-range energy transfer occurring from donor molecules to acceptor molecules on opposite sides of a silver film supporting coupled surface plasmons. It was the first evidence that one can tune the environment to observe energy transfer between fluorescent emitters on distances that are much larger than what would be allowed by dipole-dipole interaction. Three years later, Kuzyk *et al.* used the propagation properties of surface plasmons to mediate energy transfer between fluorescent emitters [34]. More precisely, they used a silver waveguide and a lithographic fabrication method to position fluorescent emitters in the near field of the metal surface. This allowed them to demonstrate the occurrence of energy transfer over distances of several micrometers. Using a different approach, Götzinger *et al.* used whispering gallery modes supported

by a silica microsphere resonator to achieve energy transfer between two fluorescent beads over a distance of several tens of micrometers [35].

On the theoretical side, several studies highlighted the potential of plasmonic structures for the coupling between fluorescent emitters. Among them, Martín-Cano *et al.* predicted a large enhancement of the energy transfer rate between two emitters using plasmonic waveguides [36]. Interestingly, they also predicted that collective emission phenomena such as superradiance and subradiance can arise from the coupling between the two emitters. This was also foreseen by Barthes *et al.* [37]. Recently, de Roque, van Hulst and Sapienza proposed a hybrid nanoantenna-waveguide system to mediate the energy transfer and numerically showed an enhancement of the transfer rate of up to 8 orders of magnitude [38].

Principle of the experiment To observe energy transfer over distances larger than what would be allowed by dipole-dipole interaction, a solution is indeed to guide the energy emitted from a donor towards an acceptor by using plasmonic structures. The work presented in this chapter intents to identify the parameters driving the range of plasmon-mediated energy transfer from an experimental point of view. To do so, we use thin silver films on top of which a large number of fluorescent emitters is dispersed. More precisely, we disperse fluorescent beads as donors and a layer of dye molecules as acceptors. Figure 2.1 illustrates the principle of the experiment. First of all, we excite a donor bead using a laser. The donor bead excites surface plasmons propagating on top of the silver film, that excite in turn acceptors molecules located several micrometres apart. With a high numerical aperture objective, we collect the fluorescence photons emitted by these acceptors as a signature of the occurrence of energy transfer. Using this scheme, we can experimentally determine the distance dependence of the energy transfer and compare it to theoretical results. This work is published in Physical Review Letters [39].

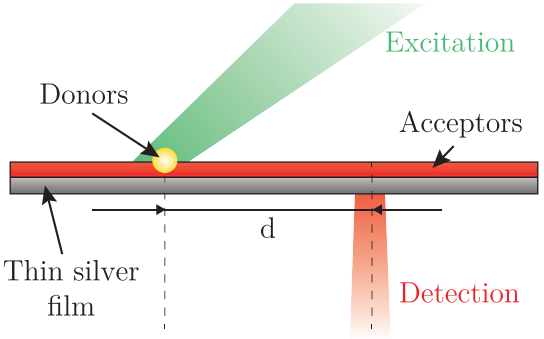

Figure 2.1 – *Principle of the experiment: fluorescent dyes (donors) embedded in a nanobead are excited by a laser and decay by exciting surface plasmons propagating on top of a thin silver film. A continuous layer of dye molecules (acceptors) dispersed on the sample can absorb the energy carried by surface plasmons and emit fluorescence photons. We spectrally characterise these photons to study the occurrence of plasmon-mediated energy transfer between the donors and the acceptors.*

2.2 Properties of surface plasmons

In this section, we describe the properties of surface plasmons, acting as an intermediate between donors and acceptors in the energy transfer experiment.

2.2.1 Dispersion relations

Noble metals such as gold or silver are good candidates to interact with light because they exhibit a resonant behaviour at optical frequencies. These resonances, named *plasmon resonances*, are due to the collective oscillations of free electrons at the interface of a metal and a dielectric medium when an external electric field is applied. Interestingly, these oscillations can propagate along the interface; they are then called *surface plasmons*.

To derive the propagation properties of surface plasmons, we describe the response of the metal to an applied electric field through a complex relative permittivity $\epsilon(\omega)$. The Lorentz–Drude model is a phenomenological description of this response that takes into account both the free-electron and the interband parts of the dielectric response of a metal. The classical Drude model describes the free-electron response of the metal from the plasma frequency ω_p, the associated damping constant γ_0 and the oscillator strength f_0. The n interband contributions are described by Lorentzian functions respectively characterised by their resonant frequency ω_j, their damping constant γ_j and their oscillator strength f_j. Using this model introduced by Ehrenreich and Philipp [40], the relative permittivity of a metal is expressed by[1]

$$\epsilon(\omega) = 1 - \frac{f_0\omega_p^2}{\omega^2 + i\gamma_0\omega} + \sum_{j=1}^{n} \frac{f_j w_p^2}{(\omega_j^2 - \omega^2) - i\omega\gamma_j} \,. \tag{2.1}$$

The parameters involved in this expression depend on the properties of the material and can be found in the literature [41]. From this model, we can derive the dispersion relation for surface plasmons propagating at the interface between a metal and a dielectric medium, defined by their respective relative permittivities ϵ_m and ϵ_d. This configuration is represented in Fig. 2.2.

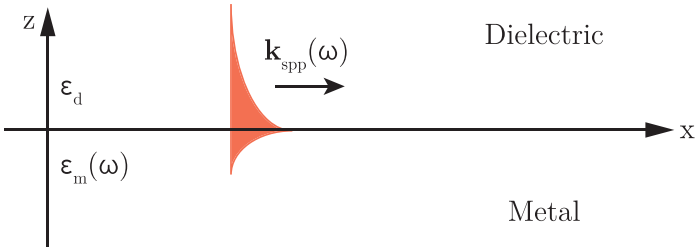

Figure 2.2 – *Representation of a surface plasmon propagating at an interface between two semi-infinite media.*

Considering that the interface is located in the xy-plane, the interface condition satisfied by the electromagnetic field requires that a wave for which the electric field is in the plane of incidence – referred to as a a *p-polarised wave* – is characterised by the following dispersion relations [42]:

$$k_x^2 = \frac{\omega^2}{c^2}\left(\frac{\epsilon_d\epsilon_m}{\epsilon_d + \epsilon_m}\right) \,, \tag{2.2a}$$

$$k_{z,m}^2 = \frac{\omega^2}{c^2}\left(\frac{\epsilon_m^2}{\epsilon_d + \epsilon_m}\right) \,, \tag{2.2b}$$

[1] We opt for the convention $\epsilon = \epsilon' + i\epsilon''$ where ϵ' and ϵ'' are respectively the real and imaginary parts of the relative permittivity. A different convention ($\epsilon = \epsilon' - i\epsilon''$) is used by the authors in Ref. [41], resulting in a slightly different expression for Eq. (2.1).

$$k_{z,d}^2 = \frac{\omega^2}{c^2}\left(\frac{\epsilon_d^2}{\epsilon_d + \epsilon_m}\right) . \tag{2.2c}$$

We are interested in solutions characterised by a purely imaginary wavenumber in the transverse direction for both media. Furthermore, the wavenumber in the propagation direction must have a real part. This is typically true whenever $\mathrm{Re}(\epsilon_d + \epsilon_m) < 0$ and $\mathrm{Re}(\epsilon_d \epsilon_m) < 0$. These conditions are notably satisfied for several metal-dielectric combinations at optical frequencies. In this configuration, the wave is confined in the z-direction but can propagate in the x-direction. However, the imaginary part of k_x is generally larger than zero and the wave is also attenuated in the direction of propagation. Physically, this attenuation is due to ohmic losses in the metal.

2.2.2 Propagation length

The confinement of an electromagnetic wave along the direction defined by the unit vector $\mathbf{u}$ can be characterised by a propagation length l_u defined by $l_u^{-1} = 2\,\mathrm{Im}(k_u)$. This corresponds to the distance over which the wave propagates in this direction until its intensity has decreased by a factor of $1/e$. From Eqs. (2.2), we may define three typical lengths characterising surface plasmons. The surface-plasmon propagation length characterises the propagation in the x-direction or any other in-plane direction. The decay lengths of the surface-plasmon intensity characterise the intensity decay along the z-direction for both sides of the interface. In general, these three typical lengths depend on the emission frequency – or equivalently the wavelength in free space λ_0 – as well as the considered materials. Let us consider the frequency dependence of these typical lengths for an interface between a dielectric medium (ϵ_d =2.25) and either silver or gold. In the visible range, the propagation length is larger for silver than for gold (Fig. 2.3a), and it increases with λ_0. Furthermore, the decay length in the transverse direction is smaller on the metal side than on the dielectric side (Fig. 2.3b), and the decay length on the dielectric side increases with λ_0.

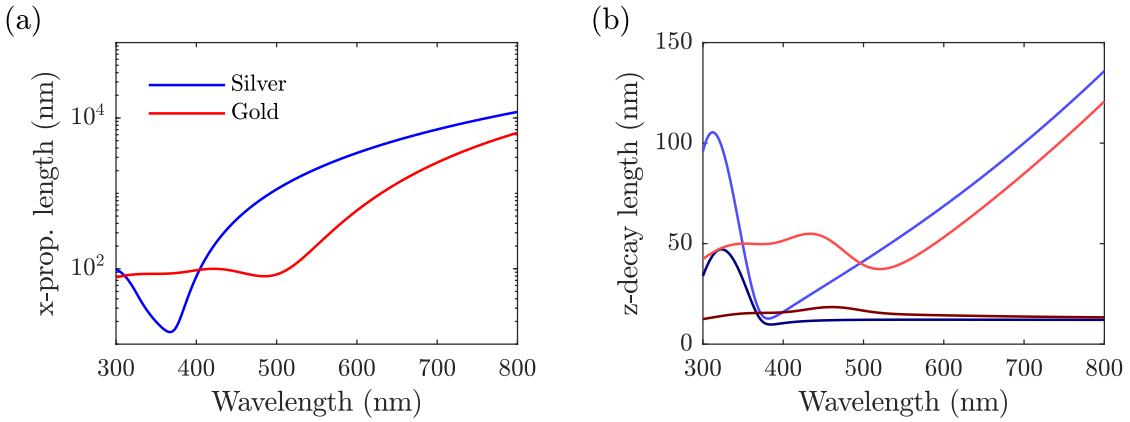

Figure 2.3 – *Typical lengths versus free-space wavelength λ_0 for a surface plasmon propagating at a metal-dielectric interface. Red curves refer to gold and blue curves refer to silver. (a) Propagation length along the x-direction. (b) Decay lengths along the z-direction. Light curves refer to the dielectric side and dark curves to the metal side.*

The surface-plasmon intensity is strongly localised for silver around $\lambda_0 = 400$ nm, since the propagation length in the x-direction and the decay lengths of the surface-plasmon intensity in the z-direction are very short. Around this frequency, the response of the electrons in the metal to an applied electric field is strong but associated with large losses. For the energy transfer experiment, the surface plasmon must strongly be confined along the z-direction but must propagate along the x-direction over long distances. Using a silver mirror at a wavelength $\lambda_0 = 610$ nm, the propagation in the x-direction is characterised by a propagation length of 3.7 µm. In this case, surface plasmons can thus propagate along the x-direction while they are confined in the z-direction over 70 nm on the dielectric side and over 15 nm on the metal side.

2.3 Sample preparation and experimental setup

Now, we describe the emitters involved in the experiment. We also present the configuration of the sample, and we detail the optical setup used for its characterisation.

2.3.1 Selection of a donor-acceptor pair

In practice, the development of an energy transfer experiment requires the choice of a donor and an acceptor among the several types of fluorescent emitters used by experimentalists. The most common ones are dye molecules, semiconductor quantum dots (QDs) and nitrogen-vacancy (NV) centres in diamond nanocrystals. We require the emitter to be characterised by a low photobleaching rate under typical excitation conditions, a large absorption cross-section and an intrinsic quantum yield close to unity. Furthermore, a necessary condition for energy transfer to occur is that the emission spectrum of the donor overlaps with the absorption spectrum of the acceptor. In order to satisfy these conditions, we use the following ensembles of emitters for the donors and the acceptors:

- As donors, we use dye molecules embedded in polystyrene beads (Red FluoSpheres, ThermoFisher Scientific) and characterised by a diameter of 109±7 nm. Due to the large number of molecules embedded in the bead and the protecting polymer matrix, these beads are relatively insensitive to photobleaching even under intense illumination conditions.
- As acceptors, we use dye molecules (Atto665, AttoTec Gmbh) embedded in a thin polyvinyl alcohol (PVA) layer to protect the molecules from photobleaching.

For this donor-acceptor pair, spectral overlap occurs between the donor emission and the acceptor absorption (Fig. 2.4). One could argue that we could have chosen another donor-acceptor pair with a better overlap. Indeed, we opt for this configuration in order to be able to clearly distinguish the emission spectrum of the acceptor from the emission spectrum of the donor. Moreover, the wavelength of the excitation laser (λ_0=532 nm) is slightly shifted with respect to the donor's maximum absorption in order to limit direct excitation of the acceptor. Importantly, the propagation length of surface plasmons propagating at an interface between silver and PVA is large for the overlap frequencies. The surface-plasmon propagation length is indeed of the order of 5 µm at $\lambda_0 = 650$ nm, as shown in Fig. 2.3a.

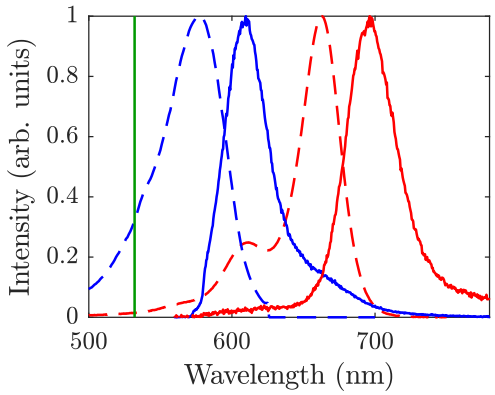

Figure 2.4 – *Emission and absorption spectra of the donor (blue curves) and of the acceptor (red curves). Dashed lines are the absorption spectra and solid lines are the emission spectra. A green line represents the excitation laser.*

2.3.2 Sample preparation

To prepare the sample, we evaporate a 50 nm thick silver layer on a glass coverslip by e-beam evaporation[2], at a pressure of 10^{-8} bar and at a rate of 0.3 nm/s, that we cover by a 10 nm thick silica (SiO_2) layer. While the silver film is required for the existence of surface plasmons, the silica layer protects the metal against oxidation. An aqueous solution of donor beads, acceptor molecules and PVA is then spin-coated on the silica layer. The concentration of acceptor molecules in the solution (0.001 mg/mL) is a trade-off between the high effective absorption characterising highly concentrated solutions and the occurrence of auto-FRET in-between acceptor molecules arising for such high concentrations. The spin-coating process is performed in two steps. Firstly, the sample rotates at 500 rpm for 10 s in order to spread the solution over the coverslip and let the beads deposit on the coverslip. Secondly, it rotates at 1500 rpm for 30 s to evacuate the surplus of solution. Using this procedure, the resulting sample consists in a homogeneous layer of acceptors embedded in a PVA matrix with a few isolated donor beads, as represented in Fig. 2.5.

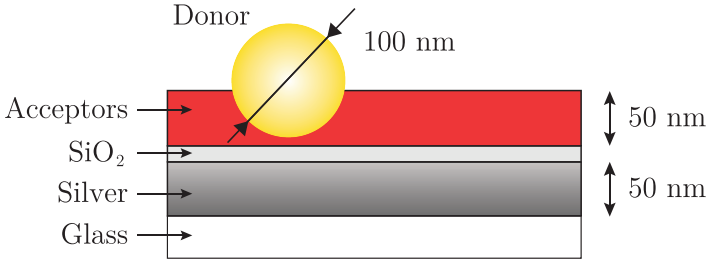

Figure 2.5 – *Sketch of the sample.*

On average, the distance between two close-by donors is more than 20 µm. Thus, the excitation laser can easily address a single donor bead and we can study the occurrence of energy transfer over a large range of distances between this donor bead and the surrounding acceptor molecules. From AFM measurements, we determine the thickness of the acceptor layer, which is of the order of 50 nm. Note that the spatial extent of both the donor beads

[2]Best practices for the deposition of dense metallic films with high purity and low surface roughness can be found in Ref. [43].

(∼100 nm) and the acceptor layer (∼50 nm) reasonably match the decay length of the surface-plasmon intensity in the transverse direction on the dielectric side (∼70 nm). This optimises the number of donor molecules that can excite surface plasmons on the silver film as well as the number of acceptor molecules that can absorb their energy.

The thickness of the silver layer (50 nm) is larger than the decay length of the surface-plasmon intensity on the metal side, which is of the order of 15 nm at $\lambda_0 = 650$ nm. More precisely, it follows from Eq. (2.2b) that only 2% of the intensity of the surface plasmon reaches 50 nm on the metal side. Thus, the thickness of the silver film ensures that coupling effects between the surface plasmons propagating on each side of the silver film can be neglected. However, we also need to limit the thickness of the silver film since we measure the fluorescence photons through the silver film using an objective located below the sample, as we will see in Sect. 2.3.3.

From these considerations, we can model the silver film by a semi-infinite medium. Moreover, PVA and SiO_2 have a similar relative permittivity ($\epsilon_d \approx 2.25$). The thickness of this dielectric layer and the decay length of the surface-plasmon intensity on the dielectric side have the same order of magnitude. In addition, the thickness of the PVA layer is too small for the apparition of guided modes in the layer. We may consequently consider that the dielectric side is semi-infinite as a first approximation. By describing the geometry of the sample by this simple model, we can find analytical solutions for wave propagation in this system. This is an advantage in comparison to more elaborate nanostructures that must be numerically studied.

2.3.3 Optical setup

To study the occurrence of the plasmon-mediated energy transfer, we excite the donor and we measure the photons emitted by the acceptors over a wide range of distances. The characterisation of energy transfer over distance of several micrometres requires the development of a microscope constituted of two independent optical paths for excitation and detection, as represented in Fig. 2.6. To this end, we use a single-mode micro-lensed fibre (Nanonics Imaging Ltd.) in which we inject the excitation laser, while detection is performed using an oil objective (×100, NA = 1.4, Olympus). The micro-lensed fibre is mounted on a three-axis piezoelectric nanopositioner required to bring the microlens 4 µm above the sample, at its working distance. The focal spot has then a diameter of about 1.5 µm.

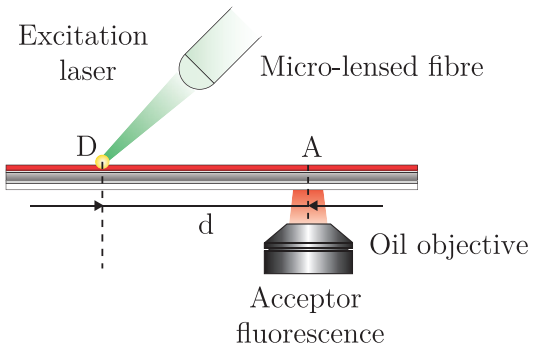

Figure 2.6 – *Optical microscope with two independent paths for excitation and detection.*

This configuration allows to properly control the distance d between the excitation and

the detection area. Indeed, the position of the microscope objective is fixed while both the sample and the micro-lensed fibre can be translated with a nanometric precision. To perform the measurements, we keep the micro-lensed fibre focused on the donor and we simultaneously move the sample and the fibre away from the microscope objective. Thus, we can measure the fluorescence of the acceptors for different distances d. In the following paragraphs, the excitation and the detection paths will be described in detail.

Excitation The excitation part of the optical setup is represented in Fig. 2.7. It is dedicated to the excitation of the donor as well as to the measurement of its fluorescence. The excitation source is a supercontinuum pulsed laser (Fianium SC450) with a repetition rate of 10 MHz. The laser light is filtered at 532 nm (FF01-532/18, Semrock) before being injected into the micro-lensed fibre that focuses the laser within a diameter of approximately 1.5 µm. Fluorescence photons from the donor are also collected via the micro-lensed fibre and detected by a single-photon avalanche diode (SPCM-AQR, Perkin-Elmer). By maximising the number of collected photons on this detector, we ensure that the donor excitation is constant and always optimised. Moreover, this detector is essential to monitor the fluorescence of the donor during the experiment in order to verify that it does not photobleach. The decay histogram of the donor can also be measured using a time-correlated single-photon counting (TCSPC) system (HydraHarp 400, PicoQuant).

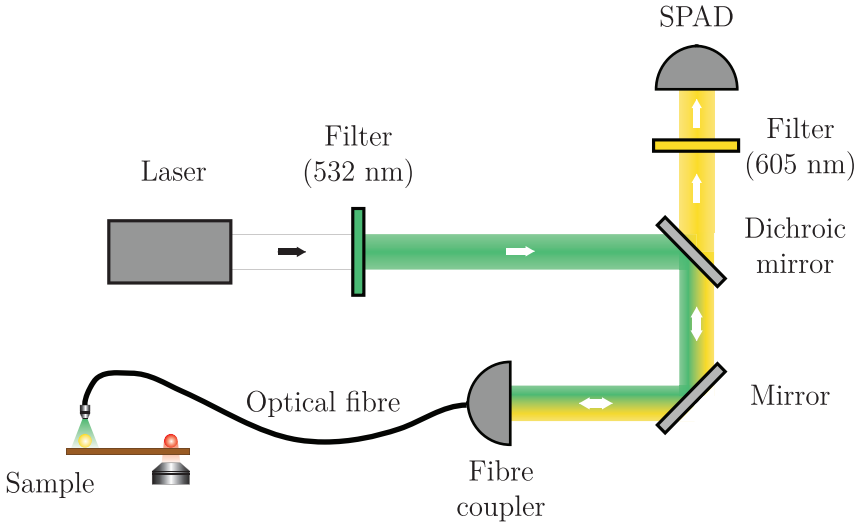

Figure 2.7 – *Excitation part of the optical setup. SPAD stands for single-photon avalanche diode.*

Detection The detection part of the optical setup is represented in Fig. 2.8. It is dedicated to the measurement of the fluorescence coming from the acceptor. Fluorescence photons emitted from the sample are filtered by a dichroic mirror and focused onto the core of a multimode fibre, characterised by a 50 µm fibre core diameter and connected to a spectrometer (Acton SP2300, Princeton Instruments). Thus, the signal measured by the spectrometer arises from the 500-nm-sized region of the sample that is optically conjugated to the detection system. An EM-CCD camera (iXon 897, Andor) allows to record wide-field images of the sample. The camera is used for alignment procedures, such as bringing the micro-lensed fibre at its working distance and choosing the area of

the sample that is to be studied. It also provides us with useful information in order to monitor any drift during the acquisition.

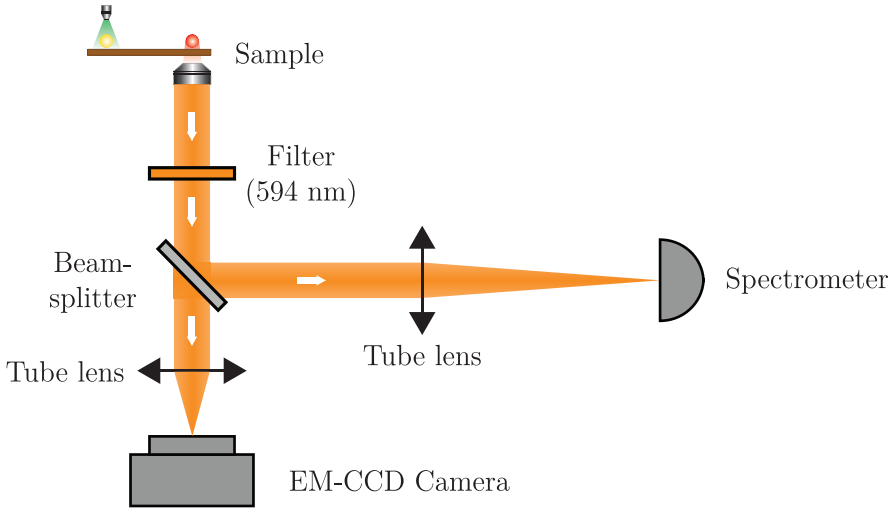

Figure 2.8 – *Detection part of the optical setup. EM-CCD stands for electron-multiplying charge-coupled device.*

2.4 Evidences of the occurrence of energy transfer

Using this experimental setup, we can characterise the energy transfer process by measuring either the decay histogram of the donor bead or the fluorescence spectrum of the acceptors. These two approaches give different insights on the energy transfer process: while the modification of the decay rate is mainly due to dipole-dipole interaction and characterises the occurrence of energy transfer between donors and close-by acceptors, we can demonstrate the occurrence of long-range plasmon-mediated energy transfer using spectral measurements.

2.4.1 Decay rate of the donor

In Sect. 1.3, we highlighted that the energy transfer rate is directly given by the increase in the LDOS at the position of the donor due to the presence of the acceptor. The energy transfer rate is thus given by

$$\Gamma_{D\to A} = \Gamma_{DA} - \Gamma_D \,, \tag{2.3}$$

where Γ_{DA} and Γ_D are respectively the decay rate of the donor in the presence and in the absence of the acceptor. Furthermore, the *energy transfer efficiency*, defined as the probability for the donor of exciting the acceptor among all the possible decay processes, is directly given by

$$\eta_{et} = \frac{\Gamma_{D\to A}}{\Gamma_{DA}} \,. \tag{2.4}$$

Experimentally, we measure the decay histogram of a donor bead (for $d = 0$ µm) in the presence of surrounding acceptors, on the sample described in Sect. 2.3.2. Then, we prepare

a donor-only sample – that is, a sample without acceptor dyes – to measure the decay histogram of a donor bead on silver in the absence of acceptors. To this end, we spin-coat donor beads on a silver film, following the procedure described in Sect. 2.3.2 except that acceptor dyes are not added to the solution. By fitting a mono-exponential distribution to the measured histograms (Fig. 2.9), we determine that the decay rate of the donor bead in the presence of the acceptors is increased by a factor of 1.4 with respect to the situation without acceptors. This corresponds to an overall energy transfer efficiency of 30%. This value is determined by the dipole-dipole interaction between the molecules inside the donor bead and the acceptors located at distances of the order of a few nanometers from the bead. Indeed, FRET is much more efficient than long-range energy transfer, as we will see in Sect. 2.6.4. Thus, the modification of the decay rate of the donor bead does not provide us with any information about the occurrence and the efficiency of the energy transfer in the long-range regime. In order to characterise the energy transfer in this regime, we can however perform spectral measurements of the fluorescence intensity emitted by the acceptors at different distances d from the donor bead.

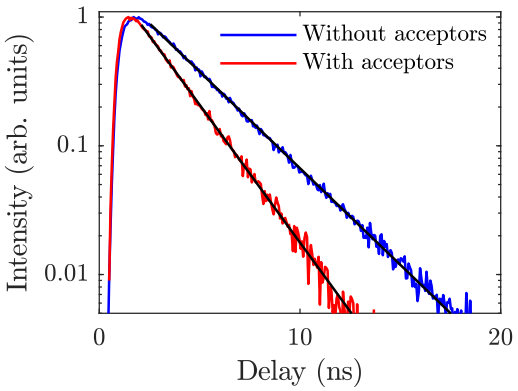

Figure 2.9 – *Decay histograms of the donor on silver in the absence of surrounding acceptor (blue curve) and in the presence of the acceptor (red curve). Black lines are mono-exponential fits to the histograms.*

2.4.2 Spectral measurements

In order to characterise the occurrence of energy transfer in the long-range regime, we study plasmonic radiative losses generated by surface plasmons excited by the donor on a silver film without acceptors. This allows us to interpret the spectral measurements performed on the sample containing both the donor and the acceptors.

Plasmonic radiative losses

Whenever surface plasmons propagate along an interface, part of their energy is lost as ohmic losses, and part of the energy is scattered by inhomogeneities located at the interface between the metal and the dielectric medium. While we measure the fluorescence intensity emitted by acceptors that are excited by surface plasmons, we also detect these scattered waves called *plasmonic radiative losses*. These radiative losses must be distinguished from the fluorescence of the acceptors. To characterise these losses, we use the donor-only sample previously mentioned. We excite a single donor bead and we measure the emission spectrum due to the radiative losses of the surface plasmons for different

distances d ranging from 2 to 6 µm. These spectra are red-shifted in comparison to the spectrum measured at $d = 0$ µm. Indeed, the donor beads emit a broadband radiation characterised by wavelengths ranging from approximately 600 to 700 nm. In this spectral range, the propagation length of surface plasmons significantly depends on the wavelength. Since longer wavelengths of the spectrum propagate over larger distances, the spectrum of plasmonic radiative losses appears as red-shifted by the propagation. In order to confirm the origin of the observed shift, we define a function given by the product between the spectrum of the donor at $d = 0$ µm and a decreasing exponential function modelling the attenuation of the surface plasmon propagating along the interface between a semi-infinite silver layer and a semi-infinite PVA layer. A good agreement between the experimental spectra and the model function is obtained by fitting this function to the experimental spectra for several distances d from 2 to 6 µm. As an example, Fig. 2.10 shows the spectrum measured at $d = 0$ µm, along with the spectrum measured at $d = 5$ µm and the results of the fit.

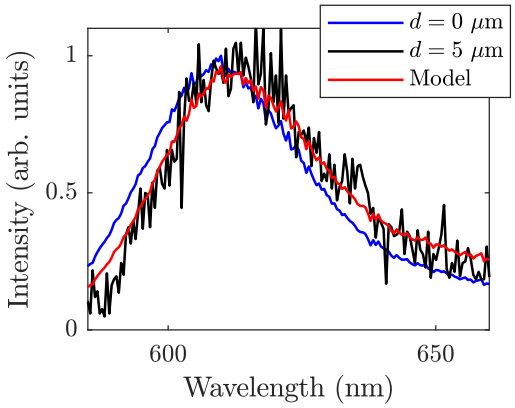

Figure 2.10 – *Normalised spectra of radiative losses of surface plasmons excited by a fluorescent bead. Blue and black curves respectively show the experimental data for d=0 µm and d=5 µm. A model function (red curve) that takes into account the wavelength dependence of the dielectric constant of silver is fitted to the spectrum measured at d=5 µm.*

Fluorescence of the acceptors

In order to have a signature of long-range energy transfer, we perform spectral measurement on a sample containing both donors and acceptors. To do so, we excite a donor using the micro-lensed fibre and we perform spectral measurements at different distances d from the donor's position, as represented in Fig. 2.6. The acquisition time is 200 s per spectrum. To have a thorough understanding of this measurement, the various processes that could contribute to the signal collected at a distance d from the donor must appropriately be considered:

- Firstly, due to the size of the excitation laser spot (diameter of 1.5 µm), acceptors located in the proximity of the donor can directly be excited by the laser. This effect is minimised by blue detuning the excitation laser with respect to the acceptor absorption spectrum but it is still present. The excited acceptors can either emit fluorescence photons or excite surface plasmons that can be detected at a distance d due to radiative losses. In both cases, the emitted photons spectrally overlap with the acceptor fluorescence and they artificially increase the signal to be measured.

- Secondly, since acceptors are present in the vicinity of the donor, short-range energy transfer (FRET) occurs. Acceptors excited by this mechanism can either emit fluorescence photons or excite surface plasmons with a spectrum overlapping with the acceptor fluorescence spectrum, which can be detected at a distance d due to radiative losses.

In order to estimate the contribution of these processes, we perform a reference experiment in which we focus the micro-lensed fibre on the layer of acceptors, in an area without any donor bead. Firstly, we measure the signal produced as a function of d. This gives us an upper limit for the contribution of the first process. Indeed, since some additional acceptor molecules are excited instead of the donor bead (diameter 100 nm), we can expect a stronger signal at the frequencies of the acceptors in the reference experiment. Secondly, we compare the spectra measured at $d = 0$ µm in the actual and the reference experiments. The first spectrum is due to fluorescence of the donor, direct excitation of the acceptors and FRET. The second spectrum is due to direct excitation of the acceptors, with some additional acceptors in comparison to the first situation. Both experiments show the same intensity due to the fluorescence of the acceptors. Therefore, the contribution of direct excitation in the reference experiment is equal to the contribution of direct excitation and FRET in the energy transfer experiment.

Figure 2.11a shows raw data measured during the energy transfer experiment at $d = 2$ µm (blue curve) along with the data measured during the reference experiment for the same distance d (red curve). We can see that the same irregularities are present in both spectra. These irregularities are due to stray light and thus cancel out when the reference spectrum is subtracted to the raw measurement. Figure 2.11b shows the background corrected spectrum determined using this procedure. This spectrum shows two distinct peaks. While the peak centred at 610 nm is due to radiative losses of surface plasmons excited by the donor, the peak centred at 695 nm is the fluorescence of the acceptors excited by surface plasmons. This second peak is therefore a signature of the occurrence of energy transfer through surface plasmons.

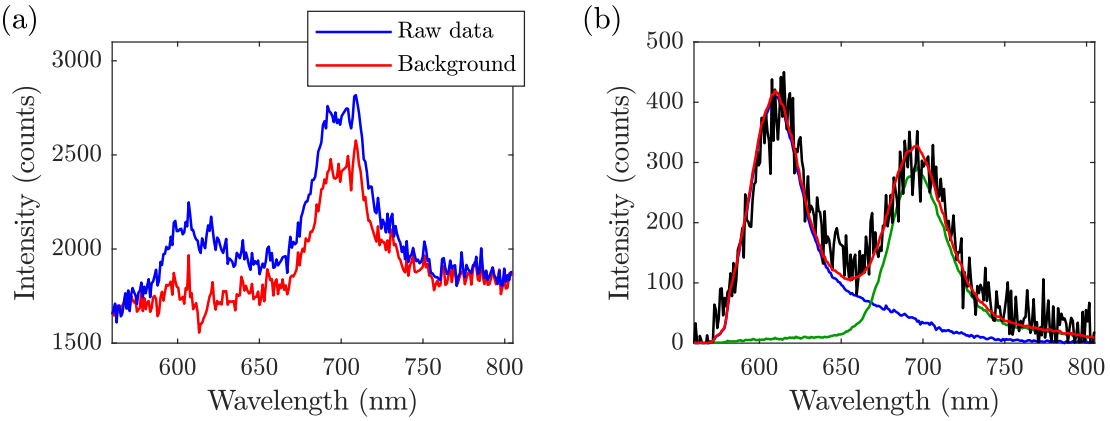

Figure 2.11 – *(a) Raw spectrum measured at d=2 µm (blue curve) and associated background estimate (red curve). (b) Background corrected signal at d=2 µm (black curve). A model function (red curve) defined as the sum of the acceptor fluorescence spectrum (green curve) and the plasmonic radiative losses spectrum (blue curve) is fitted to the spectrum.*

To support these conclusions, we consider a model function given by the sum of the spectrum of plasmonic radiative losses (including the red-shift induced by propagation)

and of the spectrum of acceptor fluorescence on silver. Then, we fit this function to the background-corrected spectra using only two free parameters that are normalisation constants. In total, we perform this analysis for six spectra measured at distances d ranging from 2 to 7 µm. The good agreement between the model function and the experimental data (Fig. 2.12) confirms that the two peaks are respectively due to plasmonic radiative losses and energy transfer. Note that the relative contribution of each peak depends on the distance d. This is explained by the wavelength dependence of the surface-plasmon propagation length, as we will see in the following section. As a side experiment, we also perform similar measurements on a control sample made of donors and acceptors on a bare glass substrate, without the silver layer. On this sample and with the same integration time, we do not detect fluorescence emission from the acceptors in this range of distances. This confirms that the observation of energy transfer is allowed by the presence of the silver film in the long-range regime.

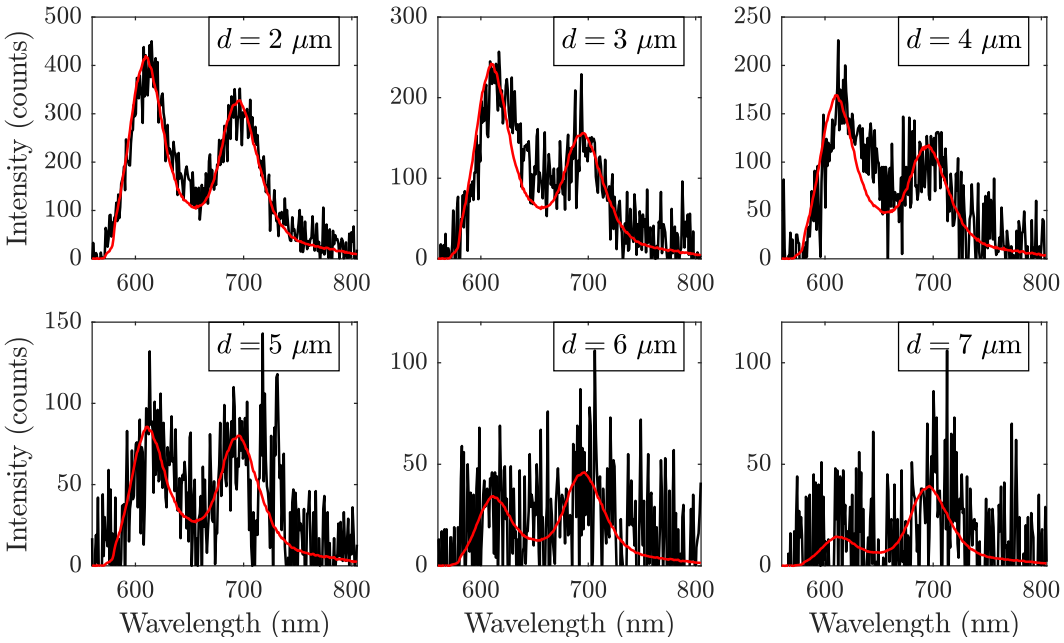

Figure 2.12 – *Measured spectra at different distances d. The black points show spectra measured at a distance d from the donor ranging from 2 to 7 µm, with an integration time of 200 s. The red curves are determined by fitting a model function to the spectra for each distance d.*

2.5 Distance dependence of the energy transfer rate

From the fluorescence spectra of the acceptors measured at several donor-to-acceptor distances, we can estimate the distance dependence of the energy transfer process. Since the energy transfer process relies on the propagation of surface plasmons excited by the donor bead, we can find a relation between the propagation length of the surface plasmons excited by the donor and the characteristic distance of the energy transfer process, which we call the *energy transfer range*.

2.5.1 Surface-plasmon propagation length

In order to estimate the spectrally averaged propagation length of the surface plasmons excited by the donor, we study the donor-only sample and we measure plasmonic radiative losses due to surface plasmons excited by a donor bead. Figure 2.13 shows the total intensity of plasmonic radiative losses as a function of the distance d. For each distance d, we also calculate the standard error on the intensity estimates by taking into account the statistical error on the number of photons determined from spectral measurements. To do so, we can assume that the number of photons N_d measured in the spectral range of the donor at each distance d is Poisson distributed. As we perform background subtraction on the data, it is also relevant to consider the number of measured background photons noted N_d^*. Thus, we can estimate the standard error σ_d on each intensity estimate using the addition property of the variance for uncorrelated variables. We obtain

$$\sigma_d = \sqrt{N_d + N_d^*}\,. \tag{2.5}$$

In this analysis, we neglect the error on the distance d. Indeed, we can accurately control the distance between the excitation and detection point in the experiment via the piezoelectric nanopositionners. Moreover, we monitor in real time the drift of the experiment using the EM-CCD camera and the SPAD collecting the fluorescence photon from the donor bead. During the 200 s acquisition time of one spectrum, this drift is negligible.

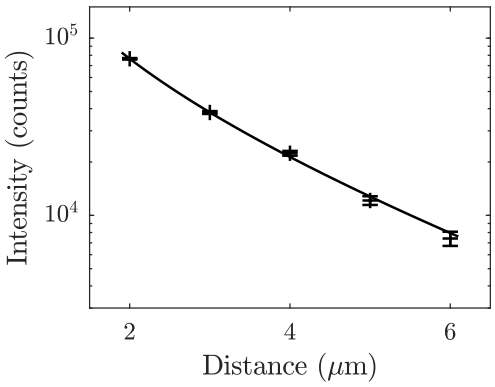

Figure 2.13 – *Scattered intensity as a function of the distance d. The black points are experimental data and the black solid line is determined by fitting the model function $d^{-1}\,exp(-d/l_D)$ to the data. Error bars correspond to a statistical significance of $\pm 1\sigma$ calculated assuming that the measured intensities are Poisson-distributed.*

The propagation length l_D of the surface plasmons excited by the donor is defined as the distance over which a one-dimensional surface plasmon propagates until its intensity has decreased of $1/e$. In the experiment, surface plasmons are supported by a silver film so that they can propagate along two dimensions. For this reason, an additional geometric factor d^{-1} must be taken into account when analysing the distance dependence of the surface-plasmon intensity. Hence, we fit a model function defined by $d^{-1}\,\exp(-d/l_D)$ to the measured data. The propagation length determined using this procedure is $l_D = 3.4 \pm 0.1$ µm. This is slightly smaller than the theoretically expected value of 3.8 µm estimated by calculating the surface-plasmon propagation length averaged over all the donor fluorescence spectral range, weighted by the fluorescence intensity at each wavelength. This difference is likely to be due to plasmonic radiative losses, since surface roughness at the silver-dielectric interface is not accounted for in the theoretical model.

2.5.2 Energy transfer range

We now study the distance dependence of the energy transfer rate. Indeed, for each distance d, the number of photons collected from the acceptors due to energy transfer is given by the integral of the function which models the acceptor fluorescence (Fig. 2.11b, green curve). Figure 2.14 shows the distance dependence of the intensity collected from the acceptors (red data point). We also fit a function $d^{-1}\exp(-d/l_{et})$ to the data in order to determine the energy transfer range l_{et}. By using this model function, the energy transfer range is defined by analogy to the surface-plasmon propagation length. Using this procedure, we obtain $l_{et} = 5.4 \pm 0.9$ µm. This is significantly larger than the surface-plasmon propagation length ($l_D = 3.4$ µm) determined on the donor-only sample. Indeed, l_D is the propagation length averaged over the entire spectrum of the surface plasmons excited by the donor, while the donor emission contributes to the energy transfer in the spectral range for which a significant overlap occurs with the acceptor absorption spectrum. In order to highlight this effect, we determine the surface-plasmon propagation length on a reduced spectral range ($635 < \lambda_0 < 680$ nm) around the maximum of the acceptor absorption spectrum (Fig. 2.14, blue data point). This data analysis gives a surface-plasmon propagation length of 5.3 ± 1 µm, in good agreement with the value of l_{et}. This observation constitutes a further evidence that the acceptors in the experiment are excited via surface plasmons originating from the donor bead.

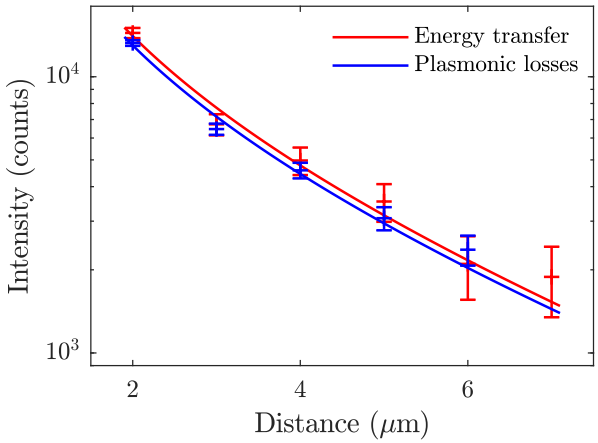

Figure 2.14 – *Distance dependence of the intensity detected from the acceptors and due to energy transfer (in red) and of the plasmonic radiative losses evaluated over the reduced spectral range $635<\lambda_0<680$ nm (in blue). Data points are experimental data and the solid lines are determined by fitting a model function to the data. Error bars correspond to a statistical significance of $\pm 1\sigma$ calculated assuming that the measured intensities are Poisson-distributed.*

2.6 Efficiency of the energy transfer process

As already pointed out, the low efficiency of the energy transfer process for large distances d prevents any experimental determination of the energy transfer rate in this regime. Nevertheless, we can theoretically estimate the plasmon-mediated energy transfer efficiency using the Green formalism.

2.6.1 Modelling of the experiment

In order to theoretically estimate the energy transfer efficiency, we must define a model for the experiment. As discussed in Sect. 2.3.2, we can model the geometry of the sample by two semi-infinite media that are respectively silver and PVA. This model is represented in Fig. 2.15. Since energy transfer occurs for the frequencies of maximum overlap between the emission spectrum of the donor and the absorption spectrum of the acceptor, the transfer frequency ω can be approximated by using the free-space wavelength $\lambda_0 = 663$ nm which corresponds to the maximum of the acceptor absorption spectrum. Moreover, a Drude-Lorentz model can be used to describe the properties of silver. We can thus calculate the dielectric constant of silver from Eq. (2.1) which gives us $\epsilon_m = -16.2 + 1.2i$. The relative permittivity of PVA is set to $\epsilon_d = 2.25$ in the model.

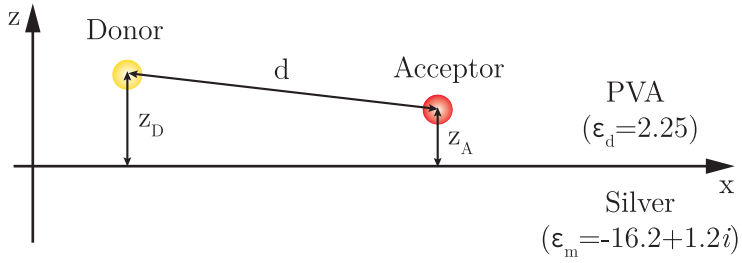

Figure 2.15 – *Model used to calculate the energy transfer efficiency. The silver film and the PVA layer are modelled by two semi-infinite media characterised by their relative permittivities.*

Let us describe the other parameters involved in the model.

Absorption cross-section of the acceptor (σ_A) In order to describe the response of the acceptors to the electric field generated by the donor bead, we can calculate the absorption cross-section of the acceptor from the molar extinction coefficient ($1.6 \times 10^5\,\mathrm{L\,mol^{-1}\,cm^{-1}}$) specified by the provider (ATTO-TEC) for molecules in a phosphate-buffered saline (PBS) solution and for their maximum absorption wavelength. This corresponds to an absorption cross-section $\sigma_A = 0.061$ nm^2 for a single molecule. The relative permittivity of PBS is around 1.77, which is slightly smaller than the relative permittivity of PVA. Nevertheless, we use the value of σ_A given above as a coarse approximation.

Intrinsic quantum yield of the donor (η_D) Concerning the donor beads (Red FluoSpheres), they are constituted of BODIPY fluorophores with a intrinsic quantum yield η_D often approaching unity according to the provider (ThermoFisher Scientific). Thus, we use $\eta_D = 1$ in the calculations.

Intrinsic quantum yield of the acceptor (η_A) The intrinsic quantum yield of acceptors in a PBS solution is of the order of 0.6 according to the provider (ATTO-TEC). It is difficult to transpose this value to the experiment, in which the emitters are embedded in a solid PVA matrix. In the calculations, we use $\eta_A = 0.6$ as a first approximation.

Orientation of the dipole moments ($\mathbf{u}_D$, $\mathbf{u}_A$) The experiment involves a large number of emitters with arbitrary orientations. It is thus relevant to average the calculations over the orientation of the transition dipoles.

Vertical distances to the mirror (z_D, z_A) It is not straightforward to define the distances from the mirror surface to the donor (noted z_D) and to the acceptor (noted z_A), since the experimental configuration involves many emitters. These emitters are spatially distributed over the size of the bead for the donors (diameter 100 nm). Plus, the acceptors are spatially distributed over the thickness of the PVA layer (thickness 50 nm). We could use the average distance to the silver mirror for each of these spatial distributions in order to define the distance of the emitters to the silver mirror. Considering the 10-nm silica spacer between the silver film and the emitters, this would correspond to $z_D \approx 60$ nm and $z_A \approx 35$ nm. In the following section, we will show another approach to estimate an effective distance between the mirror surface and each emitter.

2.6.2 Distance between the mirror and the emitters

In order to estimate an effective value for z_D and z_A, we experimentally study the decay rate enhancement of donors and acceptors due to the silver surface. For this purpose, we measure the decay histogram of a donor bead on two different samples, with and without a silver film (Fig. 2.16a). We obtain $\Gamma_D/\Gamma_{D,0} = 1.72$, where Γ_D and $\Gamma_{D,0}$ are respectively the decay rates of the donor on silver and on glass. Following the same procedure for the acceptors (Fig. 2.16b), we obtain $\Gamma_A/\Gamma_{A,0} = 1.58$, where Γ_A and $\Gamma_{A,0}$ are respectively the decay rates of the acceptor on silver and on glass.

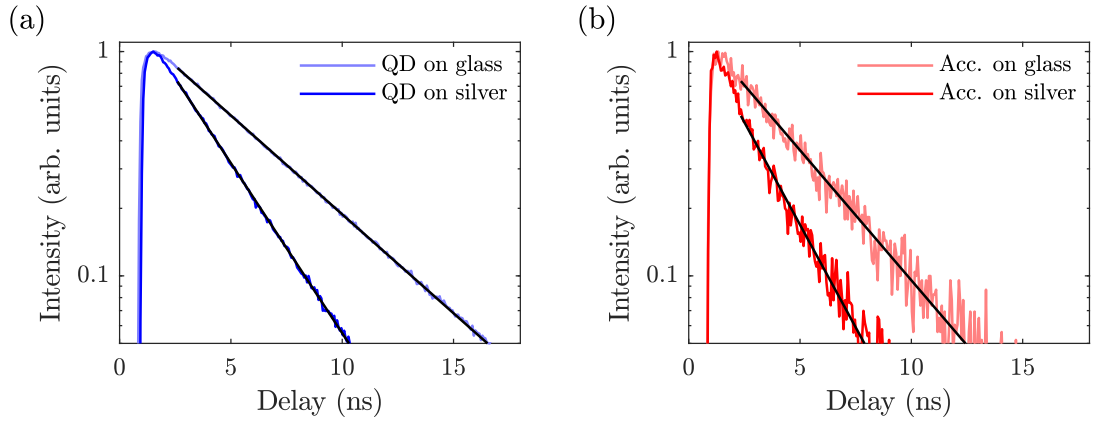

Figure 2.16 – *(a) Decay histogram of the donor in the presence (blue curve) and in the absence (dark blue curve) of the silver surface. (b) Decay histogram of the acceptor in the presence (red curve) and in the absence (dark red curve) of the silver surface. Black lines are mono-exponential fits to the histograms.*

By comparing these results with theoretically expected values, we can estimate an effective distance between the emitters and the silver surface. To do so, we define the decay rate enhancement due to the electromagnetic interaction between an emitter and its environment by Γ/Γ_0 where Γ and Γ_0 are respectively the decay rates of the emitter in its environment and in a reference medium. In the experiments described in this chapter, all of the reference measurements are performed on glass substrates, with the emitters being embedded in polymer matrices. As a reference, we consequently choose a homogeneous medium characterised by a relative permittivity $\epsilon_h = 2.25$. Then, the decay rate enhancement can be calculated from the dyadic Green's function describing the system, noted

$\mathbf{G}(\mathbf{r},\mathbf{r},\omega)$, and evaluated at the position $\mathbf{r}$ of the emitter and at the frequency ω. This reads

$$\frac{\Gamma}{\Gamma_0} = \frac{6\pi c}{\omega n}\,\mathrm{Im}\{\mathbf{u}\cdot\mathbf{G}(\mathbf{r},\mathbf{r},\omega)\,\mathbf{u}\}\ . \tag{2.6}$$

Considering the normalised decay rate averaged over the orientation $\mathbf{u}$ of the transition dipole, we obtain

$$\left\langle\frac{\Gamma}{\Gamma_0}\right\rangle_{\mathbf{u}} = \frac{2\pi c}{\omega n}\,\mathrm{Im}\left\{\mathrm{Tr}\ \mathbf{G}(\mathbf{r},\mathbf{r},\omega)\right\}\ , \tag{2.7}$$

where Tr denotes the trace operator. This expression is valid whenever the dyadic Green's function is diagonal, which is true here due to the symmetry of the modelled geometry. Furthermore, the expression of the dyadic Green's function can analytically be simplified in the specific case of two semi-infinite media, as we show in Appendix A.

Figure 2.17 shows the enhancement of the spontaneous emission rate as a function of the distance z to the silver mirror. The calculations are performed for two different frequencies respectively corresponding to the maximum of the emission spectrum for the donor ($\lambda_0 = 610$ nm) and the acceptor ($\lambda_0 = 695$ nm). As expected, we note some variations in the decay rate due to constructive and destructive interferences between the field emitted by the dipole and its reflected field.

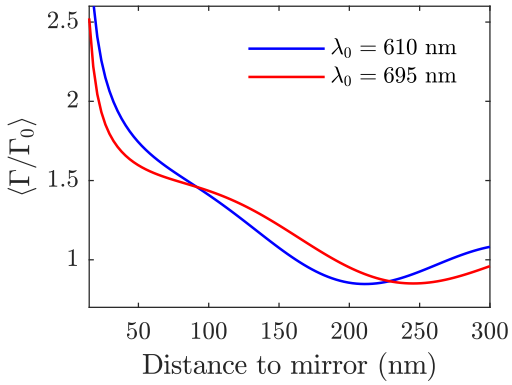

Figure 2.17 – *Calculated enhancement of the decay rate of an emitter in the near-field of a silver mirror, computed for λ_0=610 nm (blue curve) and λ_0=695 nm (red curve), and averaged over three orthogonal dipole orientations.*

To compare the theoretical model expressed by Eq. (2.7) and the values determined in the experiment, we use the relation between the intrinsic quantum yield of an emitter and the enhancement of its total decay rate that we derived in Sect. 1.2.3. This relation is expressed by

$$\frac{\Gamma^{tot}}{\Gamma_0^{tot}} = 1 + \eta_i\left(\frac{\Gamma}{\Gamma_0} - 1\right)\ , \tag{2.8}$$

where Γ^{tot} and Γ_0^{tot} are the total decay rates of the emitter in its environment and in the homogeneous medium of reference. For the donor, assuming $\eta_D = 1$, we numerically solve this equation for z_D which gives $z_D \approx 50$ nm. For the acceptor, assuming $\eta_A = 0.6$ and following the same procedure, we obtain $z_A \approx 20$ nm. In both cases, these values are consistent with the layout of the sample, and they are slightly smaller than the average distances between the spatial distributions of the emitters and the silver mirror. The calculations presented in the following sections will be performed using these values of z_D and z_A.

2.6.3 Energy transfer rate

Under the assumptions detailed in Sect. 1.3.1, the energy transfer rate Γ_{et} depends on the absolute square of the dyadic Green function and can be written as

$$\frac{\Gamma_{et}}{\Gamma_0} = 18\pi\sigma_A |\mathbf{u}_A \cdot \mathbf{G}(\mathbf{r}_A, \mathbf{r}_D, \omega)\, \mathbf{u}_D|^2 \,, \tag{2.9}$$

where Γ_0 is the decay rate of the donor in the homogeneous medium of reference and the subscripts D and A respectively refer to the position and orientation of the donor and the acceptor. The energy transfer rate averaged over the orientations of the dipole moment reads

$$\left\langle \frac{\Gamma_{et}}{\Gamma_0} \right\rangle_{\mathbf{u}} = 2\pi\sigma_A \sum_{i,j=1}^{3} |\mathbf{u}_j \cdot \mathbf{G}(\mathbf{r}_A, \mathbf{r}_D, \omega)\, \mathbf{u}_i|^2 \,, \tag{2.10}$$

where $\mathbf{u}_i$ and $\mathbf{u}_j$ are three orthonormal vectors.

Figure 2.18 shows the distance dependence of the energy transfer rate between a donor and an acceptor for $z_D = 50$ nm and $z_A = 20$ nm. We numerically investigate a large range of donor-to-acceptor distances, from $d = 30$ nm up to $d = 100$ µm. The donor and the acceptor are at the same radial position for the smallest considered distance. We specifically consider two different cases, either in the presence of the silver mirror or in the homogeneous medium of reference ($\epsilon_d = 2.25$). For distances d larger than 100 nm, the energy transfer rate in the homogeneous medium scales as d^{-2}. This distance dependence is a characteristic of far-field radiation. In the same range of distances, the energy transfer rate varies as $d^{-1}\exp(-d/l_{et})$ when the silver mirror is present. In this regime, the distance dependence of the energy transfer rate is determined by the surface-plasmon propagation length, as experimentally observed.

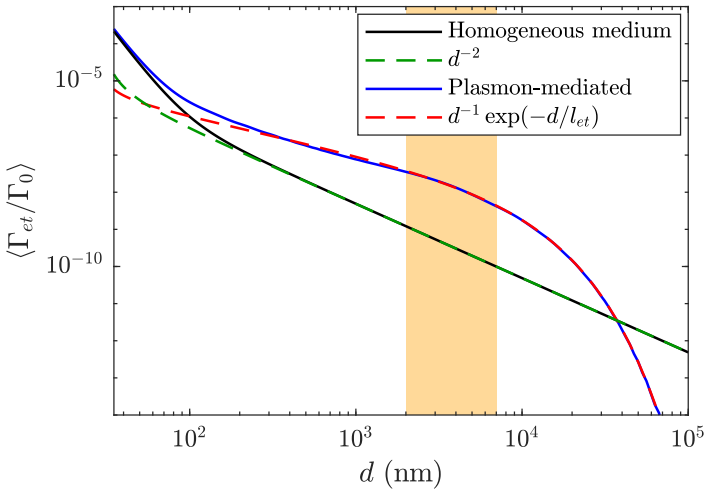

Figure 2.18 – *Normalised energy transfer rate averaged over the orientations of the dipole moment. An orange tinted area corresponds to the range of distances studied in the experiment.*

Furthermore, we can clearly identify three different ranges that characterise the plasmon-mediated energy transfer rate:

- For d smaller than 100 nm, the energy transfer rate is slightly larger in the presence of the silver mirror than in the homogeneous medium of reference: as the process

is already quite efficient in the homogeneous medium, the silver mirror does not substantially increase the energy transfer rate.

- For d between 100 and 50 µm, the energy transfer rate is much larger in the presence of the silver mirror.
- For d larger than 50 µm, the energy transfer rate is very low and dominated by far-field radiation. In this regime, the silver surface becomes a source of losses and the energy transfer rate is larger in the homogeneous medium.

2.6.4 Energy transfer efficiency and enhancement factor

In the literature, the characterisation of the energy transfer process is usually performed by calculating the *energy transfer efficiency*, defined as the probability for the donor to excite the acceptor among all the possible decay processes. Therefore, the energy transfer efficiency averaged over the orientations of the dipole moment is given by

$$\eta_{et} = \eta_D \frac{\langle \Gamma_{et} \rangle}{\langle \Gamma_D \rangle + \langle \Gamma_{et} \rangle} . \tag{2.11}$$

The energy transfer efficiency does not depend on the intrinsic quantum yield of the acceptor, as it only characterises the power absorbed by the acceptor and not the power it radiates. It does depend on the intrinsic quantum yield of the donor but we can assume that $\eta_D = 1$, as previously noted. Figure 2.19a shows the energy transfer efficiency as a function of the distance between the donor and the acceptor. We can see that the energy transfer process is more efficient without the silver mirror for distances smaller than 65 nm. It means that the slight enhancement of the energy transfer rate due to the silver mirror is not sufficient to compensate for the generated losses. In contrast, for distances larger than 100 nm, the efficiency of the process becomes higher using the silver mirror. In the range of distances studied in the experiment (between 2 and 7 µm), the efficiency of the process is of the order of 10^{-8}. This low efficiency is compensated in the experiment by the large number of molecules inside the bead (donors) and the PVA layer (acceptors).

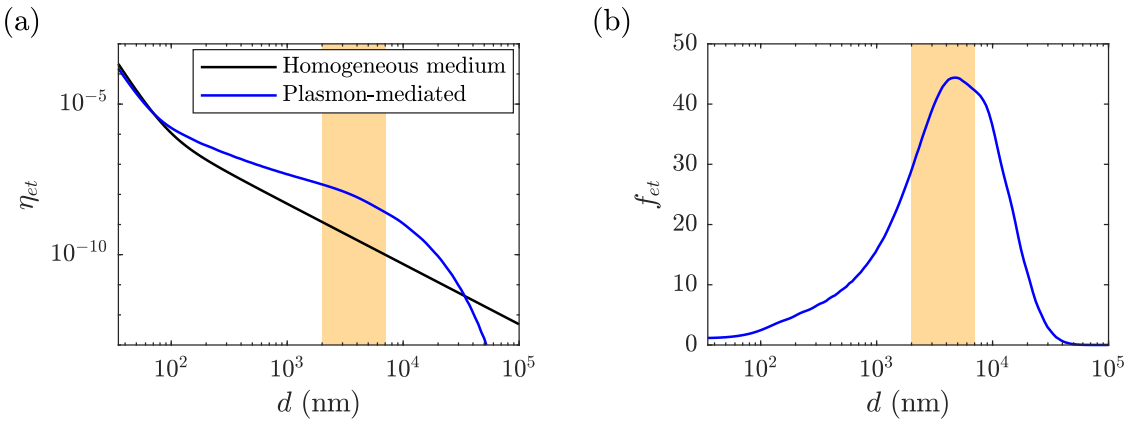

Figure 2.19 – *(a) Energy transfer efficiency for two emitters separated by a distance d in the vicinity of the mirror (blue curve) and inside a homogeneous medium (black curve). (b) Enhancement factor versus the distance d. On each figure, an orange tinted area represents the range of distances studied in the experiment.*

Another quantity which is commonly used to characterise the energy transfer process is the *enhancement factor*, defined as the ratio of the energy transfer rate in the presence of the silver mirror to the rate in the homogeneous environment of refractive index n. In this case, f_{et} reads

$$f_{et} = \frac{\langle \Gamma_{et} \rangle}{\langle \Gamma_{et,0} \rangle} \, . \tag{2.12}$$

The enhancement factor f_{et} does not depend on the intrinsic quantum yield of the two emitters. Figure 2.19b shows the enhancement factor as a function of the donor-to-acceptor distance. For distances smaller than 100 nm, the enhancement factor is slightly larger than unity, meaning that the energy transfer rate is not really affected by the presence of the silver mirror. In contrast, this enhancement is substantial for distances between 2 and 7 µm, in the range of distances associated with experimental measurements. In this range, the average value of the enhancement factor is $f_{et} \sim 40$ which means that the energy transfer rate is enhanced by a factor of 40 in comparison to the rate calculated in a homogeneous medium. The enhancement factor is maximum for distances around 5 µm and then decreases down to zero. Indeed, the presence of the silver mirror generates losses for these larger distances.

2.7 Conclusion

In this chapter, we presented an experimental study of the occurrence of energy transfer between fluorescent emitters mediated by surface plasmons. Starting from the low efficiency of the energy transfer process in free space for large donor-to-acceptor distances, we investigated a configuration in which the energy could be guided from the donor to the acceptor in a more efficient way. For this purpose, surface plasmons are good candidates, as they naturally confine waves at optical frequencies over the dimension perpendicular to the interface. Thus, we designed a sample geometry that can be easily fabricated and characterised. In practice, we used a donor bead and a continuous layer of acceptor molecules lying on top of a thin silver film. We studied two signatures of the energy transfer: the modification of the decay rate of the donor and the acceptor fluorescence conditioned by the excitation of the donor. While the first signature is sensitive to the short-range interaction, the second one turns out to be relevant for the study of long-range energy transfer. From spectral measurements, we estimated the distance dependence of the acceptors fluorescence (Fig. 2.14). Furthermore, we related the energy transfer range to the surface-plasmon propagation length and we showed that the energy transfer process is driven by the surface-plasmon propagation length at the frequencies for which maximum donor-acceptor spectral overlap occurs. Finally, we modelled the experiment and we calculated the distance dependence of the energy transfer rate using the Green formalism (Fig. 2.18).

In this work, we distinguished different regimes. In the short-range limit (typically less than 100 nm) the energy transfer process is not much affected by the silver film as it is already efficient in free space. In contrast, in the long-range limit (more than 100 nm), the energy transfer is very inefficient in free space and the silver film greatly enhances its efficiency. In this range, the distance dependence of the energy transfer rate is determined by the surface-plasmon propagation length and the energy transfer rate is fastened by the silver mirror by approximately a factor of 40. Nevertheless, the absolute efficiency of the long-range process is still very low, of the order of 10^{-8} in the range of distances considered

in the experiment. This is mainly a consequence of free-space emission of the donor and of ohmic losses induced by the metal surface. We compensated for these competing processes by using a high concentration of fluorescent emitters in the experiment.

It is possible to use other geometric configurations to achieve higher energy transfer rates. Importantly, we pointed out that the planar geometry of the sample introduced an additional d^{-1} dependence since the wave propagates over two dimensions. In the following chapter, we will tackle this issue by using a silver nanowire to support surface plasmons over only one dimension. This will substantially enhance the energy transfer efficiency, as numerically predicted by Martín-Cano *et al.* [36]. For this reason, we will be able to use a single-photon emitter as a donor and to investigate the occurrence of energy transfer mediated by single plasmons.

CHAPTER 3

Energy transfer mediated by single plasmons

In this chapter, we present a study of micrometre-range energy transfer mediated by single plasmon. We specifically demonstrate micrometre-range plasmon-mediated energy transfer between a single CdSe/CdS/ZnS quantum dot and a fluorescent nanobead located in the near field of a silver nanowire . First of all, we introduce the principle of the experiment and the context of this work. We then present the experimental setup, the choice of the donor-acceptor pair and the characterisation of single surface plasmon generation by a single quantum dot coupled to a silver nanowire. We then show two independent experimental evidences of micrometre-range energy transfer occurring between the single quantum dot and the fluorescent nanobead. We notably show that the decay histogram of the acceptor measured during the experiment is determined by the convolution of the decay histograms of the donor and the acceptor independently excited. We also demonstrate the correlated blinking of the two emitters. As a conclusion, we discuss the experimental conditions required to demonstrate an antibunching in the donor and the acceptor emission.

3.1 Introduction

The foundations of the quantum theory of light and atoms date back to Planck's attempt to solve the ultraviolet catastrophe. In 1901, he proposed the hypothesis that blackbody radiation is emitted in discrete energy packets called *quanta*. Four years later, Einstein used this theory to explain the photoelectric effect, even though this did not demonstrate the quantum nature of light since the results could be explained by the quantisation of matter. The work of Planck and Einstein inspired the development of the theory of quantum mechanics at the beginning of the 20^{th} century.

In 1954, Hanbury Brown and Twiss developed a new type of interferometer designed to resolve the angular diameter of stars [44], based on the correlation in the intensity fluctuations between two separate detectors. Two years later, they studied the correlation between photons coming from a thermal light emitted by a mercury lamp and impinging

on two different detectors [45]. They specifically measured the correlation between the two signals as a function of the angular separation between the detectors and they demonstrated a positive correlation for zero separation, a phenomenon called *photon bunching*. This observation inspired various experiments based on correlation and anti-correlation effects in the intensities received by two detectors from a beam of particles (such as photons, electrons, atoms, etc.). Kimble, Dagenais and Mandel notably demonstrated photon antibunching from the fluorescence of sodium atoms in 1977 [46], providing a strong evidence of the quantisation of the electromagnetic field.

In the recent years, the development of efficient single-photon emitters such as semiconductor quantum dots or nitrogen-vacancy defects led to the observation of single plasmons exhibiting properties similar to those of photons [47]. In 2007, Akimov *et al.* coupled a single quantum dot to a silver nanowire and demonstrated photon antibunching between the photons emitted in free space by the quantum dot and the surface plasmons scattered at the end of the nanowire [48]. Two years later, Kolesov *et al.* observed self-interferences of single surface plasmons excited by a nitrogen-vacancy defect coupled to a silver nanowire, evidencing the wave-particle duality in the properties of surface plasmons [49]. Besides single-photon emitters, heralded single-photon sources can also be used to generate single plasmons. For instance, Dheur *et al.* recently used a plasmonic beamsplitter to demonstrate the wave-particle duality for a single surface plasmon freely propagating along a planar metal-air interface [50].

In the experiment presented in Chapter 2, surface plasmons were used to observe the energy transfer occurring between a large number of fluorescent emitters located above a silver film. While similar observations of micrometre-range plasmon-mediated energy transfer so far involved ensembles of fluorescent emitters [34, 51], the coupling of two quantum emitters mediated by single surface plasmons would allow one to perform interesting experiments in the field of quantum optics. For instance, Dzsotjan, Sørensen and Fleischhauer theoretically investigated the coupling of two quantum emitters mediated by a silver nanowire [52]. This work notably showed that subradiance and superradiance could be observed as a result of the plasmon-mediated interaction between the two emitters. In addition, it was theoretically shown by Gonzalez-Tudela *et al.* that plasmonic waveguides are good candidates to generate an entangled system from the coupling of two distant quantum emitters [53].

Principle of the experiment With the idea of going towards quantum systems, we now use a single-photon emitter as donor to experimentally study micrometre-range energy transfer mediated by single plasmons. To this end, a silver nanowire is used as a surface-plasmon waveguide. We excite the donor with a pulsed laser and we collect the fluorescence of both the donor and the acceptor with an immersion microscope objective. Then, we demonstrate the occurrence of energy transfer between a single quantum dot (donor) and a fluorescent nanobead (acceptor) located on the same nanowire 8.7 µm away from each other. Figure 3.1 illustrates the principle of this experiment. Using time-resolved measurements, we perform a comprehensive analysis of the relation between photon emission of the quantum dot and the fluorescent nanobead by studying the decay rate of the acceptor and by demonstrating the correlated blinking of the two emitters. This work is published in Physical Review A [54].

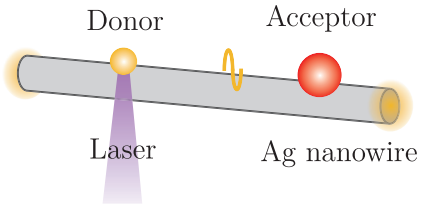

Figure 3.1 – *Principle of the experiment: a single quantum dot (donor) is excited by a pulsed laser diode and excites single surface plasmons that can be absorbed by a fluorescent bead (acceptor), distant from the quantum dot of several micrometres. The emission of fluorescence photons by the acceptor bead is a signature of the energy transfer.*

3.2 Sample preparation and experimental setup

In this section, we describe the setup of the experiment, including the choice of a donor-acceptor pair. While acceptors are fluorescent nanobeads, we use single CdSe/CdS/ZnS nanocrystals as single-photon donors. These quantum dots (QDs) are chemically synthesised by Emmanuel Lhuillier[1] (Institut des Nanosciences de Paris).

3.2.1 Donor-acceptor pair

QDs are semiconductor crystals with a diameter of a few nanometres. When a photon is absorbed by a QD, it creates a bound state composed of an electron and a hole interacting with each other through the electrostatic force. This state can then recombine by emitting a photon. As the size of the crystal approaches the electron-hole distance, quantum confinement effects take over. For a spherical crystal, these effects can roughly be modelled by an infinite potential well, in which the exciton can freely move – this model is also known as the *particle in a box* model. In such a model, the energy band gap increases when the size of the box is reduced. For this reason, the emission wavelength of semiconductor quantum dots can be tuned by controlling the time of growth of the nanocrystals.

The QDs used in the experiment are composed of a CdSe core as well as CdS and ZnS shells. It was indeed shown by Talapin *et al.* that a core/shell/shell architecture can be used to obtain a more efficient confinement of the electron-hole wave function inside the nanocrystal [55]. The spectrum of these QDs is relatively narrow and centred around different wavelengths depending on the geometry of the QD, as one can see by measuring the emission spectra of CdSe/CdS/ZnS quantum dots of different sizes (Fig. 3.2a). The spectral properties of these QDs make them excellent donors for the observation of micrometre-range energy transfer, essentially for two reasons. Firstly, at the excitation wavelength ($\lambda_0 = 405$ nm), surface plasmons are strongly damped, preventing an excitation of the acceptor by surface plasmons directly excited by the excitation laser. Secondly, the emission spectrum of quantum dots is narrower than the one of fluorescent beads. This is convenient in order to spectrally distinguish the photons emitted by the QDs. Hence, we use CdSe/CdS/ZnS nanocrystals as donors in the experiments. We specifically select QDs emitting at a wavelength around 600 nm. From transmission electron microscopy (TEM) measurements, we estimate their diameter to be 7.5 ± 0.5 nm.

[1] More details on quantum dot synthesis are given in Ref. [54].

Since the donors emit at wavelengths around 600 nm, we require the acceptors to be characterised by a large absorption cross-section for these wavelengths. We select fluorescent nanobeads with a diameter of 176 ± 12 nm and which contain a large number of fluorescent molecules (Dark Red Fluospheres, Thermo Fisher Scientific). Their emission and absorption spectra are reported in Fig. 3.2b. Note that the overlap between the donor emission spectrum and the acceptor absorption spectrum is not optimised in this configuration. This is required in order to properly separate the emission spectra of the two emitters. Indeed, since acceptor beads have a large diameter, they can scatter surface plasmons excited by the QD. This creates an undesirable signal at the donor emission wavelengths that we can properly filter by detuning the donor and the acceptor emission spectra.

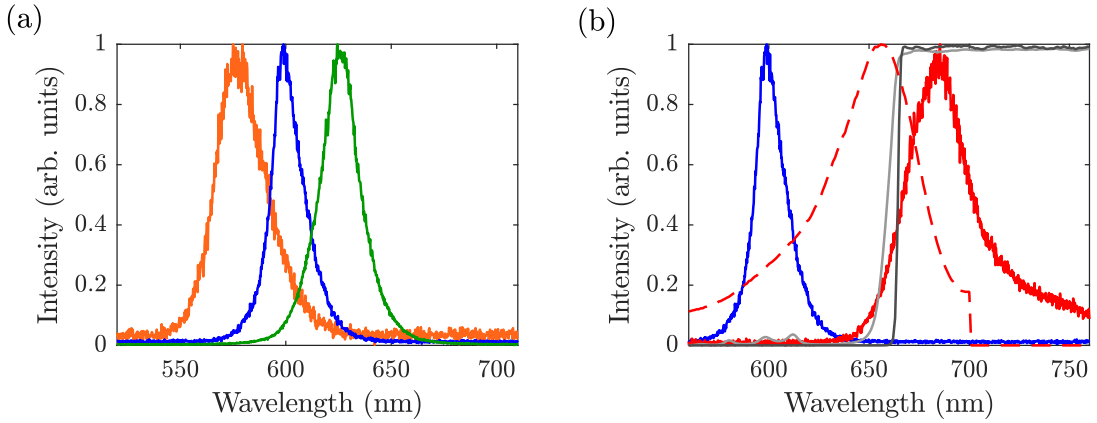

Figure 3.2 – *(a) Spectrum of CdSe/CdS/ZnS nanocrystals of different sizes, synthesised by Emmanuel Lhuillier. (b) Emitters selected for the energy transfer experiment. The donor is a QD (blue curve) and the acceptor is a fluorescent bead (red curve). Dichroic and long-pass filter transmission curves are represented in grey.*

To begin with the sample preparation, we spin-coat chemically synthesised silver nanowires (Sigma Aldrich) on a glass coverslip. These silver nanowires are characterised by a diameter of approximately 115 nm and lengths ranging from 5 to 50 µm. Then, we spin-coat a dilute solution of CdSe/CdS/ZnS nanocrystals and acceptor beads; the emitters are preferentially dispersed in the close vicinity of the nanowires using this procedure. As a result, we obtain a sample presenting isolated silver nanowires near-field coupled with single QDs and single acceptor beads.

3.2.2 Optical setup

In order to measure the fluorescence intensities emitted by the QDs and the acceptor beads, we use an inverted fluorescence microscope designed for time-resolved measurements, as represented in Fig. 3.3. This microscope includes a pulsed excitation laser and two single-photon avalanche diodes (SPADs). Since the optical arrangement of the SPADs recalls the intensity interferometer developed by Hanbury Brown and Twiss, we refer to this setup as a "HBT" configuration.

QDs are excited by using a laser diode at a repetition rate of 40 MHz and emitting at 405 nm (LDH Series P-C-405M, PicoQuant) with an average power on the sample of the order of 2 µW. For sample excitation and fluorescence collection, we use an oil immersion microscope objective with a $\times 100$ magnification and a 1.4 numerical aperture

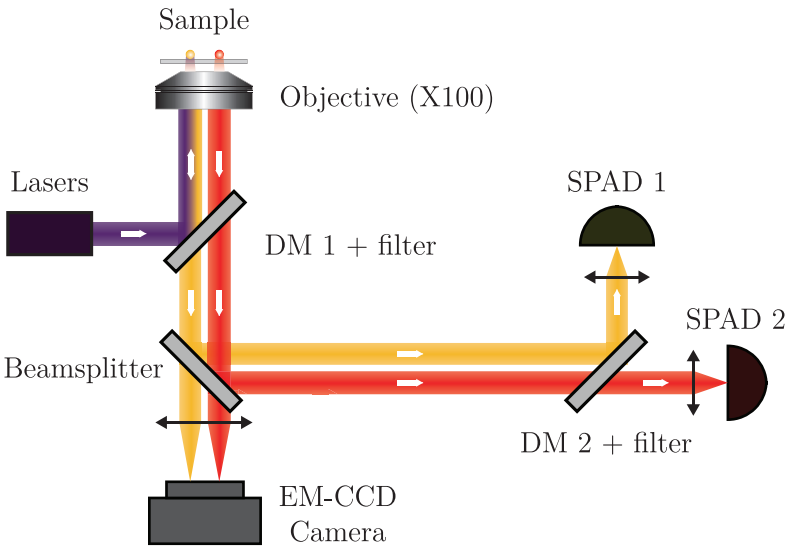

Figure 3.3 – *Optical setup, based on an inverted fluorescence microscope combined with time-resolved single-photon detection. DM stands for dichroic mirror and EM-CCD stands for electron-multiplying charge-coupled device.*

(UPLSAPO 100XO, Olympus). A dichroic mirror (Di01-R488, Semrock) and a long-pass filter (BLP01-488R, Semrock) select the fluorescence photons emitted from the sample. By passing through a 50:50 beamsplitter, fluorescent photons are detected by an EM-CCD camera (iXon 897, Andor) and by two SPADs (PDM-R, Micro Photon Devices) developed by Angelo Gulinatti and Ivan Rech (Politecnico di Milano) and based on a silicon avalanche photodiode technology providing an enhanced sensitivity in the near infrared [56].

Light coming from the donor and the acceptor is separated by a second dichroic mirror (ZT647rdc, Chroma) and a long-pass filter (ET665lp, Chroma) and then focused onto the two SPADs. The first SPAD, called "SPAD 1", collects the donor fluorescence and the second SPAD, called "SPAD 2", collects the acceptor fluorescence. The dichroic mirror can be replaced by a 50:50 beam-splitter to characterise the emission properties of individual emitters. In both cases, the signal collected by the photodiodes arises from the 500-nm-sized region of the sample that is optically conjugated with the detection system. Additionally, a removable mirror can be inserted in the optical path to direct photons towards a fibred spectrometer (Acton SP2300, Princeton Instruments). A piezoelectric positioning system (PXY 200SG, Piezosystem Jena) is used to perform lateral displacements of the sample in the object plane of the microscope. Hence, we can select a single QD and an acceptor bead, both of them located in the near field of a 16-µm-long silver nanowire.

To align the detectors without exciting the emitters, we use a supercontinuum laser (Fianium SC450) filtered either at 560 or 680 nm. To start with, we focus the laser at $\lambda_0 = 560$ nm onto the QD and we align SPAD 1 using the signal coming from the laser. We then use the same procedure with the laser at $\lambda_0 = 680$ nm to align SPAD 2 with the acceptor bead. After the alignment procedure, the fluorescence of the donor is thus detected by SPAD 1 while the fluorescence of the acceptor is detected by SPAD 2.

3.2.3 Determination of the donor-to-acceptor distance

In the experiment, we focus the pulsed laser at $\lambda_0 = 405$ nm onto the QD and we measure the fluorescence of both the QD and the acceptor bead using the SPADs. We then proceed with the determination of the donor-to-acceptor distance. To do so, we use a wide-field-image acquired by the EM-CCD camera during the experiment with an acquisition time of 15 s (Fig. 3.4a). The brightest spot is due to the free-space emission of the QD (the donor), and is conjugated to SPAD 1. We observe two other bright spots at both ends of the nanowire, due to the scattering by the extremity of the nanowire of the surface plasmons excited by the QD. Finally, we detect a bright spot at the position of the fluorescent bead (the acceptor), which is due to the scattering of the surface plasmons by the bead at the emission wavelength of the donor as well as the fluorescence from the acceptor molecules inside the bead. We only measure the fluorescence of the acceptor molecules using SPAD 2 since we filter the scattered surface plasmon using an appropriate set of filters.

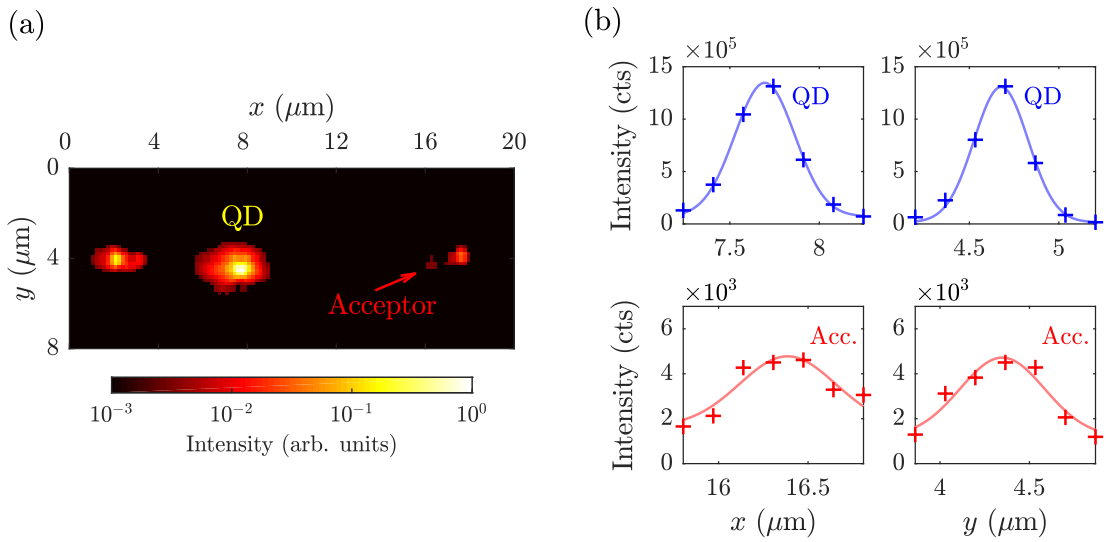

Figure 3.4 – *(a) Wide-field image of the experiment measured by an EM-CCD camera. The intensity is plotted in log-scale. (b) Measured point spread functions (data points) and Gaussian fits to the data (solid lines) used to estimate the coordinates of the emitters. From left to right: x- and y-coordinates of the donor (blue curves), x- and y-coordinates of the acceptor (red curves).*

By using the wide-field image measured by the EM-CCD camera, we can localise both the QD and the acceptor bead by fitting a Gaussian function to the measured point spread functions, as shown in Fig. 3.4b. Using this procedure, we estimate a distance d of 8.7 µm between the QD and the bead. The precision of this estimation depends on the number of photons detected from the emitters, as we will see in Chapter 6. However, the standard error on the position estimates is usually of the order of 10 nm, which is very small in comparison to the considered distance. Note that the point spread function (PSF) is wider for the acceptor, which may be due to several reasons. Firstly, QDs are small objects with a diameter of the order of 10 nm and can be considered as pointlike emitters. In comparison, the diameter of fluorescent beads is approximately 200 nm, which is non negligible in comparison to the spread of the PSF. Secondly, the acceptor emission wavelengths are slightly larger than those of the donor, resulting in a wider PSF.

3.3 Generation of single surface plasmons

We now characterise the ability of the CdSe/CdS/ZnS nanocrystals to emit single photons and excite single plasmons. From these properties, we can expect the energy transfer between the QD and the acceptor bead to occur at the single-plasmon level.

3.3.1 Demonstration of photon antibunching from single quantum dots

Light absorption by a QD can generate one or several electron-hole pairs named *excitons* defining several distinct energy states. Importantly, QDs at room temperature generally have a large single-exciton quantum yield in comparison to the quantum yield associated with multi-excitons. Thus, most of the photons emitted by a QD come from the radiative recombination of single excitons. This behaviour can be observed by exciting a QD with a pulsed laser. If the pulse width is shorter than the excited-state lifetime of the QD, only one fluorescence photon can be emitted by the QD during the time delay in-between two pulses, called the *repetition period*. Single photon emission can then be evidenced with two detectors in HBT configuration: by using a 50:50 beam-splitter ahead of two SPADs, the fluorescence intensity emitted by the QD is then split with equal probability towards the two photon detectors (SPAD 1 and SPAD 2). Because of the quantum nature of light, each photon is either directed towards SPAD 1 or SPAD 2. Consequently, the signal on the two detectors is anticorrelated within the same repetition period. We can quantify this behaviour with the *second-order correlation function*, which is expressed as a function of the delay τ by

$$g^{(2)}(\tau) = \int_{\Delta t} I_1(t) I_2(t+\tau)\,\mathrm{d}\,t\ , \tag{3.1}$$

where $I_1(t)$ and $I_2(t)$ are the intensities measured by each detector at the time t and Δt is the total acquisition time.

We thus perform measurements of the $g^{(2)}$ correlation function on single CdSe/CdS/ZnS nanocrystals. For a single nanocrystal located on a glass coverslip and excited with an average laser power of ~ 0.5 µW, an absence of coincidences at zero delay is observed (Fig. 3.5a). This phenomenon, called *photon antibunching*, is a characteristic of a good single-photon emitter [57]. For a single nanocrystal in the near field of a silver nanowire and excited with an average power of ~ 2 µW, the $g^{(2)}$ correlation function shows a small peak at zero delay (Fig. 3.5b) which means that the radiative recombination of multi-excitons in the QD is not negligible any more. This might be a direct consequence of the reduction of the excited-state lifetime induced by the presence of the silver nanowire. Indeed, it was shown by Klimov *et al.* that the Auger effect – which is a non-radiative recombination process – plays an important role in the dynamics of multi-excitons by reducing their quantum yield [58]. When the excited-state lifetime is strongly reduced, spontaneous emission can become faster than the Auger effect, resulting in the emission of two photons within the same repetition period. Furthermore, the excitation intensity is enhanced due to the higher laser power as well as to the presence of the silver nanowire, which locally enhances the intensity of the excitation field due to plasmon resonance. As a high intensity increases the probability of multi-excitons formation, it also increases the probability of measuring more than one photon within the same repetition period. Thus, both the reduction of the excited-state lifetime and the enhancement of the excitation intensity are likely to contribute to the observed radiative recombination of multi-excitons.

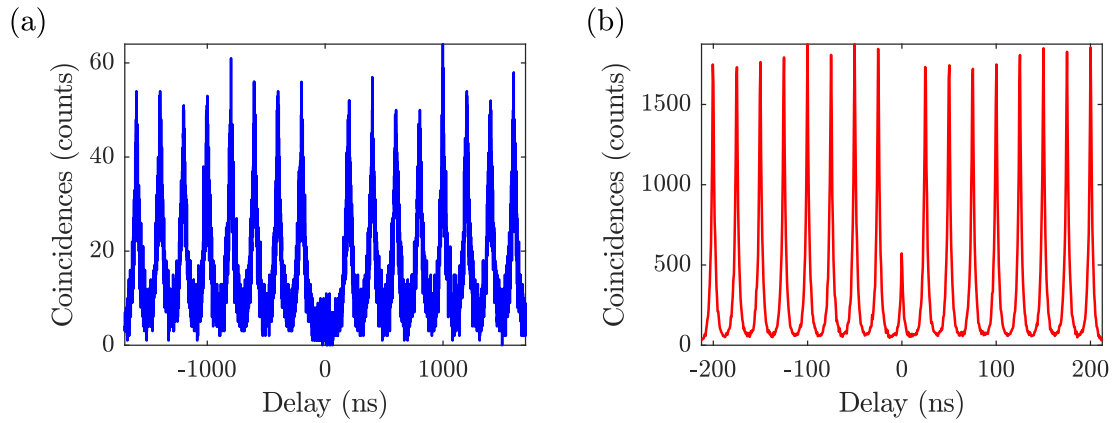

Figure 3.5 – *Measurements of the $g^{(2)}$ correlation function. (a) Measurement on a single nanocrystal on glass using a repetition rate of 5 MHz. (b) Measurement on a single nanocrystal coupled to a silver nanowire using a repetition rate of 40 MHz.*

The measurement of the $g^{(2)}$ correlation function can be relevant in different situations. For instance, it can be used to determine the number of independent emitters in the case of several close-by emitters [59]. In the case of a single emitter, it can also be used to find the contribution of multi-excitons to the photon emission process. Assuming that only energy states involving one and two excitons contribute to the emission process, it was notably shown by Nair, Zhao and Bawendi that $g^{(2)}$ measurements allow one to estimate the biexcition-to-exciton ratio [60]: whenever white noise can be neglected, the biexciton-to-exciton ratio is given by the ratio of the area under the zero delay peak to the mean value of the adjacent ones. In the following sections, we will show how the contribution of white noise in the measurements can be accounted for in order to determine the biexciton-to-exciton ratio more accurately.

3.3.2 Statistical properties of the second-order correlation function

For an experiment with two detectors in HBT configuration, it is interesting to compute the expectation of the $g^{(2)}$ correlation function as defined by Eq. (3.1) depending on the statistical relationship between the intensities $I_1(t)$ and $I_2(t)$ measured by the two detectors. We will study the three different cases in which $I_1(t)$ and $I_2(t)$ are independent, anticorrelated and correlated. It will notably provide us with reference values for the number of coincidences measured by the two SPADs during the energy transfer experiment. In addition, it will also allow us to accurately estimate the biexciton-to-exciton ratio for the QDs used in the experiment.

Number of coincidences Let us consider an experiment with a pulsed excitation laser and two detectors in HBT configuration, with n_1 photons detected on detector 1 and n_2 photons detected on detector 2. We note Δt the total acquisition time and r the repetition rate of the excitation laser. The number of repetition periods during the whole experiment is then $n_t = r\Delta t$. By definition, the value of the $g^{(2)}$ correlation function is given by the number of repetition periods for which a photon is detected by each detector. In order to characterise the distribution followed by the number of coincidences, we can assume that no more than one photon is detected during one repetition period. Strictly speaking,

this requires the repetition period to be smaller than the dead time of the detectors, which is of the order of 80 ns. In practice, the probability of detecting more than one photon in a repetition period is usually low under typical acquisition conditions and can be neglected. The number of coincidences then follows a binomial distribution as the result of n_t independent experiments. The expectation of this distribution is given by

$$\mathrm{E}(n_{1,2}) = n_t \; p(1,2) \; , \tag{3.2}$$

where $p(1,2)$ is the probability of simultaneously measuring a photon on each detector and $n_{1,2}$ is the random variable describing the number of coincidences. Moreover, the variance of the number of coincidences is

$$\mathrm{Var}(n_{1,2}) = n_t \; p(1,2) \; [1 - p(1,2)] \; . \tag{3.3}$$

To compute both the expectation and the variance of the number of coincidences, we can express the probability $p(1,2)$ of simultaneously measuring a photon on each detector as a conditional probability, which reads

$$p(1,2) = p(2|1) \; p(1) \; , \tag{3.4}$$

where $p(1)$ is the probability of measuring a photon on detector 1 and $p(2|1)$ is the probability of measuring a photon on detector 2 given that a photon has been detected on detector 1. Assuming that the probability of measuring a photon on a given detector is time independent, we can directly write $p(1) = n_1/n_t$. Therefore, the expectation and the variance of $n_{1,2}$ are determined by the conditional probability $p(2|1)$. This probability can be calculated by making different assumptions concerning the statistical relationship between the intensities measured by the two detectors. We will detail three different assumptions in the following paragraphs.

Independent intensities (hypothesis $\mathcal{H}_i$) If the intensities $I_1(t)$ and $I_2(t)$ measured by the two detectors are independent, the probability of detecting a photon on detector 2 given that a photon has been detected on detector 1 is given by $p(2|1,\mathcal{H}_i) = p(2) = n_2/n_t$ where $\mathcal{H}_i$ is the hypothesis of independent intensities. It follows that the probability of simultaneously measuring a photon on each detector is

$$p(1,2|\mathcal{H}_i) = \frac{n_1 \; n_2}{n_t^2} \; . \tag{3.5}$$

This expression can for instance be used to calculate the expectation of the $g^{(2)}$ correlation function at zero delay in the classical limit, which corresponds in practice to a sample with a large number of emitters. It can also be used to calculate the expectation of $g^{(2)}$ for large delays, as $I_1(t)$ and $I_2(t+\tau)$ are usually independent in the limit of large delays, even in the case of a single photon emitter.

Anticorrelated intensities (hypothesis $\mathcal{H}_a$) Let us consider that the intensity measured by each detector i can be decomposed into two separate contributions so that $I_i(t) = F_i(t) + B_i(t)$ where $F_i(t)$ and $B_i(t)$ are respectively due to fluorescence and noise. If the intensities $F_1(t)$ and $F_2(t)$ are perfectly anticorrelated and if the intensities $B_1(t)$ and $B_2(t)$ are independent, the probability of detecting a photon on detector 2 given that a photon has been detected on detector 1 is given by

$$p(2|1,\mathcal{H}_a) = \frac{b_2}{n_t} + \frac{f_2}{n_t} \; \frac{b_1}{n_1} \; , \tag{3.6}$$

where $\mathcal{H}_a$ is the hypothesis of anticorrelated fluorescence intensities and f_i and b_i are respectively the number of photons due to fluorescence and white noise. It follows that the probability of simultaneously measuring a photon on each detector is

$$p(1,2|\mathcal{H}_a) = \frac{f_1\, b_2 + f_2\, b_1 + b_1\, b_2}{n_t^2}\ . \tag{3.7}$$

This expression can for instance be used to calculate the expectation of the $g^{(2)}$ correlation function at zero delay in the case of a perfect single-photon emitter and in the presence of background noise.

Correlated intensities (hypothesis $\mathcal{H}_c$) As in the preceding paragraph, we consider that the intensity measured by each detector i can be decomposed into two contributions $F_i(t)$ and $B_i(t)$. If the two fluorescence intensities $F_1(t)$ and $F_2(t)$ are simultaneously equal to zero for n_d "dark" repetition periods (with $n_d < n_t$), it follows that these intensities are correlated. This hypothesis is noted $\mathcal{H}_c$. Assuming that the intensities $B_1(t)$ and $B_2(t)$ are independent over the whole experiment, the probability of detecting a photon on detector 2 given that a photon has been detected on detector 1 is given by

$$p(2|1,\mathcal{H}_c) = \frac{b_2}{n_t} + \frac{f_2}{n_t}\,\frac{b_1}{n_1} + \frac{f_2}{n_b}\,\frac{f_1}{n_1}\ , \tag{3.8}$$

where $n_b = n_t - n_d$ is the number of "bright" repetition periods for which the fluorescence intensities are considered as independent. It follows that the probability of simultaneously measuring a photon on each detector is

$$p(1,2|\mathcal{H}_c) = \frac{f_1\, b_2 + f_2\, b_1 + b_1\, b_2}{n_t^2} + \frac{f_1\, f_2}{n_t\, n_b}\ . \tag{3.9}$$

This expression can be used in the case of a blinking emitter such as a single quantum dot. Indeed, the emission of QDs usually fluctuates between a bright and a dark state, as we will see in Sect. 3.5.1. Hence the fluorescence intensities measured by the two detectors are correlated and Eq. (3.9) can be used to calculate the expectation of the $g^{(2)}$ correlation function for delays shorter than the typical time scale τ_b characterising the blinking behaviour of the QD. In addition, if the considered QD emits single photons, then $F_1(t)$ and $F_2(t)$ are also anticorrelated for time scales shorter than the repetition period $\tau_r = 1/r$. In such cases, Eq. (3.9) can thus be used to calculate the expectation of $g^{(2)}$ for near-zero delays ($\tau_r < \tau < \tau_b$).

Numerical experiment In order to corroborate these results, we perform a numerical experiment that simulates the emission of photons by a single QD excited at a repetition rate $r = 10$ MHz during $\Delta t = 2$ s. We consider two detectors disposed in HBT configuration, and each detector is characterised by a 1% probability of detecting a fluorescence photon in a given repetition period. In the simulation, the QD is supposed to be a perfect single-photon emitter so that the fluorescence intensities $F_1(t)$ and $F_2(t)$ measured by both detectors are perfectly anticorrelated on time scales smaller than the repetition period (100 ns). Furthermore, the QD is characterised by a blinking behaviour between a bright and a dark state, so that $F_1(t)$ and $F_2(t)$ are correlated on time scales of the order of one millisecond. Furthermore, we model the dark count rates of the detectors by considering a 0.02% probability of detecting a count due to noise by each detector in a given

repetition period, and the noise intensities $B_1(t)$ and $B_2(t)$ measured on both detectors are considered as independent.

Figure 3.6a shows the $g^{(2)}$ correlation function associated with a given realisation of the numerical experiment. It is calculated from the intensities $I_i(t) = F_i(t) + B_i(t)$ with a resolution of 100 ns. We can clearly identify the antibunching dip at zero delay due to single-photon emission, as well as a positive correlation for near-zero time scales. This positive correlation is observed over time scales larger than 100 ns but smaller than one millisecond. Figure 3.6b shows the same results plotted for delays of the order of the repetition period. We observe that the expectation of the number of coincidences does not depend on the delay in this range, except at zero delay for which the fluorescence intensities are anticorrelated .

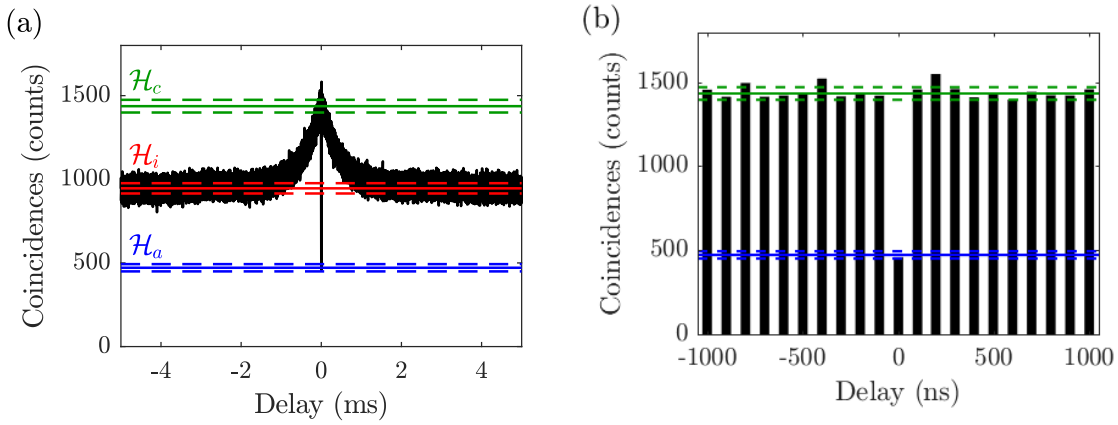

Figure 3.6 – *Calculation of the $g^{(2)}$ correlation function for a 2 s numerical experiment simulating data obtained from a perfect single-photon emitter blinking between a bright and a dark state on millisecond time scales. The expectations of the number of coincidences under different hypothesis are represented by solid lines. Dashed lines correspond to a statistical significance of $\pm 1\sigma$. (a) Results for a given realisation of the experiment and for delays up to 5 ms. (b) Same results plotted for delays up to 1 µs, representing each point by a bar.*

For comparison purposes, we calculate the expectation of the number of coincidences as given by Eq. (3.2) for each of the three hypothesis previously detailed concerning the statistical relationship between the intensities $I_1(t)$ and $I_2(t)$. For each of these hypothesis, we also calculate the corresponding interval $[\mu-\sigma;\mu+\sigma]$ where μ is the expectation of the number of coincidences and σ its standard deviation. One can see that the $g^{(2)}$ correlation function is correctly estimated for large delays (red lines) using Eq. (3.5). We observe a similar agreement between the $g^{(2)}$ correlation function calculated at zero delay and the estimate (blue lines) given by Eq. (3.7), as well as between the $g^{(2)}$ correlation function calculated for near-zero delays and the estimate (green lines) given by Eq. (3.9).

3.3.3 Quantitative characterisation of single-photon emission

As a direct application of this analysis, we can compare the expectation of the $g^{(2)}$ correlation function to the number of coincidences experimentally measured on CdSe/CdS/ZnS nanocrystals (Sect. 3.3.1). By doing so, we can accurately estimate the number of coinci-

dences due to fluorescence photons, and thus the quality of the QDs used in the experiment as single-photon emitters.

For each experiment, we start by estimating the number of events detected on each SPAD due to background noise by using the decay histograms. From this knowledge and the total number of events detected by each SPAD, we can calculate the expectation of the number of coincidences per repetition period, assuming that the QD is a perfect single-photon emitter. Then, we group the intensities measured by the SPADs into bins – with a bin size given by the repetition period of the laser – and we calculate the number of coincidences for the QD on glass (Fig. 3.7a) and for the QD coupled to the silver nanowire (Fig. 3.7b). For this analysis, we select only the time intervals for which the emitter is in the bright state. In practice, this is done by performing a post-processing gating on the intensities collected by the two detectors. By doing so, we remove a contribution due to white noise and thus lower the variance of the measured number of coincidences.

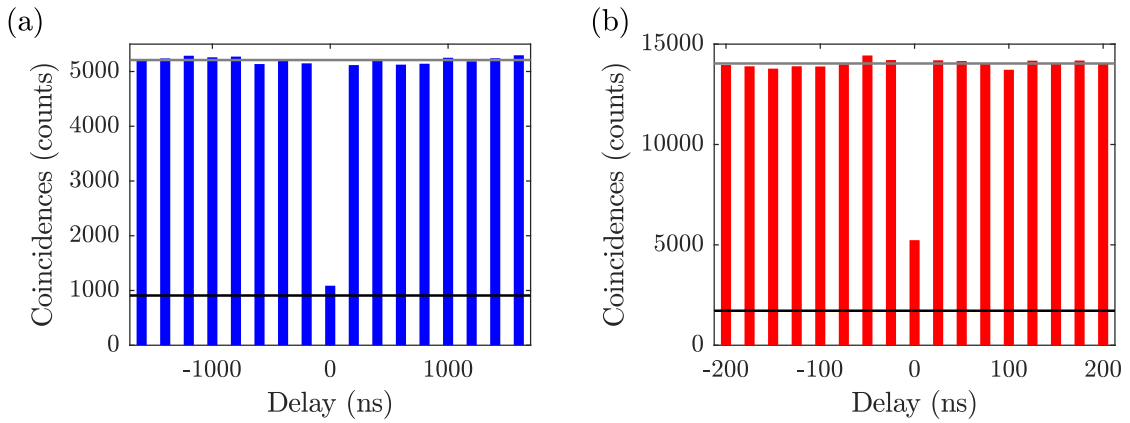

Figure 3.7 – *Number of coincidences per repetition period for (a) a single QD on glass and (b) a single QD coupled to a silver nanowire. These results are the same as those presented in Fig. 3.5, except that the bin size equals the repetition period of the laser. The expectation of the number of coincidences assuming anticorrelated fluorescence intensities are represented by black lines. Greys lines represent the mean values of the number of coincidences for non-zero delays.*

We already mentioned that the ratio of the area under the zero delay peak to the mean value of the adjacent ones gives an estimate of the biexciton-to-exciton ratio in a noise-free experiment. We can adapt this formula to account for the presence of white noise in the measurements. To do so, we estimate the contribution of the noise by the expectation of the number of coincidences calculated for a perfect single-photon emitter. From this knowledge, we can thus subtract the contribution of the noise to each peak. By using this procedure, we obtain a biexciton-to-exciton ratio of 4% for the QD on glass and of 29% when the QD is in the near field of a silver nanowire.

3.3.4 Observation of single plasmons on silver nanowires

It was shown that the coupling of a single-photon emitter to a silver nanowire generates single surface plasmons exhibiting properties similar to those of single photons [48,49]. The demonstration relies on the fact that a QD in the near field of a silver nanowire cannot simultaneously emit a photon in free space and excite a surface plasmon. For the sake of

completeness, we perform the same experiment with the experimental setup described in Sect. 3.2. Thus, we study a single CdSe/CdS/ZnS nanocrystals in the near field of a single nanowire using two detectors in HBT configuration: the first detector detects the photons emitted in free space by the QD while the second detector detects the photons generated by the scattering of surface plasmons by the end of the nanowire. In this experiment, we estimate the distance between the QD and the end of the wire to be approximately 7.2 µm by using a wide-field image recorded by the EM-CCD camera. Figure 3.8a shows the $g^{(2)}$ correlation function calculated between the intensities measured by the two detectors, which exhibits an absence of coincidences at zero delay. Furthermore, by grouping the intensities per repetition period and by estimating the contribution of white noise in the measurements, we show that the fluorescence intensities are perfectly anticorrelated (Fig. 3.8b), indicating that only one quantum of energy is emitted by the QD for each repetition period.

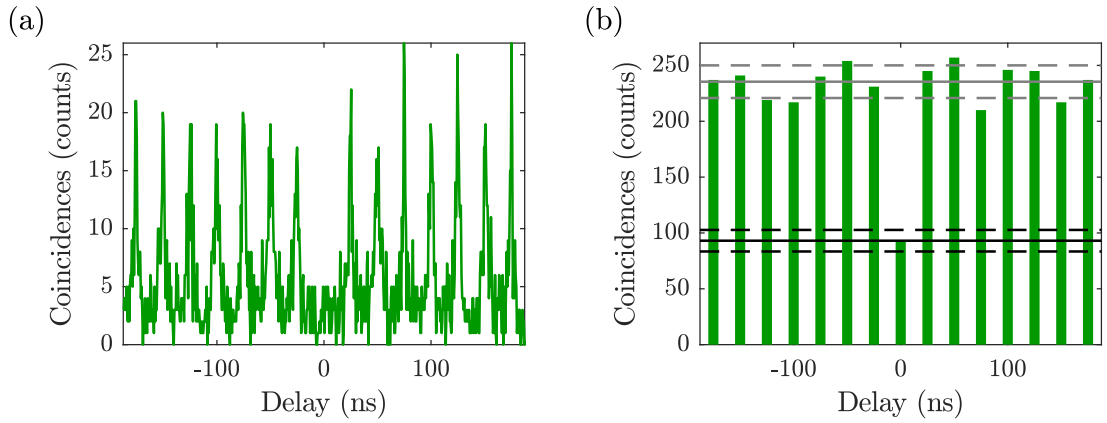

Figure 3.8 – *(a) Measurement of the $g^{(2)}$ correlation function between the photons emitted in free space by a QD coupled to a silver nanowire and the photons generated by the scattering of surface plasmons at the end of the nanowire. (b) Same results with a bin size equal to the repetition period (25 ns). The expectation of the number of coincidences assuming anticorrelated intensities is represented by a black solid line. A grey line represents the mean value of the number of coincidences for non-zero delays. Dashed lines correspond to a statistical significance of $\pm 1\sigma$.*

3.4 Study of decay histograms

As we confirmed that CdSe/CdS/ZnS nanocrystals excite single surface plasmons when coupled to a silver nanowire, we can now present the first evidence of the occurrence of micrometre-range energy transfer mediated by single plasmons. The proof relies on the analysis of the decay histograms measured from both the donor QD and the acceptor bead.

3.4.1 Decay histogram of the quantum dot

In general, the decay rate of a QD is directly determined by the transition matrix elements connecting the energy states involved in the emission process. It strongly depends on the geometry of the QD as well as on the temperature. The excited-state lifetime of a QD

is usually of the order of 10-100 ns, which is relatively large in comparison to the typical decay rate of fluorescent molecules. As explained by van Driel *et al.* [61], this is due to the thermal population of states with low transition probabilities, called *dark states*.

In the energy transfer experiment, we can estimate the decay rate of the donor QD by measuring its decay histogram. For comparison purposes, we also study a single CdSe/CdS/ZnS nanocrystal on a glass substrate, excited with an average laser power of ∼0.5 µW at a repetition rate of 5 MHz. While this histogram follows a mono-exponential distribution characterised by a decay rate of 0.034 ns^{-1}, we observe that the decay rate of the QD involved in the energy transfer experiment is strongly modified by the presence of the silver nanowire (Fig. 3.9a). Notably, the decay histogram of the QD follows a bi-exponential distribution. This can be expressed as a function of Γ_1 and Γ_1^* which are the two decay rates characterising the distribution. The lifetime probability density function (PDF) of the QD then reads

$$h_d(t) = \eta_1 \Gamma_1 \exp(-\Gamma_1 t) + \eta_1^* \Gamma_1^* \exp(-\Gamma_1^* t) \,, \tag{3.10}$$

where $\eta_1 = N_1/N_t$ and $\eta_1^* = N_1^*/N_t$ with N_1 and N_1^* the number of photons respectively associated with each contribution and $N_t = N_1 + N_1^*$ the total number of measured photons.

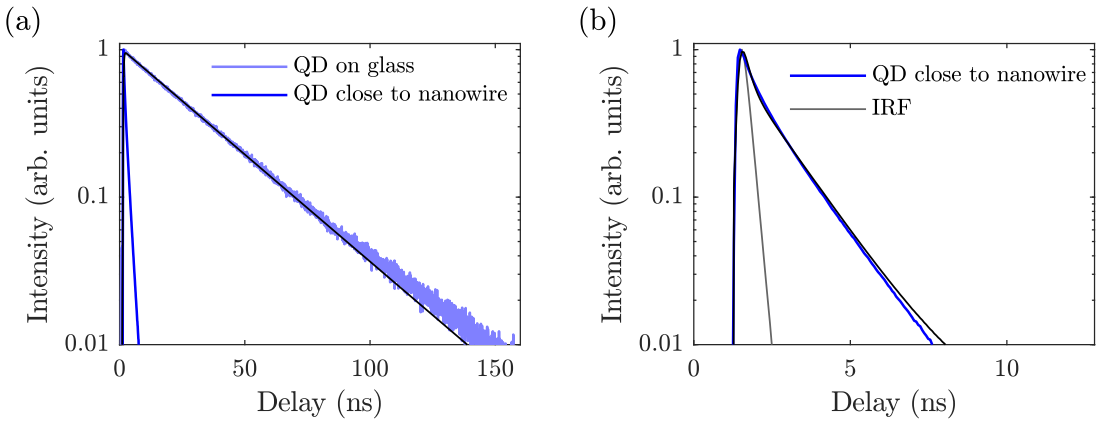

Figure 3.9 – *(a) Decay histograms of the donor QD (dark blue) and of a single QD on glass (light blue). The black curve is a mono-exponential fit to the decay histogram of the QD on glass. (b) Decay histogram of the donor QD, represented using a shorter time scale. The black curve is a bi-exponential fit to the decay histogram and the grey curve is the IRF.*

In order to estimate the two decay rates characterising the distribution, we fit the convolution of the instrument response function (IRF) and a bi-exponential function to the measured decay histogram (Fig. 3.9b). The main contribution accounts for 80% of the total photon emission and its decay rate is $\Gamma_1 = 0.67$ ns^{-1}. This corresponds to an enhancement factor of the order of 20 with respect to the reference measurement on the glass substrate. The remaining 20% of the photons shows a faster decay rate ($\Gamma_1^* > 12$ ns^{-1}) which is a characteristic of the radiative recombination of biexciton states. This fast decay cannot be resolved with the setup used for the experiment since it is shorter than the IRF. Based on this analysis, we can estimate that the biexciton-to-exciton ratio is of the order of 25%. We already presented measurements of the $g^{(2)}$ correlation function on a single QD within the same experimental conditions (Fig. 3.8b) and we demonstrated that the biexciton-to-exciton ratio is of 29% for this QD. Both values are consistent and indicate that the donor QD is likely to be a good single-photon emitter.

In order to check measurement repeatability, we perform several measurements on different CdSe/CdS/ZnS nanocrystals coupled to silver nanowires. The slower decay as well as its contribution to the total histogram varies for different emitters, but the faster decay usually accounts for less than 30% of the total photon emission. From the slower decay, we typically obtain enhancement factors ranging from 5 to 20 with respect to free-space emission. This large range of values is expected as we do not control neither the distance between the QD and the nanowire nor the orientation of the dipole moment of the QD relative to the nanowire axis.

3.4.2 Decay histogram of the acceptor bead under laser excitation

Before presenting the decay histogram of the acceptor bead measured by SPAD 2 during the energy transfer experiment, it is interesting to investigate the coupling between the acceptor bead and the silver nanowire. Hence, we measure the decay histogram of the acceptor bead under the different excitation schemes represented in Fig. 3.10.

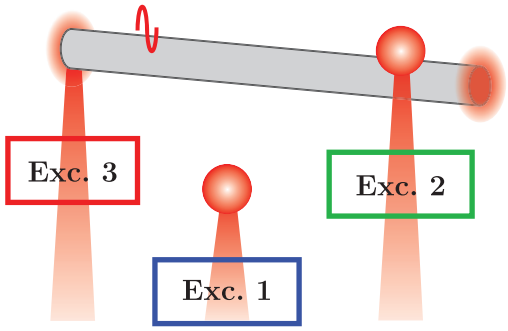

Figure 3.10 – *Measurement of the decay histogram of the acceptor bead for different excitation schemes: bead not coupled to the nanowire (Exc. 1), bead coupled to the nanowire and excited from the far field (Exc. 2), bead coupled to the nanowire and excited by surface plasmons (Exc. 3).*

As a reference, we measure the decay histogram of a bead on a glass coverslip. We then compare it to the decay histogram obtained for the acceptor bead coupled to the silver nanowire in two different situations. The bead is either excited by a laser focused on it or by surface plasmons propagating on the silver nanowire. In this last configuration, surface plasmons are excited by focusing the excitation laser onto the extremity of the nanowire (the left end on Fig. 3.4). The laser wavelength is set to 640 nm for these measurements. This wavelength is indeed in the overlap region between the donor emission spectrum and the acceptor absorption spectrum, so that surfaces plasmons excited by the laser act like the surface plasmons excited by the QD in the energy transfer experiment.

As expected, the decay rate of the acceptor bead coupled to the wire is larger than on glass for both excitation schemes (Fig. 3.11a). Moreover, the decay rate obtained with a far-field excitation is smaller than the one obtained when the bead is excited via surface plasmons. Indeed, all the molecules inside the bead can be excited in the first situation while only the molecules located closer to the wire can be excited in the second situation. To obtain a quantitative estimate of the decay rate of the acceptor bead, we model the measured distribution of decay rates by a lognormal distribution, as proposed by Nikolaev

et al. [62]. The lognormal distribution is defined by

$$\Phi(\Gamma) = \exp\left(-\frac{\ln^2(\Gamma/\Gamma_{mf})}{w^2}\right) , \tag{3.11}$$

where Γ_{mf} is the most frequent decay rate and w is a parameter characterising the width of the distribution. We can use this distribution to define the lifetime PDF of the bead, which reads

$$h_a(t) \propto \int_{\Gamma=0}^{+\infty} \Phi(\Gamma)\exp(-\Gamma t)\mathrm{d}\Gamma . \tag{3.12}$$

We thus fit the convolution of the IRF and the lifetime PDF of the bead to the measured decay histograms. As a result, we determine the distribution of decay rate $\Phi(\Gamma)$ presented in Fig. 3.11b and associated with the three different excitations schemes. We observe that the width w of these distributions significantly depends on the excitation scheme. The mono-exponential approximation is justified if w is smaller than the lifetime of the emitter. This approximation notably holds for the measurement on glass. However, the mono-exponential approximation fails for the measurements concerning the bead coupled to the nanowire. Hence, we use the average value of $\Phi(\Gamma)$ to compute the enhancement of the decay rate in these particular situations. Using this approach, we obtain an effective decay rate enhancement of 1.5 for the bead excited via the far field and of 2.3 for the bead excited via surface plasmons.

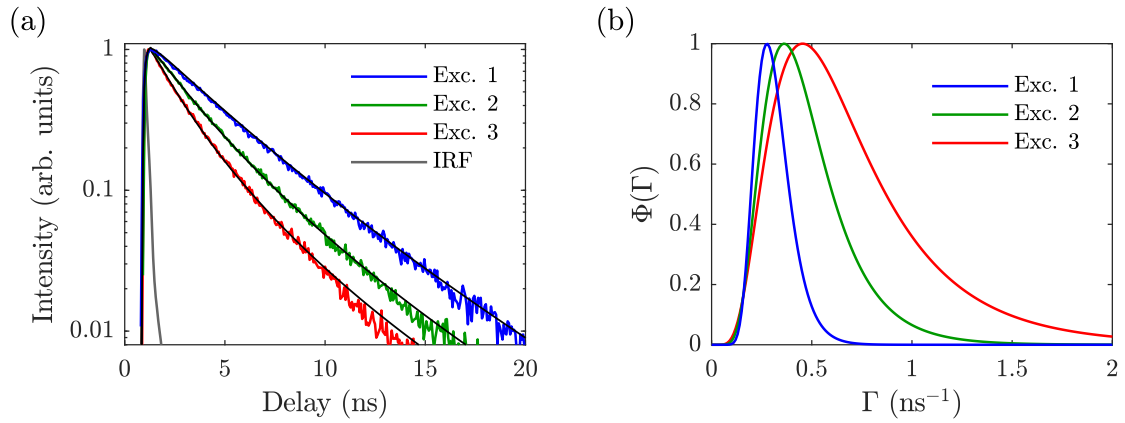

Figure 3.11 – *(a) Measured decay histograms in three different situations: bead not coupled to a nanowire (blue curve), bead coupled to a nanowire and directly excited by the laser (green curve), bead excited by surface plasmons launched by focusing a laser on the extremity of the nanowire (red curve). The grey curve is the measured IRF and the black curves are log-normal fits to the decay histograms. (b) Log-normal distributions of decay rate for these three situations.*

3.4.3 Evidence of the occurrence of energy transfer

In the energy transfer experiment, the occurrence of the energy transfer between the QD and the acceptor bead can be demonstrated by studying the measured decay histograms. A common procedure is to determine the enhancement of the decay rate of the donor due

to the presence of the acceptor. However, no significant differences would be observed in this case due to the low efficiency of the process. Nevertheless, it is possible to measure the decay histogram of the acceptor bead, which can be significantly different when excited by the QD with respect to the case in which the acceptor is directly excited by the laser. Indeed, in the energy transfer experiment, the acceptor cannot be excited until the donor decays to the ground state. From the lifetime PDFs of the donor and the acceptor, respectively noted $h_d(t)$ and $h_a(t)$, the lifetime PDF of the acceptor excited via the donor is

$$h_{et}(t) = h_{irf}(t) * h_d(t) * h_a(t) \ , \tag{3.13}$$

where $h_{irf}(t)$ is the IRF and the asterisk $(*)$ represents the convolution product. While $h_d(t)$ was determined in Sect. 3.4.1 from the decay histogram measured by SPAD 1 during the experiment, we determined $h_a(t)$ in Sect. 3.4.2 by exciting the acceptor bead via surface plasmons excited by focusing a pulsed laser at $\lambda_0 = 640$ nm onto an edge of the wire. Figure 3.12 shows the expected decay histogram of the acceptor excited via the donor using Eq. (3.13). This PDF is significantly wider than the lifetime PDF of the donor as well as the lifetime PDF of the acceptor independently excited.

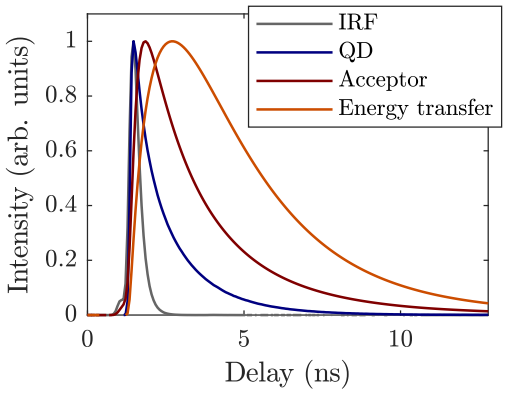

Figure 3.12 – *Model functions associated with the decay histograms of the QD (blue curve) and the acceptor (red curve) independently excited. The model function associated to the decay histogram of the acceptor excited by the QD is their convolution (orange curve). The IRF is represented by a grey curve.*

From this knowledge, we can now analyse the decay histogram of the acceptor bead measured during the energy transfer experiment. Figure 3.13a shows the measured decay histogram with a 64 ps resolution. It is characterised by two components, a slow decay which is a characteristic of the occurrence of the energy transfer and another decay characterised by a very short lifetime. This component is attributed to silver luminescence. Indeed, such a fast component of the decay histogram is also observed in test experiments performed on bare silver nanowires deposited on a glass coverslip under pulsed excitation at $\lambda_0 = 405$ nm. Luminescence is characterised by a very broad spectrum and can propagate along the nanowire via surface plasmons for finally being scattered by the acceptor bead and detected by the detector. We consequently fit the IRF to the luminescence peak and we subtract it from the decay histogram. Figure 3.13b shows the corrected decay histogram along with a fit of the expected lifetime PDF to the decay histogram. The excellent agreement between them is an evidence that the observed acceptor fluorescence comes from the energy transfer originating from the QD and mediated by surface plasmons. From this decay histogram, we estimate that $f_2 = 1010 \pm 50$ fluorescence photons are detected from the acceptor during the experiment. At the same time, $f_1 = 1.6 \times 10^7$

fluorescence photons are collected from the QD.

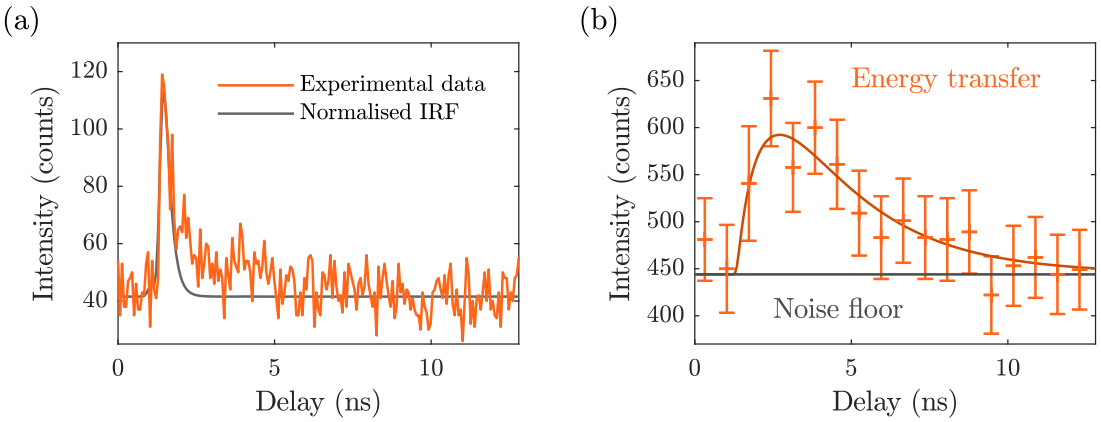

Figure 3.13 – *(a) Raw decay histogram measured by SPAD 2 with a resolution of 64 ps. The IRF is fitted to the measured decay histogram. (b) Corrected decay histogram of the acceptor with a resolution of 700 ps, along with the model function (orange curve). Error bars correspond to a statistical significance of $\pm 2\sigma$ calculated assuming that the measured intensities are Poisson-distributed.*

3.5 Intensity fluctuations due to blinking

We now demonstrate the correlated blinking of the QD and the acceptor bead as a second evidence of the occurrence of micrometre-range energy transfer between the two emitters.

3.5.1 Blinking of the quantum dot

At the single-crystal level, the emission of a QD usually fluctuates between bright and dark states. In a bright state, the electron-hole pair recombines by emitting a photon. In contrast, the recombination process does not involve spontaneous emission if the QD is in a dark state. This well-known property of QDs is referred to as *blinking*. It is often considered as a drawback since it reduces the average intensity emitted by a QD. It was notably shown that the blinking behaviour of QDs can be limited by tuning the structure of the nanocrystals [63,64]. The CdSe/CdS/ZnS nanocrystals used in the experiments are most of the time in a bright state, even though they show a fast blinking behaviour.

As already mentioned, SPAD 1 is used to measure the fluorescence of the donor during the energy transfer experiment. Figure 3.14a shows the fluorescence counts of the donor $I_1(t)$ as a function of time. Due to the blinking of the QD, we observe strong fluctuations on time scales larger than the millisecond between a bright and a dark state for nearly 70 s before photobleaching. A slight drift of the experiment from optimum alignment is responsible of a continuous loss of collected signal with time. By applying a linear correction to compensate for this drift, we obtain a corrected intensity distribution of the number of photons detected per millisecond (Fig. 3.14b), on which the bright and the dark states clearly appear. This clear distinction between two states and the abrupt decrease in the measured intensity due to the photobleaching of the QD attest that the donor is indeed a single QD.

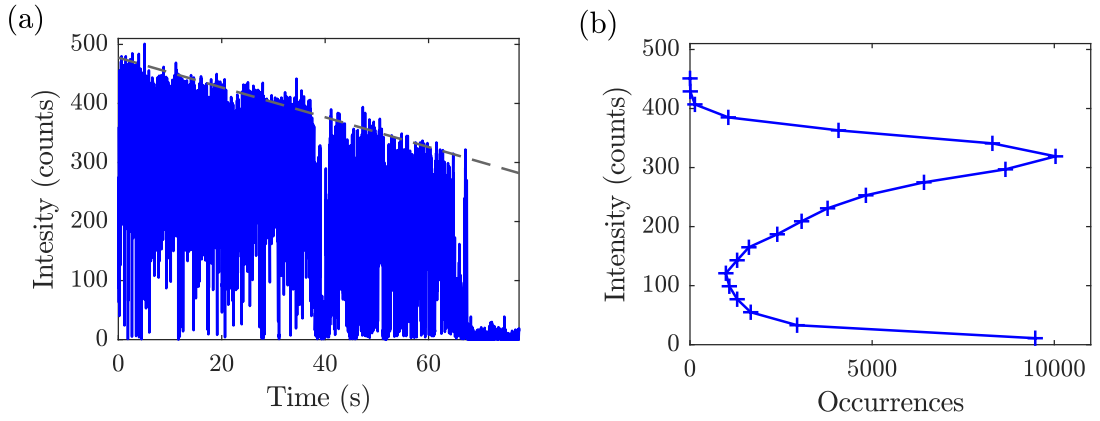

Figure 3.14 – *(a) Time dependence of the fluorescence counts of the QD, with a resolution of 1 ms (blue curve). The drift of the experiment is represented by a dashed line. (b) Distribution of detected events taking into account a linear correction for the drift of the experiment.*

3.5.2 Characterisation of blinking by second-order correlations

As we collect a low number of photons from the acceptor bead, we cannot directly observe the fluctuations in the fluorescence counts of the acceptor bead $I_2(t)$ as we do for the QD. However, we can take advantage of the measurements performed by the two detectors and use the $g^{(2)}$ correlation function to demonstrate the correlated blinking of the QD and the acceptor bead. Indeed, if the fluorescence intensities $F_1(t)$ and $F_2(t)$ measured by each detector are correlated, the expectation of the $g^{(2)}$ correlation function for near-zero delays is significantly larger as compared to the case of independent fluorescence intensities, as shown in Sect. 3.3.2. However, while it is easy to compute the $g^{(2)}$ correlation function with a temporal resolution as good as the repetition period for delays close to zero, the numerical evaluation of $g^{(2)}$ for a large range of delays requires a large computational power. Under typical acquisition conditions, the best option to observe the blinking of an emitter on time scales of the order of the millisecond is to group the detected events into temporal bins and then to perform the computation of $g^{(2)}$. Furthermore, this procedure increases the higher signal-to-noise ratio for the number of coincidences due to the binning process. In this case, the analysis carried out in Sect. 3.3.2 does not hold, because more than one photon can be measured into one bin. Additionally, single-photon emission cannot be demonstrated using this approach, as a direct consequence of the binning process.

In this section, we do not calculate the expectation of the $g^{(2)}$ correlation function[2] but its upper limit in the case of a linear relationship between $F_1(t)$ and $F_2(t)$. Let w_{bin} be the bin size in unit of repetition periods. From Eq. (3.1), the $g^{(2)}$ correlation function can be written as

$$g^{(2)}(\tau) = \frac{w_{bin}\, n_1\, n_2}{\Delta t} + \mathrm{Cov}[I_1(t), I_2(t+\tau)]\,, \tag{3.14}$$

where n_1 and n_2 are the number of photons measured by each detector during the acqui-

[2]To calculate the expectation of $g^{(2)}$ with the same formalism as the one used in Sect. 3.3.2, we would consider that the number of coincidences follows a multinomial distribution, as the result of n_t/w_{bin} independent experiments. However, this approach requires to model the blinking dynamics of the QD, which is not needed for the method presented in this section.

sition time Δt. The covariance operator is defined by

$$\mathrm{Cov}(I_1, I_2) = \int_{\Delta t} (I_1(t) - \overline{I_1})(I_2(t) - \overline{I_2})\, \mathrm{d}t \,, \tag{3.15}$$

where $\overline{I_1}$ and $\overline{I_2}$ are the mean intensities measured by the two detectors. Equation (3.14) explicitly shows that the number of coincidences is the sum of the expectation of the number of coincidences assuming independent intensities and the covariance of the intensities. Indeed, the covariance of the intensities equals zero if the two intensities are independent. As a consequence, we can use the covariance to quantify a possible deviation from independence in the statistical relationship between the fluorescence intensities $F_1(t)$ and $F_2(t)$ respectively measured by detector 1 and detector 2.

By decomposing each intensity into its fluorescence and noise contributions for each detector i so that $I_i(t) = F_i(t) + B_i(t)$, it follows that

$$\begin{aligned}\mathrm{Cov}(I_1, I_2) = &\int_{\Delta t} (F_1(t) - \overline{F_1})(F_2(t) - \overline{F_2})\, \mathrm{d}t + \int_{\Delta t} (F_1(t) - \overline{F_1})(B_2(t) - \overline{B_2})\, \mathrm{d}t \\ &+ \int_{\Delta t} (B_1(t) - \overline{B_1})(F_2(t) - \overline{F_2})\, \mathrm{d}t + \int_{\Delta t} (B_1(t) - \overline{B_1})(B_2(t) - \overline{B_2})\, \mathrm{d}t \,. \end{aligned} \tag{3.16}$$

The last three terms involve the integral over Δt of a white noise and therefore equal zero in the limit of large Δt. The covariance of $I_1(t)$ and $I_2(t)$ is therefore only determined by the fluorescence counts, and reads

$$\mathrm{Cov}(I_1, I_2) = \int_{\Delta t} (F_1(t) - \overline{F_1})(F_2(t) - \overline{F_2})\, \mathrm{d}t \,. \tag{3.17}$$

In the limit of large Δt, this equation equals zero if $F_1(t)$ and $F_2(t)$ are independent. However, if a linear relation between $F_1(t)$ and $F_2(t)$ exists so that $F_2(t) = \alpha\, F_1(t)$, the covariance of $I_1(t)$ and $I_2(t)$ under this hypothesis noted $\mathcal{H}_{lin}$ reads

$$\mathrm{Cov}(I_1, I_2 \mid \mathcal{H}_{lin}) = \alpha \times \int_{\Delta t} (F_1(t) - \overline{F_1})^2\, \mathrm{d}t \,. \tag{3.18}$$

We can use this relation to define a *correlation coefficient* noted R that equals zero if $F_1(t)$ and $F_2(t)$ are uncorrelated and that equals unity if they are linearly related via the coefficient α. Under these conditions, the coefficient R reads

$$R = \frac{\mathrm{Cov}(I_1, I_2)}{\mathrm{Cov}(I_1, I_2 \mid \mathcal{H}_{lin})} \,. \tag{3.19}$$

Since $F_2(t) = \alpha\, F_1(t)$, we can directly write $\mathrm{Var}(F_1) = \alpha^2\, \mathrm{Var}(F_2)$ and the correlation coefficient R becomes

$$R = \frac{\mathrm{Cov}(I_1, I_2)}{\sqrt{\mathrm{Var}(F_1)\, \mathrm{Var}(F_2)}} \,. \tag{3.20}$$

The correlation coefficient R can be interpreted as an adaptation of the Pearson correlation coefficient for noisy signals: it equals unity if the fluorescence intensities are linearly related while it equals zero if the intensities are independent. It is important to note that the normalisation in Eq. (3.20) is not performed using the variance of the total intensities but only the contributions due to fluorescence. The contribution of white noise must consequently be determined before the analysis.

Using this approach, we can calculate the correlation coefficient R as defined by Eq. (3.20) for the numerical experiment presented in Sect. 3.3.2. Figure 3.15 shows the correlation coefficient as a function of the delay between the intensities measured by each detector. The size of the temporal bins used for $I_1(t)$ and $I_2(t)$ is 100 µs. As expected, we do not observe the antibunching in this case. Moreover, we observe that the correlation coefficient equals zero for large delays, attesting that the fluorescence intensities are independent in this limit. It is interesting to note that the correlation coefficient is slightly smaller than unity at zero delay. Indeed, $F_1(t)$ and $F_2(t)$ are not perfectly linearly related due to the random character of photon emission when the emitter is in the bright state. However, this effect is small for a large bin size w_{bin} because fluorescence intensities become almost perfectly linearly related due to the binning process.

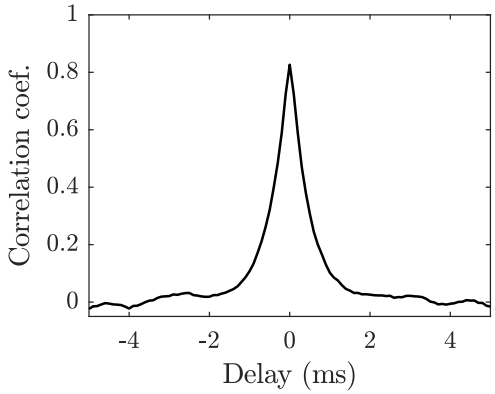

Figure 3.15 – *Correlation coefficient versus delay for the numerical experiment presented in Sect. 3.3.2. It is calculated from $I_1(t)$ and $I_2(t)$ using a resolution of 100 µs.*

3.5.3 Correlated blinking of the donor and the acceptor

We adopt this approach to evaluate the degree of linear correlation as a function of the delay between the signals detected from the donor QD and the acceptor bead. Indeed, if the blinking of the two emitters is correlated, we expect to observe a linear relation between the fluorescence intensities so that $F_2(t) = \alpha F_1(t)$ and $\mathrm{Var}(F_2) = \alpha^2 \mathrm{Var}(F_1)$. Based on the analysis of the decay histograms presented in Sect. 3.4.3, we can estimate that $\alpha = f_2/f_1 \approx 6.3 \times 10^{-5}$. Moreover, the intensity $I_1(t)$ measured by SPAD 1 is largely due to the fluorescence of the QD which strongly dominates over noise in the experiment. Since the variance of $I_1(t)$ is determined by the blinking of the QD, we can make the approximation $\mathrm{Var}(F_1) \approx \mathrm{Var}(I_1)$.

To obtain a good signal-to-noise ratio, we perform the following data processing for the calculation of the correlation coefficient:

- The covariance of the intensities measured by SPAD 1 and SPAD 2 is calculated with a time resolution of 1 ms.
- We select a 30 s time interval (from t=40 to 70 s in Fig. 3.14a) in which the QD frequently blinks. By considering this time interval, we increase even more the variance of the fluorescence intensities in comparison to the variance of the noise.
- We symmetrise the intensities $I_1(t)$ and $I_2(t)$ in order to be insensitive to the drift of the experiment.

- We select the photons on the base of their arrival time with respect to the laser excitation pulse. More precisely, we only consider the interval between 1.856 ns and 12 ns for the acceptor fluorescence. Consequently, we do not consider the luminescence peak that we identified in Fig. 3.13a.

Figure 3.16a shows the correlation coefficient $R(\tau)$ between the QD intensity and the acceptor intensity (orange curve), given by

$$R(\tau) = \frac{\mathrm{Cov}[I_1(t), I_2(t+\tau)]}{\alpha \, \mathrm{Var}(I_1)} \, . \tag{3.21}$$

The correlation coefficient is almost of unity at zero delay, which means that the two fluorescence intensities $F_1(t)$ and $F_2(t)$ are almost perfectly linearly related. This observation proves that the blinking of the donor and the acceptor is correlated. Moreover, the correlation coefficient goes to zero for large delays, on time scales characterising the blinking of the QD (of the order of 500 ms). The small deviation from unity at zero delay has two origins. Firstly, we slightly overestimate the variance of $F_1(t)$ by making the approximation $\mathrm{Var}(F_1) \approx \mathrm{Var}(I_1)$. Secondly, we do not expect a perfectly linear relation between $F_1(t)$ and $F_2(t)$ due to the random character of photon emission. This effect was already observed in the context of the numerical experiment presented in Fig. 3.15.

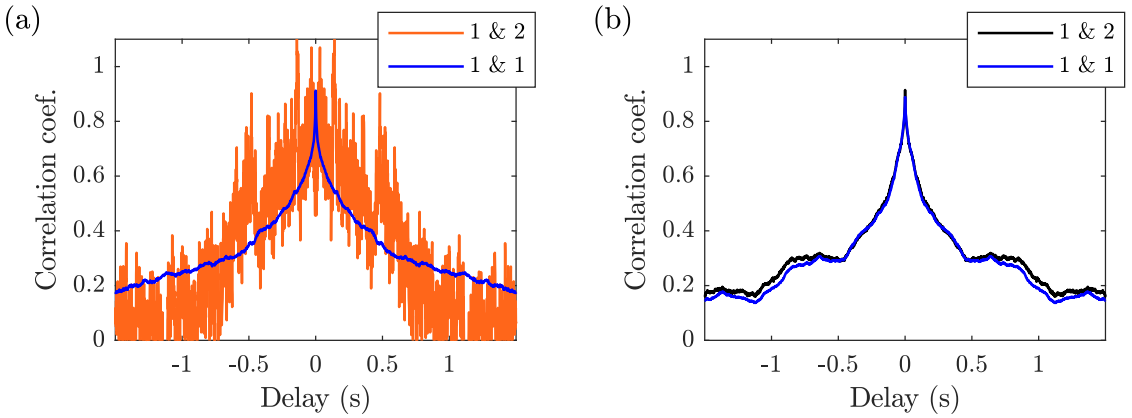

Figure 3.16 – *(a) Correlation coefficient between the fluorescence of the QD and the fluorescence of the acceptor bead (orange curve). (b) Correlation coefficient between the fluorescence of the QD and the light scattered by the end of a nanowire (black curve) determined from a side experiment. In each case, the autocorrelation coefficient measured from the free-space emission of the QD is also shown for comparison purposes (blue curves).*

For comparison purposes, we calculate the autocorrelation coefficient of the QD intensity (Fig. 3.16a, blue curve) defined as the correlation coefficient between the intensity measured from the QD and itself. The time scales of the fluctuations are effectively the same for both the QD and the acceptor fluorescence, which corroborates the analysis. The quantitative agreement between them[3] also validates the value of $\alpha = F_2(t)/F_1(t)$ determined from the analysis of the decay histograms. In addition, we perform the same analysis on the experiment involving a QD without an acceptor bead that we already presented in Sect. 3.3.4. In this experiment, a QD excites single surface plasmons on a silver nanowire, SPAD 1 detects the free-space emission of the QD and SPAD 2 detects

[3]The curves shown in Fig. 3.16a are calculated without any free parameter for normalisation.

the surface plasmons scattered at the nanowire end located 7.2 µm away from the QD. The autocorrelation of the QD intensity and the correlation coefficient between the QD intensity and the intensity scattered at the wire extremity are again in excellent agreement (Fig. 3.16b).

3.6 Towards a demonstration of photon antibunching

In principle, it should be possible to observe an anticorrelation between the intensities collected from the QD and the acceptor bead at zero delay and on the nanosecond time scale. However, we do not observe the antibunching in the $g^{(2)}$ correlation function due to the low number of fluorescence photons measured from the acceptor. In this section, we identify the conditions that would be required for its observation.

3.6.1 Condition required to demonstrate photon antibunching

Let us determine the condition required to demonstrate an anticorrelation in the fluorescence intensities measured by two detectors in HBT configuration. To do so, the number of coincidences in the central peak of the $g^{(2)}$ correlation function must be smaller than the number of coincidences in the adjacent peaks. However, for a given realisation of the experiment, it is not sufficient to show that the measured value of the central peak is smaller than the mean value of the adjacent peaks to prove that the fluorescence intensities measured by each detector are anticorrelated. We must indeed demonstrate that this difference is significant and cannot be attributed to shot noise. To this end, the signal to be measured must be larger than its standard deviation, which reads

$$\mathrm{E}(n_a - n_0) \gg \sqrt{\mathrm{Var}(n_a - n_0)}\,, \tag{3.22}$$

where n_0 and n_a are the random variables which respectively describe the number of coincidences for zero and near-zero delays. In order to characterise the distributions followed by these two random variables, we can assume a statistical relationship between the fluorescence intensities $F_1(t)$ and $F_2(t)$ measured by each detector, as detailed in Sect. 3.3.2. The expectations of n_0 and n_a can then be calculated using Eq. (3.2) and their variances using Eq. (3.3).

Let us assume that the fluorescence intensities $F_1(t)$ and $F_2(t)$ are perfectly anticorrelated. Then, the expectation of n_0 can be calculated from Eq. (3.7). As a matter of simplicity, we consider here that the emitter does not blink. This amounts to consider only the time intervals for which the emitter is in the bright state if the emitter does blink. Then, the expectation of n_a can be calculated from Eq. (3.5) since $I_1(t)$ and $I_2(t+\tau)$ are independent for $\tau \neq 0$. The expectation of $(n_a - n_0)$ consequently reads

$$\mathrm{E}(n_a) - \mathrm{E}(n_0) = \Delta t\, \frac{\bar{F}_1 \bar{F}_2}{r}\,, \tag{3.23}$$

where Δt is the acquisition time, r is the repetition rate of the laser and $\bar{F}_1$ and $\bar{F}_2$ are respectively the average fluorescence intensities measured by the two detectors. It follows that the expectation of the signal to be measured increases with $\bar{F}_1$, $\bar{F}_2$ and Δt and decreases with r. These parameters are generally related to one another: for instance,

increasing the repetition rate of the laser usually increases the measured fluorescence intensities.

The variance of $(n_a - n_0)$ can be calculated in the same way, even though its expression also depends on $\bar{N}_1$ and $\bar{N}_2$ that are the average noise intensities respectively measured by each detector. From this knowledge, we can calculate the value of the test statistic T_{HBT} defined as follows:

$$T_{HBT} = \frac{\mathrm{E}(n_a) - \mathrm{E}(n_0)}{\sqrt{\mathrm{Var}(n_a) + \mathrm{Var}(n_0)}} \,, \tag{3.24}$$

This test is constructed from the inequality given by Eq. (3.22), considering that n_a and n_0 are independent random variables. If $T_{HBT} \gg 1$, the measurement of the $g^{(2)}$ correlation function allows one to demonstrate the anticorrelation between $F_1(t)$ and $F_2(t)$. In contrast, if $T_{HBT} < 1$, the standard deviation of $(n_a - n_0)$ is greater than its expectation, which means that the signal-to-noise ratio is insufficient to demonstrate the anticorrelation in the fluorescence intensities. As a rule of thumb, we can assume that $T_{HBT} > 3$ is required to demonstrate the anticorrelation, as it corresponds to a statistical significance of $\pm 3\sigma$.

The test statistic T_{HBT} can be used to determine whether a specific experiment performed in HBT configuration would allow one to demonstrate an anticorrelation between $F_1(t)$ and $F_2(t)$ if the intensities are perfectly anticorrelated. Thus, it also gives the upper limit for the ability of $g^{(2)}$ measurements to demonstrate photon antibunching, regardless of the actual statistical relationship between $F_1(t)$ and $F_2(t)$. If $F_1(t)$ and $F_2(t)$ are perfectly anticorrelated, the ability of the measurement to demonstrate antibunching can be evaluated using the test statistic T_{HBT}. However, if the anticorrelation is not perfect – due to the formation of biexction states in a QD for instance – then T_{HBT} only gives the upper limit for the ability of $g^{(2)}$ measurements to demonstrate antibunching.

For typical acquisition conditions, T_{HBT} is usually larger than unity. For instance, in the two experiments respectively performed on a single QD on glass (Fig. 3.7a) and on a single QD coupled to a silver nanowire (Fig. 3.7b), the number of fluorescence photons measured by the two SPADs are large resulting in $T_{HBT} \approx 65$ for both experiments. In the experiment involving a single QD and the surface plasmon scattered by the end of the nanowire (Fig. 3.8b) the number of detected photons is smaller resulting in $T_{HBT} \approx 10$. Nevertheless, we can clearly see that all of these measurements allow us to draw a significant conclusion concerning the statistical relationship between the intensities measured by the two detectors.

3.6.2 Comparison with the current experimental conditions

Let us now summarise the characteristics of the energy transfer experiment:

- We can estimate the acquisition time from the measurement of the intensity emitted by the QD, as previously shown in Fig. 3.14a. By performing a post-processing gating in order to consider only the bright state of the QD, we obtain $\Delta t = 56$ s.
- The repetition rate of the laser is $r = 40$ MHz.
- The number of fluorescence photons measured from the QD is $f_1 = 1.6 \times 10^7$ and the number of fluorescence photons measured from the acceptor bead is $f_2 = 1010$. This respectively corresponds to average fluorescence intensities of $\bar{F}_1 = 2.9 \times 10^5$ cts/s and $\bar{F}_2 = 18$ cts/s.

- From the measured decay histograms, we can estimate the number of events due to white noise on each detector, which is $b_1 = 2.2 \times 10^5$ and $b_2 = 4500$. This respectively corresponds to average background intensities of $\bar{N}_1 = 3900$ cts/s and $\bar{N}_2 = 80$ cts/s.

We can now calculate the value of T_{HBT} in order to evaluate whether the current experimental conditions can allow the demonstration of single-photon emission or not. We obtain $T_{HBT} = 0.85$ which is clearly insufficient to demonstrate an antibunching.

In order to get a better understanding of the limitations of the experiment, we can calculate the expectation and the standard deviation of the number of coincidences as a function of the parameters described above. To start with, we calculate the expectation and the standard deviation of the number of coincidences for near-zero delays, assuming independence between the fluorescence intensities. Then, we calculate these quantities at zero delay, assuming perfect anticorrelation between the fluorescence intensities. We present here the $\pm 2\sigma$-intervals as a function of the average fluorescence intensity $\bar{F}_2$ emitted by the acceptor and measured by SPAD 2 (Fig. 3.17a). We also present the same intervals as a function of the acquisition time Δt of the experiment (Fig. 3.17b).

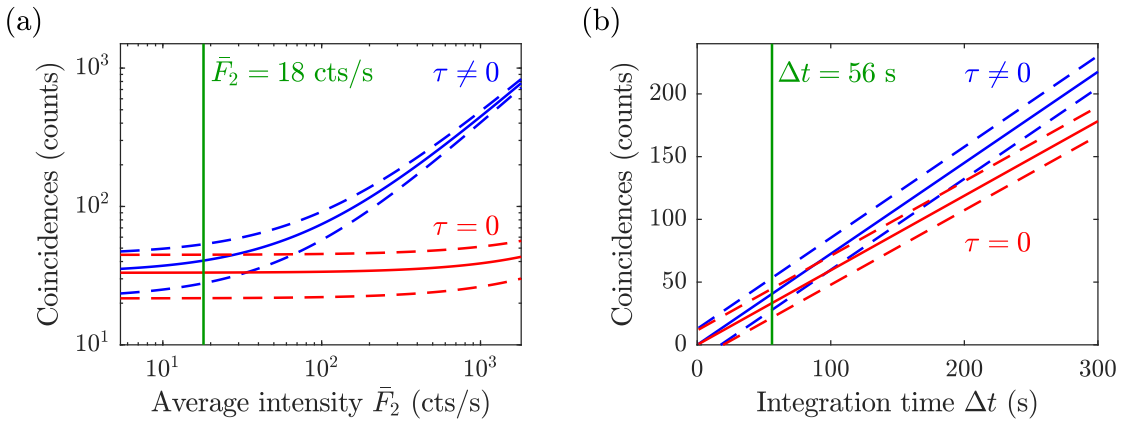

Figure 3.17 – *Expectation of the number of coincidences as a function of (a) the average fluorescence intensity $\bar{F}_2$ emitted by the acceptor and measured by SPAD 2 and (b) the acquisition time Δt of the experiment. Red curves are calculated considering anticorrelated intensities while blue curves are calculated considering independent intensities. Dashed lines correspond to a statistical significance of $\pm 2\sigma$. Green lines represent the actual experimental conditions.*

The $\pm 2\sigma$-intervals strongly overlap for the current experimental conditions, characterised by $\bar{F}_2 = 18$ cts/s and $\Delta t = 56$ s. However, an enhancement of $\bar{F}_2$ by a factor of 4 would result in a value of T_{HBT} around 3. In this case, we would be able – in theory – to demonstrate antibunching. To this end, it will probably be required to enhance the energy transfer efficiency by using more elaborated nanostructured waveguides. Another possible solution to improve the ability of the $g^{(2)}$ measurements to demonstrate antibunching is to increase the acquisition time of the experiment. By increasing the integration time up to 200 s, we would obtain a value of T_{HBT} around 3. However, in practice, the current acquisition time is limited by the photobleaching of the QD.

3.7 Conclusion

In this chapter, we presented an experimental demonstration of energy transfer occurring between a single QD and fluorescent molecules embedded inside a nanobead, for a donor-acceptor distance of 8.7 µm. To start with, we showed that CdSe/CdS/ZnS nanocrystals can excite single plasmons with a biexcition-to-exciton ratio smaller than 30%. Then, we showed that the measurement of the decay histogram of the acceptor bead can be used to demonstrate the occurrence of energy transfer between the QD and the bead (Fig. 3.13b). Furthermore, we demonstrated the existence of a positive correlation on the millisecond time scale between the intensities emitted by the QD and the bead (Fig. 3.16a). This is the main result of this chapter, which attests that the blinking of the QD and the bead is correlated while they are distant of several micrometers. This constitutes a further evidence of micrometre-range energy transfer mediated by single plasmons.

As a direct evidence of a transfer of energy mediated by single energy quanta, we expect an anticorrelated emission between the QD and the acceptor on the nanosecond time scale. Unfortunately, this observation was hindered by the noise level due to the weak efficiency of the energy transfer process. To limit ohmic losses occurring during the propagation of the surface plasmons, we also studied the energy transfer for shorter donor-to-acceptor distances. However, the direct excitation of the acceptor bead by the laser became non-negligible in these cases. It should be noted that the efficiency of the process could theoretically be estimated – as we did in Sect. 2.6 for the planar geometry – even though the dyadic Green function of the field reflected by the nanowire is more difficult to calculate [65]. Using a numerical approach such as a finite-difference time domain simulation requires a huge computational power because of the large size of the system along the nanowire axis. An alternative approach to achieve this task is to numerically determine the field created by a dipole near the nanowire and to analytically account for the propagation of the surface plasmons, as proposed by Barthes *et al.* [66].

In any case, more efficient configurations will be required to achieve a stronger coupling between the emitters. Various waveguides such as plasmonic V-grooves [67], plasmonic wedges [68] and dielectric nanofibres [69] are already used to efficiently couple single emitters to guided modes; such waveguides could therefore be used to achieve efficient long-range energy transfer. For this purpose, hybrid nanoantenna-waveguide systems appear as promising structures, as originally proposed by Oulton *et al.* [70]. In such configurations, the field generated by a donor can be efficiently coupled to a dielectric waveguide using a nanoantenna. The field can then propagate in the waveguide without attenuation so that it can be outcoupled by another nanoantenna located several micrometers away. For instance, de Roque, van Hulst and Sapienza numerically showed that the association of two plasmonic antennas with a dielectric waveguide can enhance the transfer rate for up to 8 orders of magnitude [38]. Interestingly, Biehs, Menon and Agarwal recently showed that giant energy transfer rates are also expected between a donor-acceptor pair across a hyperbolic metamaterial slab [71].

To achieve strong light-matter interaction, plasmonic antennas offer the advantage of a strong confinement of the electromagnetic field, but with significant ohmic losses. Recently, dielectric antennas were proposed to circumvent this issue. In the following chapter, we will present an experimental study of dielectric nanoantennas and we will show their ability to modify the emission properties of fluorescent emitters located in their near field.

Part II

Super-resolution imaging of the local density of states

CHAPTER 4

Spontaneous emission in the near field of silicon nanoantennas

In this chapter, we present a three-dimensional study of the near-field interaction between a fluorescent nanobead and different dielectric nanoantennas. First of all, we introduce the principle of the experiment and the context of this work. Then, we describe the antennas under study and their Mie resonances, characterised using dark-field measurements. We also detail the experimental setup, which consists in a homebuilt atomic force microscope at the tip of which a fluorescent nanobead is fixed. Finally, we present an experimental study of the spatial variations of the local density of states due to the presence of the silicon antennas. We also demonstrate that these antennas modify both the excitation field and the directionality of fluorescence emission.

4.1 Introduction

The theory of light scattering by a homogeneous sphere was formalised by Mie in 1908 [72]. He found the exact solution to Maxwell's equations for a sphere of any dimensions with respect to the wavelength of light, generalising the solution found by Rayleigh for small particles. From this work, the term *Mie scattering* is nowadays used to describe the scattering of light by structures presenting a cylindrical or spherical invariance. Such particles exhibit resonances at different frequencies depending on the size and the material of the particle. These resonances allow dielectric nanostructures to strongly interact with light at optical frequencies, resulting in the generation of fewer ohmic losses in comparison to nanostructures made of plasmonic materials.

Furthermore, Mie resonances of dielectric particles can be used to obtain an effective relative permeability that is different from unity, while the magnetic response of plasmonic particles remains almost negligible because of the vanishing electric field inside the particles [73]. Interestingly, the interaction between the electric and magnetic responses of dielectric particles opens the possibility to observe several unusual properties, such as a suppression of optical backscattering, as predicted in 1983 by Kerker, Wang and Giles [74]

and observed by Person *et al.* for nanoparticles at optical frequencies [75]. The interaction between the electric and magnetic part of the field can also be used to observe negative refraction, which was demonstrated at optical frequencies using metamaterials by Valentine *et al.* [76].

Recently, several theoretical studies investigated the possibility to use Mie resonances to build antennas at optical frequencies using dielectric materials. In 2011, Garcia-Etxarri *et al.* identified a range of frequencies in the near infrared for which both electric and magnetic resonances can be identified, without overlapping with higher order modes [77]. One year later, Rolly *et al.* showed that spherical particles can be used to promote magnetic transitions [78]. To do so, they derived analytical expressions for the decay rate of electric and magnetic transition dipoles located in the vicinity of a sphere. On the experimental side, Caldarola *et al.* recently performed ensemble measurements on emitters dispersed in the vicinity of silicon dimers, resulting in a substantial increase in the collected fluorescence [79]. Cambiasso *et al.* used a similar approach to demonstrate an increase in the decay rate of fluorescent dyes located in the gap of a gallium phosphide dimer [80]. Silicon dimers were also studied by Regmi *et al.* who performed a comprehensive analysis of the fluorescence enhancement mechanisms based on fluorescence correlation spectroscopy [81].

In the meantime, a few articles reported on the development of an original scanning-probe technique used to probe the local density of states (LDOS) in the near field of a nanostrucure. This technique is based on the grafting of a fluorescent emitter to the tip of an atomic force microscope (AFM). In 2011, Frimmer, Chen and Koenderink presented the first decay rate map characterising the near-field interaction between a fluorescent nanobead and a silver nanowire [82]. In 2013, Krachmalnicoff *et al.* presented a comprehensive study of fluorescence emission in the near field of a gold trimer by performing a simultaneous acquisition of decay rate, intensity and topography maps [22]. In 2014, Schell *et al.* used a single nitrogen vacancy center in nanodiamond to perform a three dimensional analysis of the modification of the decay rate induced by a silver nanowire [83]. This scanning-probe technique was also applied by Cao *et al.* to map the radiative and apparent non-radiative LDOS in the near field of a gold nanoantenna [84].

Principle of the experiment In this chapter, we present the results of a study performed in collaboration with different research groups at Institut Langevin, Institut Fresnel (Marseilles), Centre Interdisciplinaire de Nanoscience de Marseille (Marseilles), Institut des Nanosciences de Paris (Paris), Institut de Ciencies Fotoniques (Barcelona) and Politecnico di Milano (Milan). This work consists in a three-dimensional characterisation of the near-field interaction between a fluorescent nanobead and different dielectric antennas. This characterisation is done by means of a near-field scanning probe, relying on an AFM with a fluorescent emitter grafted at the extremity of the tip. Figure 4.1 shows an artistic view of the experiment. A sample presenting different silicon nanoantennas is scanned in the three dimensions and we perform time-resolved measurements of the emission of the bead for each position of the sample. This procedure allows us to observe the enhancement and the inhibition of the decay rate of the bead induced by different dielectric antennas. By comparing intensity measurements to numerical results, we also demonstrate that these antennas modify both the excitation field and the directionality of fluorescence emission. This work is published in Physical Review Applied [85].

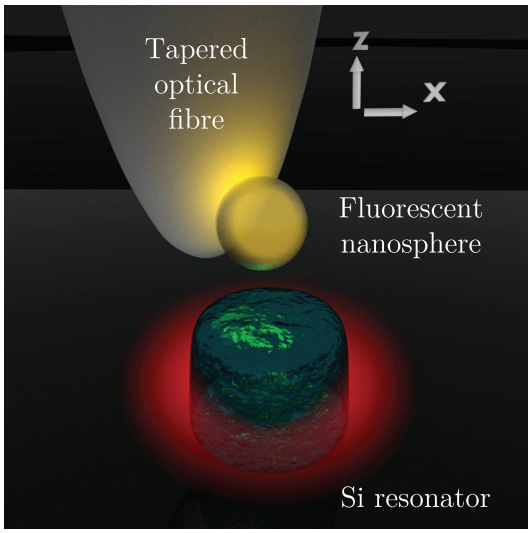

Figure 4.1 – *Principle of the experiment: a fluorescent nanobead is grafted on the tip of an AFM and is brought in the near field of different silicon nanoantennas. By scanning a specific antenna around the bead in the three dimensions, we can characterise the near-field interaction between the fluorescent bead and this antenna.*

4.2 Far-field analysis of resonant modes in silicon antennas

In Chapters 2 and 3, we showed that plasmonic materials can be used to modify the emission properties of fluorescent emitters. Now, we show that dielectric materials can also be used for this purpose, by taking advantage of resonances induced by the geometry of silicon disks.

4.2.1 Dielectric antennas

Dielectric materials are characterised by a relative permittivity with a near-zero imaginary part for a given range of frequencies. As a consequence of the Kramers-Kronig relations, the real part of the relative permittivity weakly depends on the frequency in this range. However, one can use combinations of several dielectric materials with different relative permittivities – vacuum can be one of them – and design specific structures so that the interface conditions provoke constructive or destructive interferences of the fields depending on the considered frequency. Similarly, it is possible to design dielectric structures that are resonant with the magnetic field. Note that a magnetic response can also be obtained from metallic structures such as split-ring resonators, as introduced at microwave frequencies by Pendry *et al.* [86]. While this concept works for gigahertz, terahertz and near-infrared frequencies, it fails for visible light due to ohmic losses and technological difficulties of sample fabrication [87]. In contrast, resonances of dielectric particles can be used to obtain an effective relative permeability that is different from unity at optical frequencies.

The field scattered by a spherical particle can be analytically solved. Indeed, this field can be decomposed into a multipole series characterised by the electric and magnetic Mie coefficients respectively noted a_n and b_n. In this expansion, a_1 and b_1 are associated to the electric and magnetic dipole modes. Similarly, a_2 and b_2 are associated with the electric

and magnetic quadrupole modes. When an electromagnetic field is applied on such particles, the scattered field is then given by the sum of these contributions. Importantly, the particle can show a resonant behaviour so that the scattered field is due to one particular Mie coefficient, depending on the frequency of the excitation field, the size of the sphere as well as the relative permittivities of the sphere and its environment. The modes of the electromagnetic field associated with these resonances are generally called *Mie modes*. Note that such a decomposition of the fields can also be performed for structures presenting a cylindrical invariance.

Mie modes of a dielectric antenna are usually excited from the far field by plane wave illumination. However, they can also be excited from the near field by placing an emitter in the vicinity of the dielectric antenna. Due to spontaneous emission, the emitter may excite one or several Mie modes, producing a scattered field that can interfere with the emitter's own field, giving rise to a new radiation pattern. Moreover, if the electric field at the position of the emitter is significantly affected by the scattered field, the spontaneous emission rate is modified. More precisely, depending on the antenna geometry, the interferences between the emitter's field and the scattered field can be either constructive or destructive at the position of the emitter, resulting in either an enhancement or a reduction of its decay rate.

For most dielectric nanostructures, electric and magnetic dipolar resonances occur in the same range of frequencies. Evlyukhin *et al.* notably observed this effect in the case of spherical particles [88]. Such resonances can be shifted by tuning the geometry of the structure, as we will see in the following sections.

4.2.2 Description of the sample and dark-field measurements

We study a sample fabricated by Julien Proust (Institut Fresnel, Marseille) and Bruno Gallas (Institut des Nanosciences de Paris). This sample is fabricated by electron-beam lithography and reactive ion etching in a 105-nm-thick amorphous silicon film deposited on a 1-mm-thick glass substrate [89]. The resulting sample is composed of 20 arrays of 100 disks with diameters ranging from 110 nm to 300 nm and with a disk thickness of about 100 nm. On this sample, the distance between two adjacent disks is 4 µm, so that each disk can be considered as independent from one another. In this chapter, we specifically study two of these antennas (Fig. 4.2) respectively featuring a base diameter of 170 nm and 250 nm.

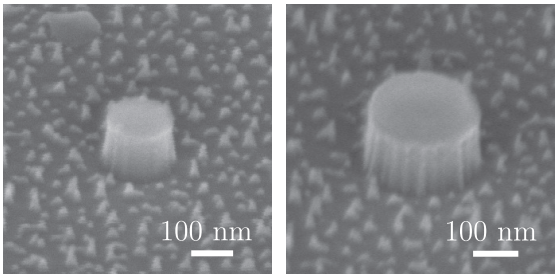

Figure 4.2 – *Images produced by scanning electron microscopy (SEM) and showing two silicon antennas with base diameters of 170 nm (left) and 250 nm (right).*

We perform a characterisation of the Mie resonances supported by these dielectric antennas using a dark-field microscope. To do so, we illuminate the sample with a broadband light

that is not collected by the objective and we measure the light scattered by the antennas using a color CCD camera (Quicam, Roper). As expected, the resonant frequencies of the antennas can be moved over the entire visible spectrum depending on their diameter (Fig. 4.3a).

We also measure the scattering spectra of the antennas using a spectrometer (Acton SP2300, Princeton Instruments). Figure 4.3b shows the scattering spectra associated with 5 antennas with diameters ranging from 130 nm to 300 nm. Only one peak can be identified on the scattering spectra of resonators with a diameter smaller than 200 nm. This peak corresponds to the overlap of magnetic and electric dipole modes that cannot be spectrally resolved. When varying the diameter from 130 nm to 200 nm, the scattered light intensity increases and its frequency shifts from the blue to the red part of the spectrum. Larger resonators feature both dipolar and quadrupolar resonances, leading to broader scattering spectra and larger cross-sections. Two distinct peaks can consequently be distinguished on their scattering spectra, the resonance at the shortest wavelength corresponding to quadrupole modes and the resonance at the largest wavelength corresponding to dipole modes.

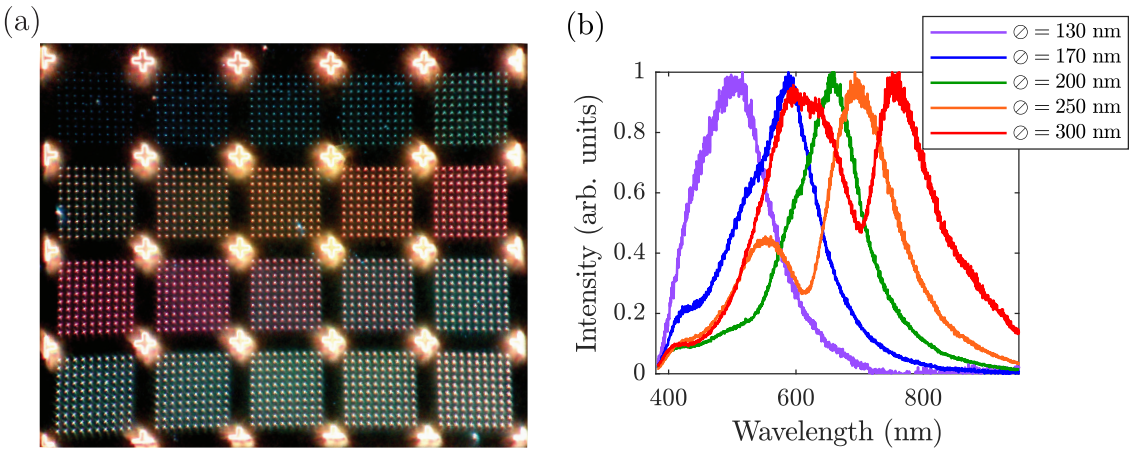

Figure 4.3 – *Dark-field characterisation of the sample, performed by Mathieu Mivelle (Institut des Nanosciences de Paris). (a) Dark-field image of the sample composed of 20 arrays of 100 silicon disks with diameters ranging from 110 nm (upper left) to 300 nm (lower right). (b) Scattering spectra of individual silicon antennas with diameters ranging from 130 nm to 300 nm.*

4.3 Experimental setup for near-field measurements

As previously discussed, a dielectric antenna can modify the emission rate of a fluorescent emitter located in its near field. To observe this behaviour, we use a scanning near-field optical microscope (SNOM) with an active probe, based on a homebuilt AFM that has been developed during the last few years at Institut Langevin [20, 21].

4.3.1 Description of the near-field fluorescence microscope

The SNOM used for the near-field characterisation of the antennas is constituted of a nanometre-scale fluorescent emitter grafted at the apex of an AFM tip made of a tapered silica fibre, as illustrated in Fig. 4.4. The position of the emitter is then controlled with nanometre precision by using the piezoelectric positioning system controlling the AFM tip. As proposed by Mühlschlegel *et al.* [90], the tuning-fork based AFM operating in shear force is arranged so that the tapered fibre is pressed against one arm of the tuning fork. The avoidance of glued connections notably facilitates the replacement of the fibre probe in this setup. Fluorescent emitters can then be grafted at the apex of the tip by bringing the emitter in contact with the tip while monitoring the process in real time with an electron-multiplying charge-coupled device (EM-CCD) camera.

Once grafted on the AFM tip, the fluorescent probe can scan the near field of nanostructures by using piezoelectric nanopositioners to control the position of the emitter with respect to the structure in three dimensions. Indeed, the interaction between the tip and the surface of the sample induces a shift of the resonance frequency of the tuning fork. This shift is then used to maintain the tip-sample distance to about 20 nm using a feedback loop. As we do not precisely control the vertical position of the emitter with respect to the end of the tip during the grafting process, the distance between the fluorescent probe and the sample can vary from about 20 nm to 200 nm.

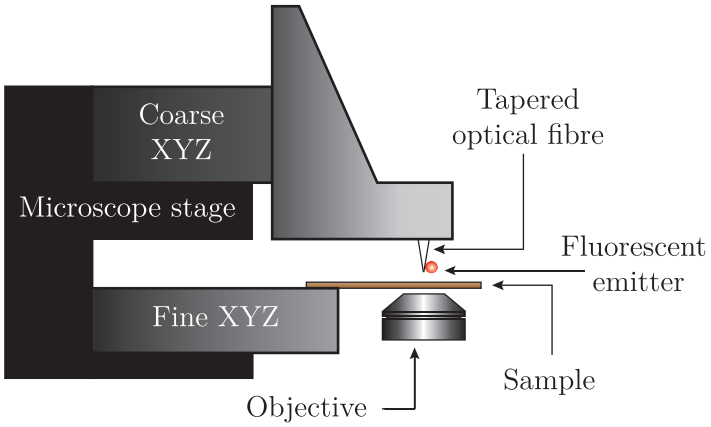

Figure 4.4 – *Sketch of the SNOM used for the near-field characterisation of the antennas. To this end, a fluorescent probe is grafted at the apex of an AFM tip and the sample is scanned around the probe in three dimensions.*

Both excitation and detection are performed through the 1-mm-thick silica substrate by using a microscope objective, characterised by a $\times 60$ magnification and a 0.7 numerical aperture. A supercontinuum pulsed laser filtered at $\lambda_0 = 560$ nm excites the emitter at a repetition rate of 10 MHz (Fianium SC450, 40 ps pulses). Fluorescence is filtered using a dichroic mirror and a high-pass filter ($\lambda_0 > 580$ nm) and detected by a single-photon avalanche diode (PDM-R, Micro Photon Devices [56]). We can thus measure the emission count rate as well as the decay histogram of the fluorescent probe while scanning the sample in three dimensions.

4.3.2 Fluorescent source

It is convenient to use a fluorescent emitter with a constant level of brightness for the characterisation of a given antenna. Fluorescent nanobeads are good candidates for this application as they are bright, non-blinking and photostable. Large beads are characterised by a large effective absorption cross-section as they contain many fluorescent molecules. However, measurements are averaged over the spatial extent of the bead, resulting in a limited spatial resolution. As a trade-off, we decide to use fluorescent beads with a diameter of 100 nm (Red FluoSpheres, Thermofisher Scientific) characterised by emission wavelengths around 610 nm. In order to probe silicon antennas with different characteristics, we select two different antennas respectively characterised by a diameter of 170 nm and 250 nm. The smallest antenna features a maximum scattering cross-section at 610 nm (Fig. 4.5, blue spectrum), corresponding to electric and magnetic dipolar resonances. In contrast, dipolar and quadrupolar resonances of the largest antenna are respectively centred on 550 nm and 710 nm, with a local minimum of the scattering cross-section around 610 nm (Fig. 4.5, orange spectrum). For this reason, the 170-nm-diameter antenna and the 250-nm-diameter antenna will respectively be called the *on-resonance* and the *off-resonance* antennas in the remainder of this chapter.

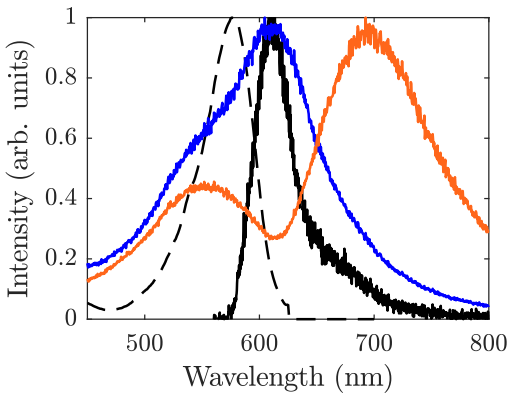

Figure 4.5 – *Experimental scattering spectra of 170-nm-diameter (blue curve) and 250-nm-diameter (orange curve) silicon antennas. Black curves are respectively the absorption (dashed curve) and emission (solid curve) spectra of the fluorescent bead.*

This dark-field characterisation is based on the field scattered by the antennas and measured in the far field. This field is expected to be quite different from the field scattered by the antennas in a near-field experiment for several reasons:

- The presence of the polystyrene bead and the tip modifies the environment of the antennas during the near-field experiments.
- The coupling between the electromagnetic field and the Mie modes supported by the antennas depends on the features of the field exciting the modes. This field is a plane wave for the dark-field measurements as opposed to the dipolar fields emitted by the molecules inside the bead for the near-field measurements.
- The dark-field characterisation is based on the intensity scattered by the antennas to the far field. In contrast, for the near-field measurements, the intensity collected from the fluorescent bead depends on the influence of the antenna upon the excitation intensity at the position of the bead.

For these reasons, the near-field interaction between a fluorescent probe and a nanoantenna cannot be directly predicted from far-field measurements.

4.4 Near-field measurements

We now present a three-dimensional study of the near-field interaction between the fluorescent bead and silicon antennas performed using the scanning-probe microscope previously described. As a matter of simplicity, we call *x-direction* any direction in the sample plane and we use the term *z-direction* for the axial direction.

4.4.1 Methods

Experimental study Experimentally, we can either perform a map in the sample plane or a line scan along the axial dimension. The typical acquisition time is approximately 15 minutes for a map in the sample plane (32×32 pixels) with an integration time of 1 s per pixel. This time is reduced to approximately 2 minutes for a line scan along the axial dimension (10 points) with an integration time of 10 s per point. This larger integration time allows to resolve smaller variations of the fluorescence decay rate. In both cases and for each bead position, we acquire a decay histogram and we determine the associated decay rate by fitting the measured histogram with a decreasing mono-exponential function. This corresponds to a value averaged over the $\sim 10^3$ randomly-oriented emitters spanning the 100-nm-diameter bead. Most of the time, the measured decay histograms follow a mono-exponential distribution. However, in some cases, the bead attached to the tip shows a bi-exponential distribution. As a matter of simplicity, we decide not to investigate this specific interaction but to change both the tip and the bead whenever this situation occurs.

Numerical study For comparison purposes, we also present the results of numerical simulations performed by Mathieu Mivelle using an in-house finite-difference time-domain (FDTD) software. These simulations allow us to estimate the evolution of the decay rate of an emitter located in the centre of a polystyrene bead as a function of the x- and z-distances to an antenna. They are specifically performed for three orthogonal electric dipole sources emitting at $\lambda_0 = 610$ nm, located in the centre of a 100-nm-diameter bead with a refractive index of 1.57. The refractive index of silicon antennas ($n = 4.55 + 0.34i$) is determined by ellipsometry, and simulations take into account a 10-nm-thick silica layer on the surface of the antennas due to silicon oxidation. The simulations consider a volume spanning ±2 µm in each direction around the nanostructures, and the grid resolution is non-uniform: it varies from 25 nm for areas far from the antennas to 5 nm for the region in the immediate vicinity of the antennas. The antennas are surrounded by air and they are located on top of glass which models the substrate. For simplicity, the tapered optical fibre is not taken into account in the simulations.

4.4.2 Spatial variations of the fluorescence decay rate

Measurements along the axial direction To begin with the three-dimensional study of the antennas, we characterise the evolution of the decay rate of the fluorescent bead

as a function of its axial distance to the centre of the antennas. The experimental results for the 170-nm-diameter antenna and the 250-nm-diameter antenna are respectively shown in Fig. 4.6a and Fig. 4.6b. They are obtained by measuring the decay histogram for 10 different positions over a range of 300 nm. In order to test the experimental repeatability, each acquisition is repeated four times in the case of the on-resonance antenna and three times in the case of the off-resonance antenna. We observe that the decay rate is maximum close to the on-resonance antenna, while it is minimum in the vicinity of the off-resonance antenna. The observed spatial variations are similar to the oscillations detected by Drexhage in 1970 [1]: as in Drexhage's experiment, the observed variations are due to constructive or destructive interferences between emitters inside the bead and the induced dipoles in the silicon antenna, whose phases depend on the emitter-antenna distance and on the polarisability of the antenna.

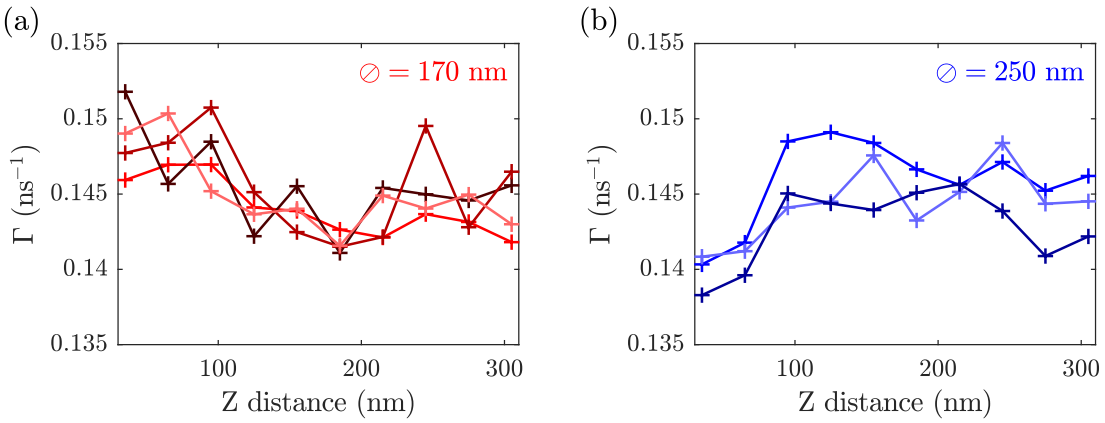

Figure 4.6 – *Experimental study of the decay rate of the fluorescent bead versus the z-distance between the bead and (a) the 170-nm-diameter or (b) the 250-nm-diameter silicon antennas.*

To confirm these observations, we compare them to the results of FDTD simulations. The decay rate Γ is calculated in the presence of the antenna from the value of the electric field at the position of the emitter. More details about the method can be found in Appendix B. We then perform a reference simulation without the antenna to calculate the reference decay rate noted Γ_0. The numerically estimated decay rate enhancement Γ/Γ_0 (Fig. 4.7a) and the experimental data averaged over the different realisations of the experiments (Fig. 4.7b) are in qualitative agreement for both antenna diameters. By comparing the simulations with the experiments, we can estimate a minimum of 35 ± 5 nm for the z-distance observed between the bead and the antennas in the experiments. This offset is due to the distance imposed by the shear-force feedback control of the tapered fibre, as well as to the grafting process of the fluorescent bead.

Numerical simulations do not take into account the spatial distribution of the fluorescent emitters over the dimensions of the fluorescent bead. For this reason, the amplitude of decay rate variations is larger in the simulations than in the experiments. Moreover, while the intrinsic quantum yield of the emitters is set to one in the simulations, a smaller intrinsic quantum yield would explain the lower contrast of the decay rate variations observed in the experiments, as explained in Sect. 1.2.3. However, we expect this effect to be of little importance, since the quantum yield of the emitters inside the beads is supposed to be close to unity according to the provider (ThermoFisher Scientific). Aside

from this amplitude mismatch, numerical results do confirm the experimental observations, including the opposite behaviour of the decay rate variations observed in the vicinity of the on-resonance and the off-resonance antennas. This highlights the possibility of tuning the phase of the polarisability of dielectric antennas to provoke constructive or destructive interferences at the position of the emitter, and thus increase or decrease its decay rate.

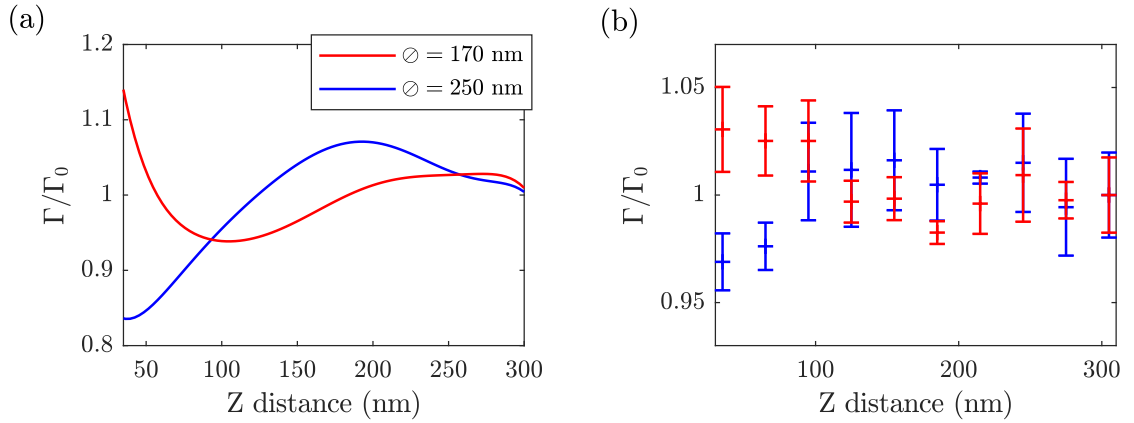

Figure 4.7 – *(a) Numerical and (b) experimental study of the decay rate enhancement versus the z-distance between the fluorescent bead and the 170-nm-diameter (red data points and solid line) or 250-nm-diameter (blue data points and solid line) silicon antennas. Error bars correspond to a statistical significance of $\pm 2\sigma$.*

Measurements in the sample plane We now investigate the evolution of the fluorescence decay rate as a function of the bead position in the sample plane with respect to the on-resonance antenna. Significant spatial variations of the decay rate can be observed for both the experimental map (Fig. 4.8a) and the simulated map (Fig. 4.8c). The decay rate is indeed enhanced for $x = 0$ nm and inhibited for $x = 200$ nm, with a typical size of the order of 100 nm for these regions. The resolution is here limited by the size of the fluorescent bead as well as by the distance between the antenna and the bead. As previously discussed, the amplitude of decay rate variations is larger in the simulations than in the experiments due to the spatial extent of the fluorescent bead. By comparing the simulations with the experiments, we can estimate a z-distance between the bead and the sample of 35 nm.

During this acquisition, we suspect a mechanical contact between the tip and the antenna in the middle of the scan, resulting in a modification of the position of the bead on the tip. This would explain the lower contrast observed in the lower half part of the experimental map. For this reason, we only use the upper half part of the map to perform a radial average of the decay rate. We thus obtain a line scan (Fig. 4.8b) that we can compare to the results of numerical simulations performed for x- and z-oriented dipoles (Fig. 4.8d). These simulations show that the maximum decay rate enhancement is of 1.6 for a vertical dipole while it is of 0.85 for a horizontal dipole. The orientation-averaged enhancement correctly explains the 15% increase in the decay rate of the bead experimentally observed when the bead is above the centre of the antenna. Once again, these results demonstrate that silicon antennas can modify the LDOS in their vicinity: either an enhancement or an inhibition of the decay rate can be achieved using the same antenna, depending on the radial position of the emitter relative to the antenna.

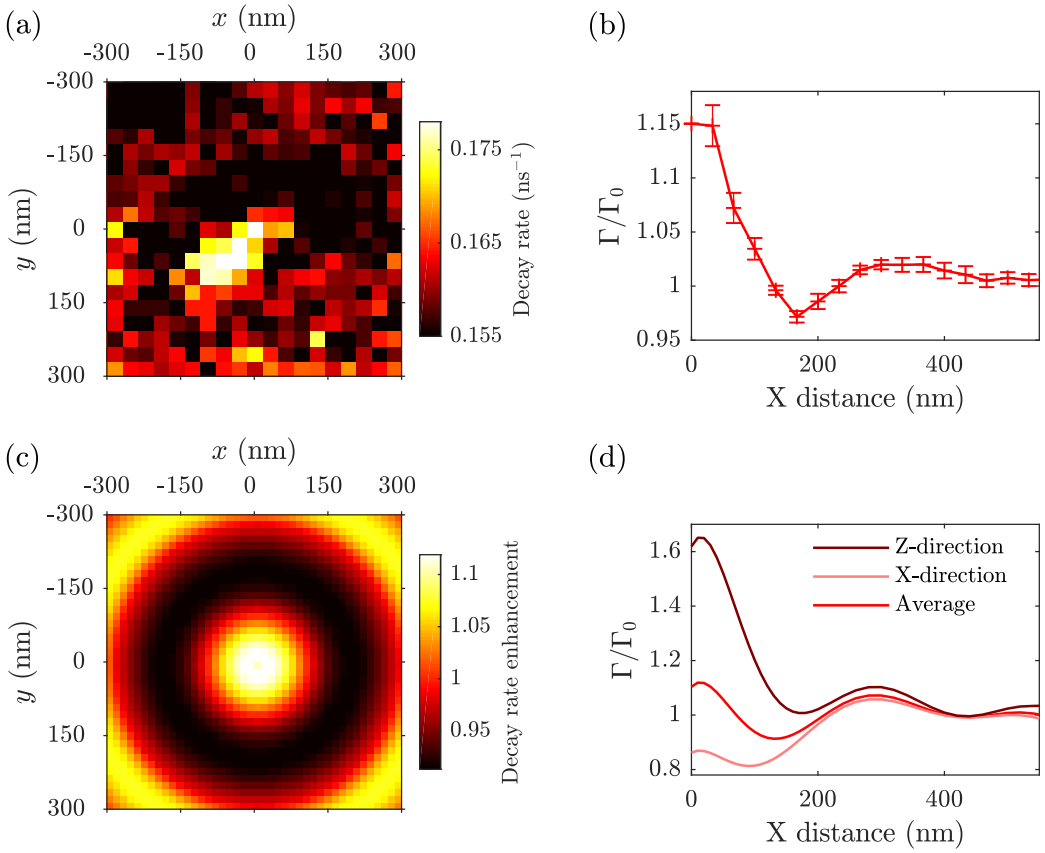

Figure 4.8 – *(a) Experimental study of the decay rate in the sample plane for the 170-nm-diameter antenna. (b) Decay rate enhancement versus the x-distance to the centre of the antenna, determined from the upper half part of the experimental map. Error bars correspond to a statistical significance of $\pm 2\sigma$. (c) Numerical study of the decay rate enhancement in the sample plane for an axial distance of z=35 nm between the bead and the sample. (d) Decay rate enhancement calculated for a dipole moment oriented in the z-direction (dark red curve) and the x-direction (light red curve). The red curve is the decay rate enhancement averaged over all the possible orientations of the dipole moment.*

4.4.3 Observation of directional emission

A silicon antenna influences not only the fluorescence decay rate of an emitter located in its near field, but also the angular radiation pattern, the radiative quantum yield and the spatial distribution of the excitation field. All these properties together determine the number of photons collected by the objective and measured by the detector.

Experimental results We present here the map of the fluorescence intensity collected from the bead in the sample plane for both the on-resonance (Fig. 4.9a) and the off-resonance (Fig. 4.9b) silicon antennas. On these maps, two different spatial distributions can clearly be identified. Interestingly, the collected fluorescence intensity increases by 12% when the bead is above the on-resonance antenna with respect to the intensity measured without the antenna. In contrast, the fluorescence intensity is reduced by 40% when the bead is on top of the off-resonance antenna. Using numerical results, we can estimate an axial separation of 120 nm between the bead and the sample plane for both experiments.

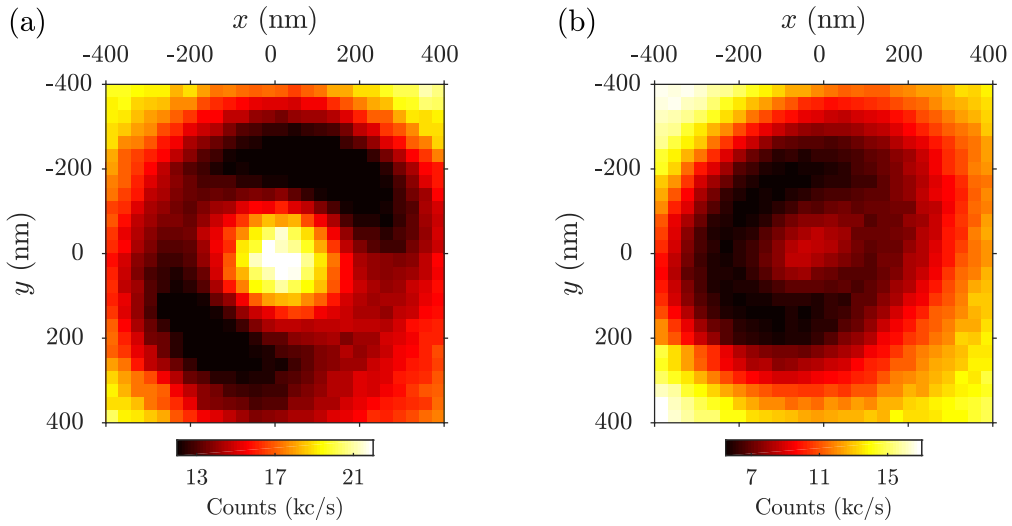

Figure 4.9 – *Maps of the fluorescence intensity measured from the bead in the vicinity of (a) the 170-nm-diameter and (b) the 250-nm-diameter antennas. The centres of the maps correspond to the bead centred on the dielectric antennas. The axial distance is approximately z=120 nm.*

In order to understand these results, we need to separately determine the influence of the antennas over the angular radiation pattern, the radiative quantum yield of the emitters and the excitation field. This can be done with FDTD simulations, by modelling the excitation field by plane waves and the fluorescent emitters by continuous dipole sources. In this model, the power transferred from the emitter to the field is directly related to its decay rate, as previously shown in Sect. 1.2. In contrast, experiments are performed under pulsed excitation. In this case, if the electromagnetic decay rate becomes faster than the internal lossy transition rate, a decay rate enhancement can induce an increase in fluorescence intensity. We observe from both experimental and numerical results that spatial variations of the decay rate are negligible for a z-distance between the antenna and the bead of 120 nm. Hence, decay rate variations have no effects on the number of photons collected from the bead, and we can directly compare the intensity variations observed in experiments to numerical results.

Excitation The modification of the excitation field at the position of the emitter due to the presence of the antennas is estimated by impinging a plane wave at $\lambda_0 = 560$ nm on the sample under normal incidence. More precisely, we calculate the *excitation enhancement* defined as the ratio of the intensities at the position of the emitter with and without the antenna. Spatial variations of the excitation intensity can be identified for both antennas (Fig. 4.10a), with two maxima for $x = 0$ nm and $x = 400$ nm and a minimum for $x = 150$ nm. For $x = 0$ nm, the on-resonance antenna notably enhances the excitation intensity by a factor of 1.2.

Collection The modification of the number of photons collected from the emitter is determined by evaluating the Poynting vector far from the antennas. We calculate the projection of the Poynting vector onto the normal to the surface of the microscope objective, and we integrate it over the solid angle limited by the numerical aperture of the

microscope objective. We then define the *collection enhancement* defined as the ratio of the intensities collected with and without the antenna. Figure 4.10b shows the evolution of the collection enhancement as a function of the x-distance for both antennas. We can see that the presence of the on-resonance antenna increases the collection by a factor of 1.4, while the collection efficiency is reduced for the off-resonance antenna.

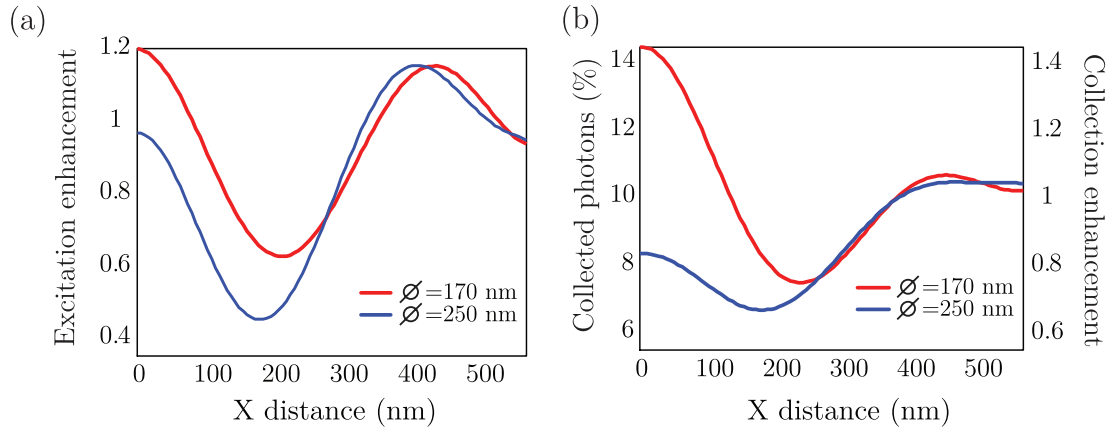

Figure 4.10 – *Numerical study of (a) the excitation enhancement and (b) the collection enhancement versus the x-distance for both silicon antenna and for an axial distance of z=120 nm.*

These variations can be explained by two separate effects. Firstly, ohmic losses in the antennas can decrease the number of photons emitted by the fluorescent bead in the far field. Secondly, the directional properties of the antennas can either increase or decrease the number of photons emitted towards the objective. To estimate the contribution of non-radiative decay channels, we define the radiative decay rate Γ_R as the rate of photons emitted in the far field and the non-radiative decay rate Γ_{NR} as the rate of photons absorbed by the surrounding structures. Then, the *radiative quantum yield* reads as follows:

$$\eta = \frac{\Gamma_R}{\Gamma_R + \Gamma_{NR} + \Gamma_{losses}} , \tag{4.1}$$

where Γ_{losses} is the decay rate due to intrinsic losses as defined in Sect. 1.2.3. In general, we assume that Γ_{losses} does not depend on the environment, as opposed to the non-radiative decay rate Γ_{NR}. In the simulations, intrinsic losses are neglected, as previously discussed. Since the imaginary part of the relative permittivity of silicon is small, we expect the radiative quantum yield to be close to unity for any position of the emitter with respect to the nanoantenna. We numerically estimate that the radiative quantum yield is minimum when the bead is straight above the antennas, with a value of the order of 0.9. We can therefore conclude that the modification of the number of photons collected from the emitter is mainly due to the directional properties of the antennas.

Numerical results By taking into account all these effects, numerical simulations allow us to determine the spatial dependence of the intensity experimentally collected from the fluorescent bead. In order to compare experimental and numerical results, we estimate the collected intensity for both the on-resonance (Fig. 4.11a) and off-resonance (Fig. 4.11b) antennas, assuming an axial separation between the fluorescent bead and the antenna of 120 nm.

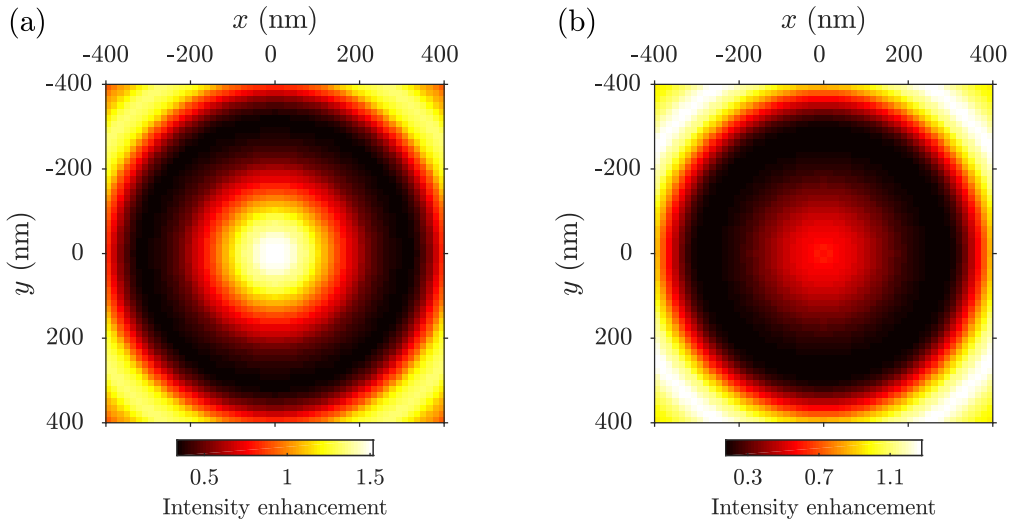

Figure 4.11 – *Numerical study of the fluorescence intensity measured from a bead in the vicinity of (a) the 170-nm-diameter and (b) the 250-nm-diameter antennas and for an axial distance between the bead and the sample of z=120 nm.*

The good agreement observed between the numerical results and the experimental maps validates the analysis. In a nutshell, for $z = 120$ nm, the decay rate is not affected by the presence of the antennas, as opposed to the excitation field and to the radiation pattern which both depend on the diameter of the antenna. The specific intensity distributions measured from the bead are explained by both the directional properties of the antennas and the reduction of the excitation intensity around the antennas for $x \sim 200$ nm. Furthermore, the radiative quantum yield stays close to unity due to the weak ohmic losses generated by dielectric antennas.

4.5 Conclusion

In this chapter, we showed that subwavelength silicon antennas can modify the photon emission dynamics of fluorescent molecules. We started by presenting several properties of cylindrical silicon antennas. Using dark-field measurements, we demonstrated that these antennas can support various Mie resonances. More precisely, we identified electric and magnetic dipole modes as well as quadrupole modes for the largest antennas. Then, we presented the scanning-probe technique used to characterise the near-field interaction between the antennas and a fluorescent bead, chosen as a near-field source to excite the Mie modes supported by the antennas. Using this technique, we performed three-dimensional measurements on two different antennas to demonstrate the ability of silicon antennas to inhibit or enhance the spontaneous emission rate. We experimentally demonstrated an enhancement of the decay rate of a fluorescent bead located above a 170-nm-diameter antenna (Fig. 4.8a). Using a numerical approach, we also demonstrated that the variations observed in the intensity collected from the bead were due to both the directional properties of the antennas and the spatial dependence of the excitation intensity around the antennas. This highlights the ability of dielectric antennas to control the directivity of fluorescence emission.

The variations of LDOS observed in the experiments were weak in comparison to the variations that can be observed by using plasmonic antennas [91, 92]. Different experimental approaches could be used to investigate the near-field interaction between emitters and dielectric antennas on shorter scales, providing us with the opportunity to study structures presenting a higher field confinement such as dielectric dimers or hollow nanocylinders. As an example, a DNA linker could be used to control the distance between a fluorescent molecule and a dielectric antenna with nanometre precision. This strategy was introduced by Acuna *et al.* to enhance the fluorescence intensity of single molecules [93]. A similar technique was also applied by Bidault *et al.* to efficiently couple single molecules to gold nanoparticle dimers [94], resulting in fluorescent nanostructures with radiative lifetimes below 100 ps. Interestingly, the coupling between the field generated the emitter and the Mie modes supported by dielectric antennas could be further improved by placing the emitters inside hollow nanocylinders [95]. A better control of the coupling between the field generated by the emitter and the various electric and magnetic Mie modes supported by the antennas could notably allow an observation of highly directive radiation patterns presenting zero backscattering [74, 75].

Stochastic approaches also provide interesting alternatives to scanning-probe techniques for the study of the near-field interaction between a fluorescent emitters and a given nanostructure. In the following chapter, we will present a stochastic technique that allows the determination of the excited-state lifetime of single molecules and their positions with a very good precision. We will notably demonstrate the performances of the technique by presenting a study of the near-field interaction between single molecules and a silver nanowire.

CHAPTER 5

Single-molecule super-resolution microscopy for lifetime imaging

In this chapter, we introduce an experimental technique based on photo-activated localisation microscopy. This technique allows the simultaneous determination of the fluorescence decay rate of single molecules and their respective position with a localisation precision of the order of 10 nm. First of all, we present the principle of the experiment and the context of this work. Then, we detail the experimental setup developed for the implementation of the technique, based on the stochastic photo-activation of single molecules and the simultaneous detection of fluorescence photons by a camera and a single-photon avalanche diode. We carefully describe the method used to analyse the large amount of data acquired during an experiment as well as the strategy adopted to associate the position of the molecules with their decay rate. Finally, we present a decay rate map with a strongly sub-wavelength resolution and we compare the observed variations of decay rate induced by a silver nanowire to theoretically expected values that are calculated using finite-difference time-domain simulations.

5.1 Introduction

The resolution limit of a microscope characterises the minimal distance in-between two point sources that can be resolved using a far-field microscope. It is classically given by the distance between the principal maximum and the first zero of the Airy function. Using this criterion – referred to as the *Rayleigh criterion* – the resolution limit is of the order of $\lambda_0/2$ with λ_0 the wavelength of the considered light.

The Rayleigh criterion is based on the assumption that only propagating fields are captured by the imaging system. This assumption restricts the spectrum of spatial frequencies that can be detected, as detailed in Sect. 1.4.1. In 1928, Synge proposed to take advantage of the evanescent part of the field to improve the resolution limit of a microscope [19]. He notably suggested that a small probe located in the near field of a sample could be used to scatter part of the evanescent field. One could thus obtain a super-resolved image of

the sample by measuring the intensity of the scattered field for different positions of the scatterer in the sample plane. The first experimental realisation of this method at optical frequencies was performed by Pohl, Denk and Lanz in 1984 [96]. In this experiment, the authors used a narrow aperture that they could move over their sample for near-field excitation. Since then, several adaptations of this method have been developed; the near-field scanning optical microscope presented in Chapter 4 is one of them.

Even though high spatial frequencies are not available in the far field, it is possible to overpass the Rayleigh criterion by using a far-field microscope. For instance, a method was introduced in 1994 by Hell and Wichmann in order to image a sample containing a large number of fluorescent emitters [97]. This technique, called *stimulated emission depletion microscopy* (STED microscopy), requires the excitation of several emitters from the far field followed by the depletion of the excited state in the outer region of the excitation spot using stimulated emission. The resolution is then increased by the non-linear inhibition of fluorescence in the outer region of the excitation spot. By scanning the sample, such a microscope can be used to obtain a super-resolved image of the sample. However, besides a complexity of implementation, one of the main drawbacks of STED microscopy is the high laser power required to obtain a good resolution.

Super-resolved images can also be obtained with a far-field microscope assuming that the signal originates from a small emitter such as a fluorescent molecule. The first optical detection of a single molecule inside a solid crystal was performed in 1989 by Moerner and Kador using absorption spectroscopy [98]. One year later, Orrit and Bernard detected fluorescence emission from a single pentacene molecule [99]. These works inspired various experiments based on the fluorescence of single molecules, notably in the field of biology [100]. Thanks to the development of photo-activatable fluorescent proteins by Patterson and Lippincott-Schwartz [101], two similar super-resolution techniques referred to as *photo-activated localisation microscopy* (PALM) were independently introduced in 2006 by Betzig *et al.* [3] and by Hess, Girirajan and Mason [102]. Meanwhile, Rust, Bates and Zhuang presented a similar technique called *stochastic optical reconstruction microscopy* (STORM) and based on the blinking of fluorescent molecules [103]. In such experiments, only one molecule can emit at a single time in a diffraction-limited region. The detected molecule is then precisely localised by fitting the expected point spread function (PSF) to the intensity distribution measured in the image plane of the microscope. This procedure allows a strongly sub-wavelength resolution, which is only limited by the standard deviation of the probability density function followed by the position estimates and by the density of detected molecules. PALM, STORM and STED microscopy encountered a great success, and these techniques are nowadays widely employed to image biological samples on the nanometre scale [104].

While PALM, STORM and STED microscopy are based on the study of the intensity emitted by fluorescent emitters, the simultaneous determination of their fluorescence lifetime would open new imaging possibilities. The first experimental determination of the fluorescence lifetime on a point-by-point basis was performed in 1993 by Gadella, Jovin and Clegg [105], introducing a technique called *fluorescence lifetime imaging microscopy* (FLIM). Since then, the contrast induced by lifetime variations was used to map different parameters on biological samples [106], such as the viscosity, the temperature, the potential of hydrogen (pH) or the interaction between two emitters due to Förster resonance energy transfer (FRET). Nevertheless, as FLIM-based techniques rely on confocal microscopy, they are usually diffraction-limited.

Besides possible biological applications, a precise localisation of fluorescent emitters together with the determination of their decay rate would allow one to study the local density of states (LDOS) on the nanometre scale. However, this is a difficult task to achieve since it would theoretically require an array of fast detectors, with a temporal resolution better than the nanosecond and with an image size on the sample plane around 100 nm for each detector. Several techniques based on intensity measurements were recently developed to overcome this difficulty. In 2016, Johlin *et al.* notably used a PALM/STORM-based technique to probe the electromagnetic interaction between dye molecules and a semiconductor nanowire [107]. The authors specifically studied the variations of the number of photons collected from the molecules located near the nanowire. Using numerical simulations, they deconvoluted the influence of emission rate enhancement, directivity modification and guided mode excitation in order to explain the observed intensity variations. Recently, Mack *et al.* studied the resonant behaviour of a nanoantenna using fluorescent molecules with a large Stokes shift [108]. In doing so, they spectrally decoupled the emission field of the molecules and the modes supported by the plasmonic system, in order to study the resonance of the antenna at the frequency of the excitation field.

However, methods based on variations of the collected fluorescence intensity generally require the use of numerical simulations to estimate the fluorescence decay rate. In 2008, Auksorius *et al.* proposed an original technique based on a direct measurement of decay histograms [109]: by associating FLIM with STED microscopy, the authors managed to probe the decay rate of fluorescent emitters on a sub-wavelength scale. In 2016, Guo, Verschuuren and Koenderink presented another technique based on the dispersion of fluorescent nanobeads at a low concentration over a lattice of identical plasmonic nanoantennas [110]. They determined the decay rate of each bead by scanning the sample and, by exploiting the periodicity of the lattice, they managed to reconstruct a map of LDOS variations in the near-field of a single nanoantenna, with a resolution determined by the diameter of the beads (40 nm). However, this method requires identical nanostructures to perform the image reconstruction, and it cannot be used to characterise an unknown sample.

Principle of the experiment In this chapter, we introduce an original experimental technique to localise fluorescent molecules and to probe their decay rate with a localisation precision of the order of 10 nm. The method relies on the stochastic photo-activation and detection of single molecules, as in PALM/STORM-based techniques. More precisely, we use a pulsed laser to excite the molecules and a 50:50 beamsplitter to split the fluorescence intensity towards an electron-multiplying charge-coupled device (EM-CCD) and a single-photon avalanche diode (SPAD). Typically, no more than one molecule is active at a single time on the area conjugated to the SPAD. We can thus estimate both the position and the decay rate of each individual molecule by respectively fitting a two-dimensional Gaussian function and a decreasing exponential function to the measured data, as illustrated in Fig. 5.1. Based on the correlation in time between the events detected by the camera and the SPAD, we perform the association between position and decay rate for more than 3,000 photo-activated molecules detected in a 10-hour-long experiment. As a result, we reconstruct a decay-rate map that shows strong variations due to the presence of a silver nanowire on the sample. In addition, we compare these results to theoretically expected values calculated using finite-difference time-domain (FDTD) simulations. This work will be published in the near future, and the technique used to determine the position and the decay rate of photo-activated single molecules is currently under patent application.

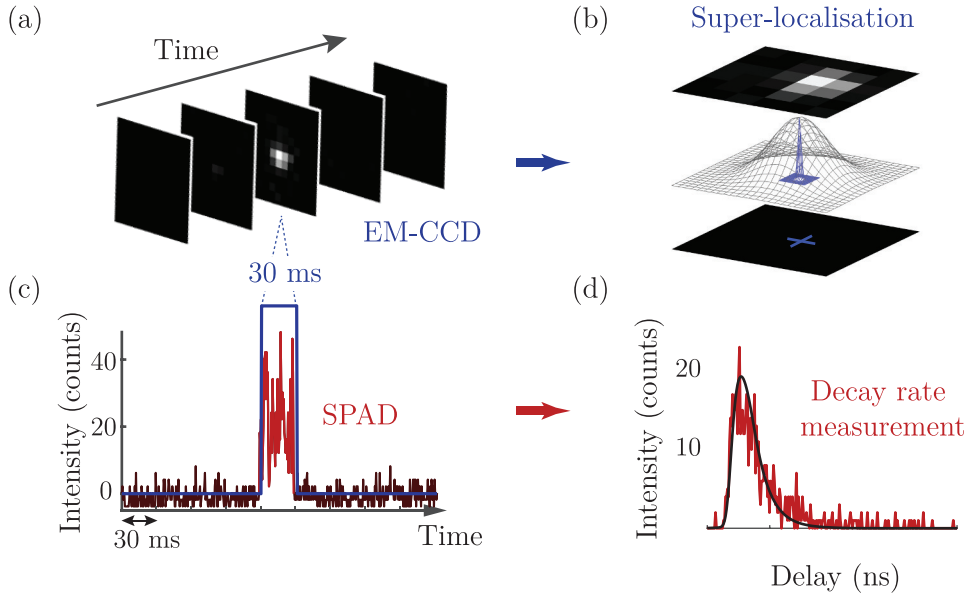

Figure 5.1 – *The scheme of the experiment. (a) An EM-CCD camera acquires 31 frames per second, with an exposure time of 30 ms per frame. A single fluorescent molecule is detected on the third frame of the sequence shown here. (b) The position of the molecule is estimated by fitting a two-dimensional Gaussian function to the measured PSF, with a localisation precision of the order of 10 nm. (c) At the same time, a SPAD detects a fluorescence burst from this molecule. (d) These photons are used to construct a decay histogram. A decreasing mono-exponential function is then fitted to this histogram in order to estimate the fluorescence decay rate of the molecule.*

5.2 Sample preparation and experimental setup

This section is dedicated to the description of the experimental setup, including the sample preparation, the optical setup and the implementation of the drift-correction system used to perform experiments for several hours.

5.2.1 Sample preparation

In order to perform a proof-of-principle experiment, we study the emission of single fluorescent molecules (Alexa Fluor 647, ThermoFisher Scientific) in the near field of chemically grown silver nanowires (Sigma Aldrich) characterised by a diameter of approximately 115 nm. These nanostructures are interesting for the elaboration of the technique, as they induce nanometre-scale variations of the fluorescence decay rate in their vicinity. Moreover, silver nanowires weakly radiate to the far field, allowing a correct localisation of near-field coupled emitters. As the sample needs to be immersed in an oxygen-reducing buffer to induce the photo-activation process of the fluorescent molecules [111], we use biotin-streptavidin linkers to bind the fluorescent molecules to the microscope coverslip, as represented in Fig. 5.2.

To prepare the sample, we spin-coat a dilute solution of silver nanowires in isopropyl alcohol on a glass coverslip for 30 s. A microfluidic chamber is then prepared as follows: we cover the sample with a ring made of parafilm, we place two micro-pipettes on opposite

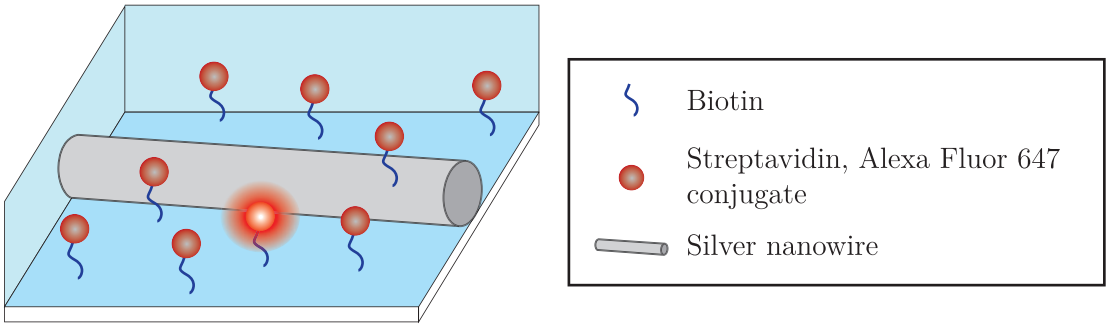

Figure 5.2 – *Scheme of the sample. The volume coloured in blue represents the buffer solution.*

sides of the parafilm ring and we cover them with another glass coverslip before heating the sample up to 70°C in order to melt the parafilm. We let the microfluidic chamber cool down for a few minutes before using the micro-pipettes to inject biotin diluted in a phosphate-buffered saline (PBS) solution at a concentration of 1 g/L. We leave this solution incubate for 2 hours. Then, we inject streptavidin-conjugated fluorescent molecules (Alexa 647) diluted in a PBS solution at a concentration of 0.005 g/L, and we leave this new solution incubate for 2 hours. We add a PBS solution containing a few polystyrene fluorescent beads 100 nm in diameter (Red FluoSpheres, ThermoFisher Scientific) which we use as fiducial markers, and we then fill the chamber with an oxygen-reducing buffer. This buffer is prepared according to the protocol described in Ref. [112]: we use a PBS solution in which we dilute dextrose (100 mg/mL), cysteamine (3.86 mg/mL), glucose oxidase (0.5 mg/mL) and catalase (1.18 µL of an aqueous solution concentrated at 20-50 mg/mL).

5.2.2 Optical setup

We now present the optical setup developed for the experiment. While the excitation path is a typical wild-field excitation scheme of PALM/STORM experiments, the detection path combines both wide-field imaging and time-resolved single-photon detection. Figure 5.3 shows a scheme of the complete optical setup.

Excitation As previously introduced, photo-activated localisation microscopy relies on the stochastic photo-activation of single fluorescent emitters and the collection of their fluorescence until photobleaching. To this end, we use two different lasers:

- To excite the photo-activatable molecules (Alexa Fluor 647), we use a pulsed laser diode emitting at $\lambda_0 = 640$ nm (LDH Series P-C-640B, PicoQuant) and at a repetition rate of 80 MHz. The intensity incident on the sample averaged over a repetition period (12.5 ns) is 10 µW/µm^2. As each pulse is characterised by a full width at half maximum (FWHM) of 240 ps, the effective intensity incident on the sample is approximately 500 µW/µm^2. The axis of the nanowire is usually set perpendicular to the polarisation of the laser, in order to minimise the backscattering of the laser light by the nanowire.
- To photo-activate the fluorescent molecules, we use a laser diode emitting at $\lambda_0 =$ 405 nm (LDH Series P-C-640B, Picoquant). During an experiment, the density of activatable molecule decreases in time since several molecules are photobleached

by the excitation laser. To compensate for this effect, we progressively turn on the photo-activation laser during the acquisition, with an average intensity on the sample up to 50 nW/µm^2.

In addition, a third laser is required for the excitation of fiducial markers (fluorescent beads) that are used for the implementation of the real-time drift correction system (see Sect. 5.3). This laser is a supercontinuum laser (Fianium SC450) filtered at $\lambda_0 = 568$ nm by an excitation filter (LL01-568, Semrock). We always choose a bead far from the centre of the area under study. In this way, the excitation laser of the bead does not perturb the measurement because it is not aligned with the excitation laser of the photo-activatable molecules.

These three lasers illuminate the sample through an oil immersion objective (UPLSAPO 100XO, Olympus) mounted on an inverted microscope and characterised by a ×100 magnification and 1.4 numerical aperture. Before the objective, a lens characterised by a focal length of 300 mm is used to obtain a wide-field illumination, over an area of approximately 200 µm^2.

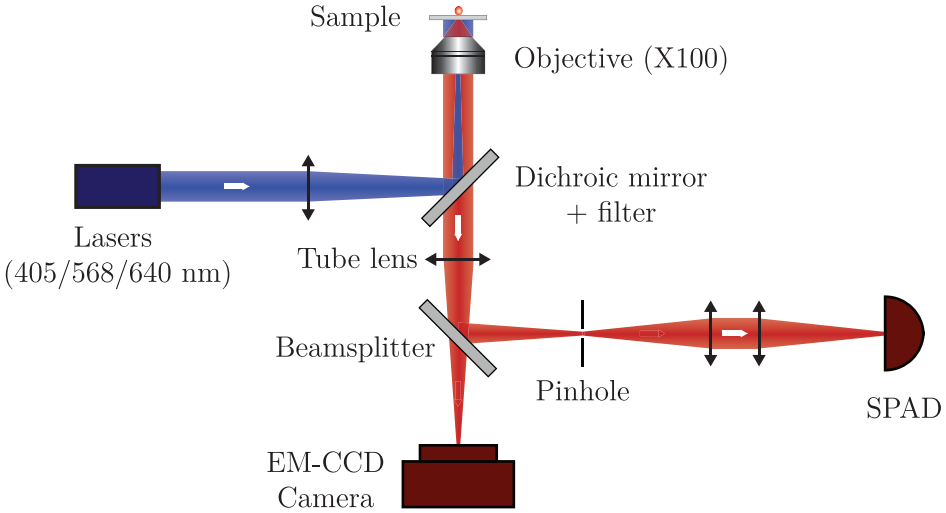

Figure 5.3 – *Optical setup for simultaneous wide-field imaging and time-resolved single-photon detection.*

Detection Fluorescence from the sample is collected by the objective and filtered by a dichroic mirror (ZT405/488/561/647rpc, Chroma) as well as two different long-pass filters (ZET405/488/561/640m, Chroma and FF01-446/523/600/677, Semrock). Then, a 50:50 beamsplitter splits the signal towards two paths:

- On the first path, fluorescence photons are directed towards an EM-CCD camera (iXon 897, Andor) to form an image of the sample with a field of view of tens of micrometers on the sample plane. We record wide-field images with an exposure time of 30 ms; these images are then used to localise the molecules with a localisation precision of the order of 10 nm.
- On the second path, a SPAD (PDM-R, Micro Photon Devices [56]) is connected to a time-correlated single-photon counting (TCSPC) system (HydraHarp400, Picoquant). This setup allows the determination of decay rates up to 10 ns^{-1}, corresponding to fluorescence lifetimes of 100 ps. On this path, we use a 50 µm confocal

pinhole to conjugate the SPAD to a small area on the sample plane (∼800 nm in diameter).

By carefully controlling the activation laser power, we ensure that no more than one molecule is typically active at a single time on the area conjugated to the SPAD. This condition allows us to correctly associate the position of the molecules with their decay rate, as we will see in Sect. 5.4. Consequently, the acquisition time of an experiment is usually of several hours, so that several thousands of fluorescent molecules can be detected.

5.2.3 Data acquisition

Before starting data acquisition, we select an area on the sample in which a silver nanowire can be identified by basic transmission imaging. Then, we place the area of interest in the middle of the field of view of the camera by using a piezoelectric stage (PXY 200SG, Piezosystem Jena) controlling the in-plane position of the sample. This area is conjugated to the SPAD, as illustrated in Fig. 5.4. In order to perform real-time drift correction in the sample plane and along the axial direction, we also select an area of the sample in which a fluorescent bead can be identified. The fluorescent molecules surrounding the bead are photobleached using the laser diode emitting at $\lambda_0 = 640$ nm before starting the acquisition: in this way, we improve the signal-to-noise ratio for the localisation of the bead.

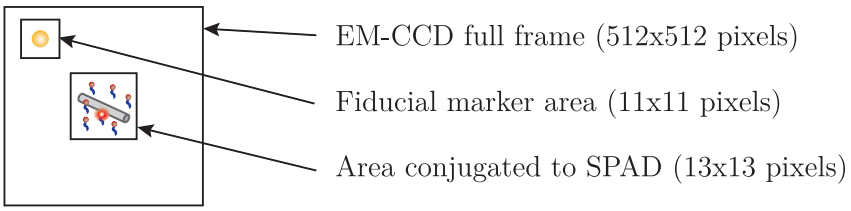

Figure 5.4 – *Scheme of the EM-CCD camera field of view.*

During an acquisition, we record the 13×13 pixels area of the EM-CCD camera conjugated to the area of interest on the sample as well as the 11×11 pixels area of the EM-CCD camera corresponding to the fiducial marker area. The arrival time of each photon detected by the SPAD is also recorded in real time. Using this strategy, we perform several experiments on identical samples and with an acquisition time ranging from 1 to 10 hours. In the following sections, we will analyse the results of a 10-hour-long acquisition presenting the highest density of detected molecules.

5.3 Drift correction

We now describe the implementation of the drift-correction system. In this section, the coordinates in the sample plane are noted x and y, and the coordinate along the axial direction is noted z.

5.3.1 Correction in the sample plane

To determine and correct the drift in the sample plane, we estimate the position of the fiducial marker from the wide-field images acquired by the camera and we use a feedback loop to maintain the marker at a fixed position. To this end, we identify a small area (11×11 pixels) around the marker, as previously mentioned. Every 5 s, we obtain an image with a high signal-to-noise ratio by summing the frames recorded during this time interval (∼170 frames). A two-dimensional Gaussian function is then fitted to the intensity measured in the image plane. This Gaussian function is defined by

$$f(x,y) = A \exp\left(-\frac{(x-x_0)^2 + (y-y_0)^2}{2\sigma^2}\right) + B \,, \tag{5.1}$$

where B is the level of background noise, A is the amplitude of fluorescence signal, x_0 and y_0 are the coordinates of the marker and σ is the standard deviation of the Gaussian function. The drift is calculated as the difference between the estimated coordinates and the setpoint position, defined as the centre of the 11×11 pixels area. A feedback signal is applied on the piezoelectric stage controlling the in-plane position of the sample in order to compensate for the drift. We operate the piezoelectric positioning system in open-loop mode to eliminate additional noise introduced by the sensor and the driver stabilisation system.

In order to estimate the performances of the drift-correction system, we analyse the images acquired during the 10-hour-long experiment previously mentioned. The estimation of the position of the fiducial marker associated with each frame is performed by using ThunderSTORM, a plug-in for ImageJ developped by Ovesný *et al.* [113]. In addition, we perform a sliding average of the estimated positions in the time intervals in-between the steps of the piezoelectric positioners and over a maximum of 61 frames, corresponding to a time interval of 2 s and a number of collected fluorescence photons of the order of 15,000. This procedure allows to obtain a good estimate of the error, defined as the difference between the estimated position of the marker and the setpoint value. The distributions of the estimated error for the x-coordinate and the y-coordinates are respectively shown in Figs. 5.5a and 5.5b.

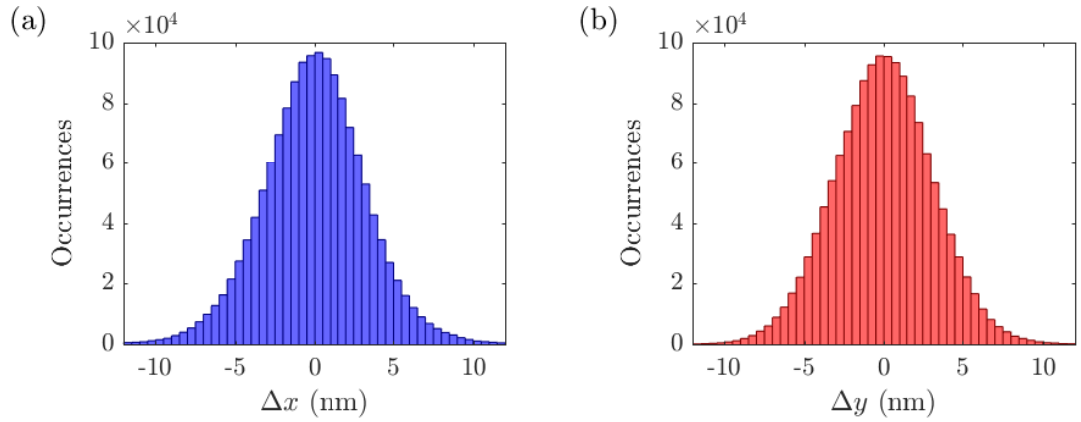

Figure 5.5 – *Distribution of the estimated error of the marker position for the 10-hour-long acquisition. (a) Error in the x-direction and (b) error in the y-direction.*

The standard deviations of these distributions are respectively 3.3 and 3.1 nm, attesting

that the drift correction system can operate for 10 hours with a very good precision. The estimated error is comparable to the limit of localisation precision, of the order of 1.5 nm for 15,000 fluorescence photons collected by the camera[1]. Therefore, the error is negligible in comparison to the localisation precision of photo-activated molecules, which is of the order of 10 nm.

5.3.2 Defocus correction

In order to estimate the drift of the sample in the z-direction with respect to the focal plane, we analyse images of the fiducial marker accumulated over several seconds. Then, the axial position of the objective with respect to the sample is corrected in real time with a piezoelectric positioning system (MIPOS 20SG, Piezosystem Jena) located between the objective and the microscope turret. The defocus-correction system is based on a real-time maximisation of the power spectral density of the measured images. Before the acquisition, we perform a scan in the z-direction in order to determine the spatial frequencies corresponding to the typical extent of the PSF when the bead is focused. During the acquisition, we calculate the Fourier transform of each image and we apply a mask to select these spatial frequencies. The power spectral density γ corresponding to these frequencies must then be compared to a setpoint value, that we define to be the maximum value of γ obtained from the 20 previous measurements. With this approach, the progressive photobleaching of the fluorescent molecules inside the bead is not an issue, because the setpoint value can decrease accordingly.

However, this strategy does not allow a direct estimation of the axial position of the objective focal plane with respect to the sample plane. It is indeed not possible to determine the direction of the drift along the z-axis. Therefore, the defocus-correction system starts the feedback in an arbitrary direction. This direction is then maintained unless the power spectral density decreases for two consecutive measurements. We specifically require that the power spectral density decreases faster between the measurements performed at times t_{i-1} and t_i than between the measurements performed at times t_{i-2} and t_{i-1}, so that $\gamma_{i-2} - \gamma_{i-1} < \gamma_{i-1} - \gamma_i$. This proportional-integral correction makes the system less sensitive to noise as compared to a purely proportional correction.

Unlike for the drift correction in the sample plane, the acquisition time used to determine the axial drift can vary. If the estimated drift is large, the defocus-correction system only accumulates a few frames before the next estimation of the drift – with a minimum of 20 frames corresponding to less than 1 s. Thus, the feedback system can rapidly react to a strong defocus. In contrast, the acquisition time becomes much larger if the estimated drift is small – with a maximum of 500 frames corresponding to ∼15 s. In this case, the feedback system is slower but more precise. In order to test the performances of the feedback system, we induce 4 step-like defocuses of arbitrary direction during a 5 min acquisition. The amplitude of each defocusing step is of the order of 1 µm and the time interval in-between each step is approximately 1 min. As expected, the power spectral density strongly decreases after each defocusing step (Fig. 5.6a), a correction is accordingly applied (Fig. 5.6c) and the position of the piezoelectric stage readily compensates for that defocus (Fig. 5.6e). The feedback system typically corrects the defocus in less than 5 s once it is detected.

[1] This limit can be calculated using the Fisher information, as we will see in Chapter 6 (Sect. 6.3.5).

The performance of the feedback system is also very satisfactory for the 10-hour-long experiment. Due to progressive photo-bleaching of the fluorescent molecules inside the bead, the power spectral density decreases in time during the experiment (Fig. 5.6b), but the regulation still manages to compensate for the drift of the system by doing small steps of the order of 10 nm (Fig. 5.6d). Over the whole experiment, we observe an overall defocus of the order of 1 µm compensated in real time by the defocus-correction system (Fig. 5.6f). The strong drift detected during the first hour is likely to be due to the thermal stabilisation of the experiment.

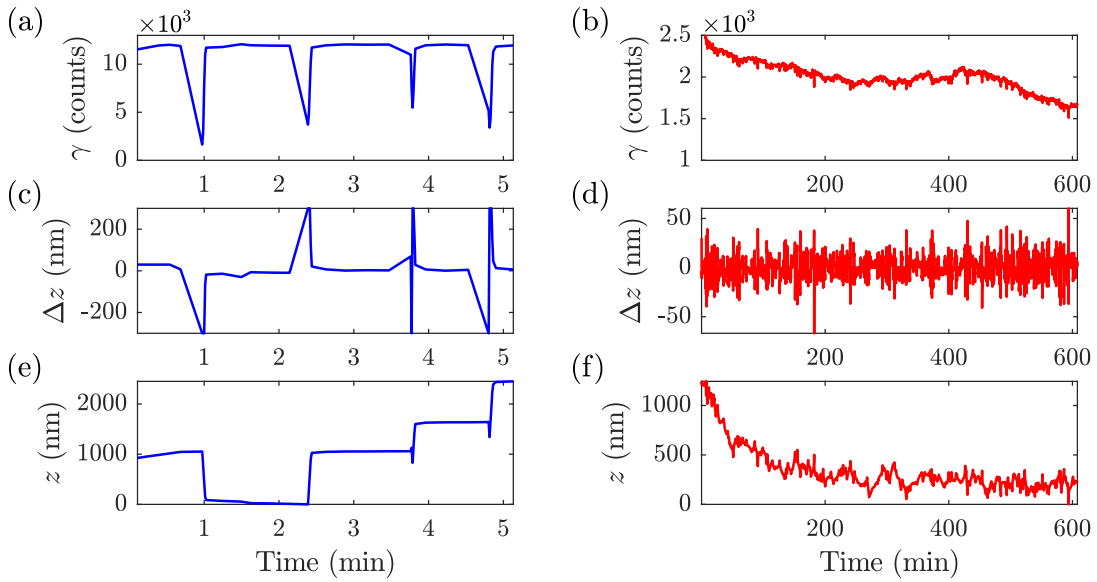

Figure 5.6 – *Performances of the defocus-correction system for intentional, strong defocuses (left) and during the 10-hour-long acquisition (right). (a) and (b): Power spectral density of the images. (c) and (d): Correction applied by the defocus-correction system. (e) and (f): Absolute z-position.*

Both the performances of the in-plane drift-correction system and the defocus-correction system are satisfactory and allow a good stability of the sample during the 10-hour-long experiment. In practice, it is possible to perform experiments with an even longer acquisition time (more than 20 hours) before a failure of the drift-correction system due to complete photobleaching of the fluorescent molecules inside the bead.

5.4 Position and decay rate association

We now describe the post-processing analysis performed on the data to associate the position of the molecules with their decay rate.

5.4.1 Position and decay rate estimations

To start with, we independently estimate the positions and the decay rates of the molecules from the data respectively measured by the EM-CCD camera and the SPAD.

Position estimations The EM-CCD camera acquires 31 frames per second with an acquisition time of 30 ms per frame. The full sequence of wide-field images saved by the camera (13×13 pixels) is imported by ImageJ and the positions of the photo-activated molecules are estimated using ThunderSTORM [113]. First of all, each frame is filtered using a wavelet filter, as proposed by Izeddin *et al.* [114]. For each frame, approximate localisation of the molecules is then performed by applying a threshold that depends on the signal-to-noise ratio of the camera data. For this acquisition, we set it to 2.7 times the standard deviation of the intensity values obtained in the filtered image. Finally, sub-pixel localisation of the molecules is performed by fitting a two-dimensional Gaussian function to the data using the weighted least squares method on a restricted domain around the molecule (7×7 pixels). As an illustration, we present here a frame in which a single molecule can be identified (Fig. 5.7a); a two-dimensional Gaussian function is fitted to the measured PSF in order to estimate the position of the molecule (Fig. 5.7b).

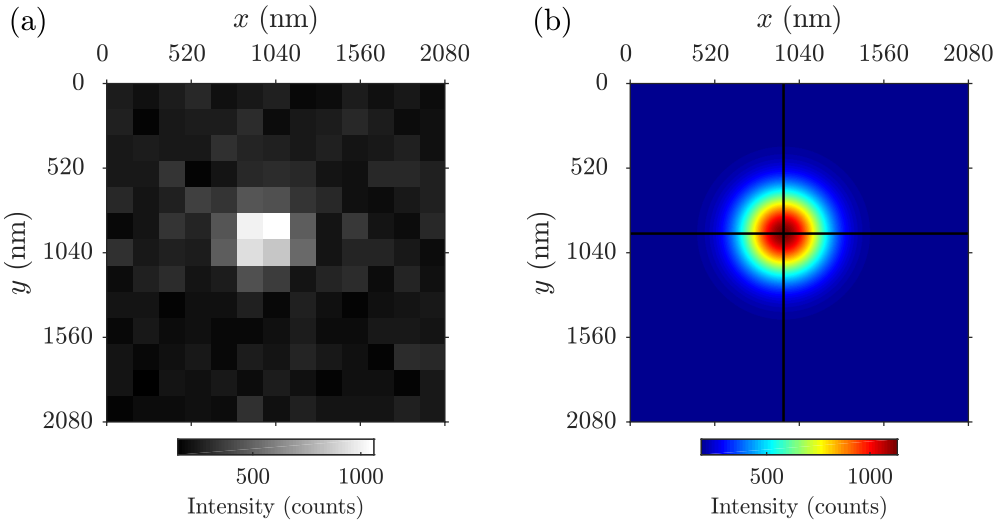

Figure 5.7 – *(a) Detection of a single molecule by the EM-CCD camera. (b) Gaussian function fitted to the measured PSF. Black lines represent the estimated coordinates of the molecule.*

As some molecules can be identified over consecutive frames, we perform a merging of the data acquired by the camera if the estimated distance between successive detections is less than 40 nm. Then, the position of the molecule is determined by using the average value of the positions estimated from the different frames. Using this strategy, we obtain approximately 24,000 different detections for the whole experiment. This number is limited by the weak activation power required to ensure that no more than one molecule is typically active at a single time on the area conjugated to the SPAD.

Decay rate estimations In addition to EM-CCD images, we also record the arrival time of each photon detected by the SPAD. To deal with the large size of the resulting file (∼15 GB), the 10-hour-long acquisition is split into several sequences of approximately 50 minutes. Then, we compute the number of detected photons as a function of time with a resolution of 500 µs. The intensity of background noise associated with this signal usually decreases during the experiment due to a decreasing number of activated molecules in the periphery of the detection area. Hence, the intensity time trace is Fourier filtered in order

to remove low frequency components associated with temporal fluctuations longer than 30 s. Then, we consider that a molecule is potentially detected for each burst surpassing a given threshold that depends on the signal-to-noise ratio of the SPAD data. For each 50-minutes-long sequence, we set it to 2.6 times the standard deviation of the filtered signal. If another burst occurs within the typical blinking time scale (20 ms), it is attributed to the same molecule. As an illustration, we present here a small part of the intensity time trace in which a burst can be identified (Fig. 5.8a). In total, we identify approximately 14,000 events over the 10-hour-long acquisition. This value is small in comparison to the number of detections obtained from camera data. Indeed, the area of the sample conjugated to the SPAD ($\sim 800 \times 800$ nm) is smaller than the area over which the localisation is performed ($\sim 1100 \times 1100$ nm).

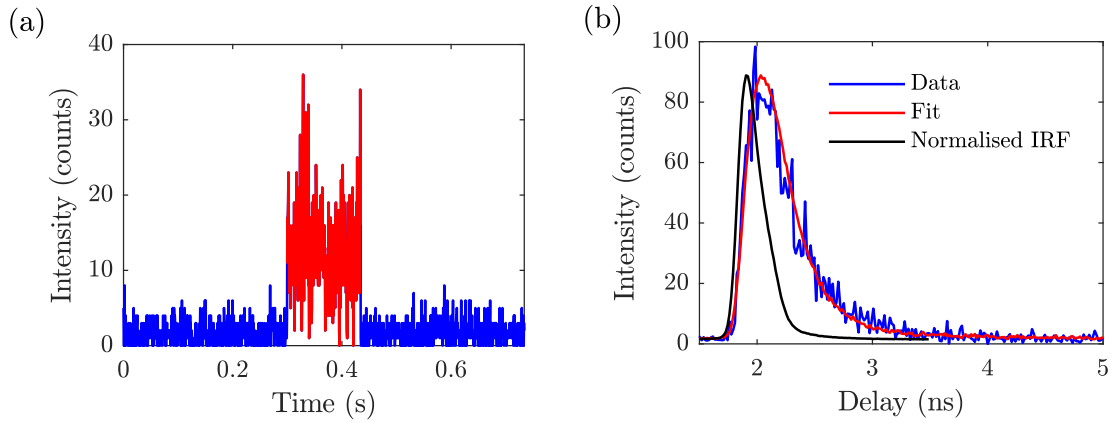

Figure 5.8 – *(a) Identification of a burst in the intensity time trace – this burst corresponds to the detection shown in Fig. 5.7a. (b) Estimation of the decay rate from the decay histogram. The estimated decay rate is here 4.7 ns^{-1}.*

For each SPAD event, we build the associated decay histogram with a resolution of 16 ps in order to estimate the decay rate (Fig. 5.8b). To do so, the contribution of background noise is estimated by using close-by time intervals in which no burst can be identified. Then, the convolution of the instrument response function (IRF) and a decreasing mono-exponential function is fitted to the decay histogram using the least-squares method. The value of the decay rate is set to 10 ns^{-1} if the fit yields a value higher than this limit. Indeed, the IRF of the setup is characterised by a FWHM of approximately 240 ps (corresponding to 4 ns^{-1}) and we consider that estimates above 10 ns^{-1} are not meaningful even after the deconvolution process. This point will be discussed in detail in Chapter 6 (Sect. 6.4.4).

5.4.2 Temporal and spatial correlations

The detections identified from camera data and the bursts identified from SPAD data are strongly time-correlated, as previously illustrated in Fig. 5.1. We now precisely characterise the spatio-temporal correlation between SPAD events and camera detections in order to associate the position of a large number of molecules with their decay rate. For simplicity, we use the subscript i when referring to a detection identified using camera data and the subscript j when referring to an event identified using SPAD data.

Temporal correlation In the beginning of the experiment, the acquisition of both camera and SPAD data is started by using an in-house software, and we can expect a time offset of several milliseconds between the two different channels. In order to precisely determine this time offset, we build two binary representations respectively associated with the SPAD events and the camera detections (1 for a SPAD event or a camera detection, 0 otherwise). We then calculate the time correlation of these binary representations with a resolution of 500 µs, as shown in Fig. 5.9 for a typical sequence of 50 minutes. The maximum of this correlation coefficient gives an accurate estimate of the time offset between the camera and the SPAD. This delay is typically around 20 ms, which is consistent with the data acquisition procedure. Note that the correlation coefficient does not reach unity but is typically between 0.3 and 0.5. Indeed, the conditions required for the detection of a molecule by the camera and by the SPAD are different. In comparison to the SPAD, the camera is characterised by a larger field of view and a larger quantum efficiency. However, its lower temporal resolution makes the identification process less efficient for molecules characterised by fast temporal fluctuations. Hence we can expect some molecules to be detected by only one of the two detectors, resulting in a value smaller than unity for the maximum of the correlation coefficient.

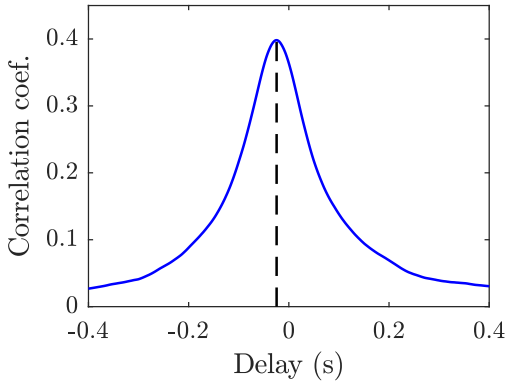

Figure 5.9 – *Correlation coefficient calculated from binary representations of the SPAD events and the camera detections. A dashed line represents the estimated time offset between the two channels.*

Once the time offset between the camera and the SPAD is estimated and compensated, we can quantify the time overlap between a camera detection and a SPAD event. To do so, we simply calculate the ratio of the time overlap Δt_{ij} to the time interval Δt_j corresponding to the SPAD event. The camera detection and the SPAD event are likely to be associated to the same molecule whenever this ratio is close to unity.

Spatial correlation In order to characterise the spatial correlation between SPAD events and camera detections, we must identify the pixels of the camera that are conjugated to the area of the sample seen by the SPAD. Hence, we measure the response of the SPAD by scanning a fluorescent bead with a diameter of 100 nm over a large area in the sample plane. Figure 5.10a shows the number of photons detected by the SPAD as a function of the bead position. The FWHM value of the measured profile is of the order of 500 nm, as expected from the diameter of the confocal pinhole (50 µm) and the magnification of the optical system (×100). We can model this response by a function $h(x, y)$ which is the convolution of a 500 nm gate and a two-dimensional Gaussian function. Figure 5.10b shows a fit of the model function to the experimental data. The good agreement between

them attests that the function $h(x, y)$ can be used to describe the response of the SPAD.

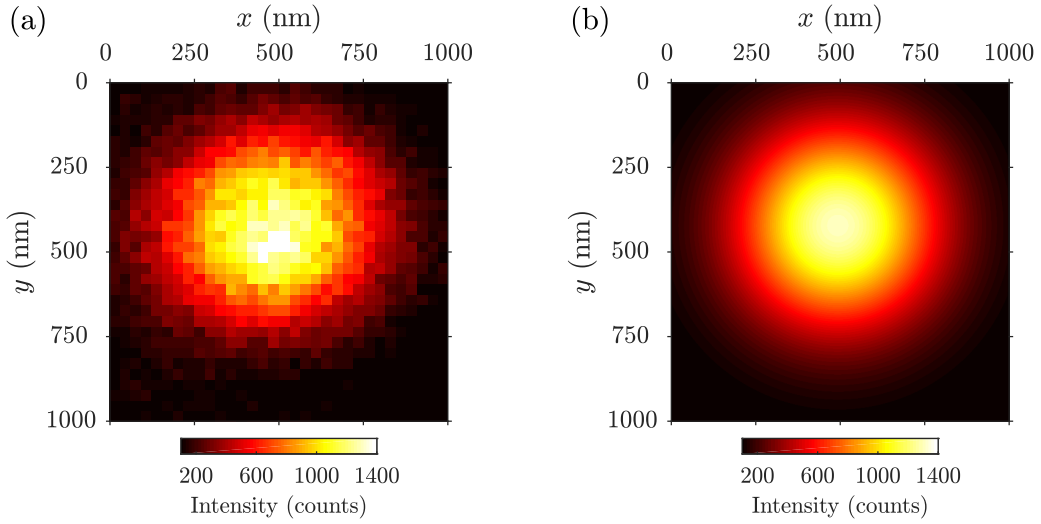

Figure 5.10 – *(a) Measured response of the SPAD while scanning a fluorescent bead in the sample plane. (b) Model function fitted to the measured response of the SPAD.*

Using this characterisation, we can estimate the number of photons to be detected by the SPAD from a given camera detection. Let x_i and y_i be the coordinates in the sample plane corresponding to this detection and N_i the number of fluorescence photons measured by the camera, we can simply assume that the number of photons to be detected by the SPAD is proportional[2] to $N_i\, h(x_i, y_i)$.

5.4.3 Association conditions

By using the estimation of the time offset between the camera and the SPAD as well as the characterisation of the spatial conjugation between the detectors, we now identify the molecules for which both the position and the decay rate can be determined. We can associate position and decay rate in the following situations:

- In 77% of the cases, the association between position and decay rate is straightforward. In such cases, only one camera detection is identified in the emission time Δt_j corresponding to a SPAD event. In addition, this SPAD event is the only one identified in the emission time Δt_i corresponding to the camera detection. Therefore, the camera detection i and the SPAD event j can be associated.
- In 18% of the cases, several camera detections are identified in Δt_j. In such cases, we evaluate the likelihood of each detection to be the one corresponding to the SPAD event, based on the number of fluorescence photons measured by the camera, the distance to the centre of the detector and the temporal overlap between the SPAD event and the considered frame. An association condition can thus be obtained on

[2]One can compare the quantum efficiencies of the camera (~ 0.9) and the SPAD (~ 0.5) to obtain an estimate of the number of photons to be detected by the SPAD. This is however not required for a comparison between different detections identified from the camera data.

the base of the value taken by the following variable:

$$T_{ij} = N_i \, h(x_i, y_i) \times \frac{\Delta t_{ij}}{\Delta t_j} \, . \tag{5.2}$$

After the identification of the detection k associated with the maximum value of T_{ij}, we consider that the association between position and decay rate can be performed only if $T_{kj} > \alpha_a \sum_{i=1}^{n} T_{ij}$ where n is the number of camera detections in Δt_j and α_a is a threshold characterising the association condition. If α_a is low, camera detections are more frequently associated to SPAD events. However, this increases the number of cases in which the measured decay histograms are the sum of different decay histograms that cannot be properly separated by a post-processing analysis. As a trade-off, we use $\alpha_a = 80\%$ in the experiment.

- In 5% of the cases, several SPAD events are identified in Δt_i. Then, if the difference between these decay rates is smaller than 30%, we merge the SPAD events and we calculate the average decay rate. Otherwise, we evaluate the likelihood of each event to be the one corresponding to the camera detection, based on the number of fluorescence photons measured by the SPAD. To do so, we identify the event k associated with the highest number of photons N_k and we perform the association between position and decay rate only if $N_k > \alpha_a \sum_{i=1}^{n} N_i$ where N_i is the number of photons associated with the overlapping SPAD events and α_a is the threshold previously mentioned ($\alpha_a = 80\%$).

Two additional conditions are required in order to correctly perform the association between position and decay rate. For each molecule, at least 150 fluorescence photons must be detected on each detector. Moreover, the standard deviation of the Gaussian function fitted to the camera data must be smaller than 190 nm. These two conditions avoid the occurrence of false detections that would be due to noise. Using this procedure, we associate the position of 3,581 camera detections with their decay rate. We then perform post-processing filtering to account for the few remaining loopholes of the procedure. To do so, we compare each decay rate to the decay rate of the 10 closest detections. On average, this corresponds to a distance of 19 nm between the detection and its neighbours. Then, we perform an outlier identification based on the median absolute deviation (MAD). A decay rate Γ is rejected if the decay rates Γ_k of the closest neighbours satisfy the following condition:

$$|\Gamma - \mathrm{Med}(\Gamma_k)| > \alpha_r \ \mathrm{Med}\left[\frac{|\Gamma_k - \mathrm{Med}(\Gamma_k)|}{0.675}\right] \, , \tag{5.3}$$

where Med is the median operator and α_r is a rejection threshold. The factor 0.675 is used so that MAD and standard deviation are approximately equal for large normal samples [115]. It should be noted that no outlier identification is performed if more than 50% of the neighbours have a decay rate equal to the upper limit previously mentioned ($10\ \mathrm{ns}^{-1}$) since the right-hand side of Eq. (5.3) equals zero in this case. With the approach expressed by Eq. (5.3), using a small threshold α_r allows the identification of many outliers but may also identify actual detections as outliers. As a trade-off, we use $\alpha_r = 5$ resulting in the identification of 6% of outliers. By removing them, the number of actual detections reduces to 3,352.

5.5 Experimental results

From the results of the 10-hour-long experiment, we can study the enhancement of the decay rate of the molecules induced by the presence of the silver nanowire. Before analysing these results, we describe the strategy used to build a decay rate map from the position and the decay rate of the detected molecules.

5.5.1 Reconstruction of the decay rate map

We can now build a decay rate map with sub-wavelength resolution that takes into account the position of the molecules, their decay rate and the localisation precision. First of all, we discretise the xy-plane with a resolution of 1 nm. As we will see in Chapter 6 (Sect. 6.3.5), the typical standard deviation of the probability density function followed by the position estimates is 6 nm. Hence, we represent each molecule by a circular area with a diameter of 15 nm, which is the FWHM of the associated Gaussian distribution. If only one molecule is detected in this area, then the colour of the area is determined by the decay rate of the molecule. However, if n molecules are detected in the same area, we compute a weight function $\Phi(x, y)$ for each point of the overlap area. This function expresses the probability amplitude of detection per unit area, which reads

$$\Phi(x,y) = \sum_{i=1}^{n} \left[\frac{1}{2\pi\sigma_{x,y}^2} \exp\left(-\frac{d_i}{2\sigma_{x,y}^2} \right) \right] , \tag{5.4}$$

where $\sigma_{x,y}$ is the typical localisation precision of the molecules and d_i is the distance between this molecule and the considered point (x, y). The decay rate $\Gamma(x, y)$ associated with each point of the overlap area is then calculated as a weighted average over the decay rates Γ_i of the detected molecule, according to

$$\Gamma(x,y) = \frac{1}{\Phi(x,y)} \times \sum_{i=1}^{n} \left[\frac{\Gamma_i}{2\pi\sigma_{x,y}^2} \exp\left(-\frac{d_i}{2\sigma_{x,y}^2} \right) \right] . \tag{5.5}$$

Figure 5.11 shows the reconstructed decay rate map over an area of 1 µm^2 including 93% of the detected molecules. On this map, we can clearly identify the location of the silver nanowire, which induces an enhancement of the fluorescence decay rate by at least a factor of 15. The upper limit of the decay rate map is set to 10 ns^{-1}, as already mentioned in Sect. 5.4.1. We indeed consider that we cannot correctly estimate such high decay rates due to the IRF of the setup.

Spatial variations of the decay rate are observed well below the diffraction limit, demonstrating the ability of the technique to simultaneously determine the position and the decay rate of single molecules with a very good precision. The performance of the technique relies on both the localisation precision and the density of detected molecules. We already mentioned that the FWHM of the Gaussian distribution typically followed by the position estimates is 15 nm. Moreover, the average distance between two nearby detections is 7.5 nm, but the density of detected molecules is clearly not uniform over the map[3].

[3] For comparison purposes, we can calculate the average distance between two nearby detections under the assumption that the density of detected molecules ρ is uniform. In this case, the distance r to the nearest neighbour follows the probability density function $H(r) = 2\pi\rho r \exp(-\pi\rho r^2)$ [116], and the expectation of r is $\mathrm{E}(r) = 1/(2\sqrt{\rho})$. The resulting value (9 nm) is slightly larger that the mean value obtained from experimental data (7.5 nm), since some areas are more dense than others on the experimental map.

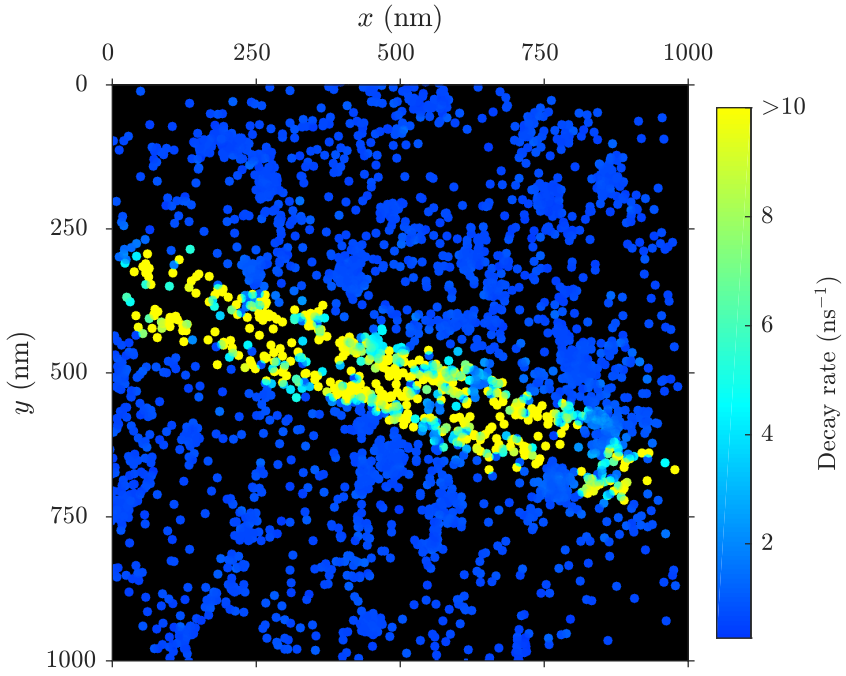

Figure 5.11 – *Map of the decay rate of 3,119 single molecules in the near field of a silver nanowire.*

The centre of the map shows a higher density of detected molecules, as the pinhole does not filter any photon from this area. Inhomogeneities that can be observed on smaller scales are likely to be due to an inhomogeneous repartition of fluorescent molecules on the substrate due to the sample preparation procedure. Furthermore, the density of detected molecules is lower along the nanowire axis. This effect is likely to be due to the reduced excitation intensity at this location, as we will see in the following section.

5.5.2 Density of detected molecules

As in usual PALM/STORM experiments, we can study the spatial variations of the density of detected molecules. Figure 5.12a shows the number of detected molecules as a function of the distance d to the nanowire axis. On average, we can see that twice as many molecules are detected for $d = 50$ nm as for $d = 0$ nm. This may be due to different effects:

- Fluorescent molecules are present on both the silver nanowire and the glass substrate. As we measure a projection of the system on the sample plane, the apparent density of molecules is higher close to the nanowire.
- The interaction between the excitation field and the nanowire results in a non-uniform excitation intensity distribution.
- The photo-activation and the photobleaching of the fluorescent molecules might be affected by the proximity of the nanowire.

In order to estimate the influence of the excitation field on the observed density variations, we perform a numerical study of the system using MEEP, a finite-difference time-domain software developed by Oskooia *et al.* [117]. The relative permittivity of the silver nanowire is modelled with a Lorentz–Drude model as expressed by Eq. (2.1), the relative permittivity

of the buffer solution is set to 1.77 and the relative permittivity of glass is set to 2.25. We simulate the illumination of a nanowire located on a glass substrate by a plane wave at $\lambda_0 = 640$ nm polarised perpendicular to the nanowire, as in the experiment. In this configuration, a two-dimensional simulation gives the exact solution due to the invariance of the structure and the source along the longitudinal dimension. As a result, we obtain a map of the time-averaged intensity in the vicinity of the silver nanowire (Fig. 5.12b). It shows a local enhancement of the excitation intensity on the sides of the nanowire, with an extension of about 20 nm, as well as a reduction of the excitation intensity on the top of the wire. This supports the observed variations of the density of detected molecules: the molecules located in the intensity hot spots have a larger probability to be excited, and their fluorescence can surpass the noise level to be detected by the SPAD and the camera.

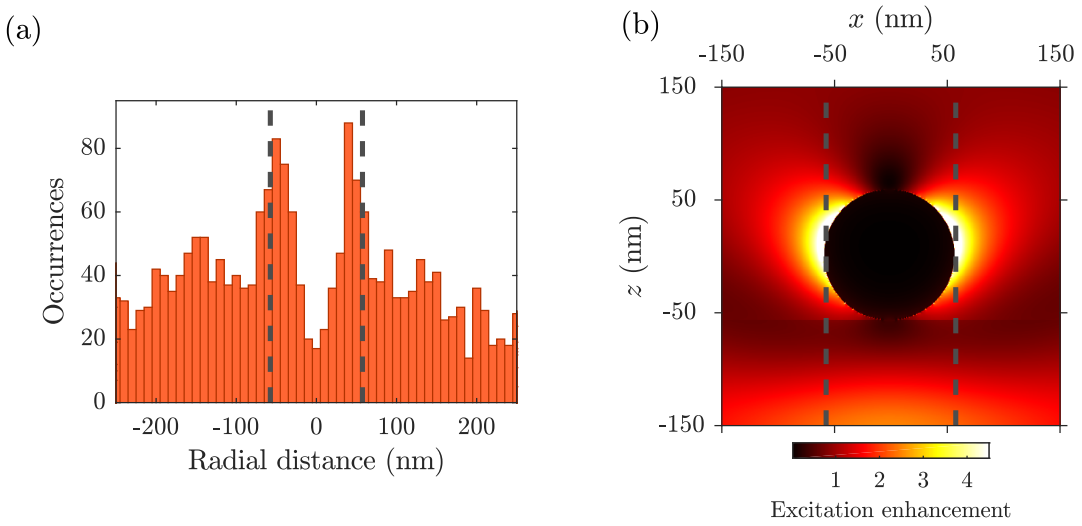

Figure 5.12 – *(a) Number of detected molecules as a function of the distance to the nanowire axis. (b) Time-averaged intensity of the excitation field in the vicinity of the silver nanowire calculated from the results of a FDTD simulation. Dashed lines represent the edges of the nanowire.*

5.5.3 Decay rate enhancement

To get a deeper insight into the spatial variations of the decay rate observed in the experiment, we study the dependence of the decay rate on the distance d to the nanowire axis (Fig. 5.13a). For the molecules detected far from the nanowire axis ($d > 200$ nm), the decay rate distribution is characterised by an average value of 0.68 ns^{-1} and a standard deviation of 0.17 ns^{-1}. In contrast, the decay rate is higher than 10 ns^{-1} for molecules detected at distances $d < 60$ nm from the nanowire axis. This distance approximately corresponds to the radius of the nanowire, which confirms that molecules with the largest decay rates are those attached to the nanowire or in its closest vicinity – the procedure used for sample preparation allows both the coverslip and the silver nanowire to be labelled with fluorescent molecules. In comparison to the average decay rate of the molecules located far from the nanowire, the decay rate of these molecules is enhanced by at least a factor of 15.

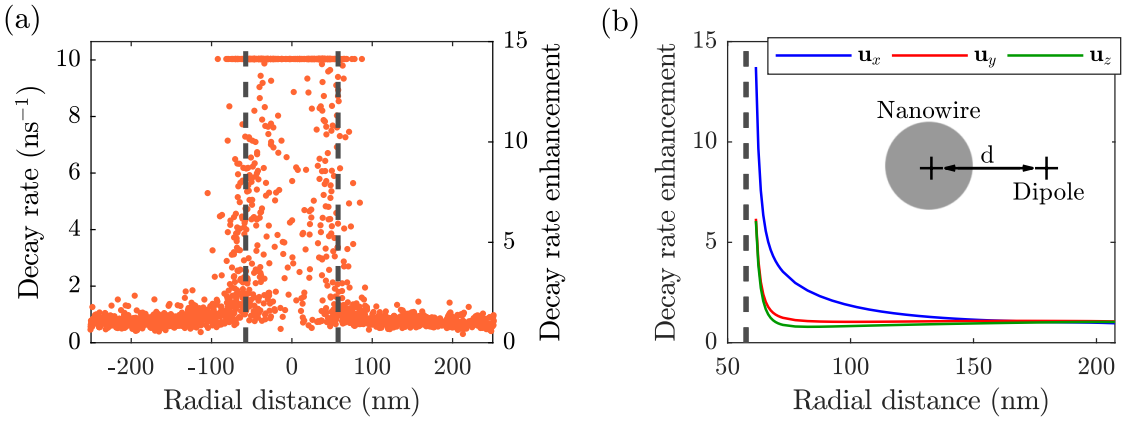

Figure 5.13 – *(a) Distribution of decay rate and decay rate enhancement versus distance to the wire axis. (b) Decay rate enhancement as a function of the distance to the nanowire for the three orientations of the dipole moment. Inset: Cross-section of the system numerically studied. Dashed lines represent the edges of the nanowire.*

To complete these experimental results, we numerically study the enhancement of the decay rate due to the nanowire using MEEP [117]. Unlike for the numerical study presented in Sect. 5.5.2, we model the system in three dimensions, with a mesh resolution of 1 nm. As the effect of the substrate on the decay rate is small due to the low contrast between the relative permittivities of the buffer solution and the glass coverslip, we perform the simulations without the substrate to limit the computational time. In each simulation, the emitter is modelled as an electric dipole source that generates a Gaussian pulse at $\lambda_0 = 670$ nm, and the decay rate is estimated according to the method detailed in Appendix B. We assume that the intrinsic quantum yield of Alexa Fluor 647 dyes is $\eta_i = 0.33$ as specified by the provider (ThermoFisher Scientific). Using this model, we numerically investigate distances between the nanowire and the emitter ranging from 4 nm to 150 nm. We also compute the decay rate without the nanowire as a reference value used for normalisation.

Figure 5.13b shows the decay rate enhancement induced by the nanowire for each of the three orientations of the dipole moment respectively defined by the unitary vectors $\mathbf{u}_x$, $\mathbf{u}_y$ and $\mathbf{u}_z$. The decay rate enhancement for radially oriented dipoles (x-direction) is large in the vicinity of the nanowire edge, with a maximum value of about 14 at a distance of 4 nm from the nanowire. The decay rate enhancement of longitudinally (y-direction) and azimuthally (z-direction) oriented dipoles is of the order of 6 at the same distance. The decay is mainly non radiative at these very short distances, and the contribution of quenching is large. Furthermore, the distance dependence of the decay rate enhancement is very different depending on the dipole orientation. At distances between 10 and 100 nm from the nanowire edge, radially oriented dipoles specifically present high decay rates due to the coupling between dipolar emission and surface-plasmon modes. This was studied by Barthes *et al.*, who performed a detailed analysis of the interaction between a dipole and a plasmonic waveguide [66].

Experimental and numerical results are in good qualitative agreement, supporting the validity of the experimental technique. A precise knowledge on both the dipole orientation of the molecules and the distance to the nanowire is however required for a quantitative analysis of the experimental results. The fluorescent molecules used for the experiment

(Alexa Fluor 647) are bound to the microscope coverslip using biotin-streptavidin linkers. From the size of the linkers, we estimate the minimum distance between the probes and the nanowire to be of the order of 5 nm. Since these short distances are comparable to the microscopic length scale of the free-electron gas, the description of the metal by a nonlocal dielectric function can be necessary. This would lead to an enhancement of the nonradiative decay [118, 119] that is not taken into account by FDTD simulations. This effect may consequently explain the large number of detected molecules characterised by a decay rate larger than 10 ns^{-1}. Furthermore, we do not control the orientation of the dipole moment nor the degree of intrinsic rotational mobility of the attached fluorescent probes, which depends on the rigidity of their linkers. In order to obtain a quantitative agreement between the experiment and the numerical simulations, a better understanding of the orientation of the molecules could be achieved by using polarised superresolution microscopy [120, 121].

5.6 Conclusion

In this chapter, we introduced a new experimental technique to determine the decay rate of photo-activated single molecules along with their position with a localisation precision of the order of 10 nm. This technique relies on the simultaneous detection of fluorescence photons by two different detectors, an EM-CCD camera and a SPAD. Since no more than one molecule is typically active at a time on the area conjugated to the SPAD, we could associate the position of more than 3,000 single molecules with their decay rate from data acquired during a 10-hour-long experiment. We thus reconstructed a map of the fluorescence decay rate of the molecules (Fig. 5.11), and we observed an increase in the LDOS induced by the presence of a silver nanowire, in qualitative agreement with numerical simulations. A quantitative agreement would require a better knowledge of the orientation of the molecules as well as the consideration of possible non-local effects in the simulations.

The technique presented in this chapter is a interesting tool to investigate light-matter interaction on the nanometre scale, as it allows a direct characterisation of the LDOS with a strongly sub-wavelength resolution. We can also expect this method to be used for the study of biological samples. For instance, different target-search strategies were identified by Izeddin *et al.* using a technique that combines single-particle tracking (SPT) and PALM techniques [122]. For such an application, a real-time determination of the fluorescence decay rate could be of great interest. This could be achieved by tagging proteins of interest with donor and acceptor fluorescent molecules: by tracking photo-activated donors and by studying the variations of their decay rate due to FRET, one could monitor the interaction occurring between the protein and the target. Nevertheless, most biological applications will require to increase the field of view of the technique. To this end, a possibility relies on SPAD arrays constituted of several independent channels and covering an area of tens of micrometres in the sample plane [123].

It would also be beneficial to use fluorescent molecules with a higher intrinsic quantum yield. Indeed, the variations of the decay rate induced by the environment of the molecules would be easier to observe. Another possible improvement of the technique would be to localise the molecules in the three dimensions. Huang *et al.* notably introduced a technique characterised by an axial localisation precision of the order of 60 nm [124]. The authors used a cylindrical lens to induce an asymmetry in the PSF of the emitters in

order to estimate the axial position of the emitter from this asymmetry. An alternative approach based on decay rate variations induced by a thin gold film was proposed by Chizhik *et al.* [125], allowing a more precise axial localisation. Performing the experiment at cryogenic temperatures could also be an interesting perspective. Indeed, Weisenburger *et al.* recently demonstrated cryogenic localisation of single molecules [126], increasing the number of photons collected from a given molecule by several orders of magnitude.

In the experiment, we determined the position and the decay rate of the molecules using an EM-CCD camera and a SPAD. However, we can split the fluorescence intensity emitted from the molecules towards several different detectors and simultaneously determine various physical quantities. For instance, a spectrometer could be added to the optical path. By using photo-activatable probes with distinct colours [127], it would be possible to probe LDOS variations at different frequencies. However, the splitting of the fluorescence intensity towards different detectors reduces the precision of the estimations, since the achievable precision directly depends on the number of detected fluorescence photons. In the following chapter, we will investigate the precision that can be reached by estimating the position and the decay rate of a single molecule using EM-CCD and SPAD measurements.

CHAPTER 6

Fundamental limit on the precision of position and lifetime estimations

In this chapter, we assess a lower bound on the precision of the estimations performed from the data presented in Chapter 5. This is done by calculating the Cramér-Rao lower bound on the variance of position and decay rate estimators. First of all, we detail the context of this work and we introduce the basics of estimation theory. We then calculate the information matrix associated with camera measurements and we give the Cramér-Rao bound on the variance of position estimators. We similarly analyse measurements performed with the single-photon avalanche diode to evaluate the lower bound on the variance of decay rate estimators. In both cases, we assess the precision of actual estimations using numerical results. Finally, we use the Cramér-Rao bound in order to provide some guidelines to design the experimental setup.

6.1 Introduction

For many applications in physics, it is useful to evaluate the best precision achievable in the estimation of one or several physical quantities using a given experimental setup. To this end, one must study the variance of *estimators*, which are the random variables used to estimate these quantities. The derivation of a lower bound on the variance of unbiased estimators was performed by Rao in 1945 [128]. One year after the publication of Rao's work, Cramér independently published a book containing a similar demonstration [129]. This result is referred to as the *Cramér-Rao lower bound*, and is nowadays widely used as a tool for the optimisation of experimental setups. To do so, one must find a model for the probability density function followed by the experimental observations, called the *likelihood function*. By calculating the information matrix characterising the amount of information contained in the measurements about the parameters to be estimated, it is then possible to obtain a lower bound on the variance of these parameters.

Since the development of single-molecule microscopy, estimating the precision of single-molecule localisation became a challenge. At first, this was achieved using a technique

introduced by Bobroff that relies on the least-squares method [130]. From this work, a simple formula describing the localisation precision was derived by Thompson, Larson and Webb [131]. In 2004, Ober, Ram and Ward introduced a more general approach based on the calculation of the Cramér-Rao bound [18], assuming isotropic photon emission and modelling the noise with a Gaussian probability density function. While this model is appropriate for data measured by a CCD camera, it could be adapted to correctly model the effect of the multiplication register of an electron-multiplying charge-coupled device (EM-CCD) [132]. Moreover, a comprehensive study of the precision of position estimations was performed by Mortensen *et al.*, who compared different estimators assuming either isotropic or dipole photon emission [133]. The approach based on the calculation of the Cramér-Rao bound is now widely adopted by the community of experimental physicists and biologists working with single molecules. A comprehensive review of this work was recently proposed by Deschout *et al.* [134]. Moreover, a tutorial that summarises and illustrates the practical calculation of the Cramér-Rao bound in the context of single-molecule microscopy was published by Chao, Ward and Ober [135].

In the context of fluorescence lifetime estimation, the performances of different estimators were compared by Bajzer *et al.* in 1991 [136]. This study notably included the *maximum likelihood method*, which relies on the calculation of the likelihood function. The precision and the bias of maximum-likelihood estimators were also compared to other estimators by Tellinghuisen and Wilkerson in 1993 [137]. These two studies relied on a simple model for the likelihood function, which was notably improved by Rowley *et al.* in 2011 [138]. In this work, the authors developed an estimator that combines maximum-likelihood estimation and prior information about the parameters to be estimated, a technique referred to as a *Bayesian method*. A similar estimator was recently studied by Kane *et al.* for lifetime imaging based on Förster resonance energy transfer [139]. Along with these studies based on comparisons between different estimators, the calculation of the Cramér-Rao bound on the variance of lifetime estimators was performed in 1992 by Köllner and Wolfrum using the multinomial approach [140].

Definition of the problem In this chapter, we calculate the Cramér-Rao bound on the variance of both position and decay rate estimators in the context of the experiment performed in Chapter 5. While we follow Ref. [135] to estimate the Cramér-Rao bound on the variance of position estimators, we derive an expression of the Cramér-Rao bound on the variance of decay rate estimators that is more general than the one given in Ref. [140]. This expression notably includes the instrument response function (IRF) and is compatible with experiments characterised by high repetition rates. This work allows us to get a satisfactory answer to the two following questions:

- What is the precision of position and decay rate estimations performed in Chapter 5?
- What are the general rules that must be followed to design the experimental setup?

6.2 Estimation theory

To start with, we introduce the conceptual framework necessary to calculate the Cramér-Rao bound on the variance of any estimator using a classical frequentist reasoning: the

parameters of interest are assumed to be deterministic but unknown[1].

6.2.1 Estimators and sampling distributions

Any experiment can be analysed as the result of n measurements which constitute the data set, noted $\mathbf{X}$. One particular measurement can then be described by a data item X_i where i takes integer values between 1 and n. As the n measured values are likely to be different for each realisation of the experiment, we can consider them as a set of n random variables described by a n-dimensional joint probability density function (PDF) noted $p(\mathbf{X})$. The n measurements are often independent; in this case, the n-dimensional PDF can be factorised into the product of n one-dimensional PDFs, which reads

$$p(\mathbf{X}) = \prod_{i=1}^{n} p(X_i) \; . \tag{6.1}$$

In general, the functional form of the population is unknown and we intend to retrieve some of its features from the measured data. We define $\boldsymbol{\theta}$ as a set of parameters characterising the PDF. As the data depend on the parameters, the PDF of $\mathbf{X}$ is noted $p(\mathbf{X};\boldsymbol{\theta})$. Since any estimate of the parameters must be a function of the data, any estimator $\hat{\boldsymbol{\theta}}$ of these parameters is a function of $\mathbf{X}$. An estimator is consequently a random variable that can be described by a PDF noted $p(\hat{\boldsymbol{\theta}};\boldsymbol{\theta})$ called the *sampling distribution*.

In theory, any function of the data could be used as an estimator. However, some estimators are better than others. Any useful estimator must give the correct values for all the parameters in the limit of an infinite number of data items. An estimator which satisfies this property is a *consistent* estimator, and thus verifies

$$\lim_{n\to\infty} \hat{\boldsymbol{\theta}} = \boldsymbol{\theta} \; . \tag{6.2}$$

In practice, there is a finite number of data items, and a consistent estimator may not retrieve on average the true value of the parameters: the estimator is then *biased*. The bias $\mathcal{B}$ is defined as the difference between the expectation of $\hat{\boldsymbol{\theta}}$ for n data items and the true value of the parameters $\boldsymbol{\theta}$. Hence the bias generally depends on n as well as on $\boldsymbol{\theta}$ and $\hat{\boldsymbol{\theta}}$. It can be expressed as

$$\mathcal{B}(\boldsymbol{\theta}) = \mathrm{E}(\hat{\boldsymbol{\theta}}) - \boldsymbol{\theta} \; , \tag{6.3}$$

where E is the expectation operator defined as follows:

$$\mathrm{E}(\hat{\boldsymbol{\theta}}) = \int \hat{\boldsymbol{\theta}}\, p(\hat{\boldsymbol{\theta}};\boldsymbol{\theta})\, \mathrm{d}\,\hat{\boldsymbol{\theta}} \; . \tag{6.4}$$

The variance of an estimator describes the spread of values of $\hat{\boldsymbol{\theta}}$ about its expectation. It is expressed in terms of the sampling distribution as

$$\mathrm{Var}(\hat{\boldsymbol{\theta}}) = \int \left[\hat{\boldsymbol{\theta}} - \mathrm{E}(\hat{\boldsymbol{\theta}})\right]^2 p(\hat{\boldsymbol{\theta}};\boldsymbol{\theta})\, \mathrm{d}\,\hat{\boldsymbol{\theta}} \; . \tag{6.5}$$

[1] An alternative view to the frequentist reasoning is the Bayesian approach, in which parameters to be estimated are viewed as realisations of random variables. In addition to the frequentist analysis performed in this chapter, it would be interesting to assess the variance of position and decay rate estimators from the Bayesian perspective, as it would notably allow to easily include a possible prior knowledge about parameters in the model [141].

Finally, the error on the estimate of one given component θ_j of $\boldsymbol{\theta}$ is usually characterised by the standard error on the estimates, which is noted σ_{θ_j} and is given by

$$\sigma_{\theta_j} = \sqrt{\mathrm{Var}(\hat{\theta}_j)} \, . \tag{6.6}$$

The bias and the standard error are used to quantify the *accuracy* and the *precision* of an estimator, as illustrated in Fig. 6.1. While the accuracy describes the deviation of the expectation of the estimator from the true value of the parameter, the precision describes the spread of the estimates of the parameter around its expectation[2].

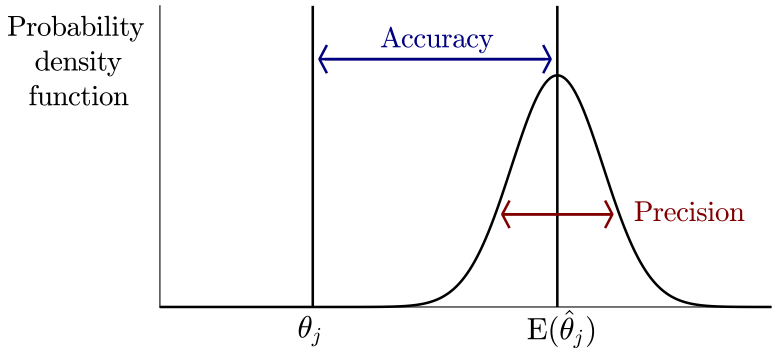

Figure 6.1 – *Illustration of the precision and the accuracy of an estimator.*

6.2.2 Cramér-Rao lower bound

For an unbiased estimator, a theoretical limit can be calculated for the minimum variance of any component $\hat{\theta}_j$ of $\hat{\boldsymbol{\theta}}$. This limit is the so-called *Cramér-Rao lower bound* and can be calculated assuming the following regularity condition [142]:

$$\mathrm{E}\left[\frac{\partial \ln p(\mathbf{X};\boldsymbol{\theta})}{\partial \boldsymbol{\theta}}\right] = \mathbf{0} \, . \tag{6.7}$$

The regularity condition holds if the order of the expectation operator and the differentiation operator can be interchanged, which is generally true if the definition domain of $p(\mathbf{X};\boldsymbol{\theta})$ does not depend on $\boldsymbol{\theta}$. Then, as a consequence of the Cauchy-Schwartz inequality[3], the variance of any unbiased estimator $\hat{\boldsymbol{\theta}}$ must satisfy the following condition:

$$\mathrm{Var}(\hat{\theta}_j) \geq \left[\boldsymbol{\mathcal{I}}^{-1}(\boldsymbol{\theta})\right]_{jj} \, , \tag{6.8}$$

where $\boldsymbol{\mathcal{I}}$ is the Fisher information matrix defined by

$$\left[\boldsymbol{\mathcal{I}}(\boldsymbol{\theta})\right]_{jk} = \mathrm{E}\left[\left(\frac{\partial \ln p(\mathbf{X};\boldsymbol{\theta})}{\partial \theta_j}\right)\left(\frac{\partial \ln p(\mathbf{X};\boldsymbol{\theta})}{\partial \theta_k}\right)\right] \, . \tag{6.9}$$

The inequality expressed by Eq. (6.8) is referred to as the *Cramér-Rao inequality*. An unbiased estimator is called *efficient* if its variance equals the theoretical limit given by

[2] This is the common definition of precision and accuracy, used for instance in Ref. [134]. This differs from the definition set by the norm ISO 5725-1:1994, used for instance in Ref. [135]. According to this latter convention, both precision (a small variance) and trueness (a small bias) are required for an estimator to be accurate.

[3] The demonstration can be found in Appendix 3B of Ref. [142].

the Cramér-Rao bound. Moreover, any estimator that satisfies the equality condition in Eq. (6.8) is necessarily unbiased.

As shown in Ref. [143], an equivalent expression of Eq. (6.9) is given by

$$[\boldsymbol{\mathcal{I}}(\boldsymbol{\theta})]_{jk} = -\,\mathrm{E}\left[\left(\frac{\partial^2 \ln p(\mathbf{X};\boldsymbol{\theta})}{\partial\theta_j \partial\theta_k}\right)\right] . \tag{6.10}$$

The coefficients of the information matrix are therefore determined by the curvature of the natural logarithm of $p(\mathbf{X};\boldsymbol{\theta})$. If $p(\mathbf{X};\boldsymbol{\theta})$ strongly depends on the parameter θ_j, it means that the data set $\mathbf{X}$ provides a lot of information about θ_j. Hence, the information matrix can be used to assess the amount of information about the parameters contained in a given data set. Assuming that the n data items are independent, Eq. (6.1) can be used to simplify the expression of the information matrix, which then reads

$$[\boldsymbol{\mathcal{I}}(\boldsymbol{\theta})]_{jk} = \sum_{i=1}^{n} \mathrm{E}\left[\frac{1}{[p(X_i;\boldsymbol{\theta})]^2}\left(\frac{\partial p(X_i;\boldsymbol{\theta})}{\partial\theta_j}\right)\left(\frac{\partial p(X_i;\boldsymbol{\theta})}{\partial\theta_k}\right)\right] . \tag{6.11}$$

The information matrix is thus additive for independent measurements.

6.2.3 Data modelling

In data modelling, we adopt the hypothesis $\mathcal{H}$ that the n-dimensional joint PDF has a particular form that can be expressed as a function of a set of parameters $\boldsymbol{\theta}$. In this case, the PDF is named the *likelihood function*. To obtain a model for the likelihood function, we can firstly assume a functional form $f(\boldsymbol{\theta})$ for the population, from which an expectation f_i can be calculated for each data item. We can secondly assume a functional form for the likelihood functions $p(X_i|\boldsymbol{\theta},\mathcal{H})$ associated with each data item. As a matter of simplicity, these likelihood functions will be noted $p_i(X|\boldsymbol{\theta})$ in the following sections. Assuming that the hypothesis $\mathcal{H}$ is correct, the information matrix can then be calculated using Eq. (6.11).

Generally, we do not estimate all the parameters involved in the model from the data. Indeed, the estimation precision increases for all the parameters whenever we can estimate the value of one or several parameters from independent experiments. If the parameters do not have definite values but are described by probability distributions, we can use the median values of the measured distributions in the calculations. Such a procedure allows to obtain a *typical* value of the estimation precision for the parameters that are to be estimated from the data.

6.3 Precision of position estimations

Using the framework previously detailed, we can calculate the Cramér–Rao lower bound on the variance of position estimators in the context of single-molecule microscopy, using wide-field images acquired by an EM-CCD camera.

6.3.1 Point spread function

We consider the simple situation in which a far-field microscope is used to collect the photons emitted by a single molecule located in the object plane. In the image plane, the

intensity distribution depends on the orientation of the dipole moment of the molecule, as detailed in Sect. 1.4.2. However, we showed that the Airy pattern – which is the exact solution considering a molecule in a homogeneous medium with a dipole moment in the sample plane – is a good approximate of the pattern averaged over all the possible orientations of the dipole moment of the molecule. Indeed, the emission collected from a dipole oriented along the normal to the object plane is much smaller than that of a dipole in the sample plane, even by using a microscope objective with a high numerical aperture. Hence we assume that the 2-dimensional PDF describing the intensity distribution in the image plane is given by Eq. (1.30). This PDF can be expressed from the coordinates in the image plane noted (x', y') and the coordinates of the molecule in the object plane noted (x_0, y_0) as follows:

$$q(x', y') = \frac{J_1^2\left(\dfrac{2\pi \mathrm{NA}\sqrt{(x' - Mx_0)^2 + (y' - My_0)^2}}{M\lambda_0}\right)}{\pi\left[(x' - Mx_0)^2 + (y' - My_0)^2\right]}, \tag{6.12}$$

where J_1 is the first-order Bessel function of the first kind, NA is the numerical aperture of the objective, M is the magnification and λ_0 is the free-space emission wavelength.

The expression of the point spread function (PSF) given by Eq. (6.12) is valid assuming that the emitter is inside a homogeneous medium. This is clearly not the case in the experiment presented in Chapter 5, since the molecules are located in the near field of a silver nanowire. However, we can use Eq. (6.12) as a first approximation as long as the inhomogeneities in the environment (the nanowire) weakly radiate to the far field. In contrast, it was shown that this approximation is not reasonable in the case of photon emission in the vicinity of a resonant antenna [144, 145]. The mislocalisation was notably estimated in the case of an emitter coupled to a gold nanoparticle [146].

The expectation of each data item – that is, the expectation of the value measured on each pixel by the camera – is then expressed as follows:

$$f_i = N \int\limits_{(x',y')\in pixel} q(x', y')\,\mathrm{d}\,x'\,\mathrm{d}\,y' + N_b \int\limits_{(x',y')\in pixel} q_b(x', y')\,\mathrm{d}\,x'\,\mathrm{d}\,y', \tag{6.13}$$

where N is the total number of photons emitted by the molecule and detected by the camera and N_b is the number of photons due to background noise which follows a PDF noted $q_b(x', y')$. In Eq. (6.13), the integration is performed over the area that defines the considered pixel.

6.3.2 EM-CCD data model

We can now derive a functional form for the likelihood function that describes the number of events measured on each pixel by the camera. To start with, let us review the different processes involved in photon detection by an EM-CCD camera. When photons impinge the active area of the camera, they are transformed into photoelectrons that are accelerated in the multiplication register. These photoelectrons are then accumulated in a potential well until they are converted by an analog-to-digital converter (ADC). The electronic offset used to avoid the observation of negative values – called the *baseline* of the camera – is usually subtracted before data analysis.

Assuming that fluorescence photons detected by the camera can be independently described, the number of photons impinging on each pixel during a given time interval follows a Poisson distribution of expectation f_i. The noise associated with the standard deviation of this distribution is referred to as *shot noise*. If we do not consider the additional noise arising from the detection process, the PDF associated with the observation of X photoelectrons on a given pixel is

$$p_i^p(X;\boldsymbol{\theta}) = \frac{f_i^X}{X!}\exp(-f_i)\ . \tag{6.14}$$

This sets the fundamental limit achievable by a perfect camera. However, the multiplication register of an EM-CCD camera enhances the number of generated photoelectrons in order to beat the readout noise of the camera, and the PDF followed by the number of photoelectrons generated by the process depends on the gain g. As shown in Ref. [132], this PDF noted $p_i^e(X;\boldsymbol{\theta})$ can be approximated, for large gain values, by

$$p_i^e(X;\boldsymbol{\theta}) = \begin{cases} \exp(-f_i)\ , & \text{for } X = 0\ , \\ \dfrac{\exp\left(-\dfrac{X}{g} - f_i\right)\sqrt{\dfrac{f_i X}{g}}\, I_1\left(2\sqrt{\dfrac{f_i X}{g}}\right)}{X}\ , & \text{for } X > 0\ , \end{cases} \tag{6.15}$$

where I_1 is the first-order modified Bessel function of the first kind. In addition, the readout process induces a Gaussian noise on each pixel characterised by an expectation η_g and a standard deviation σ_g. This Gaussian noise can be described by the following PDF:

$$p^g(X;\boldsymbol{\theta}) = \frac{1}{\sigma_g\sqrt{2\pi}}\exp\left(-\frac{(X-\eta_g)^2}{2\sigma_g^2}\right)\ . \tag{6.16}$$

The PDF describing the readout noise of the camera is the same for all the pixels. Therefore, we can consider that the PDF describing the number of photoelectrons per pixel for a real EM-CCD camera is given by

$$p_i(X;\boldsymbol{\theta}) = [p_i^e(X;\boldsymbol{\theta})] * [p^g(X;\boldsymbol{\theta})]\ , \tag{6.17}$$

where the asterisk ($*$) represents the convolution product.

In practice, we can use different models to identify the limits of the experiment:

- The fundamental limit is obtained by assuming no background noise ($B = 0$) and by considering a perfect camera. The PDF describing the number of photoelectrons per pixel is then given by Eq. (6.14). This is the hypothesis $\mathcal{H}_l$.
- The limit of the measuring instruments is set by assuming no background noise ($B = 0$) and by considering a real camera. More precisely, we use Eq. (6.17) for the PDF describing the number of photoelectrons per pixel. This is the hypothesis $\mathcal{H}_e$.
- The limit of the actual experiment is obtained by estimating the background noise B and by using Eq. (6.17) for the PDF of the number of photoelectrons per pixel. This is the hypothesis $\mathcal{H}_a$.

These models involve a large number of parameters but many of them can be independently determined. In the following section, we will assume that λ_0, NA, M, g, η_g,σ_g, N_b and $q_b(x', y')$ are precisely determined from side experiments. The set of parameters to be estimated from the data will therefore be $\boldsymbol{\theta} = (x_0, y_0, N)$.

6.3.3 Calculation of the information matrix

In order to calculate the information matrix associated with EM-CCD images, we must calculate the partial derivatives of the likelihood functions $p_i(X;\boldsymbol{\theta})$ with respect to each parameter. This can be done by using the chain rule, which reads

$$\frac{p_i(X;\boldsymbol{\theta})}{\partial\theta_j} = \frac{p_i(X;\boldsymbol{\theta})}{\partial f_i}\,\frac{\partial f_i}{\partial\theta_j}\,. \tag{6.18}$$

We start by differentiating Eq. (6.13) with respect to each parameter. We obtain the following expressions:

$$\frac{\partial f_i}{\partial x_0} = N \int\limits_{(x',y')\in pixel} \frac{\partial q(x',y')}{\partial x_0}\,\mathrm{d}\,x'\,\mathrm{d}\,y'\,, \tag{6.19a}$$

$$\frac{\partial f_i}{\partial y_0} = N \int\limits_{(x',y')\in pixel} \frac{\partial q(x',y')}{\partial y_0}\,\mathrm{d}\,x'\,\mathrm{d}\,y'\,, \tag{6.19b}$$

$$\frac{\partial f_i}{\partial N} = \int\limits_{(x',y')\in pixel} q(x',y')\,\mathrm{d}\,x'\,\mathrm{d}\,y'\,. \tag{6.19c}$$

The partial derivatives involved in Eqs. (6.19a) and (6.19b) can be analytically calculated. Under the hypothesis $\mathcal{H}_l$, we must differentiate Eq. (6.14) by f_i. This reads

$$\frac{\partial p_i^p(X;\boldsymbol{\theta})}{\partial f_i} = \left(\frac{f_i^X}{X!}\exp(-f_i)\right)\left(\frac{X-f_i}{f_i}\right)\,. \tag{6.20}$$

Under the hypothesis $\mathcal{H}_e$ and $\mathcal{H}_a$, we must differentiate Eq. (6.17) by f_i. This reads

$$\frac{\partial p_i(X;\boldsymbol{\theta})}{\partial f_i} = \left[\frac{\partial p_i^e(X;\boldsymbol{\theta})}{\partial f_i}\right] * \left[p^g(X;\boldsymbol{\theta})\right]\,. \tag{6.21}$$

The partial derivative involved in this expression can be numerically evaluated using a finite-difference scheme.

We can now compute the coefficients of the information matrix as given by Eq. (6.11). Several of these coefficients equal zero since they involve an integral over the product of two functions of opposite parity. For this reason, the information matrix has the following form:

$$\boldsymbol{\mathcal{I}}(\boldsymbol{\theta}) = \begin{pmatrix} \mathcal{I}_{xx} & 0 & 0 \\ 0 & \mathcal{I}_{yy} & 0 \\ 0 & 0 & \mathcal{I}_{NN} \end{pmatrix}\,. \tag{6.22}$$

Under the hypothesis $\mathcal{H}_e$ and $\mathcal{H}_a$, the coefficients of this matrix can be numerically evaluated by using

$$\left[\boldsymbol{\mathcal{I}}(\boldsymbol{\theta})\right]_{jk} = \sum_{i=1}^{n}\left(\frac{\partial f_i}{\partial\theta_j}\right)\left(\frac{\partial f_i}{\partial\theta_k}\right)\int\limits_{X=0}^{+\infty}\frac{\mathrm{d}\,X}{p_i(X;\theta)}\left[\frac{\partial p_i(X;\theta)}{\partial f_i}\right]^2\,. \tag{6.23}$$

Under the hypothesis $\mathcal{H}_l$, this expression can be simplified. As $p_i(X;\boldsymbol{\theta})$ is a Poisson distribution of expectation f_i, the variance of this distribution is also equal to f_i. Equations (6.20) and (6.23) consequently yield

$$\left[\boldsymbol{\mathcal{I}}(\boldsymbol{\theta})\right]_{jk} = \sum_{i=1}^{n}\frac{1}{f_i}\left(\frac{\partial f_i}{\partial\theta_j}\right)\left(\frac{\partial f_i}{\partial\theta_k}\right)\,. \tag{6.24}$$

Equations (6.23) and (6.24) can be used to calculate the Cramér-Rao bound expressed by Eq. (6.8) in the context of single-molecule localisation.

6.3.4 Experimental conditions

In order to calculate the information matrix associated with the experiment described in Chapter 5, we must estimate the value of the parameters involved in the model. Let us review the characteristics of the experiment:

Emission wavelength The emission wavelength of the molecules (Alexa Fluor 647) is measured using a spectrometer and is centred around $\lambda_0 = 670$ nm.

Detection setup The numerical aperture of the objective used for collection is NA=1.4 and the magnification of the optical system is $M = 100$. The gain of the EM-CCD camera used for the experiment is $g = 100$, and the number of photoelectrons per A/D counts is 12.3 as specified by the provider (Andor). The pixels of the camera are squared, with a size of 16×16 µm, and position estimations are performed using a reduced frame of 7×7 pixels. For the calculations, we will assume that the position of the molecules on the sample plane is conjugated to the centre of a pixel. This is of low importance, as the precision of position estimators weakly depends on this parameter if the sampling is sufficiently good.

Readout noise Readout noise is an intrinsic property of the camera that characterises the readout process. It is usually estimated from a measurement in complete darkness with a short integration time. In practice, we perform the measurement of 4,000 frames (17×17 pixels) with a integration time of 30 ms per frame, as in the experiment. The number of photoelectrons associated with the readout noise follows a Gaussian distribution (Fig. 6.2a), with a mean value of $\eta_g = 1194$ and a standard deviation of $\sigma_g = 53.6$. We can safely neglect the small deviation from the Gaussian model: indeed, readout noise is negligible in the experiment because we use a high value for the electron-multiplying gain.

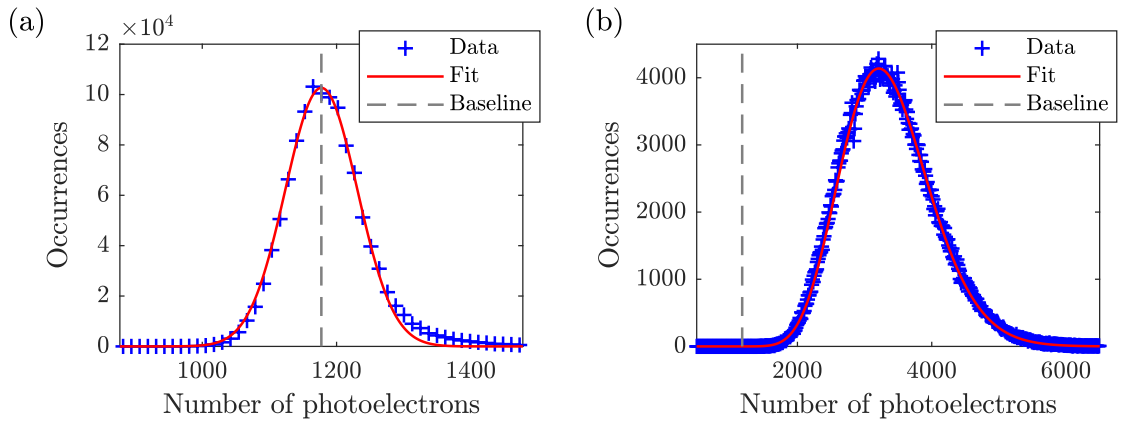

Figure 6.2 – *(a) Measurement of the readout noise. A Gaussian function is fitted to the data (red curve). (b) Measurement of the background noise due to luminescence of the sample. The PDF given by Eq. (6.17) is fitted to the data (red curve). On each figure, a grey dashed line represents the baseline.*

Background noise Background mainly originates from the luminescence of the glass substrate, which is a consequence of the high excitation power used for the experiment. As we do not detect any luminescence signal from the silver nanowire, the function $q_b(x', y')$ is uniform over the whole frame. Therefore, we can define B as the expectation of the number of background photons impinging on each pixel during the acquisition time of one frame (30 ms). Since B does not depend on the presence of an active molecule on the frame, we can estimate B from the data acquired during the experiment. To this end, we measure the number of photoelectrons per pixel on the frames in which no molecule can be identified and we fit the PDF given by Eq. (6.17) to the data (Fig. 6.2b). As a result, we obtain an estimate of the number of background photons per pixel on each frame ($B = 21.9$). Such a number of photons approximately generates $g \times B \approx 2,000$ photoelectrons due to the multiplication register of the camera.

Measurement time For each molecule, we must estimate the measurement time Δt which corresponds to the time spent in the bright state by the molecule. Figure 6.3a shows the distribution of the measurement time Δt for each molecule, determined from the number of frames associated with each detection. The median value of this distribution is 2 frames, corresponding to a measurement time of 60 ms.

Number of fluorescence photons The number of photons detected from each molecule by the camera ranges from 150 to more than 10,000 fluorescence photons (Fig. 6.3b). The median value of this distribution is 1,228 photons, which means that a molecule is typically detected on 2 successive frames with 614 fluorescence photons detected on each frame. The distribution is truncated: as explained in Sect. 5.4.3, we use a threshold of 150 photons for the data analysis in order to discriminate between spurious and real events.

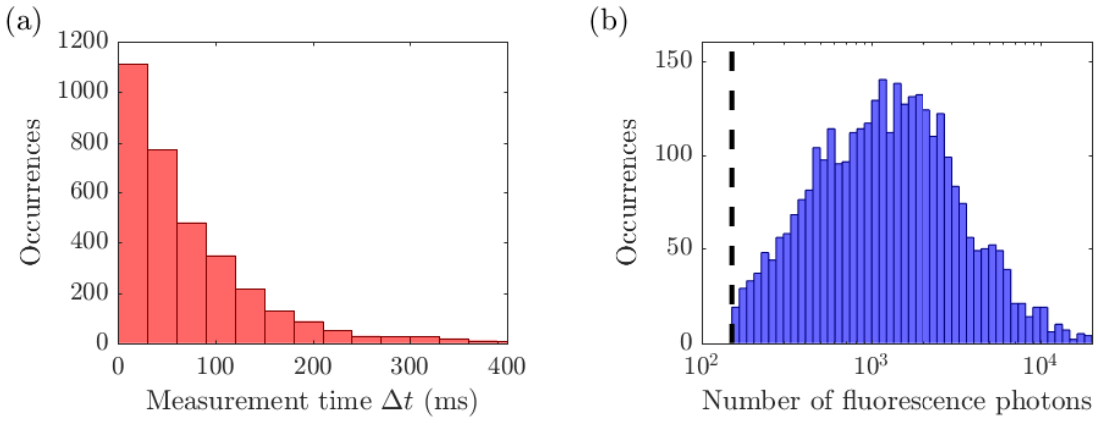

Figure 6.3 – *Distribution of (a) the measurement time Δt and (b) the number of photons detected from each molecule during the experiment. A red curve shows a log-normal fit to the data, and a dashed line represents the condition $N>150$ used for the data analysis.*

6.3.5 Numerical results

We can now compute the Cramér-Rao bound on the variance of position estimators using Eq. (6.8) in order to evaluate a lower bound on the standard error $\sigma_{x,y}$ on the position es-

timates performed using one frame. Assuming that there is no preferred direction in space – this is not exactly true because of the shape of the pixels, but is a good approximation for squared pixels – the Cramér-Rao inequality reads

$$\sigma_{x,y} \geq \sqrt{\frac{1}{\mathcal{I}_{xx}}} = \sqrt{\frac{1}{\mathcal{I}_{yy}}} \,. \tag{6.25}$$

In the experiment, a molecule is typically detected on two successive frames, as detailed in Sect. 6.3.4. Its position is then estimated by the mean of the individual estimates, so that the standard error on the resulting position estimate is $\sigma_{\bar{x},\bar{y}} = \sigma_{x,y}/\sqrt{2}$. We specifically perform the calculation of $\sigma_{\bar{x},\bar{y}}$ for the different hypothesis introduced in Sect. 6.3.2. The fundamental limit (Fig. 6.4, red curve) is calculated under the hypothesis $\mathcal{H}_l$: it only includes the shot noise and the finite size of the pixels. As expected, the Cramér-Rao bound decreases when the number of detected photons increases. The instrumental limit (Fig. 6.4, green curve) is calculated under the hypothesis $\mathcal{H}_e$. It is slightly larger than the fundamental limit since it also accounts for the readout noise of the camera and the noise introduced by the electron multiplying process. Note that the variance of the readout noise can actually be neglected due to the large gain value used in the experiment ($g = 100$). The actual experimental limit (Fig. 6.4, blue curve) is calculated under the hypothesis $\mathcal{H}_a$. It is significantly larger than the fundamental limit for a low number of detected photons. In this regime, a lower background would be appreciable to enhance the localisation precision. This could for instance be done by using a quartz substrate instead of glass.

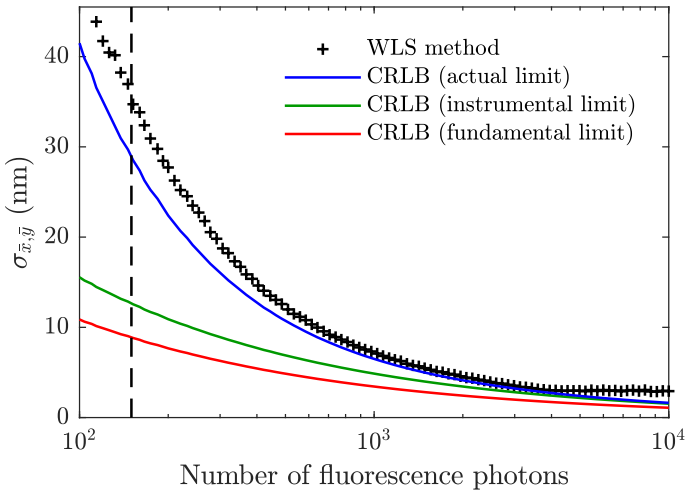

Figure 6.4 – *Cramér-Rao lower bound (CRLB) on the standard error on the position estimates as a function of the number of fluorescence photons detected by the camera, calculated for Δt=60 ms (2 frames). Dark blue points are the average square-root deviation of the position, retrieved using the weighted least-squares method. A dashed line represents the condition N>150 used for the data analysis.*

While the Cramér-Rao bound gives the lower bound on the standard error on position estimates, we can also characterise the variance of the actual estimator. To this end, we numerically generate a set of 10^4 frames with a fixed number of fluorescence photons N ranging from 100 to 10,000. This is performed by describing the number of events detected on each pixel with the PDF expressed by Eq. (6.17). We then calculate the cumulative distribution function and we use it to randomly generate numbers according

to the considered PDF based on the inversion principle [147]. The parameters used for the calculations are the ones described in Sect. 6.3.4. As in the actual experiment, we use the ImageJ plug-in ThunderStorm [113] to estimate the position of the molecules using the weighted least-squares (WLS) method. From these data, we compute the root-mean-square (RMS) deviation of the estimates as a function of the number of collected fluorescence photons (Fig. 6.4, black points).

As expected, the RMS deviation calculated using the actual estimator is always larger than the lower bound calculated using the information matrix. However, we can see that the variance of the estimator approaches the Cramér-Rao bound for a number of fluorescence photons around 1,000. For the median value of the measured distribution ($N = 1,228$), we obtain a RMS deviation of 6 nm while the Cramér-Rao bound on the standard error on the estimates is 5.5 nm. This provides us with an indication about the typical precision of position estimations performed in the experiment.

The RMS deviation saturates to approximately 3 nm for larger number of photons. This might be due to the fact that the estimator used by ThunderStorm fits a Gaussian function to a numerically-generated PSF that follows an Airy distribution. For this reason, we cannot entirely retrieve the information from the data using this estimator. Moreover, maximum-likelihood estimators are theoretically more efficient and could be used to enhance the localisation precision [148]. Considering the actual experiment, the achievement of a better localisation precision would certainly require to improve the model itself. It would notably be interesting to know the orientation of the dipole moment of the molecules and to investigate the modification of the radiation pattern by the nanostructure. From this knowledge, we would be able to improve the function used to model the measured PSF. This would ultimately enhance the localisation precision.

6.4 Precision of decay rate estimations

We can similarly calculate the Cramér-Rao bound on the variance of decay rate estimators in the context of single-molecule microscopy. We specifically study estimations based on the decay histograms acquired by a single photon avalanche photodiode (SPAD).

6.4.1 SPAD data model

In the weak-coupling regime, the PDF of the excited-state lifetime of a two-level system is a decreasing exponential function characterised by its decay rate Γ, as detailed in Sect. 1.2.2. By modelling a molecule by a two-level system, the PDF that describes the photon emission time t is given by

$$q_{fluo}(t) = \Gamma \exp(-\Gamma t) \, . \tag{6.26}$$

The decay rate of a given molecule may vary with time. This can happen if the molecule moves with respect to its local environment, or if the orientation of its dipole moment varies with time. In the experiment presented in Chapter 5, the molecules are attached to the substrate but they are likely to precess since they are in a liquid medium. Furthermore, the modification of the decay rate induced by the silver nanowire depends on the orientation of the dipole moment, as shown by the numerical results presented in Sect. 5.5.3. However, since the agreement between experimental data and the mono-exponential model is satisfactory, we assume here that the decay rate is constant over the whole measurement.

In an ideal experiment, an infinitely short laser pulse would excite a molecule and an ideal time-correlated single-photon counting (TCSPC) detection system would measure the photon detection time with an infinitely good precision. However, in a real experiment, the laser has a finite pulse duration. In addition, the TCSPC electronics induces a lost of precision over the photon detection time due to the jitter of the system. These two effects can be accounted for by measuring the IRF of the system, which is described by a PDF noted $q_{irf}(t)$. Therefore, the PDF followed by the photon detection time measured by the experimental system is

$$q(t) = q_{irf}(t) * [\Gamma \exp(-\Gamma t)] \ . \tag{6.27}$$

From this expression, we can find the expectation of each data item; that is, the expectation of each data point of the decay histogram. We obtain

$$f_i = N \sum_{l=0}^{+\infty} \int_{t_i+lT}^{t_{i+1}+lT} q(t)\,\mathrm{d}\,t + N_b \int_{t_i}^{t_{i+1}} q_b(t)\,\mathrm{d}\,t \ , \tag{6.28}$$

where N is the number of photons emitted by the molecule and detected by the system, N_b is the number of detected photons due to background noise which follows a PDF noted $q_b(t)$, and T is the repetition period of the laser. If the fluorescence lifetime of the molecule is much smaller than the repetition period, only the first term of the sum in Eq. (6.28) is significant.

In general, SPADs have negligible readout noise and the dark count rate contributes to the background noise. Thus, we can model the distribution of photons detected for each data point by a Poisson distribution of expectation f_i. The PDF associated with the observation of X events on a given data point is then expressed by

$$p_i(X;\boldsymbol{\theta}) = \frac{f_i^X}{X!} e^{-f_i} \ . \tag{6.29}$$

The set of parameters that must be estimated from the data is $\boldsymbol{\theta} = (N, \Gamma)$, while we estimate $q_{irf}(t)$, $q_b(t)$ and N_b with independent measurements.

6.4.2 Calculation of the information matrix

The likelihood functions $p_i(X;\boldsymbol{\theta})$ expressed by Eq. (6.29) are the same as in Eq. (6.14). The expression of the information matrix is consequently given by Eq. (6.24), namely,

$$[\boldsymbol{\mathcal{I}}(\boldsymbol{\theta})]_{jk} = \sum_{i=1}^{n} \frac{1}{f_i} \left(\frac{\partial f_i}{\partial \theta_j}\right) \left(\frac{\partial f_i}{\partial \theta_k}\right) \ . \tag{6.30}$$

We now make the change of variable $u = \Gamma t$ in order to obtain dimensionless quantities for the parameters involved in the calculations. In addition, we define the normalised repetition period $r = \Gamma T$ and the normalised intensity of background noise $\beta = N_b/(rN)$. Using the variable u, the PDF characterising the IRF and the background noise distribution are respectively

$$\tilde{q}_{irf}(u) = \frac{q_{irf}(u/\Gamma)}{\Gamma} \ , \tag{6.31a}$$

$$\tilde{q}_b(u) = \frac{q_b(u/\Gamma)}{\Gamma} \ . \tag{6.31b}$$

The calculation of the information matrix is performed in Appendix C in the more general case of a bi-exponential distribution with unknown background. Since the parameters to be estimated are here $\boldsymbol{\theta} = (N, \Gamma)$, the information matrix reduces to

$$\boldsymbol{\mathcal{I}}(\boldsymbol{\theta}) = \begin{pmatrix} \mathcal{I}_{NN} & \mathcal{I}_{N\Gamma} \\ \mathcal{I}_{N\Gamma} & \mathcal{I}_{\Gamma\Gamma} \end{pmatrix} , \tag{6.32}$$

where the matrix coefficients are expressed by

$$\mathcal{I}_{NN} = \frac{1}{N} \sum_{i=1}^{n} \frac{(J_i^{\mathrm{I}})^2}{J_i^{\mathrm{I}} + \beta J_i^{\mathrm{B}}} , \tag{6.33a}$$

$$\mathcal{I}_{\Gamma\Gamma} = \frac{N}{\Gamma^2} \sum_{i=1}^{n} \frac{(K_i^{\mathrm{I}})^2}{J_i^{\mathrm{I}} + \beta J_i^{\mathrm{B}}} , \tag{6.33b}$$

$$\mathcal{I}_{N\Gamma} = \frac{1}{\Gamma} \sum_{i=1}^{n} \frac{J_i^{\mathrm{I}} K_i^{\mathrm{I}}}{J_i^{\mathrm{I}} + \beta J_i^{\mathrm{B}}} , \tag{6.33c}$$

and $\mathbf{J}^{\mathrm{I}}$, $\mathbf{K}^{\mathrm{I}}$ and $\mathbf{J}^{\mathrm{B}}$ are defined as follows:

$$J_i^{\mathrm{I}} = \sum_{l=0}^{+\infty} \int_{u_i+lr}^{u_{i+1}+lr} [\tilde{q}_{irf}(u) * \exp(-u)] \, \mathrm{d}\, u , \tag{6.34a}$$

$$K_i^{\mathrm{I}} = \sum_{l=0}^{+\infty} \int_{u_i+lr}^{u_{i+1}+lr} [\tilde{q}_{irf}(u) * (1-u)\exp(-u))] \, \mathrm{d}\, u , \tag{6.34b}$$

$$J_i^{\mathrm{B}} = r \int_{u_i}^{u_{i+1}} \tilde{q}_b(u) \, \mathrm{d}\, u . \tag{6.34c}$$

In this case, the cross-terms of the information matrix must be considered. Physically, it means that a lack of information about one parameter influences the estimation precision of other parameters.

6.4.3 Experimental conditions

In order to calculate the information matrix associated with the experiment described in Chapter 5, we experimentally determine the value of the different parameters involved in the model. Let us review the characteristics of the experiment:

TCSPC system The resolution of the acquisition board is 16 ps and the repetition rate of the laser is 80 MHz; hence the repetition period is 12.5 ns and there are 782 data points.

IRF The PDF associated with the IRF – noted $q_{irf}(t)$ – is determined by removing the fluorescence filter between the sample and the SPAD. Figure 6.5a shows the resulting normalised decay histogram, characterised by a full width at half maximum (FWHM) of 240 ps.

Noise distribution The PDF noted $q_b(t)$ and followed by the number of events due to background noise is estimated by using different periods of time in which no molecule is detected. Figure 6.5b presents the measured histogram normalised as a PDF. This

noise strongly depends on the considered data point: indeed, we expect the detection of luminescence photons to be correlated to the laser pulses, since luminescence of the substrate is excited by the laser pulses.

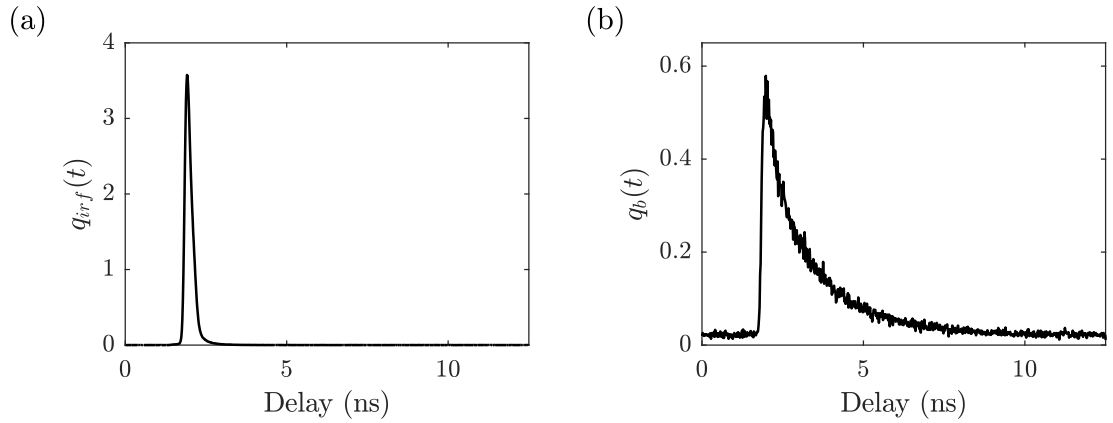

Figure 6.5 – *(a) Measurement of the IRF for the determination of the PDF noted $q_{irf}(t)$. (b) Decay histogram associated with background noise for the determination of the PDF noted $q_b(t)$.*

Background noise The intensity of background noise per repetition period is constant over the whole experiment, and the average noise intensity is $I_b = 1.21$ cts/ms. Let Δt be the time interval in-between photo-activation and photobleaching of a detected molecule. During this time interval, the expectation of the number of background photons is simply $N_b = I_b \Delta t$. Figure 6.6a shows the measured distribution of the measurement time Δt determined from SPAD data. Since the median value of this distribution is 66 ms, it follows that the typical value of N_b is 80 background photons per molecule detected. The measured distribution is similar to the distribution obtained using the EM-CCD images and shown in Fig. 6.3a. However, the temporal resolution offered by the SPAD is much better than the one of the camera, limited by the acquisition time of a frame (30 ms).

Number of fluorescence photons The number of fluorescence photons measured from each molecule ranges from 150 to 10,000, with a median value of 367 photons (Fig. 6.6b). This value is lower than the typical number of photons detected by the camera (1,228 photons). Indeed, due to the pinhole used on the optical path leading to the SPAD, fluorescence is partly filtered if the molecule is not exactly at the centre of the image of the pinhole on the sample plane. In addition, the quantum efficiency of the SPAD (~ 0.5) is lower than the one of the camera (~ 0.9). These two effects explain why the typical number of collected photons is lower for the SPAD. It should also be noted that SPAD measurements are more sensitive to the noise due to luminescence of the substrate. Noise is indeed integrated over a large effective area in the case of SPAD measurements – that is, the area conjugated to the chip of the detector. In contrast, this area is reduced to the area conjugated to one pixel in the case of camera measurements.

Since the SPAD typically detects a smaller number of fluorescence photons than the camera, the condition $N > 150$ used for the SPAD data analysis indirectly influences the distribution of the number of photons detected by the camera and previously

shown in Fig. 6.3b. For less than 1,000 photons detected by the camera from a given molecule, it becomes less likely that the corresponding number of photons detected by the SPAD fulfils the condition $N > 150$. In this regime, the distribution of the number of photons collected by the camera decreases when N decreases, as observed in Fig. 6.3b.

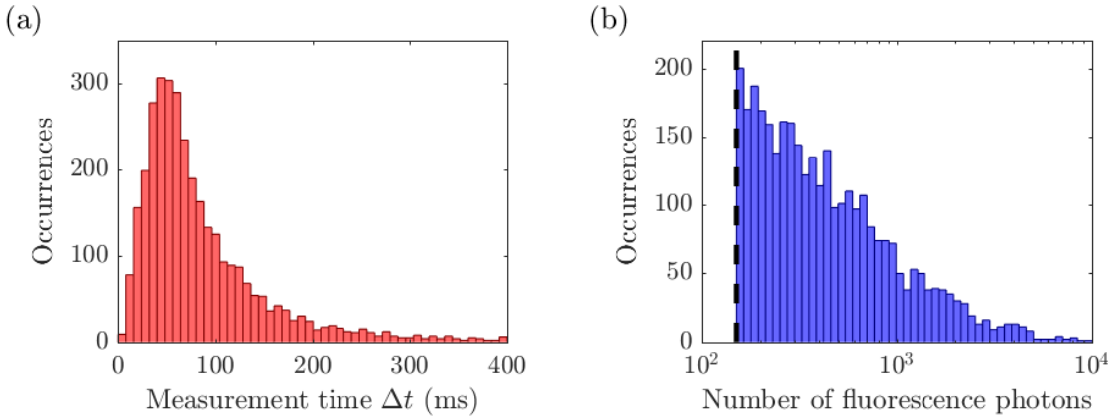

Figure 6.6 – *Distribution of (a) the measurement time Δt and (b) the measured number of photons from each molecule detected during the experiment. A model function (red curve) accounting for the pinhole transmission is fitted to the data. A dashed line represents the condition $N>150$ used for the data analysis.*

6.4.4 Numerical results

With these values for the parameters, we can use Eq. (6.8) to compute the Cramér-Rao bound on the standard error σ_Γ on the decay rate estimates. Using the notations introduced in Sect. 6.4.2, the Cramér-Rao inequality can be expressed as

$$\frac{\sigma_\Gamma}{\Gamma} \geq \frac{1}{\sqrt{N}} \times \psi\left(r, k, \tilde{q}_{irf}, \beta, \tilde{q}_b\right) \ , \tag{6.35}$$

where k is the number of data points per lifetime and ψ is calculated by inverting the information matrix. The function ψ describes the influence of the various parameters involved in the model on the value of the Cramér-Rao bound, as we will see in Sect. 6.5.2. It is always greater than unity and equals unity when the shot noise limit is reached.

Using this expression, we study the Cramér-Rao bound on the relative standard error σ_Γ/Γ as a function of the number of fluorescence photons detected by the SPAD. The experimental limit on the error is computed by taking into account the background noise calculated using $\Delta t = 66$ ms. We specifically calculate the Cramér-Rao bound assuming a relatively slow decay rate of $\Gamma = 0.7$ ns^{-1} (Fig. 6.7a, green curve), which is the typical decay of the molecules when they are located far away from the nanowire. For comparison purposes, we also calculate the Cramér-Rao bound assuming a faster decay rate of $\Gamma = 7$ ns^{-1} (Fig. 6.7a, blue curve). The fundamental limit on the relative standard error σ_Γ/Γ (Fig. 6.7a, red curve) is found by assuming that $\psi = 1$; that is, no background noise ($N_b = 0$), an ideal IRF as well as an infinite number of data points. We can observe that the Cramér-Rao bound on the relative standard error σ_Γ/Γ deviates from the fundamental limit when the number of measured fluorescence photons is low. This effect is due to the

background noise, as already observed in Sect. 6.3.5 when we calculated the Cramér-Rao bound on the variance of position estimators. We also observe that the influence of the IRF is larger for $\Gamma = 7$ ns^{-1} than for $\Gamma = 0.7$ ns^{-1}. For $\Gamma = 7$ ns^{-1}, the excited-state lifetime is indeed reduced to 140 ps and becomes comparable to the FWHM of the IRF (240 ps), thus reducing the amount of information given by each data item.

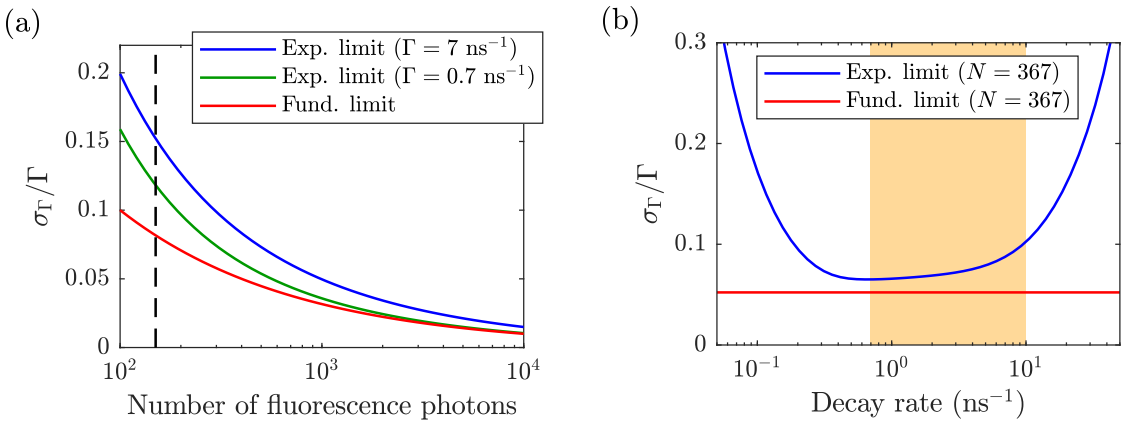

Figure 6.7 – *(a) Cramér-Rao bound on the standard error on the decay rate estimates as a function of the number of fluorescence photons. A dashed line represents the condition $N>150$ used for the data analysis. (b) Cramér-Rao bound on the standard error on the decay rate estimates as a function of the decay rate. An orange tinted area represents the range of values determined in the experiment.*

Whereas the fundamental limit on the relative standard error on the decay rate estimates does not depend on Γ, the introduction of a finite IRF and a non-uniform background noise induces a dependence of the relative standard error upon Γ. To demonstrate this effect, we study the lower bound on the relative standard error σ_Γ/Γ as a function of the decay rate Γ for $N = 367$ photons (Fig. 6.7b). The Cramér-Rao bound on the relative standard error is large when Γ is large, due to the influence of the IRF. In this regime, we could improve the precision of the estimations by using a detection system with a smaller jitter and an excitation laser with a shorter pulse width. The Cramér-Rao bound on the relative standard error also increases when Γ is small. In this regime, the background noise has a large influence, because the expected numbers of background and fluorescence photons are on the same order of magnitude for every point of the decay histogram. This is not the case for larger Γ, because most of the fluorescence photons are then measured within a short time, resulting in a higher signal-to-noise ratio for the first data points. Importantly, the Cramér-Rao bound on the absolute standard error σ_Γ becomes larger than 1 ns^{-1} for $\Gamma > 10$ ns^{-1}. This justifies the threshold used in Sect. 5.5.1 to present the decay rate map of the molecules around the silver nanowire.

We can also study the variance of the actual estimators using numerically generated data. To do so, we numerically generate a set of 10^4 decay histograms with a fixed number of fluorescence photons N ranging from 100 to 10,000 photons and with $\Delta t = 66$ ms. Each histogram is then analysed in order to estimate the decay rate using two different algorithms based on least-squares minimisation, the first one with no weights and the second one taking the results of the first estimation to compute the weight of each data point. For comparison purposes, a third algorithm based on maximum likelihood estimation is also tested. Finally, we compute the RMS deviation of the estimates for each value of N.

By comparing the Cramér-Rao bound to the calculated RMS deviations for $\Gamma = 7$ ns^{-1} (Fig. 6.8a) and $\Gamma = 0.7$ ns^{-1} (Fig. 6.8b), we can see that the efficiency of the estimators based on the weighted least-squares (WLS) and on the maximum likelihood (ML) methods is good for any number of detected fluorescence photons. In contrast, the estimator based on the least-square (LS) method is less efficient, especially for a low number of detected photons. For $N = 367$ photons and $\Gamma = 0.7$ ns^{-1}, the RMS deviation calculated using the LS method is of 10%, while the Cramér-Rao bound on the relative standard error is of 7%. For $\Gamma = 7$ ns^{-1}, these values increase to 12% for the LS method and 9% for the Cramér-Rao bound. The decay rate of the molecules is actually estimated using the LS method in the experiment: indeed, the algorithm based on the LS method is more robust with respect to any deviation from the model. We could use a WLS method or a ML method to estimate the decay rate of the molecules with a better efficiency. To this end, it would however be required to consider possible deviations from the mono-exponential model assumed in the analysis.

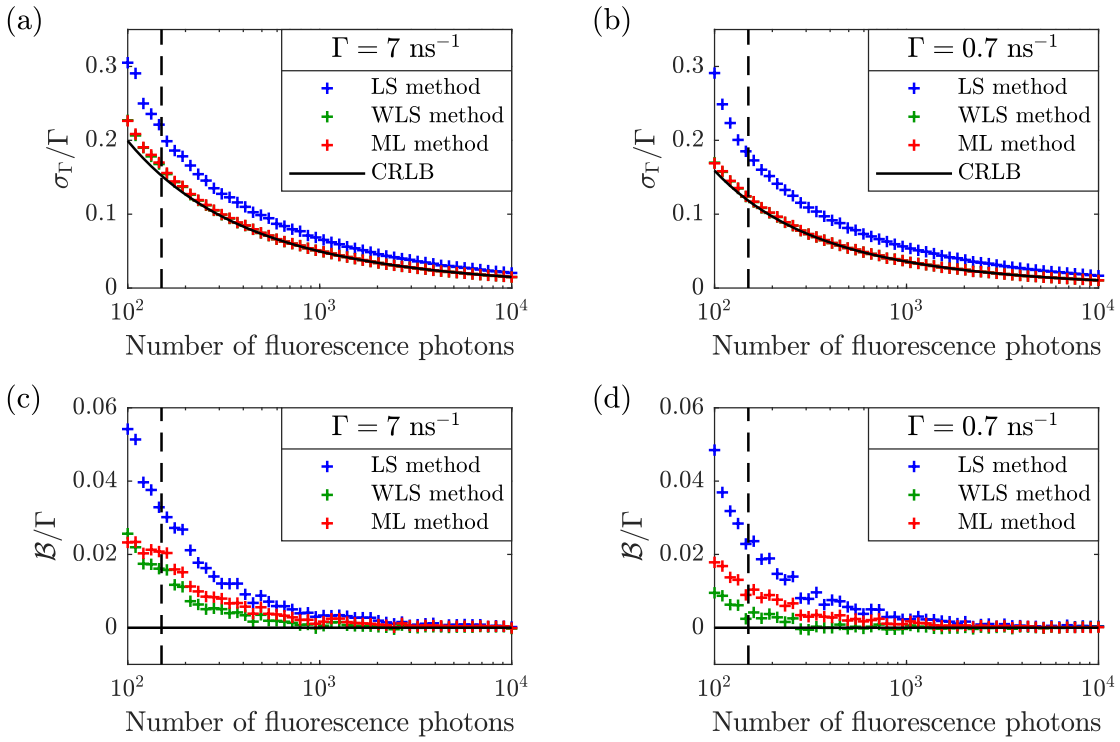

Figure 6.8 – *Test of the estimators based on the least-squares and weighted least-squares methods. Dashed lines represent the condition N>150 used for the data analysis.*

Additionally, we can also evaluate the bias $\mathcal{B}$ of each estimator, as defined by Eq. (6.3). Therefore, we study $\mathcal{B}/\Gamma$ as a function of the number of detected fluorescence photons N for $\Gamma = 7$ ns^{-1} (Fig. 6.8c) and $\Gamma = 0.7$ ns^{-1} (Fig. 6.8d). We observe that the bias is larger for a low number of photons N and is always positive, which means that we tend to overestimate Γ when a few photons are collected from the molecules. As expected, we also observe that the bias of the WLS and ML estimators is smaller than the bias of the LS estimator.

6.5 Towards an optimisation of the experimental setup

In this section, we discuss the importance of several parameters by calculating the Cramér-Rao bound for different configurations of the experimental setup. It should be mentioned that the Cramér-Rao bounds on the relative standard error on the decay rate estimates σ_Γ/Γ and on the lifetime estimates σ_τ/τ are strictly the same, as shown in Appendix C. Hence results concerning decay rate estimators also apply to lifetime estimators.

6.5.1 Beamsplitter transmission

In the experiment described in Chapter 5, a 50:50 beamsplitter allows the detection of fluorescence photons by both the EM-CCD camera and the SPAD. By changing the transmission-reflection features of the beamsplitter, we can decide to promote either position or decay rate estimations, as the number of collected photons determines the achievable precision. To show this effect, we study the influence of the beamsplitter transmission upon the Cramér-Rao bound on the standard error on position and decay rate estimates. We perform the calculation of $\sigma_{\bar{x},\bar{y}}$ and σ_Γ by using the typical values of the experimental parameters, as detailed in Sects. 6.3.4 and 6.4.3. Transmitted and reflected photons are respectively directed towards the SPAD and the camera. Figure 6.9 shows that a wide range of beamsplitter transmissions can allow a reasonable precision of both position and decay rate estimation. For a transmission of 0.1, we obtain $\sigma_{\bar{x},\bar{y}} = 4.5$ nm and $\sigma_\Gamma/\Gamma = 14\%$. For a transmission of 0.9, these values are $\sigma_{\bar{x},\bar{y}} = 13$ nm and $\sigma_\Gamma/\Gamma = 5\%$. From these considerations, one can choose the appropriate beamsplitter depending on the expected decay rate variations and the desired spatial resolution.

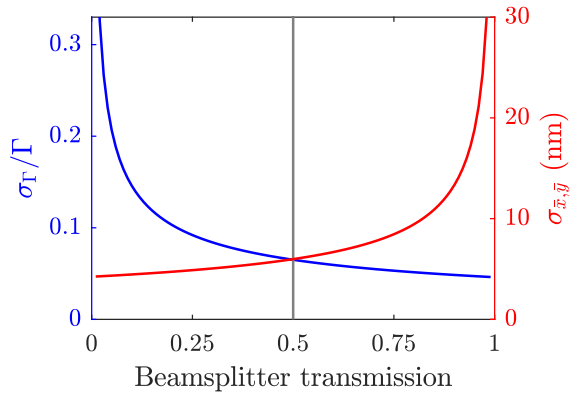

Figure 6.9 – *Cramér-Rao bound on the standard error on decay rate (blue curve) and position (red curve) estimates. A grey line represents the current configuration of the experiment (a 50:50 beamsplitter).*

6.5.2 Optimisation of the TCSPC setup

We now turn into more general considerations and we discuss the experimental conditions required to obtain a satisfying estimation precision. Since an exhaustive literature on the subject is already available for position estimations [18, 131, 134], we focus here on decay rate estimations. The Cramér-Rao inequality is expressed by Eq. (6.35) in the case of

a mono-exponential distribution. As already mentioned, the function ψ is calculated by inverting the information matrix and describes the influence of the different parameters involved in the model on the value of the Cramér-Rao bound. It is always greater than unity and equals unity when the shot noise limit is reached. It is therefore interesting to study how ψ varies as a function of the parameters involved in the model in order to identify best practices for designing a TCSPC setup. Table 6.1 summarises the parameters used in the model. In the third column, we recall the definitions of the dimensionless parameters constructed using N and Γ as references. We can therefore study how ψ varies as a function of the number of data points k, the repetition period r, the PDF associated with the IRF noted $\tilde{q}_{irf}(u)$ and the level of background noise β. In the following paragraphs, we will study the influence of each parameter upon the function ψ. To this end, the value of all the other parameters will be set in order to approach the fundamental limit of the Cramér-Rao bound. As an illustration, we compare these results to the conditions of the experiment previously analysed[4].

	Parameters	Dimensionless parameters
Fluorescence decay	N and Γ	
Repetition period	T	$r = \Gamma T$
Number of data points	n	$k = n/r$
Instrument response function	$q_{irf}(t)$	$\tilde{q}_{irf}(u)$
Background noise	N_b and $q_b(t)$	$\beta = N_b/(rN)$ and $\tilde{q}_b(u)$

Table 6.1 – *Parameters involved in the TCSPC data model for a mono-exponential distribution.*

Noise intensity Figure 6.10a presents the dependence of ψ on the dimensionless parameter describing background noise β, which is defined as the number of background photons measured in one fluorescence lifetime divided by the total number of fluorescence photons. Assuming uniform background noise, an ideal IRF, a large number of data points and a large repetition period, we can use the integral form of the information matrix expressed by Eq. (C.20). In this case, the function ψ only depends on β, and the influence of background noise on the precision of the estimations is small ($\psi < 1.2$) when $\beta < 0.01$. These results indicate that the contribution of background noise is significant in the experiment, as β ranges from 0.01 to 1.

Number of data point Figure 6.10b presents the dependence of ψ on the number of data points per lifetime k. This parameter is set by the resolution of the acquisition board. For the calculations, we assume a large repetition period ($r = 100$) and an ideal IRF. Without noise, $k > 10$ is largely sufficient to achieve the best possible precision ($\psi < 1.0004$). The presence of uniform noise slightly increases the number of points required to obtain a good precision of decay rate estimations. These results indicates that the number of data point is sufficient in the experiment, as k ranges from 6 to 90.

[4]This is only an approximation, since the calculations are performed assuming different idealised versions of the experiment. The analysis corresponding to the actual experimental conditions was presented in Sect. 6.4.4.

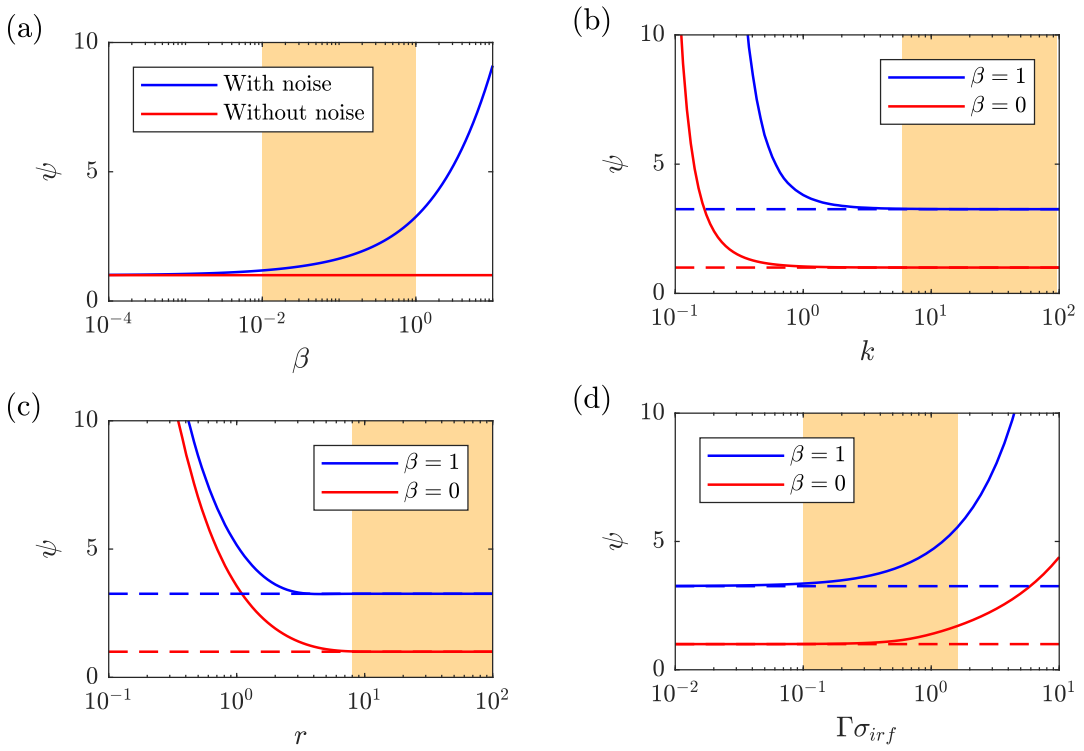

Figure 6.10 – *Study of the precision of decay rate estimations as a function of (a) the noise intensity, (b) the number of data point, (c) the repetition period and (d) the standard deviation of the IRF. Dashed lines represent the asymptotic values. On each figure, an orange tinted area represents the range of values relevant to the experiment.*

Repetition period Figure 6.10c presents the dependence of ψ on the number of fluorescence lifetimes r per repetition period. This parameter is set by the repetition rate of the pulsed laser. For the calculations, we use a large number of data points ($k = 500$) and an ideal IRF. Without noise, $r > 5$ is required in order to achieve a good precision of decay rate estimations ($\psi < 1.1$). In the presence of uniform noise, the repetition period has a similar influence on ψ in comparison to the background-free case. These results indicate that the repetition period is large enough in the experiment, as r ranges from 8 to 125.

Instrument response function We model the IRF by an inverse Gaussian distribution, defined by the mean of the distribution μ and a shape parameter λ. This distribution is defined on $]0, +\infty[$ and its standard deviation σ_{irf} equals $\sqrt{\mu^3/\lambda}$. Performing the change of variable $u = \Gamma t$, we obtain for $\tilde{q}_{irf}$ the following expression:

$$\tilde{q}_{irf}(u) = \sqrt{\frac{\lambda_g}{2\pi u^3}} \exp\left(\frac{-\lambda_g (u - \mu_g)^2}{2\mu_g^2 u}\right) , \tag{6.36}$$

where $\lambda_g = \lambda\Gamma$ and $\mu_g = \mu\Gamma$. Figure 6.10d shows the influence of the standard deviation of $\tilde{q}_{irf}$ – which is equal to $\Gamma\sigma_{irf}$ – on the precision of decay rate estimations. For the calculations, we use a large repetition period ($r = 100$) as well as a large number of data points ($k = 500$). As expected, the precision of decay rate estimations is good ($\psi < 1.4$) when $\Gamma\sigma_{irf}$ is smaller than unity. In the presence of uniform noise, the standard deviation of the IRF has a larger influence on ψ than in the background-free case. These results

indicate that the contribution of the IRF can be significant in the experiment, as $\Gamma\sigma_{irf}$ ranges from 0.1 to 1.5.

6.5.3 TCSPC models with several unknown parameters

In Sects. 6.4 and 6.5.2, we calculated the information matrix assuming that the decay histogram follows a mono-exponential distribution and that all the parameters except N and Γ are precisely estimated from independent measurements. This model can be extended to any time-dependence of the decay histogram with any number of unknown parameters. In Appendix C, we show the calculation of the information matrix for a bi-exponential distribution with 5 unknown parameters, namely, the decay rates and the numbers of fluorescence photons characterising each decay as well as the number of photons due to background noise. In the following paragraphs, we will detail two particular cases: the mono-exponential model with unknown noise intensity and the bi-exponential model.

Mono-exponential model with unknown noise intensity Let us assume that the decay histogram follows a mono-exponential distribution and that the set of unknown parameters are $\boldsymbol{\theta} = (N, \Gamma, N_b)$. In this case, it is important to use a large repetition period in comparison to the fluorescence lifetime of the emitter, in order to estimate N_b with a good precision. If this condition is not satisfied, the precision of the estimations for all the parameters is degraded. To show this effect, we calculate the value of ψ as a function of r when the expectation of N_b is known or unknown (Fig. 6.11a). For the calculations, we use a large number of data points ($k = 500$), an ideal IRF and uniform background noise. We observe that the precision of decay rate estimations dramatically decline for small values of r when the noise intensity is unknown. In the case the expectation of N_b is known and for $\beta = 1$, the value of ψ exceed the asymptotic value by a factor of 10% if the repetition period of the laser is equal to twice the lifetime of the emitter ($r = 2$). In the case the expectation of N_b is unknown and for the same level of noise, $r = 13$ is required to achieve the same precision of decay rate estimation. This clearly highlights the importance of independently estimating the background intensity whenever high repetition rates are used. In the range of values relevant to the experiment, estimating the number of background photons from independent measurements actually improves the precision of decay rate estimations. Indeed, for $\beta = 1$ and $r = 8$, we obtain $\psi = 3.9$ if N_b is unknown whereas $\psi = 3.3$ if N_b is known.

Bi-exponential model In the mono-exponential model, the PDF describing the time of emission of a photon is given by Eq. (6.26). We now assume that the decay histogram follows a bi-exponential distribution characterised by two decay rates Γ_1 and Γ_2 so that the lifetime PDF becomes

$$q_{fluo}(t) = \eta_1\Gamma_1 \exp(-\Gamma_1 t) + \eta_2\Gamma_2 \exp(-\Gamma_2 t) \,, \tag{6.37}$$

where η_1 and η_2 respectively characterise the contribution of each decay. Let N be the total number of collected fluorescence photons. We suppose that the set of unknown parameters is $\boldsymbol{\theta} = (N_1, \Gamma_1, N_2, \Gamma_2)$ where $N_1 = \eta_1 N$ and $N_2 = \eta_2 N$. In this case, the Cramér-Rao bound reads

$$\frac{\sigma_{\Gamma_1}}{\Gamma_1} \geq \frac{1}{\sqrt{N_1}} \times \psi\left(\alpha, \gamma, r, k, \tilde{q}_{irf}, \beta, \tilde{q}_b\right) \,, \tag{6.38}$$

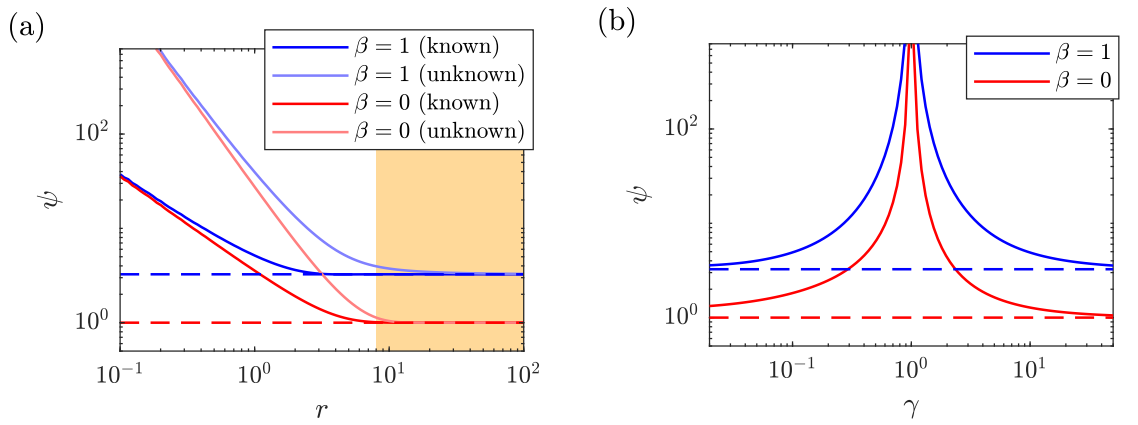

Figure 6.11 – *(a) Study of the precision of decay rate estimations as a function of r when β is known (dark curves) and β must be estimated from the data (light curves). Dashed lines represent the asymptotic values, and an orange tinted area represents the range of values relevant to the experiment. (b) Study of the precision of decay rate estimations as a function of γ. Dashed lines represent the asymptotic values, corresponding to the mono-exponential cases.*

where $\alpha = N_2/N_1$ and $\gamma = \Gamma_2/\Gamma_1$. Notably, the precision of decay rate estimations strongly depends on the ratio of the two decay rates γ, as shown in Fig. 6.11b. For the calculations, we use $\alpha = 1$ as well as a large number of data points ($k = 500$), a large repetition period ($r = 100$), an ideal IRF and a uniform background noise. We observe that ψ tends to infinity for γ close to unity. Indeed, a large number of photons is required to obtain a satisfactory precision when the ratio between the two decay rates approaches one. In contrast, when the two decay rates differ by more than one order of magnitude, ψ approaches the theoretical limit given by the mono-exponential model. Let us compare the precision of decay rate estimations in the absence of noise for a mono-exponential and a bi-exponential distribution. In the mono-exponential case, the Cramér-Rao bound on the relative standard error is 10% for $N = 100$ photons. The same relative standard error is achieved in the bi-exponential case for $N = 1,000$ photons if $\Gamma_2 = 1.5\,\Gamma_1$ and for $N = 10,000$ photons if $\Gamma_2 = 1.1\,\Gamma_1$.

In a nutshell, a large number of photons is generally required to get a satisfactory precision if many parameters are unknown. In practice, we can use independent measurements to enhance the estimation precision of one or several given parameters. Then, the information matrix is the sum of the information matrices calculated from each independent measurement.

6.6 Conclusion

In this chapter, we used the Fisher information to calculate the lower bounds on the variance of position and decay rate estimators. Thus, we were able to assess the precision of the estimations performed in Chapter 5. To start with, we modelled the data measured by the EM-CCD camera and we calculated the information matrix associated with actual experimental conditions. We studied how the lower bound on the standard error on the position estimates depends on the number of fluorescence photons (Fig. 6.4), and we

tested the algorithm used to retrieve the position of the molecules. From these results, we showed that the typical standard error on the position estimates is of the order of 6 nm in the experiment. Then, we used the same strategy to evaluate the precision of decay rate estimations. We studied how the lower bound on the standard error on the position estimates depends on the number of fluorescence photons (Fig. 6.7a) but also on the value of the decay rate (Fig. 6.7b). We tested the algorithm used to estimate the decay rates and we showed that the typical relative standard error on the decay rate estimates is of the order of 10-12%. Finally, we discussed the experimental conditions required to obtain a good precision of the estimations. We highlighted that the Fisher information cannot be used to accurately determine the precision of the estimations, as it depends on the actual estimator used for the data analysis. Moreover, we also discussed the approximations used to model the measured PSF by an Airy function and the PDF of the excited-state lifetime by a decreasing exponential function. The elaboration of a more advanced model would require a full characterisation of the interaction between the molecules and their environment, including a precise knowledge of the orientation of the dipole moment of the molecules.

We pointed out that a lack of information about one parameter influences the estimation precision of other parameters if the cross-terms of the information matrix are non-zero. In the case of position estimations, the cross-terms of the information matrix are zero due to the symmetry properties of the PSF. In contrast, the cross-terms are non-zero for decay rate estimations, even in the mono-exponential case. This is mainly due to the difficulty of simultaneously estimating the number of fluorescence photons and the intensity of background noise from a decay histogram. In the experiment, background noise can be estimated from an independent measurement, and the respective contribution of signal and noise can be precisely determined. As a result, cross-terms do not significantly contribute to the variance of decay rate estimates. Cross-terms strictly equal zero in the case of background-free estimations, as we can see from Eq. (C.21).

The results presented in this chapter inform us about the experimental features which can be improved to optimise the precision of the estimations. For instance, the general result expressed by Eq. (6.38) provides us with a valuable tool for the optimisation of a TCSPC setup, as it allows the direct calculation of a reliable benchmark for the precision of decay rate estimations. Indeed, the calculation of the Cramér-Rao bound allows to easily identify the parameters that must be optimised in order to achieve precise, shot-noise limited estimations, as we did in Sects. 6.3.5 and 6.4.4 in the context of the experiment presented in Chapter 5. We notably showed that the IRF is a limitation for the estimation of decay rates higher than 10 ns^{-1}. We also showed that the noise due to luminescence has a large impact on both the position and decay rate estimations if the number of collected fluorescence photons is small. Note that we could easily calculate the lower bound on the variance of intensity estimators that would be used to estimate the number of fluorescence photons emitted by a molecule and detected by the detectors. Using the same mathematical framework, we could also characterise any deviation of the excited-state lifetime distribution to a reference situation.

General conclusion and perspectives

In this thesis, we studied different aspects of spontaneous emission and energy transfer in the near field of nanostructured materials. We now summarise the main results, and we present some perspectives.

As an introduction, we presented a classical description of the interaction between fluorescent emitters and their environment (Chapter 1). With a Green function formalism, we obtained simple analytical expressions for several physical quantities relevant to the experiments presented in this thesis, including the decay rate of a quantum emitter and the rate of energy transfer between two emitters. We recalled that, while the decay rate of an emitter is proportional to the local density of states (LDOS) at the emission frequency, the rate of energy transfer between two emitters is proportional to the absolute square of the dyadic Green function at the transfer frequency. We also discussed near-field and far-field approaches to fluorescence microscopy. With a far-field microscope, the position of a fluorescent emitter must be estimated from the intensity detected in the image plane. In contrast, a scanning near-field optical microscope with an active probe can be used to achieve a deterministic control over the emitter's position.

By tuning the environment of fluorescent emitters, both the rate and the range of energy transfer can be strongly enhanced. Based on this idea, we showed that simple plasmonic nanostructures can be used to achieve micrometre-range energy transfer between fluorescent emitters. We specifically investigated plasmon-mediated energy transfer in two configurations, a thin silver film (Chapter 2) and a silver nanowire (Chapter 3). In the thin film configuration, we determined the distance dependence of the energy transfer rate using spectral measurements, and we demonstrated that this rate directly depends on the surface-plasmon propagation length at the transition energy of the emitters. Moreover, we used the Green formalism to estimate the energy transfer rate in the experiment. From these calculations, we identified different ranges of interaction specific to plasmon-mediated energy transfer. In the nanowire configuration, we presented an experimental demonstration of energy transfer occurring between a single quantum dot (QD) and fluorescent molecules embedded inside a nanobead, located 8.7 µm away. We showed that the decay histogram of the acceptor measured during the experiment is determined by the convolution of the decay histograms of the donor and the acceptor independently excited. In addition, we demonstrated the existence of a positive correlation on the millisecond

time scale in the intensities measured from the quantum dot and the bead, which attests that the blinking of the quantum dot and the bead is correlated while they are located several micrometres away from each other. These results constitute an indirect evidence of the occurrence of energy transfer mediated by single plasmons. As a direct evidence, we expected an anticorrelated emission between the QD and the acceptor on the nanosecond time scale, but its observation was hindered by the noise level due to the weak efficiency of the energy transfer process. Indeed, plasmonic waveguides are characterised by significant propagation losses due to ohmic losses. Moreover, the coupling of the emitters to surface plasmons modes competes with other decay processes, such as free-space emission and quenching.

In this context, a stimulating perspective is to use hybrid plasmonic-dielectric waveguides for the realisation of long-range energy transfer, as proposed in Ref. [38]. In this scheme, two emitters coupled to plasmonic antennas could interact over a large range of distances via the guided modes of a dielectric waveguide. Propagation losses would be much smaller as compared to a plasmonic waveguide, and antennas would allow an efficient coupling of the emitters to the guided modes of the waveguide. Work in this direction is already in progress at Institut Langevin. A project in collaboration with Université de Technologie de Troyes relies on the association of a TiO_2 waveguide with two triangular plasmonic antennas. Another approach in collaboration with Laboratoire Kastler Brossel involves two gold nanorods located on a stretched optical fibre. In both cases, a challenging task will be to precisely position the emitters in the near field of the plasmonic antennas. To this end, a possible solution relies on placing the emitters on the antennas by nano-manipulation using the homebuilt near-field optical microscope described in this thesis. Several techniques could alternatively be implemented to precisely depose the emitters on the antennas, such as photo-lithography [149], electro-hydrodynamic printing [150], or electron beam lithography combined with chemical functionalisation [151]. These plateforms could ultimately be used to perform interesting experiments involving an efficient coupling between two distant quantum emitters. For instance, a long-distance entanglement was recently observed between two SiV centres inside a photonic crystal cavity [152]. This experiment was performed at cryogenic temperature, but the recent observation of plasmon-mediated superradiance at room temperature raises the question of the robustness of superradiance against temperature-induced decoherence [153].

Most of the time, optical antennas are made of plasmonic materials, which provide a deeply subwavelength mode volume due to plasmon resonances. However, the rate of photons emitted by a nearby emitter is generally reduced by quenching due to ohmic losses in the metal. As a lossless alternative to plasmonic antennas, we investigated the possibility to take advantage of Mie resonances in order to build antennas at optical frequencies using dielectric materials (Chapter 4). To this end, we performed a three-dimensional analysis of the near-field interaction between a fluorescent nanobead and two different antennas using a scanning probe microscope. We showed that dielectric antennas can either increase or decrease the fluorescence decay rate, and we detected spatial variations of the measured fluorescence intensity due to the directivity properties of the antennas and their ability to modify the excitation field. The observed decay-rate variations were weak in comparison to the variations that can be observed by using plasmonic antennas, but numeral simulations performed by Mathieu Mivelle at Institut des NanoSciences de Paris (INSP) showed that a larger enhancement is expected when the emitter is located inside the antenna. Moreover, dielectric antennas are able to interact with both the electric and the magnetic part of the field. Hence, it would be interesting to use emitters with a strong magnetic dipole

transition for the study of dielectric antennas with non-overlapping electric and magnetic Mie modes. The coupling of europium ions to dielectric hollow nanocylinders is currently studied at INSP. By means of near-field scanning-probe microscopy, it should be possible to assess the relative importance of electric and magnetic dipole emission. This work could ultimately allow to tune both the electric and magnetic decay rate using a lossless antenna.

While scanning near-field optical microscopy allows a deterministic control over the position of a fluorescent emitter, the technique remains difficult to implement. Moreover, in some cases, the interaction between the tip and the structure can perturb the measurement and provoke sample damage. We proposed an alternative approach for the determination of the fluorescence decay rate of photo-activated single molecules and their respective positions (Chapter 5), with a localisation precision of the order of 10 nm. The technique is implemented by splitting the fluorescence intensity towards two different detectors, a camera and a single-photon avalanche photodiode (SPAD). As a proof-of-principle experiment, we studied the interaction between fluorescent molecules and a silver nanowire. By ensuring that no more than one molecule was typically active at a time on the area conjugated to the SPAD, we could associate the position of more than 3,000 single molecules with their decay rate from data acquired during a 10-hour-long experiment. We detected decay rate variations well below the diffraction limit, with an enhancement by at least a factor of 15 in the vicinity of the nanowire. In the context of this experiment, we used the Fisher information to assess lower bounds on the precision of the estimations (Chapter 6). We calculated the Cramér-Rao lower bounds on the variance of both position and decay rate estimators, and we compared them to numerically generated data in order to estimate the performances of the estimators used for the analysis of experimental data. We also provided some guidelines to design the experimental setup, primarily focusing on decay rate estimations using time-resolved single-photon detection. We notably discussed the influence of the instrument response function and the repetition rate of the laser upon the estimation precision. We also highlighted that the trade-off between the precision of position and decay rate estimations can be controlled by choosing the appropriate beamsplitter depending on the expected decay rate variations and the desired spatial resolution.

This technique is an interesting tool to investigate light-matter interaction, as it provides a direct characterisation of the LDOS with a strongly sub-wavelength resolution. While the study of resonant antennas can be complicated due to the mislocalisation of the fluorescent emitters involved in the emission process, the technique can directly be applied to the study of non-radiative processes such as quenching. We also expect this technique to open interesting possibilities in the field of biology, as it allows to access the contrast provided by the modification of the excited-state lifetime of fluorescent emitters (as in fluorescence-lifetime imaging microscopy) with a high localisation precision (as in photo-activated localisation microscopy). For instance, this technique could be used to precisely map different parameters on biological samples such as the viscosity, the pH or the interaction between two proteins tagged with fluorescent emitters via the lifetime variations induced by the occurrence of Förster resonance energy transfer (FRET). For such applications, the estimation of lower bounds on the variance of lifetime estimators will be helpful to design experimental setups allowing shot-noise limited estimations. Since most biological applications will require to increase the field of view of the technique, the utilisation of SPAD arrays is currently investigated at Institut Langevin, in collaboration with Politecnico di Milano. Different strategies for the axial localisation of the fluorescent molecules are also considered. Using a cylindrical lens to induce an asymmetry in the point spread

function is a possibility, but another technique based on the decay rate variations induced by a gold film could be used to achieve a higher axial localisation precision [125]. In this configuration, the in-plane localisation would be performed from the measured point spread function, while the axial position would be estimated from the decay rate of the emitter. Thus, it should be possible to perform a precise three-dimensional localisation of photo-activated molecules, with a lateral precision of 10 nm and an axial precision of the same order of magnitude.

Appendices

APPENDIX A

Dyadic Green function at an interface

A.1 Definition of the problem

We are interested in the spatial distribution of the electric field generated by a dipole in the near field of a silver mirror. This problem can be solved by finding the reflected part of the dyadic Green function at an interface $\mathbf{G}_{11}(\mathbf{r}_1, \mathbf{r}_2, \omega)$. In the general case, the Green tensor depends on the position of the emitter $\mathbf{r}_1 = (x_1, y_1, z_1)$, the position of the receptor $\mathbf{r}_2 = (x_2, y_2, z_2)$ and the frequency of the light ω. The geometry of the problem is represented in Fig. A.1.

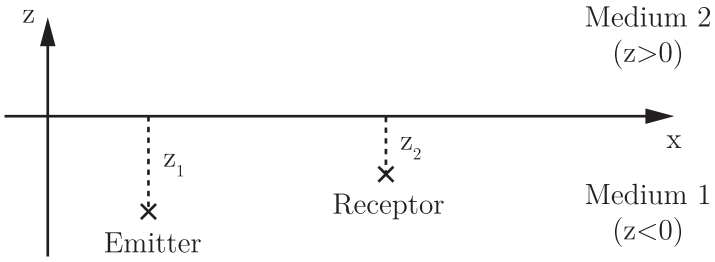

Figure A.1 – *Geometry of the problem.*

$\mathbf{G}_{11}(\mathbf{r}_1, \mathbf{r}_2, \omega)$ can be decomposed as the sum of the homogeneous Green tensor $\mathbf{G}_0$ and the contribution due to the field scattered by the interface $\mathbf{S}_{11}$. Due to the symmetry in the geometry, the scattered Green tensor only depends on z_1,z_2, ω and $d = \|\mathbf{r}_1 - \mathbf{r}_2\|$, while the homogeneous green tensor only depends on d and ω. This reads

$$\mathbf{G}_{11}(\mathbf{r}_1, \mathbf{r}_2, \omega) = \mathbf{G}_0(d, \omega) + \mathbf{S}_{11}(d, z_1, z_2, \omega) \; . \tag{A.1}$$

The development of an expression for the homogeneous Green tensor can be found for instance in the work of Levine and Schwinger [154]. For $d \neq 0$, it is expressed as

$$\mathbf{G}_0(d, \omega) = \frac{\exp(ikd)}{4\pi d} \left[\mathbf{I} - \mathbf{u} \otimes \mathbf{u} + \frac{ikd - 1}{(kd)^2} (\mathbf{I} - 3\mathbf{u} \otimes \mathbf{u}) \right] \; , \tag{A.2}$$

where $\mathbf{I}$ is the unit dyadic, $\mathbf{u} = (\mathbf{r}_1 - \mathbf{r}_2)/d$ and $k = n\omega/c$. For $d = 0$, the real part of the homogeneous Green tensor is singular [155] but its imaginary part has a finite limit which reads as follows:

$$\lim_{d\to 0} \left(\mathrm{Im}\left\{\mathbf{G}_0(d,\omega)\right\}\right) = \frac{k}{6\pi}\mathbf{I}\,. \tag{A.3}$$

A.2 Notations

In order to develop an expression for $\mathbf{S}_{11}$, we consider an interface between two media of respective index $n_i = \sqrt{\epsilon_i}$ and an incident plane wave of a given amplitude defined by its wavevector $\mathbf{k}_1^+ = (\mathbf{K}, \gamma_1)$. From the conservation of the transverse components of the wavevector $\mathbf{K} = (k_x, k_y)$, the magnitude of the longitudinal wavevector in both media is given by

$$\gamma_i = \sqrt{k_i^2 - K^2}\,, \tag{A.4}$$

where $k_i^2 = \epsilon_i k_0^2$ and the norm of transverse wavenumber is $K = \sqrt{k_x^2 + k_y^2}$. Thus, the wavevector of the reflected wave is $\mathbf{k}_1^- = (\mathbf{K}, -\gamma_1)$ while the wavevector of the transmitted wave is $\mathbf{k}_2^+ = (\mathbf{K}, \gamma_2)$.

Following the notations introduced by Sipe [156], we pose the problem in terms of s- and p-polarised waves, as represented in Fig. A.2. The unitary vectors in each directions read

$$\hat{\mathbf{s}} = \hat{\mathbf{K}} \times \hat{\mathbf{z}}\,, \tag{A.5a}$$

$$\hat{\mathbf{p}}_i^{\pm} = \frac{1}{k_0 n_i}\left(K\hat{\mathbf{z}} \mp \gamma_i \hat{\mathbf{K}}\right)\,. \tag{A.5b}$$

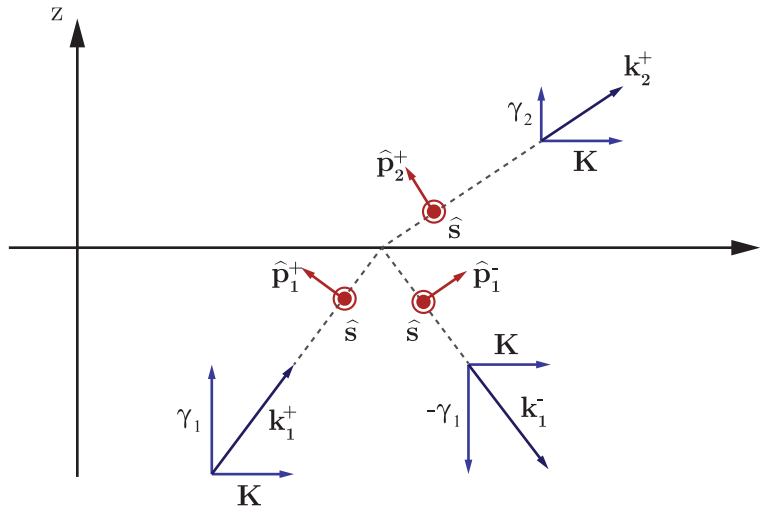

Figure A.2 – *Definition of the problem in terms of s- and p-polarised waves.*

A.3 Fresnel coefficients

The Fresnel coefficients for the reflected wave read

$$r_{12}^s = \frac{\mu_2\gamma_1 - \mu_1\gamma_2}{\mu_2\gamma_1 + \mu_1\gamma_2}\,, \tag{A.6a}$$

$$r_{12}^{p} = \frac{\epsilon_2\gamma_1 - \epsilon_1\gamma_2}{\epsilon_2\gamma_1 + \epsilon_1\gamma_2} \,. \tag{A.6b}$$

Defining u by $u^2 = K^2/k_1^2$, the magnitude of the longitudinal wavevector in both media is expressed by

$$\gamma_1 = k_1\sqrt{1-u^2} \,, \tag{A.7a}$$

$$\gamma_2 = k_1\sqrt{k_2^2/k_1^2 - u^2} \,. \tag{A.7b}$$

The Fresnel coefficients can be expressed as a function of u with

$$r_{12}^{s} = \frac{\mu_2\sqrt{1-u^2} - \mu_1\sqrt{(k_2/k_1)^2-u^2}}{\mu_2\sqrt{1-u^2} + \mu_1\sqrt{(k_2/k_1)^2-u^2}} \,, \tag{A.8a}$$

$$r_{12}^{p} = \frac{\epsilon_2\sqrt{1-u^2} - \epsilon_1\sqrt{(k_2/k_1)^2-u^2}}{\epsilon_2\sqrt{1-u^2} + \epsilon_1\sqrt{(k_2/k_1)^2-u^2}} \,. \tag{A.8b}$$

A.4 Angular spectrum representation

By performing a Fourier transform along the transverse coordinates, the scattered Green tensor is expressed by

$$\mathbf{S}_{11}(d, z_1, z_2, \omega) = \iint \mathbf{s}_{11}(\mathbf{K}, z_1, z_2) \exp\left(i\mathbf{K}\cdot(\mathbf{r}_1 - \mathbf{r}_2)\right) \mathrm{d}\, k_x \,\mathrm{d}\, k_y \,, \tag{A.9}$$

where $\mathbf{s}_{11}(\mathbf{K}, z_1, z_2)$ is the two-dimensional Fourier transform of $\mathbf{S}_{11}(d, z_1, z_2, \omega)$. The plane wave expansion of the scalar Green's function is known as the *Weyl identity* and is expressed by

$$\frac{\exp(ik_1 d)}{4\pi d} = \frac{i}{8\pi^2} \iint \frac{\exp(i\gamma_1|z|)}{\gamma_1} \exp\left(i\mathbf{K}\cdot(\mathbf{r}_1 - \mathbf{r}_2)\right) \mathrm{d}\, k_x \,\mathrm{d}\, k_y \,. \tag{A.10}$$

Using this identity along with Fresnel theory, it follows that

$$\mathbf{s}_{11}(\mathbf{K}, z_1, z_2) = \frac{i}{8\pi^2}(\hat{\mathbf{s}}\; r_{12}^{s}\; \hat{\mathbf{s}} + \hat{\mathbf{p}}_1^{-}\; r_{12}^{p}\; \hat{\mathbf{p}}_1^{+}) \frac{\exp\left(i\gamma_1|z_1 + z_2|\right)}{\gamma_1} \,. \tag{A.11}$$

A s-polarised wave reflects at an interface with a coefficient r_{12}^{s} and keeps the same direction $\hat{\mathbf{s}}$, while a p-polarised wave reflects at an interface with a coefficient r_{12}^{p} and its direction gets changed to $\hat{\mathbf{p}}_1^{-}$.

A.5 Simplified expression

Changing from Cartesian to polar coordinate system, the scattered Green tensor is

$$\mathbf{S}_{11}(d, z_1, z_2, \omega) = \int_{K=0}^{+\infty} \mathrm{d}\, K \frac{Ki}{8\pi^2\gamma_1} \exp(i\gamma_1|z_1 + z_2|) \int_{\theta=0}^{2\pi} \mathrm{d}\,\theta \; (\hat{\mathbf{s}}\; r_{12}^{s}\; \hat{\mathbf{s}} \;+\; \hat{\mathbf{p}}_1^{-}\; r_{12}^{p}\; \hat{\mathbf{p}}_1^{+}) \exp\left(iKd\cos(\theta - \phi)\right) \,. \tag{A.12}$$

The integral over the angle θ can be explicited using Bessel functions of the first kind, using the following properties:

$$\int_{\theta=0}^{2\pi} \exp(ix\cos(\theta-\phi))\cos(n\theta)\ \mathrm{d}\,\theta = 2\pi i^n J_n(x)\cos(n\phi)\ , \tag{A.13a}$$

$$\int_{\theta=0}^{2\pi} \exp(ix\cos(\theta-\phi))\sin(n\theta)\ \mathrm{d}\,\theta = 2\pi i^n J_n(x)\sin(n\phi)\ . \tag{A.13b}$$

Due to the rotational symmetry of the system, we can choose any angle ϕ for the calculation and it is convenient to choose $\phi = 0$. We obtain a simplified expression of the scattered Green tensor using the integration variable u, which reads

$$\mathbf{S}_{11}(d,z_1,z_2,\omega) = \frac{ik_1}{8\pi}\int_{u=0}^{+\infty} \frac{u\,\mathrm{d}\,u}{\sqrt{1-u^2}} \times \exp\left(ik_1\sqrt{1-u^2}|z_1+z_2|\right)\left[\mathbf{A}(u)r_{12}^s(u)+\mathbf{B}(u)r_{12}^p(u)\right]\ , \tag{A.14}$$

where $\mathbf{A}(u)$ and $\mathbf{B}(u)$ are two matrices defined by

$$\mathbf{A}(u) = \begin{pmatrix} A_{xx} & 0 & 0 \\ 0 & A_{yy} & 0 \\ 0 & 0 & 0 \end{pmatrix}\ , \tag{A.15a}$$

$$\mathbf{B}(u) = \begin{pmatrix} B_{xx} & 0 & B_{xz} \\ 0 & B_{yy} & 0 \\ B_{zx} & 0 & B_{zz} \end{pmatrix}\ , \tag{A.15b}$$

and the matrix elements are

$$\begin{aligned} A_{xx} &= J_0(k_1du) + J_2(k_1du)\ , \\ A_{yy} &= J_0(k_1du) - J_2(k_1du)\ , \\ B_{xx} &= (u^2-1)[J_0(k_1du) - J_2(k_1du)]\ , \\ B_{yy} &= (u^2-1)[J_0(k_1du) + J_2(k_1du)]\ , \\ B_{zz} &= 2u^2 J_0(k_1du)\ , \\ B_{xz} &= -B_{zx} = 2iu\sqrt{1-u^2}J_1(k_1du)\ . \end{aligned} \tag{A.16}$$

APPENDIX B

Numerical evaluation of the LDOS

B.1 Power dissipated by a dipole

Numerical simulations can be used to determine the spatial variations of the LDOS, or equivalently the decay rate enhancement of a dipole due to the interaction between this emitter and a structure in its vicinity. This requires two simulations, one in the presence of the structure and one in its absence. It is possible to compute the decay rate Γ of a quantum emitter from the power P transferred by a classical emitter to the electromagnetic field using the following relation:

$$\frac{\Gamma}{\Gamma_0} = \frac{P}{P_0} \, , \tag{B.1}$$

where P_0 (Γ_0) is the power transferred by the dipole to the field (the decay rate of the emitter) in the absence of the structure. The power transferred by the dipole to the field is directly found by considering the Lorentz force acting on charges due to the electric field and reads

$$P(t) = \mathbf{j}(\mathbf{r}_0, t) \cdot \mathbf{E}(\mathbf{r}_0, t) \, , \tag{B.2}$$

where the current $\mathbf{j}$ and the electric field $\mathbf{E}$ are evaluated at the dipole position $\mathbf{r}_0$. In a numerical simulation, a dipole is generated by creating an oscillating current $\mathbf{j}$ at the dipole position. The amplitude of the generated current can be controlled and is generally the same in the simulations with and without the structure. Thus, the power transferred to the field by the dipole at a given time is directly given by the value of the electric field at this time and at the dipole position.

B.2 Poynting theorem

While the power emitted by a dipole is given by Eq. (B.2), one can be interested in the power radiated out of the system, which occupies a volume V and is delimited by a closed surface ∂V. This is directly given by the total flux of the Poynting vector across a

closed surface around the structure. The Poynting theorem is a direct consequence of the conservation of energy and reads as follows:

$$-\frac{\partial}{\partial t}\iiint_V u \,\mathrm{d}\,V = \oiint_{\partial V} \mathbf{S}\cdot \mathrm{d}\,\mathbf{A} + \iiint_V \mathbf{j}\cdot\mathbf{E}\,\mathrm{d}\,V\ . \tag{B.3}$$

This theorem states that the rate at which the energy density u changes equals the outward flux of the Poynting vector $\mathbf{S} = \mathbf{E}\times\mathbf{H}$ plus the power transferred to the electromagnetic field due to the movement of the charges. This last term involves the power dissipated by the dipole, as well as the power dissipated by losses in the structures. In a numerical simulation, we can define a closed surface around the system and monitor the outward flux of the Poynting vector. By comparing this flux to the power dissipated by the dipole, it is thus possible to determine the rate of dissipation in the system due to ohmic losses.

B.3 Case of a continuous source

In practice, in a simulation, we can create a dipole at a fixed frequency ω defined by $\mathbf{j}(\mathbf{r}_0,t) = j(t)\,\mathbf{u}_l$ where $j(t) = j_0\exp(-i\omega t)$. Note that it is a common procedure to turn on the source with a smooth turn-on function. Running the simulation until the electromagnetic field is monochromatic, we can calculate the time averaged power transferred by the dipole to the field, which reads

$$\langle P\rangle = \frac{1}{2}\,\mathrm{Re}\{\mathbf{j}^*(\mathbf{r}_0)\cdot\mathbf{E}(\mathbf{r}_0)\}\ . \tag{B.4}$$

This expression shows that determining the time average of the component of $\mathbf{E}$ in the direction of the dipole is sufficient to compute the enhancement of the power transferred by a dipole to the field due to the structure, from the two simulations which are performed with and without the structure using the same current density $\mathbf{j}$ to model the dipole.

Moreover, we can also consider the time averaged version of the Poynting theorem, which is

$$\oiint_{\partial V}\langle\mathbf{S}\rangle\cdot\mathrm{d}\,\mathbf{A} = -\frac{1}{2}\iiint_V \mathrm{Re}\{\mathbf{j}^*\cdot\mathbf{E}\}\,\mathrm{d}\,V\ , \tag{B.5}$$

where $\langle\mathbf{S}\rangle = 1/2\,\mathrm{Re}\{\mathbf{E}\times\mathbf{H}^*\}$ is the time average of the Poynting vector. The power radiated out of the system is then directly given by the outward flux of the time average Poynting vector. By comparing the power dissipated by the dipole and the power radiated out of the system, we can access the rate of losses in the system.

B.4 Case of a Gaussian pulse

Instead of running the simulation until the field is monochromatic, we can compute the power transferred to the field by an impulsive source at a given frequency ω, and run the simulation until all the energy has left the system. A possible temporal dependence of the source is a Gaussian pulse, defined by

$$j(t) = j_0\exp\left(-i\omega t - \frac{(t-t_0)^2}{2w^2}\right)\ . \tag{B.6}$$

The field is not monochromatic, because of the broadband character of the pulse. To calculate the power dissipated by the pulse at a given frequency, it is required to Fourier transform the time-dependent quantities into the frequency domain. The power spectrum of the Gaussian pulse can easily be accessed from Eq. (B.6). The discrete Fourier transform of the electric field can be evaluated by

$$\hat{\mathbf{E}}(\mathbf{r}_0, \omega) = \frac{\Delta t}{\sqrt{2\pi}} \sum_{n=0}^{N-1} \mathbf{E}(\mathbf{r}_0, n\Delta t)\ \exp(-i\omega n \Delta t)\ . \tag{B.7}$$

From Eq. (B.2), it directly follows that

$$\hat{P}(\mathbf{r}_0, \omega) = \hat{\mathbf{j}}(\mathbf{r}_0, \omega) * \hat{\mathbf{E}}(\mathbf{r}_0, \omega)\ . \tag{B.8}$$

Again, we can see that only the contribution of the field in the direction of the dipole will contribute to the power dissipated by the dipole. In the case of linear medium, Oskooi and Johnson [157] showed that this expression can be rewritten as a product between the spectrum of the pulse and the Fourier transform of the electric field.

APPENDIX C

Fisher information matrix for decay rate estimations

C.1 Definition of the problem

Let us assume that we have n measurements and that we can model the distribution of events detected for each data point by a Poisson distribution of expectation f_i. Then, the coefficients of the information matrix are given by

$$[\boldsymbol{\mathcal{I}}(\boldsymbol{\theta})]_{jk} = \sum_{i=1}^{n} \frac{1}{f_i} \left(\frac{\partial f_i}{\partial \theta_j} \right) \left(\frac{\partial f_i}{\partial \theta_k} \right) \ . \tag{C.1}$$

We consider the estimation of the parameters characterising the excited-state probability density function of a molecule using SPAD measurements. We assume that the fluorescence signal is bi-exponential, with Γ_1 and Γ_2 the decay rates of each component and N_1 and N_2 the numbers of photons characterising each component. The background noise is characterised by the probability density function $q_b(t)$ and the number of associated photons N_b. The instrument response function (IRF) is described by its probability density function $q_{irf}(t)$. In this situation, the set of parameters that are to be estimated from the data is $\boldsymbol{\theta} = (N_1, \Gamma_1, N_2, \Gamma_2, N_b)$. Considering n data items, the expectation f_i for each data item reads

$$\begin{aligned} f_i = N_1 \sum_{l=0}^{+\infty} \int_{t_i+lT}^{t_{i+1}+lT} \left[q_{irf}(t) * \Gamma_1 e^{-\Gamma_1 t} \right] \mathrm{d}\, t + N_2 \sum_{l=0}^{+\infty} \int_{t_i+lT}^{t_{i+1}+lT} \left[q_{irf}(t) * \Gamma_2 e^{-\Gamma_2 t} \right] \mathrm{d}\, t \\ + N_b \int_{t_i}^{t_{i+1}} q_b(t) \, \mathrm{d}\, t \ . \end{aligned} \tag{C.2}$$

C.2 Discrete formulation

Nondimensionalisation of the problem Let us take Γ_1 as a reference, and make the change of variable $u = \Gamma_1 t$. Then, we can define r from the repetition period T so that $r = \Gamma_1 T$. Therefore, r and T are respectively given by $r = u_{n+1} - u_1$ and $T = t_{n+1} - t_1$. We also define $\alpha = N_2/N_1$, $\gamma = \Gamma_2/\Gamma_1$ and $\beta = N_b/(rN_1)$. Moreover, using the variable u instead of t, the probability density functions associated with the IRF and the background noise are respectively

$$\begin{aligned} \tilde{q}_{irf}(u) &= \frac{q_{irf}(u/\Gamma_1)}{\Gamma_1} \,, \\ \tilde{q}_b(u) &= \frac{q_b(u/\Gamma_1)}{\Gamma_1} \,. \end{aligned} \tag{C.3}$$

All these notations are summarised in Table C.1.

	Parameters	Dimensionless parameters
First fluorescence decay	N_1 and Γ_1	
Second fluorescence decay	N_2 and Γ_2	$\alpha = N_2/N_1$ and $\gamma = \Gamma_2/\Gamma_1$
Repetition period	T	$r = \Gamma_1 T$
Number of data points	n	$k = n/r$
Instrument response function	$q_{irf}(t)$	$\tilde{q}_{irf}(u) = q_{irf}(u/\Gamma_1)/\Gamma_1$
Background noise	N_b and $q_b(t)$	$\beta = N_b/(rN_1)$ and $\tilde{q}_b(u) = q_b(u/\Gamma_1)/\Gamma_1$

Table C.1 – *Parameters involved in the TCSPC data model for a bi-exponential decay.*

Using these notations, Eq. (C.2) can be rewritten as

$$\begin{aligned} f_i = N_1 \Bigg(\sum_{l=0}^{+\infty} \int_{u_i+lr}^{u_{i+1}+lr} \left[\tilde{q}_{irf}(u) * e^{-u}\right] \mathrm{d}\, u + \alpha \sum_{l=0}^{+\infty} \int_{u_i+lr}^{u_{i+1}+lr} \left[\tilde{q}_{irf}(u) * \gamma e^{-\gamma u}\right] \mathrm{d}\, u \\ + \beta r \int_{u_i}^{u_{i+1}} \tilde{q}_b(u)\, \mathrm{d}\, u \Bigg) \,. \end{aligned} \tag{C.4}$$

Calculation of the information matrix In order to calculate the information matrix, let us define $\mathbf{J}^{\mathrm{I}}$, $\mathbf{J}^{\mathrm{II}}$, $\mathbf{K}^{\mathrm{I}}$, $\mathbf{K}^{\mathrm{II}}$ and $\mathbf{J}^{\mathrm{B}}$ as follows:

$$\begin{aligned} J_i^{\mathrm{I}} &= \sum_{l=0}^{+\infty} \int_{u_i+lr}^{u_{i+1}+lr} \left[\tilde{q}_{irf}(u) * e^{-u}\right] \mathrm{d}\, u \,, \\ K_i^{\mathrm{I}} &= \sum_{l=0}^{+\infty} \int_{u_i+lr}^{u_{i+1}+lr} \left[\tilde{q}_{irf}(u) * (1-u) e^{-u}\right] \mathrm{d}\, u \,, \\ J_i^{\mathrm{II}} &= \sum_{l=0}^{+\infty} \int_{u_i+lr}^{u_{i+1}+lr} \left[\tilde{q}_{irf}(u) * \gamma e^{-\gamma u}\right] \mathrm{d}\, u \,, \end{aligned} \tag{C.5}$$

$$K_i^{\mathrm{II}} = \sum_{l=0}^{+\infty} \int_{u_i+lr}^{u_{i+1}+lr} \left[\tilde{q}_{irf}(u) * \gamma(1-\gamma u)e^{-\gamma u}\right] \mathrm{d}\, u \ ,$$
$$J_i^{\mathrm{B}} = r \int_{u_i}^{u_{i+1}} \tilde{q}_b(u)\, \mathrm{d}\, u \ .$$

Differentiating Eq. (C.4) by each parameter yields

$$\begin{aligned} f_i &= N_1 \left(J_i^{\mathrm{I}} + \alpha J_i^{\mathrm{II}} + \beta J_i^{\mathrm{B}}\right) \ , \\ \frac{\partial f_i}{\partial N_1} &= J_i^{\mathrm{I}} \ , \\ \frac{\partial f_i}{\partial \Gamma_1} &= \frac{N_1}{\Gamma_1} K_i^{\mathrm{I}} \ , \\ \frac{\partial f_i}{\partial N_b} &= J_i^{\mathrm{B}} \ , \\ \frac{\partial f_i}{\partial N_2} &= J_i^{\mathrm{II}} \ , \\ \frac{\partial f_i}{\partial \Gamma_2} &= \frac{\alpha N_1}{\gamma \Gamma_1} K_i^{\mathrm{II}} \ . \end{aligned} \tag{C.6}$$

We can now calculate the coefficients of the information matrix as given by Eq. (C.1), which reads

$$\begin{aligned} \mathcal{I}_{N_1N_1} &= \frac{1}{N_1} \sum_{i=1}^{n} \frac{(J_i^{\mathrm{I}})^2}{J_i^{\mathrm{I}} + \alpha J_i^{\mathrm{II}} + \beta J_i^{\mathrm{B}}} \ , \\ \mathcal{I}_{\Gamma_1\Gamma_1} &= \frac{N_1}{\Gamma_1^2} \sum_{i=1}^{n} \frac{(K_i^{\mathrm{I}})^2}{J_i^{\mathrm{I}} + \alpha J_i^{\mathrm{II}} + \beta J_i^{\mathrm{B}}} \ , \\ \mathcal{I}_{N_1\Gamma_1} &= \frac{1}{\Gamma_1} \sum_{i=1}^{n} \frac{J_i^{\mathrm{I}} K_i^{\mathrm{I}}}{J_i^{\mathrm{I}} + \alpha J_i^{\mathrm{II}} + \beta J_i^{\mathrm{B}}} \ , \\ \mathcal{I}_{N_bN_b} &= \frac{1}{N_1} \sum_{i=1}^{n} \frac{(J_i^{\mathrm{B}})^2}{J_i^{\mathrm{I}} + \alpha J_i^{\mathrm{II}} + \beta J_i^{\mathrm{B}}} \ , \\ \mathcal{I}_{N_1N_b} &= \frac{1}{N_1} \sum_{i=1}^{n} \frac{J_i^{\mathrm{I}} J_i^{\mathrm{B}}}{J_i^{\mathrm{I}} + \alpha J_i^{\mathrm{II}} + \beta J_i^{\mathrm{B}}} \ , \\ \mathcal{I}_{\Gamma_1N_b} &= \frac{1}{\Gamma_1} \sum_{i=1}^{n} \frac{J_i^{\mathrm{B}} K_i^{\mathrm{I}}}{J_i^{\mathrm{I}} + \alpha J_i^{\mathrm{II}} + \beta J_i^{\mathrm{B}}} \ , \\ \mathcal{I}_{N_2N_2} &= \frac{1}{N_1} \sum_{i=1}^{n} \frac{(J_i^{\mathrm{II}})^2}{J_i^{\mathrm{I}} + \alpha J_i^{\mathrm{II}} + \beta J_i^{\mathrm{B}}} \ , \\ \mathcal{I}_{N_1N_2} &= \frac{1}{N_1} \sum_{i=1}^{n} \frac{J_i^{\mathrm{I}} J_i^{\mathrm{II}}}{J_i^{\mathrm{I}} + \alpha J_i^{\mathrm{II}} + \beta J_i^{\mathrm{B}}} \ , \\ \mathcal{I}_{\Gamma_1N_2} &= \frac{1}{\Gamma_1} \sum_{i=1}^{n} \frac{J_i^{\mathrm{II}} K_i^{\mathrm{I}}}{J_i^{\mathrm{I}} + \alpha J_i^{\mathrm{II}} + \beta J_i^{\mathrm{B}}} \ , \\ \mathcal{I}_{N_bN_2} &= \frac{1}{N_1} \sum_{i=1}^{n} \frac{J_i^{\mathrm{B}} J_i^{\mathrm{II}}}{J_i^{\mathrm{I}} + \alpha J_i^{\mathrm{II}} + \beta J_i^{\mathrm{B}}} \ , \\ \mathcal{I}_{\Gamma_2\Gamma_2} &= \frac{\alpha^2 N_1}{\gamma^2 \Gamma_1^2} \sum_{i=1}^{n} \frac{(K_i^{\mathrm{II}})^2}{J_i^{\mathrm{I}} + \alpha J_i^{\mathrm{II}} + \beta J_i^{\mathrm{B}}} \ , \end{aligned} \tag{C.7}$$

$$
\begin{aligned}
\mathcal{I}_{N_1\Gamma_2} &= \frac{\alpha}{\gamma\Gamma_1}\sum_{i=1}^{n}\frac{J_i^{\mathrm{I}}K_i^{\mathrm{II}}}{J_i^{\mathrm{I}}+\alpha J_i^{\mathrm{II}}+\beta J_i^{\mathrm{B}}}\ ,\\
\mathcal{I}_{\Gamma_1\Gamma_2} &= \frac{\alpha N_1}{\gamma\Gamma_1^2}\sum_{i=1}^{n}\frac{K_i^{\mathrm{I}}K_i^{\mathrm{II}}}{J_i^{\mathrm{I}}+\alpha J_i^{\mathrm{II}}+\beta J_i^{\mathrm{B}}}\ ,\\
\mathcal{I}_{N_b\Gamma_2} &= \frac{\alpha}{\gamma\Gamma_1}\sum_{i=1}^{n}\frac{J_i^{\mathrm{B}}K_i^{\mathrm{II}}}{J_i^{\mathrm{I}}+\alpha J_i^{\mathrm{II}}+\beta J_i^{\mathrm{B}}}\ ,\\
\mathcal{I}_{N_2\Gamma_2} &= \frac{\alpha}{\gamma\Gamma_1}\sum_{i=1}^{n}\frac{J_i^{\mathrm{II}}K_i^{\mathrm{II}}}{J_i^{\mathrm{I}}+\alpha J_i^{\mathrm{II}}+\beta J_i^{\mathrm{B}}}\ .
\end{aligned}
$$

As Γ_1 is our reference, the Cramér-Rao inequality will be most conveniently expressed in terms of this parameter. By inverting the information matrix, we indeed obtain the following expression:

$$
\sigma_{\Gamma_1} \geq \frac{\Gamma_1}{\sqrt{N_1}} \times \psi\left(\alpha,\gamma,r,k,\tilde{q}_{irf},\beta,\tilde{q}_b\right)\ , \tag{C.8}
$$

where ψ is calculated by inverting the information matrix and σ_{Γ_1} is the standard error on the decay rate estimates.

Formulation in terms of the excited-state lifetime We can also calculate the Cramér-Rao bound on the lifetime estimator. To do so, we define the excited-state lifetime $\tau_1 = 1/\Gamma_1$ and we perform a transformation of parameter, as detailed in Appendix 3B of Ref. [142]. This reads

$$
\mathrm{Var}\left(\hat{\tau}_1\right) \geq \left[\frac{\partial(1/\Gamma_1)}{\partial\Gamma_1}\right]^2\left[\frac{\Gamma_1}{\sqrt{N_1}} \times \psi\left(\alpha,\gamma,r,k,\tilde{q}_{irf},\beta,\tilde{q}_b\right)\right]^2\ , \tag{C.9}
$$

where $\hat{\tau}_1$ is the lifetime estimator. This expression simplifies to

$$
\sigma_{\tau_1} \geq \frac{\tau_1}{\sqrt{N_1}} \times \psi\left(\alpha,\gamma,r,k,\tilde{q}_{irf},\beta,\tilde{q}_b\right)\ , \tag{C.10}
$$

where σ_{τ_1} is the standard error on the lifetime estimates. This demonstrates that the Cramér-Rao lower bounds are the same for the relative standard error on the decay rate and lifetime estimators.

C.3 Limiting cases for the discrete formulation

Ideal IRF Whenever the IRF can be considered as ideal, the set coefficients defined by Eq. (C.6) becomes

$$
\begin{aligned}
J_i^{\mathrm{I}} &= \left[e^{-u_i} - e^{-u_{i+1}}\right]\sum_{l=0}^{+\infty}e^{-lr}\ ,\\
K_i^{\mathrm{I}} &= \left[u_{i+1}e^{-u_{i+1}} - u_i e^{-u_i}\right]\sum_{l=0}^{+\infty}e^{-lr} + \left[e^{-u_{i+1}} - e^{-u_i}\right]\sum_{l=0}^{+\infty}lre^{-lr}\ ,\\
J_i^{\mathrm{II}} &= \left[e^{-\gamma u_i} - e^{-\gamma u_{i+1}}\right]\sum_{l=0}^{+\infty}e^{-\gamma lr}\ ,\\
K_i^{\mathrm{II}} &= \left[\gamma u_{i+1}e^{-\gamma u_{i+1}} - \gamma u_i e^{-\gamma u_i}\right]\sum_{l=0}^{+\infty}e^{-\gamma lr} + \left[e^{-\gamma u_{i+1}} - e^{-\gamma u_i}\right]\sum_{l=0}^{+\infty}\gamma lre^{-\gamma lr}\ .
\end{aligned} \tag{C.11}
$$

J_i^{B} remains unchanged, as it does not depend on the IRF. These expression can be further simplified, by using the following properties of geometric series:

$$\begin{aligned} \sum_{l=0}^{+\infty} e^{-lr} &= \frac{1}{1-e^{-r}} \,, \\ \sum_{l=0}^{+\infty} lre^{-lr} &= \frac{re^{-r}}{(1-e^{-r})^2} \,. \end{aligned} \tag{C.12}$$

Using these properties, we obtain

$$\begin{aligned} J_i^{\mathrm{I}} &= \frac{e^{-u_i} - e^{-u_{i+1}}}{1-e^{-r}} \,, \\ K_i^{\mathrm{I}} &= \frac{u_{i+1}e^{-u_{i+1}} - u_i e^{-u_i}}{1-e^{-r}} + \frac{re^{-r}\left(e^{-u_{i+1}} - e^{-u_i}\right)}{(1-e^{-r})^2} \,, \\ J_i^{\mathrm{II}} &= \frac{e^{-\gamma u_i} - e^{-\gamma u_{i+1}}}{1-e^{-\gamma r}} \,, \\ K_i^{\mathrm{II}} &= \frac{\gamma u_{i+1}e^{-\gamma u_{i+1}} - \gamma u_i e^{-\gamma u_i}}{1-e^{-\gamma r}} + \frac{\gamma re^{-\gamma r}\left(e^{-\gamma u_{i+1}} - e^{-\gamma u_i}\right)}{(1-e^{-\gamma r})^2} \,. \end{aligned} \tag{C.13}$$

Uniform background noise Whenever the background noise is uniform over the repetition period, the coefficient J_i^{B} becomes

$$J^{\mathrm{B}} = r/n \,. \tag{C.14}$$

C.4 Integral formulation

Let us assume that the number of data items n is large. In the case of an ideal IRF and a uniform background noise, the coefficients of the information matrix can be analytically calculated in the case of a mono-exponential decay. As a matter of simplicity, we drop the subscript "1" when referring to the expected number of photons N and the decay rate Γ. Then, in the limit of an infinite number of data items, we can replace the sum involved in the calculation of the information matrix by an integral. Equation (C.1) becomes

$$\left[\boldsymbol{\mathcal{I}}(\boldsymbol{\theta})\right]_{jk} = \frac{1}{\Gamma}\int_0^r \frac{1}{f}\left(\frac{\partial f}{\partial \theta_j}\right)\left(\frac{\partial f}{\partial \theta_k}\right)\mathrm{d}\,u \,. \tag{C.15}$$

The functions involved in the calculation of the information matrix are $J^{\mathrm{I}}(u)$, $K^{\mathrm{I}}(u)$ and J^{B}, which we define as follows:

$$\begin{aligned} J^{\mathrm{I}}(u) &= \sum_{l=0}^{+\infty} e^{-(u+lr)} = \frac{e^{-u}}{1-e^{-r}} \,, \\ K^{\mathrm{I}}(u) &= \sum_{l=0}^{+\infty} \left[1-(u+lr)\right] e^{-(u+lr)} = \frac{e^{-u}\left[1-e^{-r}-re^{-r}-u\left(1-e^{-r}\right)\right]}{(1-e^{-r})^2} \,, \\ J^{\mathrm{B}} &= 1 \,. \end{aligned} \tag{C.16}$$

As we did in Eq. (C.7), f can be expressed as

$$f(u) = \Gamma N\left(J^{\mathrm{I}}(u) + \beta J^{\mathrm{B}}\right) \,. \tag{C.17}$$

Let us define V_r and W_r by

$$\begin{aligned} V_r &= 1 - e^{-r} \,, \\ W_r &= 1 - e^{-r} - re^{-r} \,. \end{aligned} \tag{C.18}$$

The coefficients of the information matrix are then given by

$$\begin{aligned} \mathcal{I}_{NN} &= \frac{1}{NV_r} \int_0^r \frac{e^{-2u}}{e^{-u} + \beta V_r} \,\mathrm{d}\, u \,, \\ \mathcal{I}_{\Gamma\Gamma} &= \frac{N}{\Gamma^2 V_r^3} \int_0^r \frac{(W_r - uV_r)^2 e^{-2u}}{e^{-u} + \beta V_r} \,\mathrm{d}\, u \,, \\ \mathcal{I}_{N\Gamma} &= \frac{1}{\Gamma V_r^2} \int_0^r \frac{(W_r - uV_r) e^{-2u}}{e^{-u} + \beta V_r} \,\mathrm{d}\, u \,, \\ \mathcal{I}_{N_b N_b} &= \frac{V_r}{Nr^2} \int_0^r \frac{1}{e^{-u} + \beta V_r} \,\mathrm{d}\, u \,, \\ \mathcal{I}_{N N_b} &= \frac{1}{Nr} \int_0^r \frac{e^{-u}}{e^{-u} + \beta V_r} \,\mathrm{d}\, u \,, \\ \mathcal{I}_{\Gamma N_b} &= \frac{1}{\Gamma r V_r} \int_0^r \frac{(W_r - uV_r) e^{-u}}{e^{-u} + \beta V_r} \,\mathrm{d}\, u \,. \end{aligned} \tag{C.19}$$

C.5 Limiting cases for the integral formulation

Infinite repetition period In the limiting case of an infinite repetition period, $\mathcal{I}_{N_b N_b}$ diverges towards $+\infty$. This means that the amount of information over this parameter is infinite, and the information matrix becomes a 2×2 matrix. Moreover, both V_r and W_r equals unity. The coefficients then read

$$\begin{aligned} \mathcal{I}_{NN} &= \frac{1}{N} \left\{ 1 - \beta \ln\left(\frac{1+\beta}{\beta}\right) \right\} \,, \\ \mathcal{I}_{\Gamma\Gamma} &= \frac{N}{\Gamma^2} \left\{ 1 + \beta \left[\frac{\pi^2}{3} - \ln\left(\frac{1+\beta}{\beta}\right) \left(1 + \ln\left[\beta\left(\beta+1\right)\right]\right) - 2\mathrm{Li}_2\left(\frac{\beta}{\beta+1}\right) + 2\mathrm{Li}_3\left(-\frac{1}{\beta}\right) \right] \right\} \,, \\ \mathcal{I}_{N\Gamma} &= \frac{\beta}{\Gamma} \left\{ \frac{\pi^2}{6} - \frac{1}{2} \ln\left(\frac{1+\beta}{\beta}\right) \left(2 + \ln\left(\beta\left(\beta+1\right)\right)\right) - \mathrm{Li}_2\left(\frac{\beta}{\beta+1}\right) \right\} \,. \end{aligned} \tag{C.20}$$

In these expressions, Li_2 and Li_3 respectively refer to the polylogarithm functions of order 2 and 3. Using these expressions, the Cramér-Rao lower bound on the standard error on the decay rate estimates can be expressed as a product of $\Gamma/\sqrt{N}$ and $\psi\left(\beta\right)$.

Background-free measurements If the number of background photons equals zero ($N_b = 0$) the information matrix is

$$\begin{aligned} \mathcal{I}_{NN} &= \frac{1}{N} \,, \\ \mathcal{I}_{\Gamma\Gamma} &= \frac{N}{\Gamma^2} \left\{ \frac{(1-e^{-r})^2 + r^2 e^{-r}}{(1-e^{-r})^2} \right\} \,, \\ \mathcal{I}_{N\Gamma} &= 0 \,. \end{aligned} \tag{C.21}$$

In this case, the Cramér-Rao lower bound on the standard error on the decay rate estimates can be expressed as a product of $\Gamma/\sqrt{N}$ and $\psi\,(r)$.

Fundamental limit Finally, in the limiting case of an infinite repetition period and no background noise, we retrieve the following well-known result:

$$\begin{aligned} \mathcal{I}_{NN} &= \frac{1}{N} \,, \\ \mathcal{I}_{\Gamma\Gamma} &= \frac{N}{\Gamma^2} \,, \\ \mathcal{I}_{N\Gamma} &= 0 \,. \end{aligned} \tag{C.22}$$

In this case, the Cramér-Rao lower bound on the standard error on the decay rate estimates equals $\Gamma/\sqrt{N}$.

Bibliography

[1] Drexhage, K. Influence of a dielectric interface on fluorescence decay time. *Journal of Luminescence* **1**, 693–701 (1970).

[2] Langguth, L., Fleury, R., Alù, A. & Koenderink, A. F. Drexhage's Experiment for Sound. *Physical Review Letters* **116**, 224301 (2016).

[3] Betzig, E., Patterson, G. H., Sougrat, R., Lindwasser, O. W., Olenych, S., Bonifacino, J. S., Davidson, M. W., Lippincott-Schwartz, J. & Hess, H. F. Imaging Intracellular Fluorescent Proteins at Nanometer Resolution. *Science* **313**, 1642–1645 (2006).

[4] Errico, C., Pierre, J., Pezet, S., Desailly, Y., Lenkei, Z., Couture, O. & Tanter, M. Ultrafast ultrasound localization microscopy for deep super-resolution vascular imaging. *Nature* **527**, 499–502 (2015).

[5] Purcell, E. Spontaneous emission probabilities at radio frequencies. *Physical Review* **69**, 681 (1946).

[6] Barron, L. D. & Gray, C. G. The multipole interaction Hamiltonian for time dependent fields. *Journal of Physics A: Mathematical, Nuclear and General* **6**, 59–61 (1973).

[7] Karaveli, S. & Zia, R. Spectral Tuning by Selective Enhancement of Electric and Magnetic Dipole Emission. *Physical Review Letters* **106**, 193004 (2011).

[8] Taminiau, T. H., Karaveli, S., van Hulst, N. F. & Zia, R. Quantifying the magnetic nature of light emission. *Nature Communications* **3**, 979 (2012).

[9] Aigouy, L., Cazé, A., Gredin, P., Mortier, M. & Carminati, R. Mapping and Quantifying Electric and Magnetic Dipole Luminescence at the Nanoscale. *Physical Review Letters* **113**, 076101 (2014).

[10] Wylie, J. M. & Sipe, J. E. Quantum electrodynamics near an interface. *Physical Review A* **30**, 1185–1193 (1984).

[11] Carminati, R., Cazé, A., Cao, D., Peragut, F., Krachmalnicoff, V., Pierrat, R. & De Wilde, Y. Electromagnetic density of states in complex plasmonic systems. *Surface Science Reports* **70**, 1–41 (2015).

[12] Chance, R. R., Prock, A. & Silbey, R. Molecular Fluorescence and Energy Transfer Near Interfaces. In *Advances in Chemical Physics*, 1–65 (John Wiley & Sons, Inc., 1978).

[13] Carminati, R., Greffet, J. J., Henkel, C. & Vigoureux, J. M. Radiative and non-radiative decay of a single molecule close to a metallic nanoparticle. *Optics Communications* **261**, 368–375 (2006).

[14] Dung, H. T., Knöll, L. & Welsch, D.-G. Intermolecular energy transfer in the presence of dispersing and absorbing media. *Physical Review A* **65**, 043813 (2002).

[15] Novotny, L. & Hecht, B. Dipole-dipole interactions and energy transfer. In *Principles of Nano-Optics*, 284–293 (Cambridge University Press, 2006).

[16] Sheppard, C. J. R. & Wilson, T. The Image of a Single Point in Microscopes of Large Numerical Aperture. *Proceedings of the Royal Society of London. Series A, Mathematical and Physical Sciences* **379**, 145–158 (1982).

[17] Novotny, L. & Hecht, B. The point-spread function. In *Principles of Nano-Optics*, 89–95 (Cambridge University Press, 2006).

[18] Ober, R. J., Ram, S. & Ward, E. S. Localization Accuracy in Single-Molecule Microscopy. *Biophysical Journal* **86**, 1185–1200 (2004).

[19] Synge, E. H. A suggested method for extending microscopic resolution into the ultra-microscopic region. *The London, Edinburgh, and Dublin Philosophical Magazine and Journal of Science* **6**, 356–362 (1928).

[20] Castanié, E. *Émission dipolaire et absorption en champ proche de nanostructures.* Ph.D. thesis, Université Pierre et Marie Curie - Paris VI (2011).

[21] Cao, D. *Etude expérimentale de la fluorescence et du transfert non-radiatif en champ proche de nanostructures métalliques.* Ph.D. thesis, Université Pierre et Marie Curie - Paris VI (2014).

[22] Krachmalnicoff, V., Cao, D., Cazé, A., Castanié, E., Pierrat, R., Bardou, N., Collin, S., Carminati, R. & De Wilde, Y. Towards a full characterization of a plasmonic nanostructure with a fluorescent near-field probe. *Optics Express* **21**, 11536–11545 (2013).

[23] Cario, G. & Franck, J. Uber sensibilisierte Fluoreszenz von Gasen. *Zeitschrift für Physik* **17**, 202–212 (1923).

[24] Förster, T. 10th Spiers Memorial Lecture. Transfer mechanisms of electronic excitation. *Discussions of the Faraday Society* **27**, 7–17 (1959).

[25] Suzuki, Y., Yasunaga, T., Ohkura, R., Wakabayashi, T. & Sutoh, K. Swing of the lever arm of a myosin motor at the isomerization and phosphate-release steps. *Nature* **396**, 380–383 (1998).

[26] Andrew, P. & Barnes, W. L. Förster Energy Transfer in an Optical Microcavity. *Science* **290**, 785–788 (2000).

[27] Reil, F., Hohenester, U., Krenn, J. R. & Leitner, A. Förster-Type Resonant Energy Transfer Influenced by Metal Nanoparticles. *Nano Letters* **8**, 4128–4133 (2008).

[28] Blum, C., Zijlstra, N., Lagendijk, A., Wubs, M., Mosk, A., Subramaniam, V. & Vos, W. Nanophotonic Control of the Förster Resonance Energy Transfer Efficiency. *Physical Review Letters* **109**, 203601 (2012).

[29] Ghenuche, P., Mivelle, M., de Torres, J., Moparthi, S. B., Rigneault, H., Van Hulst, N. F., García-Parajó, M. F. & Wenger, J. Matching Nanoantenna Field Confinement to FRET Distances Enhances Förster Energy Transfer Rates. *Nano Letters* **15**, 6193–6201 (2015).

[30] Wubs, M. & Vos, W. L. Förster resonance energy transfer rate in any dielectric nanophotonic medium with weak dispersion. *New Journal of Physics* **18**, 53037–53056 (2016).

[31] Scholes, G. D., Fleming, G. R., Olaya-Castro, A. & van Grondelle, R. Lessons from nature about solar light harvesting. *Nature Chemistry* **3**, 763–774 (2011).

[32] Trofymchuk, K., Reisch, A., Didier, P., Fras, F., Gilliot, P., Mely, Y. & Klymchenko, A. S. Giant light-harvesting nanoantenna for single-molecule detection in ambient light. *Nature Photonics* **11**, 657–663 (2017).

[33] Andrew, P. & Barnes, W. L. Energy Transfer Across a Metal Film Mediated by Surface Plasmon Polaritons. *Science* **306**, 1002–1005 (2004).

[34] Kuzyk, A., Pettersson, M., Toppari, J. J., Hakala, T. K., Tikkanen, H., Kunttu, H. & Törmä, P. Molecular coupling of light with plasmonic waveguides. *Optics Express* **15**, 9908–9917 (2007).

[35] Götzinger, S., de S. Menezes, L., Mazzei, A., Kühn, S., Sandoghdar, V. & Benson, O. Controlled Photon Transfer between Two Individual Nanoemitters via Shared High-Q Modes of a Microsphere Resonator. *Nano Letters* **6**, 1151–1154 (2006).

[36] Martin-Cano, D., Martin-Moreno, L., Garcia-Vidal, F. J. & Moreno, E. Resonance Energy Transfer and Superradiance Mediated by Plasmonic Nanowaveguides. *Nano Letters* **10**, 3129–3134 (2010).

[37] Barthes, J., Bouhelier, A., Dereux, A. & Francs, G. C. d. Coupling of a dipolar emitter into one-dimensional surface plasmon. *Scientific Reports* **3**, 2734 (2013).

[38] Roque, P. M. d., Hulst, N. F. v. & Sapienza, R. Nanophotonic boost of intermolecular energy transfer. *New Journal of Physics* **17**, 113052 (2015).

[39] Bouchet, D., Cao, D., Carminati, R., De Wilde, Y. & Krachmalnicoff, V. Long-Range Plasmon-Assisted Energy Transfer between Fluorescent Emitters. *Physical Review Letters* **116**, 037401 (2016).

[40] Ehrenreich, H. & Philipp, H. R. Optical Properties of Ag and Cu. *Physical Review* **128**, 1622–1629 (1962).

[41] Rakic, A. D., Djurišic, A. B., Elazar, J. M. & Majewski, M. L. Optical Properties of Metallic Films for Vertical-Cavity Optoelectronic Devices. *Applied Optics* **37**, 5271–5283 (1998).

[42] Novotny, L. & Hecht, B. Surface plasmon polaritons at plane interfaces. In *Principles of Nano-Optics*, 382–393 (Cambridge University Press, 2006).

[43] McPeak, K. M., Jayanti, S. V., Kress, S. J. P., Meyer, S., Iotti, S., Rossinelli, A. & Norris, D. J. Plasmonic Films Can Easily Be Better: Rules and Recipes. *ACS Photonics* **2**, 326–333 (2015).

[44] Brown, R. H. & Twiss, R. Q. A new type of interferometer for use in radio astronomy. *The London, Edinburgh, and Dublin Philosophical Magazine and Journal of Science* **45**, 663–682 (1954).

[45] Brown, R. H. & Twiss, R. Q. Correlation between Photons in two Coherent Beams of Light. *Nature* **177**, 27–29 (1956).

[46] Kimble, H. J., Dagenais, M. & Mandel, L. Photon Antibunching in Resonance Fluorescence. *Physical Review Letters* **39**, 691–695 (1977).

[47] Marquier, F., Sauvan, C. & Greffet, J.-J. Revisiting Quantum Optics with Surface Plasmons and Plasmonic Resonators. *ACS Photonics* **4**, 2091–2101 (2017).

[48] Akimov, A. V., Mukherjee, A., Yu, C. L., Chang, D. E., Zibrov, A. S., Hemmer, P. R., Park, H. & Lukin, M. D. Generation of single optical plasmons in metallic nanowires coupled to quantum dots. *Nature* **450**, 402–406 (2007).

[49] Kolesov, R., Grotz, B., Balasubramanian, G., Stöhr, R. J., Nicolet, A. A. L., Hemmer, P. R., Jelezko, F. & Wrachtrup, J. Wave–particle duality of single surface plasmon polaritons. *Nature Physics* **5**, 470–474 (2009).

[50] Dheur, M.-C., Devaux, E., Ebbesen, T. W., Baron, A., Rodier, J.-C., Hugonin, J.-P., Lalanne, P., Greffet, J.-J., Messin, G. & Marquier, F. Single-plasmon interferences. *Science Advances* **2**, e1501574 (2016).

[51] de Torres, J., Ferrand, P., Colas des Francs, G. & Wenger, J. Coupling Emitters and Silver Nanowires to Achieve Long-Range Plasmon-Mediated Fluorescence Energy Transfer. *ACS Nano* **10**, 3968–3976 (2016).

[52] Dzsotjan, D., Sørensen, A. S. & Fleischhauer, M. Quantum emitters coupled to surface plasmons of a nanowire: A Green's function approach. *Physical Review B* **82**, 075427 (2010).

[53] Gonzalez-Tudela, A., Martin-Cano, D., Moreno, E., Martin-Moreno, L., Tejedor, C. & Garcia-Vidal, F. J. Entanglement of Two Qubits Mediated by One-Dimensional Plasmonic Waveguides. *Physical Review Letters* **106**, 020501 (2011).

[54] Bouchet, D., Lhuillier, E., Ithurria, S., Gulinatti, A., Rech, I., Carminati, R., De Wilde, Y. & Krachmalnicoff, V. Correlated blinking of fluorescent emitters mediated by single plasmons. *Physical Review A* **95**, 033828 (2017).

[55] Talapin, D. V., Mekis, I., Götzinger, S., Kornowski, A., Benson, O. & Weller, H. CdSe/CdS/ZnS and CdSe/ZnSe/ZnS Core-Shell-Shell Nanocrystals. *The Journal of Physical Chemistry B* **108**, 18826–18831 (2004).

[56] Gulinatti, A., Rech, I., Panzeri, F., Cammi, C., Maccagnani, P., Ghioni, M. & Cova, S. New silicon SPAD technology for enhanced red-sensitivity, high-resolution timing and system integration. *Journal of Modern Optics* **59**, 1489–1499 (2012).

[57] Fox, M. Photon antibunching. In *Quantum Optics : An Introduction*, 105–125 (Oxford University Press, 2006).

[58] Klimov, V. I., Mikhailovsky, A. A., McBranch, D. W., Leatherdale, C. A. & Bawendi, M. G. Quantization of Multiparticle Auger Rates in Semiconductor Quantum Dots. *Science* **287**, 1011–1013 (2000).

[59] Weston, K. D., Dyck, M., Tinnefeld, P., Müller, C., Herten, D. P. & Sauer, M. Measuring the Number of Independent Emitters in Single-Molecule Fluorescence Images and Trajectories Using Coincident Photons. *Analytical Chemistry* **74**, 5342–5349 (2002).

[60] Nair, G., Zhao, J. & Bawendi, M. G. Biexciton Quantum Yield of Single Semiconductor Nanocrystals from Photon Statistics. *Nano Letters* **11**, 1136–1140 (2011).

[61] van Driel, A. F., Allan, G., Delerue, C., Lodahl, P., Vos, W. L. & Vanmaekelbergh, D. Frequency-Dependent Spontaneous Emission Rate from CdSe and CdTe Nanocrystals: Influence of Dark States. *Physical Review Letters* **95**, 236804 (2005).

[62] Nikolaev, I., Lodahl, P., van Driel, A., Koenderink, A. & Vos, W. Strongly nonexponential time-resolved fluorescence of quantum-dot ensembles in three-dimensional photonic crystals. *Physical Review B* **75**, 115302 (2007).

[63] Chen, Y., Vela, J., Htoon, H., Casson, J. L., Werder, D. J., Bussian, D. A., Klimov, V. I. & Hollingsworth, J. A. "Giant" Multishell CdSe Nanocrystal Quantum Dots with Suppressed Blinking. *Journal of the American Chemical Society* **130**, 5026–5027 (2008).

[64] Mahler, B., Spinicelli, P., Buil, S., Quelin, X., Hermier, J.-P. & Dubertret, B. Towards non-blinking colloidal quantum dots. *Nature Materials* **7**, 659–664 (2008).

[65] Xiang, Z. & Lu, Y. Electromagnetic dyadic Green's function in cylindrically multilayered media. *IEEE Transactions on Microwave Theory and Techniques* **44**, 614–621 (1996).

[66] Barthes, J., Colas des Francs, G., Bouhelier, A., Weeber, J.-C. & Dereux, A. Purcell factor for a point-like dipolar emitter coupled to a two-dimensional plasmonic waveguide. *Physical Review B* **84**, 073403 (2011).

[67] Bermúdez-Ureña, E., Gonzalez-Ballestero, C., Geiselmann, M., Marty, R., Radko, I. P., Holmgaard, T., Alaverdyan, Y., Moreno, E., García-Vidal, F. J., Bozhevolnyi, S. I. & Quidant, R. Coupling of individual quantum emitters to channel plasmons. *Nature Communications* **6**, 7883 (2015).

[68] Kress, S. J. P., Antolinez, F. V., Richner, P., Jayanti, S. V., Kim, D. K., Prins, F., Riedinger, A., Fischer, M. P. C., Meyer, S., McPeak, K. M., Poulikakos, D. & Norris, D. J. Wedge Waveguides and Resonators for Quantum Plasmonics. *Nano Letters* **15**, 6267–6275 (2015).

[69] Gaio, M., Moffa, M., Castro-Lopez, M., Pisignano, D., Camposeo, A. & Sapienza, R. Modal Coupling of Single Photon Emitters Within Nanofiber Waveguides. *ACS Nano* **10**, 6125–6130 (2016).

[70] Oulton, R. F., Sorger, V. J., Genov, D. A., Pile, D. F. P. & Zhang, X. A hybrid plasmonic waveguide for subwavelength confinement and long-range propagation. *Nature Photonics* **2**, 496–500 (2008).

[71] Biehs, S.-A., Menon, V. M. & Agarwal, G. S. Long-range dipole-dipole interaction and anomalous Förster energy transfer across a hyperbolic metamaterial. *Physical Review B* **93**, 245439 (2016).

[72] Mie, G. Beiträge zur Optik trüber Medien, speziell kolloidaler Metallösungen. *Annalen der Physik* **330**, 377–445 (1908).

[73] Kuznetsov, A. I., Miroshnichenko, A. E., Brongersma, M. L., Kivshar, Y. S. & Luk'yanchuk, B. Optically resonant dielectric nanostructures. *Science* **354**, aag2472 (2016).

[74] Kerker, M., Wang, D.-S. & Giles, C. L. Electromagnetic scattering by magnetic spheres. *JOSA* **73**, 765–767 (1983).

[75] Person, S., Jain, M., Lapin, Z., Sáenz, J. J., Wicks, G. & Novotny, L. Demonstration of Zero Optical Backscattering from Single Nanoparticles. *Nano Letters* **13**, 1806–1809 (2013).

[76] Valentine, J., Zhang, S., Zentgraf, T., Ulin-Avila, E., Genov, D. A., Bartal, G. & Zhang, X. Three-dimensional optical metamaterial with a negative refractive index. *Nature* **455**, 376–379 (2008).

[77] García-Etxarri, A., Gómez-Medina, R., Froufe-Pérez, L. S., López, C., Chantada, L., Scheffold, F., Aizpurua, J., Nieto-Vesperinas, M. & Sáenz, J. J. Strong magnetic response of submicron Silicon particles in the infrared. *Optics Express* **19**, 4815–4826 (2011).

[78] Rolly, B., Bebey, B., Bidault, S., Stout, B. & Bonod, N. Promoting magnetic dipolar transition in trivalent lanthanide ions with lossless Mie resonances. *Physical Review B* **85**, 245432 (2012).

[79] Caldarola, M., Albella, P., Cortés, E., Rahmani, M., Roschuk, T., Grinblat, G., Oulton, R. F., Bragas, A. V. & Maier, S. A. Non-plasmonic nanoantennas for surface enhanced spectroscopies with ultra-low heat conversion. *Nature Communications* **6**, 7915 (2015).

[80] Cambiasso, J., Grinblat, G., Li, Y., Rakovich, A., Cortés, E. & Maier, S. A. Bridging the Gap between Dielectric Nanophotonics and the Visible Regime with Effectively Lossless Gallium Phosphide Antennas. *Nano Letters* **17**, 1219–1225 (2017).

[81] Regmi, R., Berthelot, J., Winkler, P. M., Mivelle, M., Proust, J., Bedu, F., Ozerov, I., Begou, T., Lumeau, J., Rigneault, H., García-Parajó, M. F., Bidault, S., Wenger, J. & Bonod, N. All-Dielectric Silicon Nanogap Antennas To Enhance the Fluorescence of Single Molecules. *Nano Letters* **16**, 5143–5151 (2016).

[82] Frimmer, M., Chen, Y. & Koenderink, A. Scanning Emitter Lifetime Imaging Microscopy for Spontaneous Emission Control. *Physical Review Letters* **107**, 123602 (2011).

[83] Schell, A. W., Engel, P., Werra, J. F. M., Wolff, C., Busch, K. & Benson, O. Scanning Single Quantum Emitter Fluorescence Lifetime Imaging: Quantitative Analysis of the Local Density of Photonic States. *Nano Letters* **14**, 2623–2627 (2014).

[84] Cao, D., Cazé, A., Calabrese, M., Pierrat, R., Bardou, N., Collin, S., Carminati, R., Krachmalnicoff, V. & De Wilde, Y. Mapping the Radiative and the Apparent

Nonradiative Local Density of States in the Near Field of a Metallic Nanoantenna. *ACS Photonics* **2**, 189–193 (2015).

[85] Bouchet, D., Mivelle, M., Proust, J., Gallas, B., Ozerov, I., Garcia-Parajo, M. F., Gulinatti, A., Rech, I., De Wilde, Y., Bonod, N., Krachmalnicoff, V. & Bidault, S. Enhancement and Inhibition of Spontaneous Photon Emission by Resonant Silicon Nanoantennas. *Physical Review Applied* **6**, 064016 (2016).

[86] Pendry, J. B., Holden, A. J., Robbins, D. J. & Stewart, W. J. Magnetism from conductors and enhanced nonlinear phenomena. *IEEE Transactions on Microwave Theory and Techniques* **47**, 2075–2084 (1999).

[87] Klein, M. W., Enkrich, C., Wegener, M., Soukoulis, C. M. & Linden, S. Single-slit split-ring resonators at optical frequencies: limits of size scaling. *Optics Letters* **31**, 1259–1261 (2006).

[88] Evlyukhin, A. B., Novikov, S. M., Zywietz, U., Eriksen, R. L., Reinhardt, C., Bozhevolnyi, S. I. & Chichkov, B. N. Demonstration of Magnetic Dipole Resonances of Dielectric Nanospheres in the Visible Region. *Nano Letters* **12**, 3749–3755 (2012).

[89] Proust, J., Bedu, F., Chenot, S., Soumahoro, I., Ozerov, I., Gallas, B., Abdeddaim, R. & Bonod, N. Chemical Alkaline Etching of Silicon Mie Particles. *Advanced Optical Materials* **3**, 1280–1286 (2015).

[90] Mühlschlegel, P., Toquant, J., Pohl, D. W. & Hecht, B. Glue-free tuning fork shear-force microscope. *Review of Scientific Instruments* **77**, 016105 (2006).

[91] Belacel, C., Habert, B., Bigourdan, F., Marquier, F., Hugonin, J.-P., Michaelis de Vasconcellos, S., Lafosse, X., Coolen, L., Schwob, C., Javaux, C., Dubertret, B., Greffet, J.-J., Senellart, P. & Maitre, A. Controlling Spontaneous Emission with Plasmonic Optical Patch Antennas. *Nano Letters* **13**, 1516–1521 (2013).

[92] Koenderink, A. F. Single-Photon Nanoantennas. *ACS Photonics* **4**, 710–722 (2017).

[93] Acuna, G. P., Möller, F. M., Holzmeister, P., Beater, S., Lalkens, B. & Tinnefeld, P. Fluorescence Enhancement at Docking Sites of DNA-Directed Self-Assembled Nanoantennas. *Science* **338**, 506–510 (2012).

[94] Bidault, S., Devilez, A., Maillard, V., Lermusiaux, L., Guigner, J.-M., Bonod, N. & Wenger, J. Picosecond Lifetimes with High Quantum Yields from Single-Photon-Emitting Colloidal Nanostructures at Room Temperature. *ACS Nano* **10**, 4806–4815 (2016).

[95] Haar, M. A. v. d., Groep, J. v. d., Brenny, B. J. M. & Polman, A. Controlling magnetic and electric dipole modes in hollow silicon nanocylinders. *Optics Express* **24**, 2047–2064 (2016).

[96] Pohl, D. W., Denk, W. & Lanz, M. Optical stethoscopy: Image recording with resolution $\lambda/20$. *Applied Physics Letters* **44**, 651–653 (1984).

[97] Hell, S. W. & Wichmann, J. Breaking the diffraction resolution limit by stimulated emission: stimulated-emission-depletion fluorescence microscopy. *Optics Letters* **19**, 780–782 (1994).

[98] Moerner, W. E. & Kador, L. Optical detection and spectroscopy of single molecules in a solid. *Physical Review Letters* **62**, 2535–2538 (1989).

[99] Orrit, M. & Bernard, J. Single pentacene molecules detected by fluorescence excitation in a p-terphenyl crystal. *Physical Review Letters* **65**, 2716–2719 (1990).

[100] Weiss, S. Fluorescence Spectroscopy of Single Biomolecules. *Science* **283**, 1676–1683 (1999).

[101] Patterson, G. H. & Lippincott-Schwartz, J. A Photoactivatable GFP for Selective Photolabeling of Proteins and Cells. *Science* **297**, 1873–1877 (2002).

[102] Hess, S. T., Girirajan, T. P. K. & Mason, M. D. Ultra-High Resolution Imaging by Fluorescence Photoactivation Localization Microscopy. *Biophysical Journal* **91**, 4258–4272 (2006).

[103] Rust, M. J., Bates, M. & Zhuang, X. Sub-diffraction-limit imaging by stochastic optical reconstruction microscopy (STORM). *Nature Methods* **3**, 793–796 (2006).

[104] Schermelleh, L., Heintzmann, R. & Leonhardt, H. A guide to super-resolution fluorescence microscopy. *The Journal of Cell Biology* **190**, 165–175 (2010).

[105] Gadella, T. W. J., Jovin, T. M. & Clegg, R. M. Fluorescence lifetime imaging microscopy (FLIM): Spatial resolution of microstructures on the nanosecond time scale. *Biophysical Chemistry* **48**, 221–239 (1993).

[106] Berezin, M. Y. & Achilefu, S. Fluorescence Lifetime Measurements and Biological Imaging. *Chemical Reviews* **110**, 2641–2684 (2010).

[107] Johlin, E., Solari, J., Mann, S. A., Wang, J., Shimizu, T. S. & Garnett, E. C. Super-resolution imaging of light–matter interactions near single semiconductor nanowires. *Nature Communications* **7**, 13950 (2016).

[108] Mack, D. L., Cortés, E., Giannini, V., Török, P., Roschuk, T. & Maier, S. A. Decoupling absorption and emission processes in super-resolution localization of emitters in a plasmonic hotspot. *Nature Communications* **8**, 14513 (2017).

[109] Auksorius, E., Boruah, B. R., Dunsby, C., Lanigan, P. M. P., Kennedy, G., Neil, M. A. A. & French, P. M. W. Stimulated emission depletion microscopy with a supercontinuum source and fluorescence lifetime imaging. *Optics Letters* **33**, 113–115 (2008).

[110] Guo, K., Verschuuren, M. A. & Femius Koenderink, A. Superresolution imaging of the local density of states in plasmon lattices. *Optica* **3**, 289–298 (2016).

[111] Heilemann, M., van de Linde, S., Schüttpelz, M., Kasper, R., Seefeldt, B., Mukherjee, A., Tinnefeld, P. & Sauer, M. Subdiffraction-Resolution Fluorescence Imaging with Conventional Fluorescent Probes. *Angewandte Chemie International Edition* **47**, 6172–6176 (2008).

[112] van de Linde, S., Löschberger, A., Klein, T., Heidbreder, M., Wolter, S., Heilemann, M. & Sauer, M. Direct stochastic optical reconstruction microscopy with standard fluorescent probes. *Nature Protocols* **6**, 991–1009 (2011).

[113] Ovesný, M., Křížek, P., Borkovec, J., Švindrych, Z. & Hagen, G. M. ThunderSTORM: a comprehensive ImageJ plug-in for PALM and STORM data analysis and super-resolution imaging. *Bioinformatics* **30**, 2389–2390 (2014).

[114] Izeddin, I., Boulanger, J., Racine, V., Specht, C. G., Kechkar, A., Nair, D., Triller, A., Choquet, D., Dahan, M. & Sibarita, J. B. Wavelet analysis for single molecule localization microscopy. *Optics Express* **20**, 2081–2095 (2012).

[115] Maronna, R. A., Martin, D. R. & Yohai, V. J. Dispersion estimates. In *Robust Statistics: Theory and Methods*, 32–34 (Wiley-Blackwell, Chichester, 2006).

[116] Torquato, S. Nearest-neighbor statistics for packings of hard spheres and disks. *Physical Review E* **51**, 3170–3182 (1995).

[117] Oskooi, A. F., Roundy, D., Ibanescu, M., Bermel, P., Joannopoulos, J. D. & Johnson, S. G. Meep: A flexible free-software package for electromagnetic simulations by the FDTD method. *Computer Physics Communications* **181**, 687–702 (2010).

[118] Larkin, I. A., Stockman, M. I., Achermann, M. & Klimov, V. I. Dipolar emitters at nanoscale proximity of metal surfaces: Giant enhancement of relaxation in microscopic theory. *Physical Review B* **69**, 121403 (2004).

[119] Castanié, E., Boffety, M. & Carminati, R. Fluorescence quenching by a metal nanoparticle in the extreme near-field regime. *Optics Letters* **35**, 291–293 (2010).

[120] Gould, T. J., Gunewardene, M. S., Gudheti, M. V., Verkhusha, V. V., Yin, S.-R., Gosse, J. A. & Hess, S. T. Nanoscale imaging of molecular positions and anisotropies. *Nature Methods* **5**, 1027–1030 (2008).

[121] Cruz, C. A. V., Shaban, H. A., Kress, A., Bertaux, N., Monneret, S., Mavrakis, M., Savatier, J. & Brasselet, S. Quantitative nanoscale imaging of orientational order in biological filaments by polarized superresolution microscopy. *Proceedings of the National Academy of Sciences* **113**, E820–E828 (2016).

[122] Izeddin, I., Récamier, V., Bosanac, L., Cissé, I. I., Boudarene, L., Dugast-Darzacq, C., Proux, F., Bénichou, O., Voituriez, R., Bensaude, O., Dahan, M. & Darzacq, X. Single-molecule tracking in live cells reveals distinct target-search strategies of transcription factors in the nucleus. *eLife* **3**, e02230 (2014).

[123] Rech, I., Marangoni, S., Resnati, D., Ghioni, M. & Cova, S. Multipixel single-photon avalanche diode array for parallel photon counting applications. *Journal of Modern Optics* **56**, 326–333 (2009).

[124] Huang, B., Wang, W., Bates, M. & Zhuang, X. Three-Dimensional Super-Resolution Imaging by Stochastic Optical Reconstruction Microscopy. *Science* **319**, 810–813 (2008).

[125] Chizhik, A. I., Rother, J., Gregor, I., Janshoff, A. & Enderlein, J. Metal-induced energy transfer for live cell nanoscopy. *Nature Photonics* **8**, 124–127 (2014).

[126] Weisenburger, S., Boening, D., Schomburg, B., Giller, K., Becker, S., Griesinger, C. & Sandoghdar, V. Cryogenic optical localization provides 3d protein structure data with Angstrom resolution. *Nature Methods* **14**, 141–144 (2017).

[127] Bates, M., Huang, B., Dempsey, G. T. & Zhuang, X. Multicolor Super-Resolution Imaging with Photo-Switchable Fluorescent Probes. *Science* **317**, 1749–1753 (2007).

[128] Rao, C. R. Information and accuracy attainable in the estimation of statistical parameters. *Bulletin of the Calcutta Mathematical Society* **37**, 81–91 (1945).

[129] Harald Cramer. Minimum variance of an estimate. Efficient estimates. In *Mathematical Methods Of Statistics*, 477–487 (1946).

[130] Bobroff, N. Position measurement with a resolution and noise-limited instrument. *Review of Scientific Instruments* **57**, 1152–1157 (1986).

[131] Thompson, R. E., Larson, D. R. & Webb, W. W. Precise Nanometer Localization Analysis for Individual Fluorescent Probes. *Biophysical Journal* **82**, 2775–2783 (2002).

[132] Chao, J., Ward, E. S. & Ober, R. J. Fisher information matrix for branching processes with application to electron-multiplying charge-coupled devices. *Multidimensional systems and signal processing* **23**, 349–379 (2012).

[133] Mortensen, K. I., Churchman, L. S., Spudich, J. A. & Flyvbjerg, H. Optimized localization analysis for single-molecule tracking and super-resolution microscopy. *Nature Methods* **7**, 377–381 (2010).

[134] Deschout, H., Zanacchi, F. C., Mlodzianoski, M., Diaspro, A., Bewersdorf, J., Hess, S. T. & Braeckmans, K. Precisely and accurately localizing single emitters in fluorescence microscopy. *Nature Methods* **11**, 253–266 (2014).

[135] Chao, J., Ward, E. S. & Ober, R. J. Fisher information theory for parameter estimation in single molecule microscopy: tutorial. *JOSA A* **33**, B36–B57 (2016).

[136] Bajzer, Ž., Therneau, T. M., Sharp, J. C. & Prendergast, F. G. Maximum likelihood method for the analysis of time-resolved fluorescence decay curves. *European Biophysics Journal* **20**, 247–262 (1991).

[137] Tellinghuisen, J. & Wilkerson, C. W. Bias and precision in the estimation of exponential decay parameters from sparse data. *Analytical Chemistry* **65**, 1240–1246 (1993).

[138] Rowley, M. I., Barber, P. R., Coolen, A. C. C. & Vojnovic, B. Bayesian analysis of fluorescence lifetime imaging data. *Proc. SPIE* **7903**, 790325 (2011).

[139] Kaye, B., Foster, P. J., Yoo, T. Y. & Needleman, D. J. Developing and Testing a Bayesian Analysis of Fluorescence Lifetime Measurements. *PLOS ONE* **12**, e0169337 (2017).

[140] Köllner, M. & Wolfrum, J. How many photons are necessary for fluorescence-lifetime measurements? *Chemical Physics Letters* **200**, 199–204 (1992).

[141] Riley, K. F., Hobson, M. P. & Bence, S. J. Maximum-likelihood method. In *Mathematical Methods for Physics and Engineering: A Comprehensive Guide*, 1225–1271 (Cambridge University Press, Cambridge ; New York, 2006).

[142] Kay, S. Cramer-Rao Lower Bound. In *Fundamentals of Statistical Processing, Volume I: Estimation Theory*, 27–82 (Prentice Hall, Englewood Cliffs, N.J, 1993).

[143] Lehmann, E. L. & Casella, G. The information inequality. In *Theory of Point Estimation*, 113–123 (Springer, New York, 2003).

[144] Wertz, E., Isaacoff, B. P., Flynn, J. D. & Biteen, J. S. Single-Molecule Super-Resolution Microscopy Reveals How Light Couples to a Plasmonic Nanoantenna on the Nanometer Scale. *Nano Letters* **15**, 2662–2670 (2015).

[145] Su, L., Yuan, H., Lu, G., Rocha, S., Orrit, M., Hofkens, J. & Uji-i, H. Super-resolution Localization and Defocused Fluorescence Microscopy on Resonantly Coupled Single-Molecule, Single-Nanorod Hybrids. *ACS Nano* **10**, 2455–2466 (2016).

[146] Fu, B., Isaacoff, B. P. & Biteen, J. S. Super-Resolving the Actual Position of Single Fluorescent Molecules Coupled to a Plasmonic Nanoantenna. *ACS Nano* **11**, 8978–8987 (2017).

[147] Devroye, L. The inversion method. In *Non-uniform Random Variate Generation*, 27–39 (Springer-Verlag New York Inc., 1986).

[148] Abraham, A. V., Ram, S., Chao, J., Ward, E. S. & Ober, R. J. Quantitative study of single molecule location estimation techniques. *Optics Express* **17**, 23352–23373 (2009).

[149] Dousse, A., Lanco, L., Suffczyński, J., Semenova, E., Miard, A., Lemaître, A., Sagnes, I., Roblin, C., Bloch, J. & Senellart, P. Controlled Light-Matter Coupling for a Single Quantum Dot Embedded in a Pillar Microcavity Using Far-Field Optical Lithography. *Physical Review Letters* **101**, 267404 (2008).

[150] Kress, S. J. P., Richner, P., Jayanti, S. V., Galliker, P., Kim, D. K., Poulikakos, D. & Norris, D. J. Near-Field Light Design with Colloidal Quantum Dots for Photonics and Plasmonics. *Nano Letters* **14**, 5827–5833 (2014).

[151] Curto, A. G., Volpe, G., Taminiau, T. H., Kreuzer, M. P., Quidant, R. & Hulst, N. F. v. Unidirectional Emission of a Quantum Dot Coupled to a Nanoantenna. *Science* **329**, 930–933 (2010).

[152] Sipahigil, A., Evans, R. E., Sukachev, D. D., Burek, M. J., Borregaard, J., Bhaskar, M. K., Nguyen, C. T., Pacheco, J. L., Atikian, H. A., Meuwly, C., Camacho, R. M., Jelezko, F., Bielejec, E., Park, H., Lončar, M. & Lukin, M. D. An integrated diamond nanophotonics platform for quantum-optical networks. *Science* **354**, 847–850 (2016).

[153] Fauché, P. *Plasmonic superradiance in metallo-dielectric nanohybrids.* Ph.D. thesis, Université de Bordeaux (2016).

[154] Levine, H. & Schwinger, J. On the theory of electromagnetic wave diffraction by an aperture in an infinite plane conducting screen. *Communications on Pure and Applied Mathematics* **3**, 355–391 (1950).

[155] Van Bladel, J. Some remarks on green's dyadic for infinite space. *IRE Transactions on Antennas and Propagation* **9**, 563–566 (1961).

[156] Sipe, J. E. New Green-function formalism for surface optics. *Journal of the Optical Society of America B* **4**, 481–489 (1987).

[157] Taflove, A., Oskooi, A. & Johnson, S. G. Currents and fields: the local density of states. In *Advances in FDTD Computational Electrodynamics: Photonics and Nanotechnology*, 73–83 (Artech House, 2013).

Résumé

Dans cette thèse, nous associons mesures expérimentales et modélisation des données pour étudier l'émission spontanée d'émetteurs fluorescents en environnement nano-structuré. Le mémoire est organisé en deux parties.

Dans la première partie, nous étudions le transfert d'énergie entre émetteurs fluorescents en environnement plasmonique et sur des distances micrométriques. Pour commencer, nous caractérisons le transfert d'énergie entre deux ensembles d'émetteurs situés en champ proche d'une surface d'argent. Nous déterminons ainsi la dépendance en distance du taux de transfert d'énergie sur des distances micrométriques. Nous couplons ensuite une boite quantique et une bille fluorescente à un nano-fil d'argent et nous étudions le transfert d'énergie entre ces deux émetteurs, distants de plusieurs micromètres. Nous démontrons notamment le clignotement corrélé de ces deux émetteurs grâce à l'étude de la fonction de corrélation de leur intensité de fluorescence.

Dans la seconde partie, nous sondons les variations spatiales de densité locale d'états électromagnétiques induites par des environnements nano-structurés grâce à différentes techniques de microscopie à super-résolution. A l'aide d'un microscope à balayage, nous réalisons tout d'abord une étude en trois dimensions de l'interaction de champ proche entre une bille fluorescente et différentes antennes en silicium. Nous introduisons ensuite une technique stochastique permettant de déterminer expérimentalement la position et le taux d'amortissement de molécules uniques photo-activées, avec une précision de localisation de l'ordre de 10 nm. Enfin, nous utilisons l'information de Fisher afin d'estimer les bornes inférieures de l'erreur type des estimations de positions et de taux d'amortissement réalisées dans le cadre de mesures sur molécules uniques.

Mots Clés

Durée de vie de fluorescence, Champ proche, Emission spontanée, Densité d'états électromagnétiques, Plasmon de surface, antenne diélectrique, Imagerie de super-résolution, Molécule unique, Borne de Cramér-Rao

Abstract

In this thesis, we perform experimental measurements and data modelling to investigate spontaneous emission of fluorescent emitters in nanostructured environments. The manuscript is organised into two main parts.

In the first part, we study micrometre-range energy transfer between fluorescent emitters in plasmonic environments. First of all, we characterise plasmon-mediated energy transfer between ensembles of fluorescent emitters located in the near field of a silver film. We thus determine the distance dependence of the energy transfer rate over micrometre distances. We then couple a single quantum dot and a fluorescent nanobead to a silver nanowire and we study evidences of the energy transfer between the two emitters, separated by several micrometres. We notably demonstrate a correlated blinking of the two emitters through the study of the correlation function of their fluorescence intensity.

In the second part, we probe sub-wavelength spatial variations of the local density of electromagnetic states induced by nanostructured environments by means of different super-resolution microscopy techniques. To start with, we perform a three-dimensional study of the near-field interaction between a fluorescent nanobead and different silicon nanoantennas using a scanning-probe microscope. We then introduce a stochastic technique to experimentally determine the position and the fluorescence decay rate of single photo-activated molecules, with a localisation precision of the order of 10 nm. Finally, we use the Fisher information to estimate lower bounds on the standard errors on position and decay rate estimates performed in the context of single-molecule microscopy.

Keywords

Fluorescence lifetime, Near field, Spontaneous emission, Electromagnetic density of states, Surface plasmon, Dielectric antenna, Super-resolution imaging, Single molecule, Cramér-Rao bound